



Universitetet
i Stavanger

FACULTY OF SCIENCE AND TECHNOLOGY

MASTER'S THESIS

Study programme/specialisation: Offshore Technology Specialization: Marine and Subsea Technology	Spring semester, June, 2018 Open access
Author: Kunal Kapoor (signature of author)
Programme coordinator: Professor Muk Chen Ong Supervisor(s): Professor Muk Chen Ong and Dr. Zhenhui Liu	
Title of master's thesis: Vortex Induced Vibration (VIV) response and multi-axial fatigue assessment of a subsea rigid jumper	
Credits: 30 ECTS	
Keywords: DNVGL-RP-F105, Subsea jumper, Vortex induced vibration, VIV response model, Modal analysis, Multimode response, Multiaxial fatigue, Critical plane energy method, Finite element analysis, Ansys Mechanical Workbench, Flexural stress, Torsional stress	Number of pages: 183 + enclosure: 89 Stavanger, June 15, 2018

ABSTRACT

Vortex induced vibrations (VIV) prediction is of interest for subsea jumpers or spools that are exposed to significant current/wave conditions near the seabed. The VIV induces cyclic flexural and torsional stresses in jumper/spool which leads to fatigue damage. Due to jumper/spool's topology characteristics, multi-axial stress states may exist. The recommended practices for such fatigue damage assessment by DNVGL-RP-F105 (2017 edition) [11] uses the first principal stress method together with the S-N curves. However, the S-N curves are normally based on uniaxial test data and do not represent the real stress state of the system.

In this study, an effort has been made to determine the VIV response using the latest edition of DNVGL-RP-F105 (2017 edition) [11]. The fatigue assessment is carried out by using Farahani [13,14]'s fatigue damage parameter for the first time. This parameter is based on critical plane energy method. The fatigue damage is calculated on a critical plane, which is determined using the maximum shear strain criterion. The phase change due to difference in response frequency of the loads is included in the calculation, which is normally ignored in design practise for VIV fatigue assessments of subsea pipelines.

Furthermore, an effort has been made to highlight the major changes in DNVGL-RP-F105 (2017 edition) [11] edition in comparison to the previous edition of 2006 for the VIV assessment to subsea jumpers/spools. The changes regarding response model and stress range calculation have been discussed as well.

ACKNOWLEDGEMENTS

I would like to thank my supervisors, Prof. Muk Chen Ong and Dr. Zhenhui Liu for their guidance and motivation throughout the course of this thesis.

I would also like to thank my parents and wife for their support and understanding.

ABBREVIATIONS

3D	Three dimensional
APDL	ANSYS Parametric Design Language
CF	Cross-flow
DNV	Det Norske Veritas
FE	Finite element
FLS	Fatigue limit state
IL	In-line
KC	Keulengan-Carpenter
MIT	Massachusetts Institute of Technology
SMT	Smith – Watson - Topper
ULS	Ultimate limit state
VIV	Vortex induced vibration

TABLE OF CONTENTS

ABSTRACT	I
ACKNOWLEDGEMENTS	II
ABBREVIATIONS	III
TABLE OF CONTENTS	IV
LIST OF FIGURES	VII
LIST OF TABLES	XVIII
1 INTRODUCTION	1
1.1 BACKGROUND AND MOTIVATION	1
1.2 OBJECTIVES	4
2 THEORY	7
2.1 VORTEX INDUCED VIBRATION	7
2.2 FATIGUE.....	17
3 LITERATURE REVIEW	27
3.1 STRESS BASED MODELS	27
3.2 CRITICAL PLANE APPROACH.....	29
3.3 ENERGY-BASED APPROACH.....	33
3.4 COMBINED CRITICAL PLANE ENERGY-BASED APPROACH.....	34
4 METHODOLOGY	41
4.1 3D MODEL.....	42
4.2 MODAL ANALYSIS	45
4.3 MODE CLASSIFICATION	47
4.4 RESPONSE MODEL BASED ON DNVGL-RP-F105 (2017 EDITION) [11].....	51
4.5 STRESS RANGE CALCULATION	63
4.6 FATIGUE ASSESSMENT	75
5 MODAL ANALYSIS	85
5.1 3D MODEL.....	85
5.2 MODAL ANALYSIS USING FEM.....	87

5.3	SINGLE POINT ANALYSIS	97
5.4	MODE CLASSIFICATION BASED ON FLOW ORIENTATION	98
5.5	DESIGN ASSESSMENT	99
5.6	DISCUSSION	108
6	RESPONSE MODEL	124
6.1	IN-LINE RESPONSE MODEL.....	124
6.2	CROSS-FLOW RESPONSE MODEL	128
6.3	MODE CLASSIFICATION BASED ON MULTIMODE RESPONSE.....	130
6.4	DISCUSSION	134
7	STRESS RANGE	136
7.1	UNIT AMPLITUDE STRESS	136
7.2	UNIT AMPLITUDE RESPONSE.....	137
7.3	STRESS RANGE	140
7.4	DISCUSSION	145
8	FATIGUE ASSESSMENT.....	154
8.1	BLOCK LOADING.....	154
8.2	CRITICAL PLANE	156
8.3	NORMAL AND SHEAR STRESS AND STRAIN RANGE.....	159
8.4	FATIGUE.....	161
8.5	DISCUSSION	164
9	COMPARISON WITH DNV-RP-F105 (2006 EDITION) [12].....	170
9.1	MODAL ANALYSIS.....	170
9.2	RESPONSE MODEL	171
9.3	STRESS RANGE CALCULATION.....	174
10	CONCLUSION	175
10.1	MODAL ANALYSIS.....	175
10.2	RESPONSE MODEL	175
10.3	STRESS RANGE CALCULATION	175
10.4	FATIGUE ASSESSMENT	176
10.5	COMPARISON BETWEEN 2017 EDITION AND 2006 EDITION OF DNVGL-RP-F105 ..	177

11 FUTURE WORK.....	178
12 REFERENCES.....	179
13 APPENDIX A	184
10° FLOW IN-LINE.....	185
10° FLOW CROSS-FLOW	187
90° FLOW IN-LINE.....	189
90° FLOW CROSS-FLOW	191
14 APPENDIX B	193
CASE-1 (A) – 10° IL LOCATION A	194
CASE-1 (A) – 10° IL LOCATION B	205
CASE-1 (B) – 10° CF LOCATION A	216
CASE-1 (B) – 10° CF LOCATION B	227
CASE-2 (A) – 90° IL LOCATION A	238
CASE-2 (A) – 90° IL LOCATION B	249
CASE-2 (B) – 90° CF LOCATION A	260
CASE-2 (B) – 90° CF LOCATION B	271

LIST OF FIGURES

Figure 1-1: (a) Fatigue damage in pipelines (Marathon Ashland pipeline LLC, Winchester, Kentucky) [35]; (b) Alexander L. Kielland Accident (Wall Street Journal).....	4
Figure 2-1: Kármán vortex street in the wake of a circular cylinder from Wikipedia [55].....	8
Figure 2-2: Effect of Reynolds number (Re) on vortex shedding pattern for a cylinder in uniform current flow according to Lienhard [27]	8
Figure 2-3: Effect of lift coefficient (CL) on the response amplitude (A/D) according to Govardhan et al. [21] and Klamo et al. [26] from Resvanis et al. [37].....	10
Figure 2-4: Effect of Reynolds number (Re) on the in-line and cross-flow response amplitude (A/D) according to Resvanis et al. [37]	11
Figure 2-5: Reynolds number (Re) and Strouhal number (St) relationship for a smooth and rough circular cylinder from Blevins [6]	12
Figure 2-6: In-line and cross-flow VIV [56].....	15
Figure 2-7: Proportional In-phase loading	20
Figure 2-8: Non-proportional out-of-phase loading	21
Figure 2-9: Transformation of planar stress state [University of Colorado Boulder].....	22
Figure 2-10: Plane of maximum shear [University of Colorado Boulder]	23
Figure 2-11: Types of shaft/pipe specimen [Laboratory Testing Inc.]	25
Figure 2-12: Types of cruciform specimen - Left to right – Cut type, Reduced section type and Strip and slop Type [22].....	25
Figure 2-13: Boxbeam specimen details [22]	25
Figure 3-1: Tubular specimen used in fatigue tests, see McDiarmid [29].....	31
Figure 3-2: In-plane (Case-A) and out-of-plane (Case-B) shear [22].....	32
Figure 3-3: Hysteresis graph showing elastic and plastic strain energy regions	35
Figure 3-4: Load histories (a) A1-A2; (b) B1-B4; C1-C4 showing change of frequencies ($A1$, $B1,C1$), effect of mean stress ($A2$, $B2$, $B4$, $C2$, $C4$) and change of phase angle ($B3$, $C3$) [29]	37
Figure 3-5: Calculation of maximum shear stress range ($\Delta\tau_{max}$), maximum shear strain range ($\Delta\gamma_{max2}$) and corresponding normal stress range ($\Delta\sigma_n$) and strain range ($\Delta\epsilon_n$) values from Mohr circle for Load History B1 [29].....	37

Figure 4-1: Flow Chart for fatigue damage assessment for M-shaped rigid jumper	42
Figure 4-2: M-shaped rigid spool jumper model – ExxonMobil’s Jumper VIV Research Program	42
Figure 4-3: Towing experimental setup – ExxonMobil’s Jumper VIV Research Program (Wang et al. [46])	43
Figure 4-4: Location of accelerometers and strain gauges on spool model.....	44
Figure 4-5: Non-straight pipe geometry showing two modes (Mode 1 and 2) and three directions of current flow ($U\theta_1$, $U\theta_2$ and $U\theta_3$) [Recreated from DNVGL-RP-F105 (2017 edition) [11]].....	50
Figure 4-6: Calculation process for multi-mode response [DNVGL-RP-F105 (2017 edition) [11]].....	52
Figure 4-7: In-line response model [DNVGL-RP-F105 (2017 edition) [11]]	56
Figure 4-8: Reduction functions ($RI\theta_1$ and $RI\theta_2$) as a function of Turbulence Intensity (I_c) [DNVGL-RP-F105 (2017 edition) [11]].....	58
Figure 4-9: Cross-flow response model based on different α , KC and fratio values [DNVGL-RP-F105 (2017 edition) [11]]	59
Figure 4-10: Cross-flow response model [DNVGL-RP-F105 (2017 edition) [11]]	59
Figure 4-11: Trench proximity/factor [Recreated from DNVGL-RP-F105 (2017 edition) [11]]	61
Figure 4-12: Added mass coefficient due to cross-flow response (C_a , $CF - RES$) [DNVGL-RP-F105 (2017 edition) [11]]	75
Figure 5-1: Rigid jumper model in Ansys SpaceClaim 17.1	86
Figure 5-2: Cross-section data for rigid jumper in Ansys SpaceClaim 17.1	87
Figure 5-3: Project schematic in Ansys Mechanical Workbench 17.1	88
Figure 5-4: Gravitational acceleration & fixed supports in Static Structural module of Ansys Mechanical Workbench 17.1	88
Figure 5-5: Engineering Data in Ansys Mechanical Workbench	89
Figure 5-6: PIPE288 geometry [3].....	91
Figure 5-7: Node numbers after meshing in Ansys Mechanical Workbench.....	91
Figure 5-8: Total deformation and mode shape for Mode – 1	93
Figure 5-9: Total deformation and mode shape for Mode – 2.....	93

Figure 5-10: Total deformation and mode shape for Mode – 3	93
Figure 5-11: Total deformation and mode shape for Mode – 4	94
Figure 5-12: Total deformation and mode shape for Mode – 5	94
Figure 5-13: Total deformation and mode shape for Mode – 6	94
Figure 5-14: Total deformation and mode shape for Mode – 7	95
Figure 5-15: Total deformation and mode shape for Mode – 8	95
Figure 5-16: Total deformation and mode shape for Mode – 9	95
Figure 5-17: Unit amplitude stresses – Flexural stresses – All modes	96
Figure 5-18: Unit amplitude stresses – Torsional stresses – All modes	97
Figure 5-19: Project Schematic – Design assessment module in Ansys Mechanical Workbench 17.1	100
Figure 5-20: Maximum combined flexural modal stresses for 10° Flow - All In-line/Cross- flow modes	101
Figure 5-21: Maximum combined flexural modal stresses for 10° Flow - All In-line/Cross- flow modes from Design assessment module	101
Figure 5-22: Maximum combined torsional modal stresses for 10° Flow - All In-line/Cross- flow modes	102
Figure 5-23: Maximum combined torsional modal stresses for 10° Flow - All In-line/Cross- flow modes from Design assessment module	102
Figure 5-24: Maximum combined flexural modal stresses for 90° Flow - IL modes.....	104
Figure 5-25: Maximum combined flexural modal stresses for 90° Flow - IL modes (Design assessment).....	104
Figure 5-26: Maximum combined torsional modal stresses for 90° Flow - IL modes.....	105
Figure 5-27: Maximum combined torsional modal stresses for 90° Flow - IL modes (Design assessment).....	105
Figure 5-28: Maximum combined flexural modal stresses for 90° Flow - CF modes	106
Figure 5-29: Maximum combined flexural modal stresses for 90° Flow - CF modes (Design assessment).....	107
Figure 5-30: Maximum combined torsional modal stresses for 90° Flow - CF modes.....	107
Figure 5-31: Maximum combined torsional modal stresses for 90° Flow - CF modes (Design assessment).....	108

Figure 5-32: Comparison of total normalized displacement for mode-1.....	109
Figure 5-33: Comparison of total normalized displacement for mode-2.....	110
Figure 5-34: Comparison of total normalized displacement for mode-3.....	110
Figure 5-35: Comparison of total normalized displacement for mode-4.....	111
Figure 5-36: Comparison of total normalized displacement for mode-5.....	111
Figure 5-37: Comparison of total normalized displacement for mode-6.....	112
Figure 5-38: Comparison of total normalized displacement for mode-7.....	112
Figure 5-39: Comparison of total normalized displacement for mode-8.....	113
Figure 5-40: Comparison of total normalized displacement for mode-9.....	113
Figure 5-41: Comparison of unit amplitude stress with Igeh [24] for Mode-1	114
Figure 5-42: Comparison of unit amplitude stress with Igeh [24] for Mode-2	115
Figure 5-43: Comparison of unit amplitude stress with Igeh [24] for Mode-3	115
Figure 5-44: Comparison of unit amplitude stress with Igeh [24] for Mode-4	116
Figure 5-45: Comparison of unit amplitude stress with Igeh [24] for Mode-5	116
Figure 5-46: Comparison of unit amplitude stress with Igeh [24] for Mode-6	117
Figure 5-47: Comparison of unit amplitude stress with Igeh [24] for Mode-7	117
Figure 5-48: Comparison of unit amplitude stress with Igeh [24] for Mode-8	118
Figure 5-49: Comparison of unit amplitude stress with Igeh [24] for Mode-9	118
Figure 5-50: Unit amplitude stress (Flexural) for Mode-8	119
Figure 5-51: Unit amplitude stress (Torsional) for Mode-8	119
Figure 5-52: Unit amplitude stress (Flexural and Torsional) for 10° IL and CF modes	120
Figure 5-53: Unit amplitude stress (Flexural and Torsional) for 90° IL modes	120
Figure 5-54: Unit amplitude stress (Flexural and Torsional) for 90° CF modes.....	121
Figure 6-1: In-line response model for 10° Flow	126
Figure 6-2: In-line response model for 90° Flow	127
Figure 6-3: Cross-flow response model for 10° Flow	129
Figure 6-4: Cross-flow response model for 90° Flow	130
Figure 6-5: Mode-1 participation along the rigid jumper arc length towards unit amplitude flexural stress for 10° flow (In-line and Cross-flow).....	132
Figure 6-6: Mode-1 participation along the rigid jumper arc length towards unit amplitude torsional stress for 10° flow (In-line and Cross-flow)	132

Figure 7-1: Unit amplitude response for contributing IL modes (Case-1(a) - 10° Flow).....	138
Figure 7-2: Unit amplitude response for contributing CF modes (Case-1(b) - 10° Flow)	138
Figure 7-3: Unit amplitude response for contributing IL modes (Case-2(a) - 90° Flow).....	139
Figure 7-4: Unit amplitude response for contributing CF modes (Case-2(b) - 90° Flow)	139
Figure 7-5: Flexural stress range for all contributing modes (Case-1(a) - 10° Flow IL) at Location A.....	140
Figure 7-6: Torsional stress range for all contributing modes (Case-1(a) - 10° Flow IL) at Location A.....	141
Figure 7-7: Flexural stress range for all contributing modes (Case-1(a) - 10° Flow IL) at Location B.....	141
Figure 7-8: Torsional stress range for all contributing modes (Case-1(a) - 10° Flow IL) at Location B.....	142
Figure 7-9: Combined flexural and torsional stress range from all contributing modes (Case- 1(a) - 10° Flow IL) at Location A	143
Figure 7-10: Combined flexural and torsional stress range from all contributing modes (Case- 1(a) - 10° Flow IL) at Location B	143
Figure 7-11: Response frequency for combined flexural and torsional stress range from all contributing modes (Case-1(a) - 10° Flow IL) at Location A.....	144
Figure 7-12: Response frequency for combined flexural and torsional stress range from all contributing modes (Case-1(a) - 10° Flow IL) at Location B.....	144
Figure 7-13: Comparison of torsional and flexural stress range with Igeh [24] for 10° Flow - IL at Location A	147
Figure 7-14: Comparison of torsional and flexural stress range with Igeh [24] for 10° Flow - CF at Location A.....	147
Figure 7-15: Comparison of torsional and flexural stress range with Igeh [24] for 10° Flow - IL at Location B	148
Figure 7-16: Comparison of torsional and flexural stress range with Igeh [24] for 10° Flow - CF at Location B	149
Figure 7-17: Comparison of torsional and flexural stress range with Igeh [24] for 90° Flow - IL at Location A.....	150
Figure 7-18: Comparison of torsional and flexural stress range with Igeh [24] for 90° Flow – CF at Location A.....	151

Figure 7-19: Comparison of torsional and flexural stress range with Igeh [24] for 90° Flow IL at Location B	152
Figure 7-20: Comparison of torsional and flexural stress range with Igeh [24] for 90° Flow – CF at Location B	152
Figure 8-1: Principal Stress (σ_{11}, σ_{33}) variation with time (s) for Case-1 (a) at Location – A for U=0.14 m/s	155
Figure 8-2: Principal Stress (σ_{11}, σ_{33}) variation with angle (θ_{11}) for Case-1 (a) at Location – A for U=0.14 m/s	155
Figure 8-3: Principal Strains ($\varepsilon_{11}, \varepsilon_{33}$) variation with angle (θ_{11}) for Case-1 (a) at Location – A for U=0.14 m/s	157
Figure 8-4: Maximum shear strain (γ_{max2}) variation with angle (θ_{11}) for Case-1 (a) at Location – A for U=0.14 m/s	157
Figure 8-5: Normal stress range ($\Delta\sigma_n$) and maximum shear stress range ($\Delta\tau_{max}$) for each full cycle of (θ_{11}) for Case-1 (a) at Location – A for U=0.14 m/s	159
Figure 8-6: Normal strain range ($\Delta\varepsilon_n$) and maximum shear strain range ($\Delta\gamma_{max2}$) for each full cycle of (θ_{11}) for Case-1 (a) at Location – A for U=0.14 m/s.....	160
Figure 8-7: Fatigue damage for block loading for Case-1 (a) at Location – A for U=0.14 m/s	162
Figure 8-8: Fatigue damage per year for (Case-1(a) - 10° Flow IL) at Location A	164
Figure 8-9: Combined fatigue damage per year for 10° Flow at Location A.....	165
Figure 8-10: Combined fatigue damage per year for 10° Flow at Location B	166
Figure 8-11: Combined fatigue damage per year for 90° Flow at Location A.....	167
Figure 8-12: Combined fatigue damage per year for 90° Flow at Location B	167
Figure 8-13: Fatigue damage per year for (Case-1(a) - 10° Flow IL) at Location A	168
Figure 8-14: Stress range (Case-1(a) - 10° Flow IL) at Location A	168
Figure 9-1: CF response model for 10-° flow (Igeh [24]) [According to DNV-RP-F105 (2006 edition)].....	172
Figure 9-2: CF response model for 10-° flow [According to DNVGL-RP-F105 (2017 edition) [11]].....	172
Figure 9-3: CF response model for 90-° flow (Igeh [24]) [According to DNV-RP-F105 (2006 edition)].....	173

Figure 9-4: CF response model for 90° flow [According to DNVGL-RP-F105 (2017 edition) [11]].....	173
Figure 13-1: Combined flexural and torsional stress range from all contributing modes (Case-1(a) - 10° Flow IL) at Location A	185
Figure 13-2: Combined flexural and torsional stress range from all contributing modes (Case-1(a) - 10° Flow IL) at Location B	185
Figure 13-3: Response frequency for combined flexural and torsional stress range from all contributing modes (Case-1(a) - 10° Flow IL) at Location A.....	186
Figure 13-4: Response frequency for combined flexural and torsional stress range from all contributing modes (Case-1(a) - 10° Flow IL) at Location B.....	186
Figure 13-5: Combined flexural and torsional stress range from all contributing modes (Case-1(b) - 10° Flow CF) at Location A.....	187
Figure 13-6: Combined flexural and torsional stress range from all contributing modes (Case-1(b) - 10° Flow CF) at Location B	187
Figure 13-7: Response frequency for combined flexural and torsional stress range from all contributing modes (Case-1(b) - 10° Flow CF) at Location A	188
Figure 13-8: Response frequency for combined flexural and torsional stress range from all contributing modes (Case-1(b) - 10° Flow CF) at Location B	188
Figure 13-9: Combined flexural and torsional stress range from all contributing modes (Case-2(a) - 90° Flow IL) at Location A	189
Figure 13-10: Combined flexural and torsional stress range from all contributing modes (Case-2(a) - 90° Flow IL) at Location B	189
Figure 13-11: Response frequency for combined flexural and torsional stress range from all contributing modes (Case-2(a) - 90° Flow IL) at Location A.....	190
Figure 13-12: Response frequency for combined flexural and torsional stress range from all contributing modes (Case-2(a) - 90° Flow IL) at Location A.....	190
Figure 13-13: Combined flexural and torsional stress range from all contributing modes (Case-2(b) - 90° Flow CF) at Location A.....	191
Figure 13-14: Combined flexural and torsional stress range from all contributing modes (Case-2(b) - 90° Flow CF) at Location B	191
Figure 13-15: Response frequency for combined flexural and torsional stress range from all contributing modes (Case-2(b) - 90° Flow CF) at Location A	192

Figure 13-16: Response frequency for combined flexural and torsional stress range from all contributing modes (Case-2(b) - 90° Flow CF) at Location B	192
Figure 14-1: σ_{11} (Case-1(a) - 10° Flow IL) at Location A.....	194
Figure 14-2: σ_{33} (Case-1(a) - 10° Flow IL) at Location A.....	195
Figure 14-3: ϵ_{11} (Case-1(a) - 10° Flow IL) at Location A.....	196
Figure 14-4: ϵ_{33} (Case-1(a) - 10° Flow IL) at Location A.....	197
Figure 14-5: $\gamma_{\max}/2$ (Case-1(a) - 10° Flow IL) at Location A	198
Figure 14-6: Θ_{cric} (Case-1(a) - 10° Flow IL) at Location A.....	199
Figure 14-7: $\Delta\tau_{\max}$ (Case-1(a) - 10° Flow IL) at Location A.....	200
Figure 14-8: $\Delta\sigma_n$ (Case-1(a) - 10° Flow IL) at Location A	201
Figure 14-9: $\Delta\gamma_{\max}/2$ (Case-1(a) - 10° Flow IL) at Location A	202
Figure 14-10: $\Delta\epsilon_n$ (Case-1(a) - 10° Flow IL) at Location A.....	203
Figure 14-11: Fatigue damage per year for (Case-1(a) - 10° Flow IL) at Location A	204
Figure 14-12: σ_{11} (Case-1(a) - 10° Flow IL) at Location B.....	205
Figure 14-13: σ_{33} (Case-1(a) - 10° Flow IL) at Location B	206
Figure 14-14: ϵ_{11} (Case-1(a) - 10° Flow IL) at Location B	207
Figure 14-15: ϵ_{33} (Case-1(a) - 10° Flow IL) at Location B	208
Figure 14-16: $\gamma_{\max}/2$ (Case-1(a) - 10° Flow IL) at Location B.....	209
Figure 14-17: Θ_{cric} (Case-1(a) - 10° Flow IL) at Location B	210
Figure 14-18: $\Delta\tau_{\max}$ (Case-1(a) - 10° Flow IL) at Location B.....	211
Figure 14-19: $\Delta\sigma_n$ (Case-1(a) - 10° Flow IL) at Location B.....	212
Figure 14-20: $\Delta\gamma_{\max}/2$ (Case-1(a) - 10° Flow IL) at Location B.....	213
Figure 14-21: $\Delta\epsilon_n$ (Case-1(a) - 10° Flow IL) at Location B	214
Figure 14-22: Fatigue damage per year for (Case-1(a) - 10° Flow IL) at Location B.....	215
Figure 14-23: σ_{11} (Case-1(b) - 10° Flow CF) at Location A	216
Figure 14-24: σ_{33} (Case-1(b) - 10° Flow CF) at Location A.....	217
Figure 14-25: ϵ_{11} (Case-1(b) - 10° Flow CF) at Location A.....	218
Figure 14-26: ϵ_{33} (Case-1(b) - 10° Flow CF) at Location A.....	219
Figure 14-27: $\gamma_{\max}/2$ (Case-1(b) - 10° Flow CF) at Location A	220
Figure 14-28: Θ_{cric} (Case-1(b) - 10° Flow CF) at Location A	221

Figure 14-29: $\Delta\tau_{\max}$ (Case-1(b) - 10° Flow CF) at Location A	222
Figure 14-30: $\Delta\sigma_n$ (Case-1(b) - 10° Flow CF) at Location A	223
Figure 14-31: $\Delta\gamma_{\max}/2$ (Case-1(b) - 10° Flow CF) at Location A	224
Figure 14-32: $\Delta\epsilon_n$ (Case-1(b) - 10° Flow CF) at Location A	225
Figure 14-33: Fatigue damage per year for (Case-1(b) - 10° Flow CF) at Location A	226
Figure 14-34: σ_{11} (Case-1(b) - 10° Flow CF) at Location B.....	227
Figure 14-35: σ_{33} (Case-1(b) - 10° Flow CF) at Location B	228
Figure 14-36: ϵ_{11} (Case-1(b) - 10° Flow CF) at Location B	229
Figure 14-37: ϵ_{33} (Case-1(b) - 10° Flow CF) at Location B	230
Figure 14-38: $\gamma_{\max}/2$ (Case-1(b) - 10° Flow CF) at Location B	231
Figure 14-39: Θ_{critic} (Case-1(b) - 10° Flow CF) at Location B.....	232
Figure 14-40: $\Delta\tau_{\max}$ (Case-1(b) - 10° Flow CF) at Location B.....	233
Figure 14-41: $\Delta\sigma_n$ (Case-1(b) - 10° Flow CF) at Location B	234
Figure 14-42: $\Delta\gamma_{\max}/2$ (Case-1(b) - 10° Flow CF) at Location B	235
Figure 14-43: $\Delta\epsilon_n$ (Case-1(b) - 10° Flow CF) at Location B.....	236
Figure 14-44: Fatigue damage per year for (Case-1(b) - 10° Flow CF) at Location B	237
Figure 14-45: σ_{11} (Case-2(a) - 90° Flow IL) at Location A.....	238
Figure 14-46: σ_{33} (Case-2(a) - 90° Flow IL) at Location A	239
Figure 14-47: ϵ_{11} (Case-2(a) - 90° Flow IL) at Location A	240
Figure 14-48: ϵ_{33} (Case-2(a) - 90° Flow IL) at Location A	241
Figure 14-49: $\gamma_{\max}/2$ (Case-2(a) - 90° Flow IL) at Location A	242
Figure 14-50: Θ_{critic} (Case-2(a) - 90° Flow IL) at Location A.....	243
Figure 14-51: $\Delta\tau_{\max}$ (Case-2(a) - 90° Flow IL) at Location A.....	244
Figure 14-52: $\Delta\sigma_n$ (Case-2(a) - 90° Flow IL) at Location A	245
Figure 14-53: $\Delta\gamma_{\max}/2$ (Case-2(a) - 90° Flow IL) at Location A	246
Figure 14-54: $\Delta\epsilon_n$ (Case-2(a) - 90° Flow IL) at Location A.....	247
Figure 14-55: Fatigue damage per year for (Case-2(a) - 90° Flow IL) at Location A	248
Figure 14-56: σ_{11} (Case-2(a) - 90° Flow IL) at Location B.....	249
Figure 14-57: σ_{33} (Case-2(a) - 90° Flow IL) at Location B	250

Figure 14-58: ϵ_{11} (Case-2(a) - 90° Flow IL) at Location B	251
Figure 14-59: ϵ_{33} (Case-2(a) - 90° Flow IL) at Location B	252
Figure 14-60: $\gamma_{\max}/2$ (Case-2(a) - 90° Flow IL) at Location B.....	253
Figure 14-61: Θ_{critic} (Case-2(a) - 90° Flow IL) at Location B	254
Figure 14-62: $\Delta\tau_{\max}$ (Case-2(a) - 90° Flow IL) at Location B	255
Figure 14-63: $\Delta\sigma_n$ (Case-2(a) - 90° Flow IL) at Location B.....	256
Figure 14-64: $\Delta\gamma_{\max}/2$ (Case-2(a) - 90° Flow IL) at Location B.....	257
Figure 14-65: $\Delta\epsilon_n$ (Case-2(a) - 90° Flow IL) at Location B	258
Figure 14-66: Fatigue damage per year for (Case-2(a) - 90° Flow IL) at Location B.....	259
Figure 14-67: σ_{11} (Case-2(b) - 90° Flow CF) at Location A	260
Figure 14-68: σ_{33} (Case-2(b) - 90° Flow CF) at Location A.....	261
Figure 14-69: ϵ_{11} (Case-2(b) - 90° Flow CF) at Location A.....	262
Figure 14-70: ϵ_{33} (Case-2(b) - 90° Flow CF) at Location A.....	263
Figure 14-71: $\gamma_{\max}/2$ (Case-2(b) - 90° Flow CF) at Location A	264
Figure 14-72: Θ_{critic} (Case-2(b) - 90° Flow CF) at Location A	265
Figure 14-73: $\Delta\tau_{\max}$ (Case-2(b) - 90° Flow CF) at Location A	266
Figure 14-74: $\Delta\sigma_n$ (Case-2(b) - 90° Flow CF) at Location A	267
Figure 14-75: $\Delta\gamma_{\max}/2$ (Case-2(b) - 90° Flow CF) at Location A	268
Figure 14-76: $\Delta\epsilon_n$ (Case-2(b) - 90° Flow CF) at Location A	269
Figure 14-77: Fatigue damage per year for (Case-2(b) - 90° Flow CF) at Location A.....	270
Figure 14-78: σ_{11} (Case-2(b) - 90° Flow CF) at Location B.....	271
Figure 14-79: σ_{33} (Case-2(b) - 90° Flow CF) at Location B	272
Figure 14-80: ϵ_{11} (Case-2(b) - 90° Flow CF) at Location B	273
Figure 14-81: ϵ_{33} (Case-2(b) - 90° Flow CF) at Location B	274
Figure 14-82: $\gamma_{\max}/2$ (Case-2(b) - 90° Flow CF) at Location B	275
Figure 14-83: Θ_{critic} (Case-2(b) - 90° Flow CF) at Location B.....	276
Figure 14-84: $\Delta\tau_{\max}$ (Case-2(b) - 90° Flow CF) at Location B.....	277
Figure 14-85: $\Delta\sigma_n$ (Case-2(b) - 90° Flow CF) at Location B	278
Figure 14-86: $\Delta\gamma_{\max}/2$ (Case-2(b) - 90° Flow CF) at Location B	279

Figure 14-87: $\Delta \epsilon_n$ (Case-2(b) - 90° Flow CF) at Location B.....280

Figure 14-88: Fatigue damage per year for (Case-2(b) - 90° Flow CF) at Location B281

LIST OF TABLES

Table 5-1: Load cases tested by McDiarmid [29].....	31
Table 5-2: Load histories as per Farahani [13,14]	39
Table 6-1: Jumper model properties	44
Table 6-2: Dimensions of segments of jumper model.....	45
Table 6-3: General Safety factors for fatigue (DNVGL-RP-F105 (2017 edition) [11]).....	62
Table 6-4: Safety factors for natural frequencies (DNVGL-RP-F105 (2017 edition) [11])....	62
Table 7-1: Jumper model properties comparison.....	85
Table 7-2: Comparison of dimensions of segments used for SpaceClaim model	86
Table 7-3: Hydrodynamic parameters used of jumper model	90
Table 7-4: Ocean data for jumper model	89
Table 7-5: Predicted eigen frequencies from modal analysis	92
Table 7-6: Mode classification for 10° and 90° flow into IL and CF for jumper model.....	98
Table 7-7: Critical location for 10° and 90° in-line and cross-flow cases (measured from left fixed end of rigid jumper)	103
Table 7-8: Unit amplitude stresses for 10° Flow – In-line and cross-flow case at the critical locations A and B	103
Table 7-9: Unit amplitude stresses for 90° Flow – In-line case at the critical locations A and B	106
Table 7-10: Unit amplitude stresses for 90° Flow – cross-flow case at the critical locations A and B	108
Table 7-11: Comparison of critical location for 10° and 90° in-line and cross-flow cases (measured from left fixed end of rigid jumper) with Igeh [24].....	122
Table 8-1: Flow velocity range for different cases	124
Table 8-2: Parameters for 10° Flow in-line response model	125
Table 8-3: Calculated parameters for 10° Flow in-line response model	125
Table 8-4: Parameters for 90° Flow in-line response model	126
Table 8-5: Calculated parameters for 90° Flow in-line response model	127

Table 8-6: Parameters for 10° Flow cross-flow response model.....	128
Table 8-7: Calculated parameters for 10° Flow cross-flow response model.....	128
Table 8-8: Parameters for 90° Flow cross-flow response model.....	129
Table 8-9: Calculated parameters for 90° Flow cross-flow response model.....	130
Table 8-10: Flow velocity range for modes to be classified as active modes.....	131
Table 8-11: Participating Modes for 10° Flow – In-line and cross-flow case at the critical locations A and B	133
Table 9-1: Unit amplitude stresses for 10° Flow – In-line case at the critical locations A and B (Contributing modes only)	137
Table 10-1: Block loading calculation for Case-1(a) - 10° flow (in-line) at Location A at current velocity of 0.14 m/s.....	156
Table 10-2: Critical planes for each half cycle of σ_{11} for Case-1(a) - 10° flow (in-line) at Location A at current velocity of 0.14 m/s	158
Table 10-3: Normal and shear stress and strain ranges ($\Delta\sigma_n$, $\Delta\tau_{max}$, $\Delta\epsilon_n$, $\Delta\gamma_{max2}$) at each full cycle of θ_{11} for Case-1(a) - 10° flow (in-line) at Location A at current velocity of 0.14 m/s.....	161
Table 10-4: Fatigue damage for each full cycle of θ_{11} for Case-1(a) - 10° flow (in-line) at Location A at current velocity of 0.14 m/s	162
Table 10-5: Fatigue damage (1/year) for Case-1(a) - 10° flow (in-line) at Location A at current velocity of 0.14 m/s.....	163
Table 10-6: Normal and shear fatigue properties of Aluminium pipe.....	163
Table 11-1: Comparison of mode classification for 10° and 90° flow (IL and CF) with Igeh [24].....	171

1 INTRODUCTION

This section presents a background and motivation for study for this thesis. It also lists down the objective of this study and gives an overview of the chapters.

1.1 Background and Motivation

Background on VIV and fatigue are discussed in the following sub-sections.

1.1.1 Vortex Induced Vibrations

Vortex induced vibration (VIV) prediction is of practical interest with respect to subsea jumper/spools that are exposed to a stream of uniform current.

From simple industrial chimneys to oil and gas risers and flare towers, accurate prediction and mitigation of VIV forms an important aspect of the engineering design. Loads imposed by the VIV on a structure can cause serious damage to its integrity and may lead to failure under ultimate limit state (ULS) or fatigue limit state (FLS) depending on the induced steady state amplitudes.

VIV due to a current or wind load depends on several factors including,

1. structural parameters such as shape and dimensions of the structure (slenderness), eigen frequencies of the structure and mode shape;
2. hydrodynamic parameters such as reduced velocity, Keulegan-Carpenter number, current flow velocity ratio, turbulence intensity, flow angle, relative to the structure and stability parameter.

These parameters are discussed in detail in Sections 2.1.4 and 4.4.

A structure such as pipeline, riser or rigid spool jumper, when exposed to subsea current dominant conditions, can experience VIV in in-line (IL) and cross-flow (CF) directions. The oscillating load due to VIV on the structure can cause fatigue damage and subsequent failure if the structure is not designed for required fatigue life. Special conditions such as VIV lock-in can further aggravate the situation by increasing the amplitude of cyclic stresses and number

of fatigue loading cycles in the lock-in region. It is hence extremely important to accurately predict VIV for subsea jumper/spool that are exposed to uniform current flow and determine its amplitude response and stress range.

Subsea spools can either be designed to avoid the formation of VIV or to mitigate the effects of VIV such as fatigue damage and impact collisions. Subsea rigid jumper is a non-straight geometry which can be planar or multi-planar in space. Currently, there exists guidelines for straight pipelines in the form of DNVGL-RP-F105 (2017 edition) [11] which can be used to predict the VIV with a response based or forced based model approach. Finite element (FE) tools such as VIVANA (SINTEF Ocean, 2016) and SHEAR7 (MIT, 2016) are also used for VIV response prediction. There is limited experience in assessing the non-straight pipelines such as rigid jumpers because of the presence of multiaxial stress state and complex interaction of different modes.

Despite the available methods for straight pipelines, VIV response prediction and fatigue damage evaluation of non-straight geometries such as the subsea rigid spool jumper is an active area of research.

1.1.2 Fatigue

Fatigue has historically been the concern for many engineering problems, from the aviation industry to oil and gas sector. Some of these, as examples, are shown in Figure 1-1. Fatigue failure, unlike other modes of failure, can occur at stress amplitudes well within the elastic limit of the material. Fatigue leads to crack initiation which can propagate at a fast rate through the material causing failure due to a brittle fracture. Since the loads are well below the elastic limits, fatigue development in material can occur un-noticed during the operating life of a structure. In addition, a short time from the initiation of crack to complete fracture means reaction time to counter fatigue at later stage is less. Hence, fatigue can be severely damaging to structures and its development and propagation can remain un-noticed until the failure occurs.

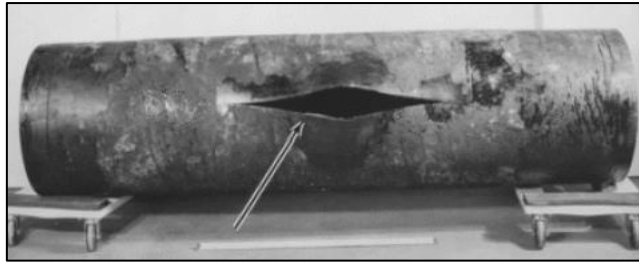
Despite the danger it brings to a structure, understanding of this phenomenon is limited. Uniaxial fatigue is better understood with the help of experimental data and various well-established fatigue life prediction models. However, biaxial and multiaxial fatigue phenomena are still an active area of research and development. In the real world, structures usually

encounter a multiaxial stress states rather than simplified uniaxial stress state. One special example is the VIV fatigue problem of subsea spools. Due to the multi-planar geometry of spools, they normally undertake both bending and torsional moment if the VIV is triggered. According to the general practice in most engineering fields, multiaxial fatigue is described either by a stress equivalent or strain equivalent approach. This is done by simplification of a multiaxial stress state to a uniaxial stress/strain state and using the uniaxial S-N or ϵ -N curves for fatigue life estimation. These methods tend to overdesign the components by a conservative fatigue design approach.

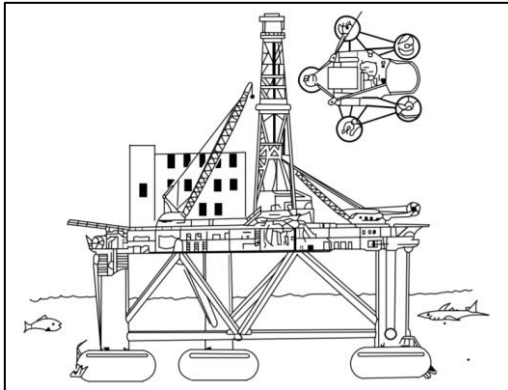
Once such simplification can be seen in the case of design of non-straight geometries using DNVGL-RP-F105 (2017 edition) [11]. DNVGL-RP-F105 is primarily used for straight pipelines. Guidance is provided for assessment of non-straight geometries using conservative simplifications and recommended use of finite element (FE) analysis. Fatigue criterion provided in the standard uses simplified S-N curves and Miner rule to determine the fatigue life and fatigue damage. Through this approach, a biaxial or multiaxial fatigue problem is assessed using empirical fatigue data from uniaxial fatigue tests. This gives rise to a highly conservative approach that leads to an overdesigned structure.

Advancement in model building tools and better understanding of multiaxial fatigue over the last two decades, has led to an increase in related research. There is a need for a more accurate design method which is generally accepted for a range of materials and is both cost and time efficient.

Over the years, several attempts were made to develop a multiaxial fatigue model based on equivalent stress, equivalent strain, critical energy and fracture mechanics. Combination of different approaches has been part of research. Each approach has its advantages and disadvantages, see Gustafsson and Saarinen [22].



(a)



(b)

Figure 1-1: (a) Fatigue damage in pipelines (Marathon Ashland pipeline LLC, Winchester, Kentucky) [35]; (b) Alexander L. Kielland Accident (Wall Street Journal)

1.2 Objectives

The objectives of the present study are:

1. To assess the use of DNVGL-RP-F105 (2017 edition) [11] response model over DNVGL-RP-F105 (2006 edition) [12] response model for VIV prediction and stress range calculations for work done by Igeh [24].
2. To assess the use of a fatigue damage parameter proposed by Farahani [13,14] as a possible alternative to S-N curves recommended by DNVGL-RP-F105 (2017 edition) [11].

First part of the study is based on the research completed by Igeh [24] and Wang et al. [47] by introducing a new method for fatigue damage evaluation using work of Farahani [13,14]. The objective is to assess the performance of the Farahani [13,14] fatigue parameter with respect to recommended practices as outlined by DNVGL-RP-F105 (2017 edition) [11].

Second part of the study highlights and implements the changes in the DNVGL-RP-F105 (2017 edition) regarding response model and VIV prediction approach over the 2006 edition which was used in the work completed by Igeh [24].

Outline of the thesis is as follows:

Chapter 1 provides a brief introduction and motivation of the study describing the need, objective and contents of the thesis.

Chapter 2 provides basic theory on vortex induced vibration and multiaxial fatigue by describing the factors which govern them and the available mitigation techniques.

Chapter 3 gives a brief literature review on the published papers and research on multiaxial fatigue including critical plane energy methods and Farahani [13,14]'s fatigue damage parameter.

Chapter 4 describes the methodology which is adopted for VIV response prediction and subsequent stress range calculation and fatigue damage assessment using DNVGL-RP-F105 (2017 edition) [11] and Farahani [13,14]'s fatigue damage parameter. This chapter also describes in brief the model testing and research done by Exxon Mobil and Wang et al. [47].

Chapter 5 provides results from the modal analysis. Eigen frequencies, mode shapes and modal stresses obtained from finite element analysis are presented here. Discussion on the results are also included.

Chapter 6 describes the cross-flow and in-line response models constructed according to DNVGL-RP-F105 (2017 edition) [11] for the rigid jumper. Results and discussions are also included.

Chapter 7 provides results from stress range calculation according to DNVGL-RP-F105 (2017 edition) [11]. Discussion on the results and correlation to Igeh [24]'s results are also included.

Chapter 8 provides detailed results from the fatigue assessment using Farahani [13,14]'s fatigue damage parameter including block loading, critical plane selection and normal and shear stress and strain range calculations. Discussion on results are also included.

Chapter 9 provides a comparative study on the major changes in the 2017 edition latest edition of DNVGL-RP-F105 compared to the last edition of 2006.

Chapter 10 included conclusions on results and discussions of Chapter 7 to Chapter 11.

Chapter 11 gives recommendations for future work.

Chapter 12 includes a list of references used in this study in alphabetical order.

Chapter 13 and 14 consists of appendices with relevant graphs from stress range calculations and fatigue assessment, respectively.

2 THEORY

The basic theory behind vortex induced vibration and multiaxial fatigue are discussed in this section.

2.1 Vortex induced vibration

Vortex induced vibration under a uniform current is a result of formation of Kármán vortex street that induced motion in in-line and cross-flow planes. This section discusses the basics of vortex induced vibration for circular cylinder in current dominant conditions.

2.1.1 Flow around circular cylinders

A circular cylinder, when placed in a uniform current flow, experiences forces in the cross-flow and in-line directions for a given range of flow velocities. The in-line forces are generated due to separation of boundary layer in the wake of the cylinder which causes a difference in pressure across the cylinder in the direction of flow. The difference in pressure results in the movement of the cylinder in the direction of flow. The movement of cylinder in the in-line direction leads to change in the added mass of the cylinder which causes the cross-flow movements. Figure 2-2 shows how vortex shedding patterns are generated for a range of Reynolds number.

2.1.2 Vortex shedding

Vortex shedding occurs due to separation of boundary layer at the top and bottom end in the wake of the cylinder at higher Reynolds number. As seen in Figure 2-2, the vortex shedding occurs in the range of Reynolds number- 5 to 40.

2.1.3 Kármán vortex street

It is defined as the repeating vortex shedding pattern in the wake of cylinder under a uniform current flow. As seen in Figure 2-2, at Reynolds number range of 40 to 150, the vortex shedding occurs periodically at the top and the bottom end of the cylinder leading to an oscillating pattern of vortex shedding called the Karman vortex street.

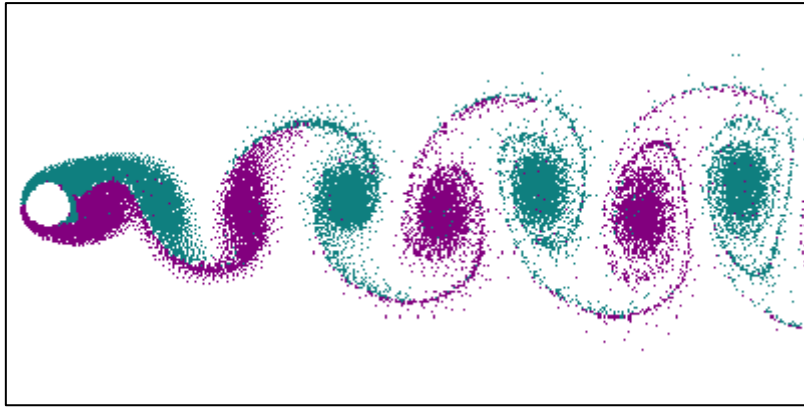


Figure 2-1: Kármán vortex street in the wake of a circular cylinder from Wikipedia [55]

Figure 2-1 shows the Kármán vortex street in the wake of circular cylinder under a uniform current. The area in green represent the vortex shedding from the top end while the area is pink represent the vortex shedding from the bottom end of the cylinder.

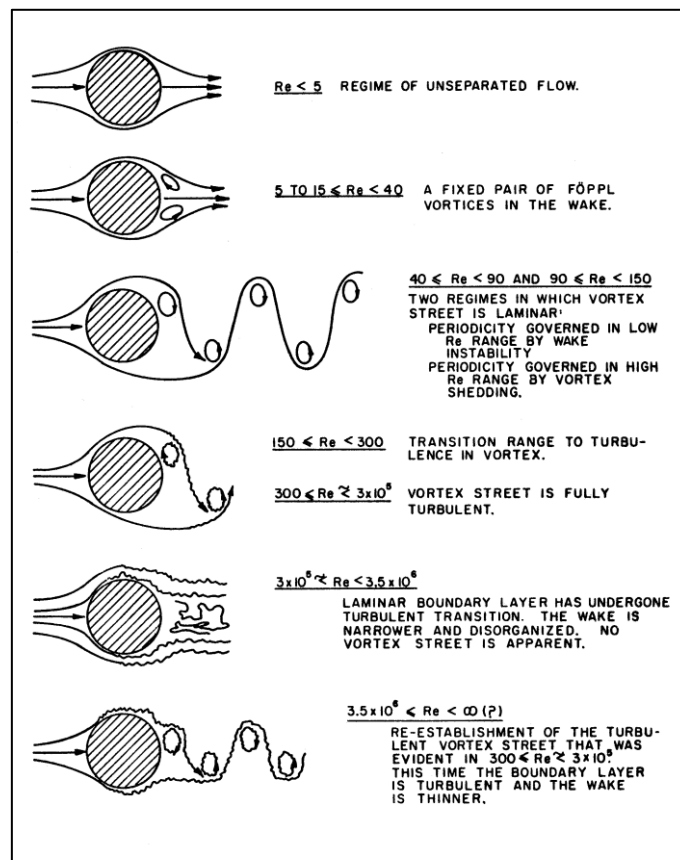


Figure 2-2: Effect of Reynolds number (Re) on vortex shedding pattern for a cylinder in uniform current flow according to Lienhard [27]

2.1.4 Parameters

The parameters which affect the vortex formation and the induced vibrations are discussed. Parameters that are used to define a vortex formation can be divided into the following types according to Masilamani [54]:

1. Fluid Parameters
 - a. Reynolds number
 - b. Keulegan-Carpenter number
 - c. Current flow velocity
 - d. Turbulence intensity
 - e. Shear fraction of flow
2. Fluid-Structure Interface parameters
 - a. Reduced velocity
 - b. Stability parameter
 - c. Strouhal number
3. Structural parameters
 - a. Geometry
 - b. Mass ratio
 - c. Damping factors

1. Reynolds number

Reynolds number (Re) is a dimensionless parameter which is obtained from the ratio of fluid's inertial force and viscous force, defined as follows:

$$Re = \frac{\text{Inertial Force}}{\text{Viscous Force}} = \frac{\rho U D}{\mu} = \frac{UD}{\nu} \quad 2-1$$

where,

ρ = Density of fluid

U = Flow velocity

D = Outer diameter of cylinder

μ = Dynamic viscosity of fluid

ϑ = Kinematic viscosity of fluid

Reynolds number affects the peak response of the vortex induced vibration as demonstrated by Govardhan et al. [21] and Klamo et al. [26] for rigid cylinders. It was shown that the Reynolds number influences the lift coefficient which in turn influences the peak amplitude of vortex induced response (A/D) as shown Figure 2-3.

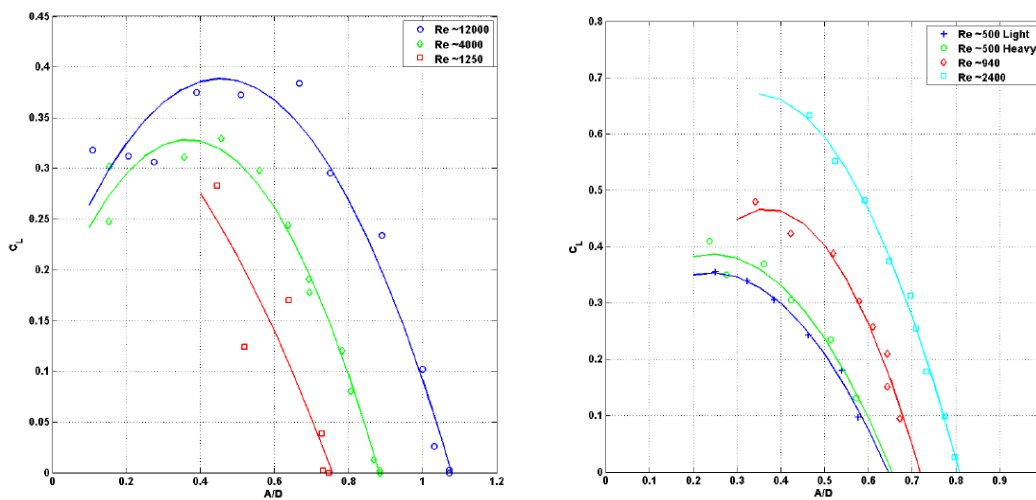


Figure 2-3: Effect of lift coefficient (C_L) on the response amplitude (A/D) according to Govardhan et al. [21] and Klamo et al. [26] from Resvanis et al. [37]

Resvanis et al. [37] showed that a similar relationship exists for the flexible cylinders under uniform current flow. Response (A/D) in in-line and cross-flow directions are plotted against the Reynold's number as shown in Figure 2-4.

Fluid flow regime is defined by Reynolds number. For low velocity of the fluid flow, the Reynolds number is small, and the flow is called laminar. As the flow velocity increases, Reynolds number increases, the effects of inertial forces increase as compared to the viscous forces, leading to turbulence in the flow. Such a flow is called turbulent flow. The range of Reynolds number values at which the laminar flow changes to turbulent flow is called the transition range.

Figure 2-2 shows the effect of Reynolds number (Re) on the vortex shedding pattern.

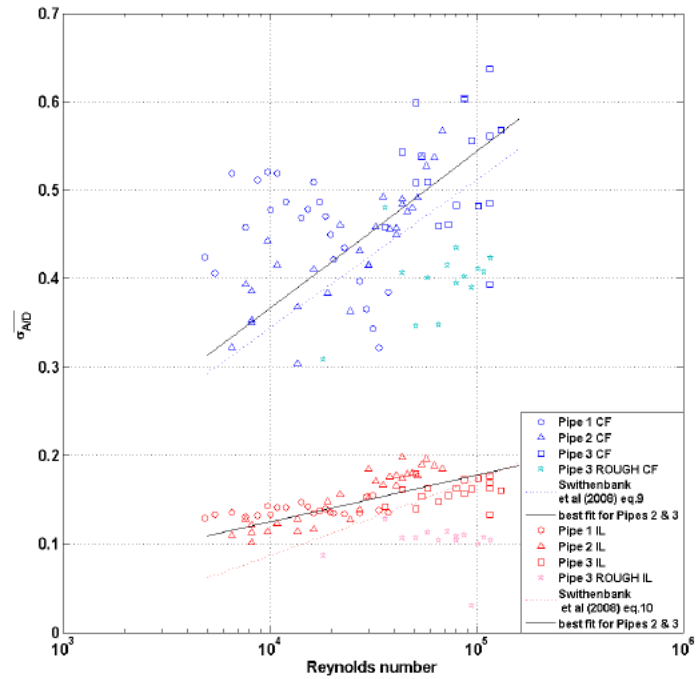


Figure 2-4: Effect of Reynolds number (Re) on the in-line and cross-flow response amplitude (A/D) according to Resvanis et al. [37]

2. Strouhal Number

Strouhal number (St), is defined as a function of vortex shedding frequency, outer diameter of the cylinder and the current velocity as follows:

$$St = \frac{f_v D}{U} \quad 2-2$$

where,

f_v = Vortex shedding frequency

D = Outer diameter of cylinder

U = Flow velocity

For a given cylinder ($D = \text{constant}$) exposed to a under a uniform flow velocity ($U = \text{constant}$), Strouhal number depends only on the vortex shedding frequency (f_v). The vortex shedding frequency has been shown to be related to the flow angle (θ_{rel}) by Ramberg [36].

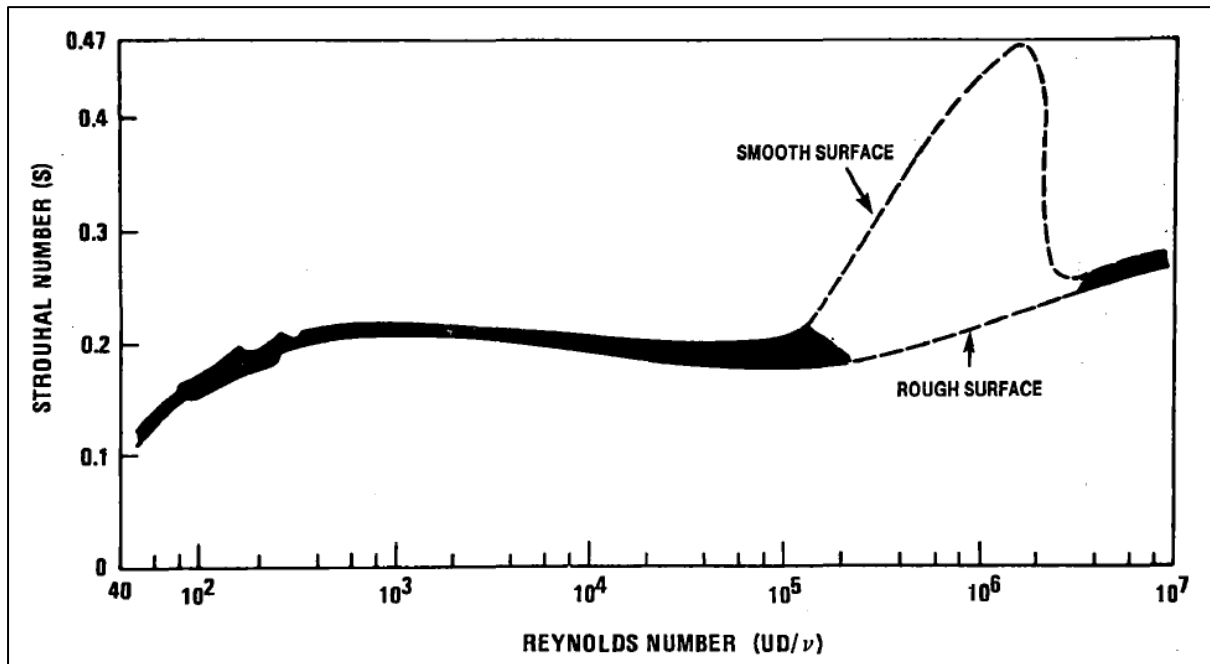


Figure 2-5: Reynolds number (Re) and Strouhal number (St) relationship for a smooth and rough circular cylinder from Blevins [6]

Figure 2-5 shows the relationship between the Reynolds number (Re) and Strouhal number (St) for a circular cylinder. For low Reynolds number region (10^3 to 10^5), the Strouhal number value remains constant around 0.2 for both smooth and rough circular cylinders. For higher values of Reynolds number ($>10^5$), roughness plays an important role and values of smooth circular cylinder are higher than the rough cylinder for the same value of Reynolds number according to Achenbach et al. [1].

3. Reduced velocity

Reduced velocity (V_r) is a dimensionless number and is defined as function of current velocity (U), natural frequency of the circular cylinder (f_v) and outer diameter of the cylinder (D) as follows:

$$V_R = \frac{\text{path length per cycle}}{\text{model width}} = \frac{U}{f_n D} \quad 2-3$$

where,

f_n = Eigen frequency of cylinder

D = Outer diameter of cylinder

U = Flow velocity

Reduced velocity is used to describe the length of path of the oscillating cylinder as a function of the structural parameters.

4. Non-dimensional frequency

Non-dimensional frequency (\hat{f}) is the inverse of reduced velocity and is defined as follows:

$$\hat{f} = \frac{Df_o}{U} \quad 2-4$$

where,

f_o = Response frequency or Oscillating frequency

D = Outer diameter of cylinder

U = Flow velocity

5. Keulegan-Carpenter number

Keulegan-Carpenter number (KC) is used for oscillating flows and describes the effects of drag forces in relation to the inertial forces due to waves in a fluid flow. It is defined as follows:

$$KC = \frac{U_w}{f_w D} \quad 2-5$$

where,

$f_w = 1/T_u$ is the significant wave frequency.

KC number is mainly used to describe the effect of wave forces on the amplitude response of vortex induced vibration for wave dominated condition. For a current dominant condition effects of wave are not considered and hence $KC = 0$

6. Stability parameter

Stability parameter (K_s) considers the hydrodynamic parameters such as the effective mass and total damping ratio along with fluid properties such as mass density. K_s is defined as follows:

$$K_s = \frac{4\pi m_e \zeta_T}{\rho D^2} \quad 2-6$$

where,

ρ = Water density

ζ_T = Total modal damping ratio

m_e = Effective mass per unit length

D = Outer diameter of cylinder

7. Mass ratio

Mass ratio (m_{ratio}) is defined as the ratio of the mass of the cylinder to the mass of the fluid it displaces. It is given as follows:

$$m_{ratio} = \frac{\text{mass per unit length of cylinder}}{\text{fluid density} \times \text{model width}^2} = \frac{m}{\rho D^2} \quad 2-7$$

where,

m = mass of the cylinder (including added mass)

ρ = Density of fluid

D = Outer diameter of cylinder

Mass ratio is used to describe the susceptibility of a light structure to vortex induced vibration.

2.1.5 VIV phenomena

VIV, as discussed earlier, occurs due to boundary layer separation and formation of Karman vortex street for a cylinder exposed to a uniform current flow. VIV can be classified as in-line and cross-flow based on the direction of vibration of the rigid jumper (in X, Y or Z direction) with respect to the direction of the uniform current for a given mode as shown in Figure 2-6.

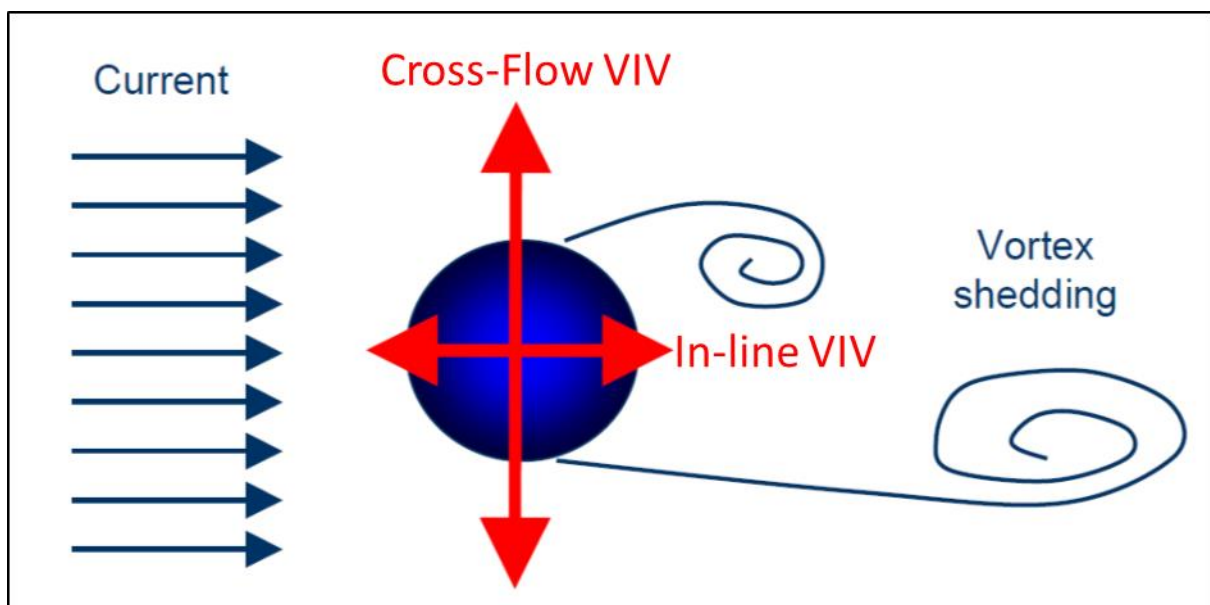


Figure 2-6: In-line and cross-flow VIV [56]

1. In-line VIV

According to Carruth et al. [52], when the direction of motion of the rigid jumper is parallel to the direction of current, the VIV is called in-line VIV. Active modes on the rigid jumper, for a given orientation of current, which excites the jumper in the parallel direction to the current direction are called in-line modes.

According to Guo et al. [53] and Masilamani [54], the amplitude response of the in-line VIV is much smaller than cross-flow VIV (of the order of 10%). It may excite at lower frequencies as compared to cross-flow VIV. Therefore, the in-line VIV forms the main design criteria for rigid jumper as compared to cross-flow VIV.

2. Cross-flow VIV

According to Carruth et al. [52], when the direction of motion of the rigid jumper is perpendicular to the direction of current, the VIV is called cross-flow VIV. Active modes on the rigid jumper, for a given orientation of current, which excites the jumper in the perpendicular direction to the current direction are called cross flow modes.

According to Masilamani [54], the cross-flow VIV have a higher amplitude response as compared to in-line VIV, but it is activated at a relatively higher vibration frequency as compared to the in-line VIV.

3. VIV Lock-in

According to Blevins [6], VIV lock-in is a condition which occurs when the vibration frequency of the rigid jumper becomes approximately equal to the vortex shedding frequency. This situation leads to high amplitude response in the rigid jumper. Once the system enters the lock-in it stays in lock-in even if the reduced velocity is increased or decreased. Only after the reduced velocity is increased or decreased significantly, the lock-in breaks and response amplitude reduced.

2.2 Fatigue

Fatigue in extremely simple words can be defined in its literal mean as “tiring of material”. The word was first introduced after the Paris Versailles rail accident in the year 1842 which occurred due to fatigue failure.

When a material is exposed to cyclic stresses, even below their elastic limits, the material can fail over a period due to accumulation of damage leading to cracks and eventually brittle failure. Fatigue is a localised phenomenon, effect of which can be seen progressively over a period on the material. Highly localised plastic deformations are caused due to cyclic loading which lead to permanent microstructural changes in the material.

A more scientific definition was first given in the year 1964 by International Organisation of Standardization, “Fatigue applies to changes in properties which can occur in a metallic material due to repeated application of stresses or strains, although usually this term applies specially to those changes which lead to cracking or failure”

Fatigue can be broadly classified based on:

1. Number of cycles to failure as;

a. High cycle fatigue

Characterised by high frequency of loading, low stress amplitudes, elastic behaviour of materials and large number of cycle ($\sim 10^5$ or more)

b. Low cycle fatigue

Characterised by higher stress amplitudes, plastic behaviour of material and smaller number of cycles to failure ($\sim 10^4$ or less)

2. Stress state;

State of stress and strain can be described acting on 3 orthogonal planes in Cartesian coordinates, X, Y and Z Plane.

Stress can be described in 6 components – Normal stress (X, Y, Z Direction) and shear stress (XY, YZ, ZX Planes)

Strain can be described in 6 components – Normal strain (X, Y, Z Direction) and shear strain (XY, YZ, ZX Planes)

Fatigue is classified based on stress state as:

a. Uniaxial fatigue

When the cyclic stresses causing the fatigue damage in a material act only in one principal direction or plane, the stress state is uniaxial, and fatigue is called uniaxial fatigue.

Example: A bar under tensile stress in X-Direction. It may be noted that even though it is in uniaxial stress state, it experiences multiaxial strain due to change in the volume.

b. Multiaxial fatigue

When the cyclic stress causing fatigue damage in a material act in two or more principal directions or planes, the stress state is called multiaxial and fatigue is called multiaxial fatigue.

Example: Thin wall cylinder under internal pressure is in a biaxial stress state due to development of hoop stresses and longitudinal stresses which can on the curved surface of the cylinder in mutually perpendicular directions.

2.2.1 Multiaxial Fatigue

In real life engineering problems, components and structures experience stresses in more than one principal direction. In addition, the stress amplitudes are not constant with respect to time. This causes a multiaxial stress state where the stresses are cyclic in nature leading to multiaxial fatigue in the material.

Multiaxial fatigue can be high cycle or low cycle depending on the amplitude of stress and its frequency. Most engineering problems need to be designed for high cycle multiaxial fatigue. This can be seen in for subsea spool exposed to VIV. The spool is exposed to bending and torsional stresses which may act at different amplitudes, frequencies and phase difference.

Igeh [24] determined the global response of a subsea spool jumper exposed to VIV due to subsea currents. The study emphasized the exposure of subsea spool to biaxial stress state. Cyclic bending and torsional stresses co-exist due to VIV causing fatigue damage.

2.2.2 Factors affecting fatigue

Fatigue is a highly localised phenomenon which progresses over time as it accumulates damage due to microstructural plastic deformities in the material. Following are some critical factors which influence fatigue generation and are studied in this project:

1. Loading

Type and nature of loading is most critical in defining the fatigue problem. Loadings can be categorised into following types:

a. Constant amplitude and variable amplitude loading

When the amplitude of load and the mean value about which it varies is constant for each consecutive cycle, it is known as constant amplitude loading. Sinusoidal loading is a class example of such loading. It is a form of simplification often used in engineering design.

Variable amplitude loading is witnessed in the real engineering problem. In real world, structures and mechanical components witness loads with varying amplitudes and mean values for each consecutive cycle. These are often simplified into constant amplitude loading through different cycle counting methods and fatigue is assessed from cumulative damage theories. Measured wind loading data on a bridge in Norway is a good example.

In both cases, the loading is cyclic and causes fatigue damage to the structure. It is easier to design a fatigue model for a constant amplitude loading as compared to variable amplitude loading. For variable amplitude loading, emphasis is given to the peak values which should be under the fatigue limits. Also, the mean stress variation is of great importance as it may reduce or increase the fatigue life of the material.

b. Proportional and Non-proportional loading

When the periodic cyclic loading does not cause a change in the orientation of the principal axis despite change in amplitude of principal stresses, it is called a

proportional loading. In a biaxial stress state, the ratio of two mutually perpendicular applied loads shall remain the same throughout the whole load cycle.

On the other hand, if the periodic cyclic loading leads to change in both amplitude and orientation of principal stresses, it is called as non-proportional loading. The ratio between the two mutually perpendicular applied loads does not remain same throughout the whole load cycle and varies with time.

c. In-phase and Out-of-phase loading

Constant amplitude loading such as sinusoidal loading in a biaxial stress state, can be proportional or non-proportional depending on the phase difference (usually represented with θ).

In-phase loading is proportional as there is no phase delay and ratio between the amplitudes of applied stresses always remains constant over time during the loading cycle. Figure 2-7 shows an in-phase longitudinal and transverse loading.

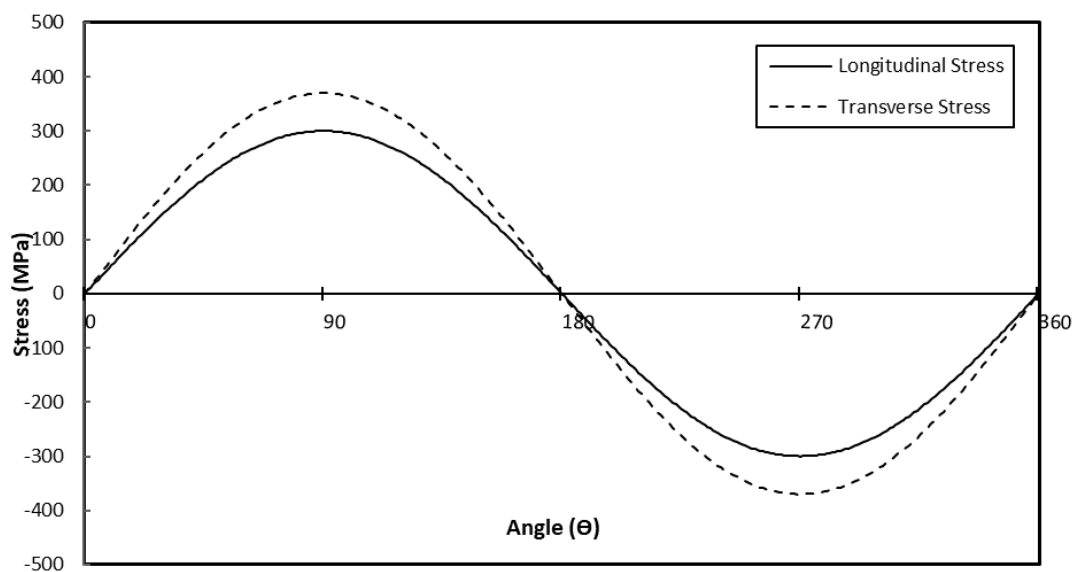


Figure 2-7: Proportional In-phase loading

For out-of-phase loading, there is a phase delay and ratio between the amplitudes of applied stresses keeps changing over time during the loading cycle. Figure 2-8 shows a phase delay of 120° between the longitudinal and transverse loadings.

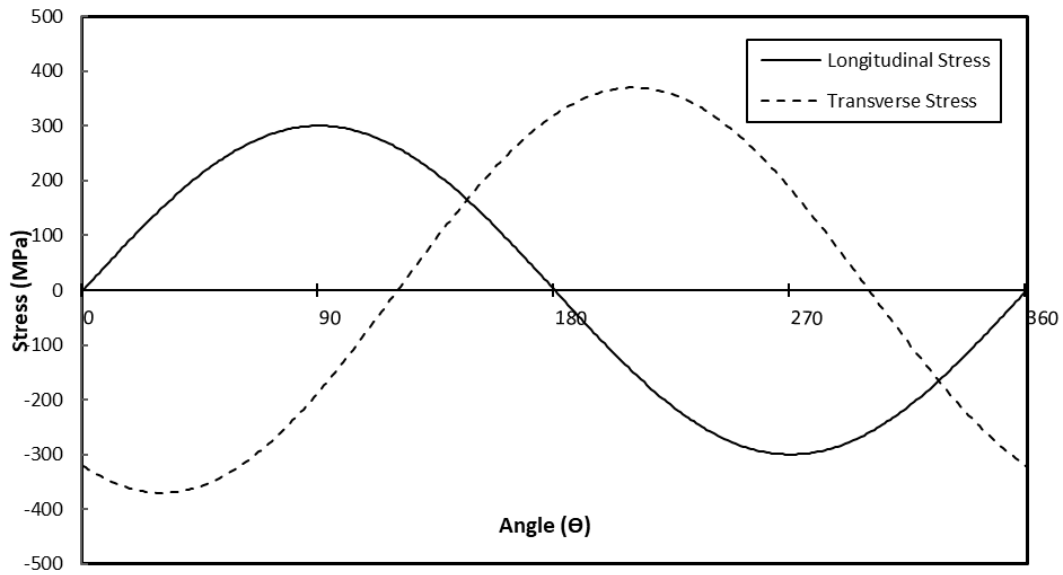


Figure 2-8: Non-proportional out-of-phase loading

For out-of-phase loading the principal stress and strain axes rotate during fatigue loading. This was shown by Carpinteri and Spagnoli [8]. This rotation of principal axes leads to additional cyclic hardening of materials. It happens both in low and high cycle fatigues.

Socie [42] and Socie and Marquis [43] showed this effect using Type 304 stainless steel material where higher range of shear and normal stress ranges were recorded for the case of out-of-phase loading as compared to in-phase-loading.

Proportional loading can be resolved into normal/principal stresses and shear stresses which act in the same direction/plane as the applied stresses.

In case of non-proportional loading, 2-dimensional and 3-dimensional stress transformation functions are used to determine the normal and shear stress and strains.

Figure 2-9 (a) shows a planar stress state (biaxial), with tensile stresses, σ_{xx} and σ_{yy} , applied in X and Y directions, respectively. Figure 2-9 (b) shows the transformed plane at an angle, Θ , where the normal stresses act perpendicular to, and the shear stress acts parallel to the two planes A and B.

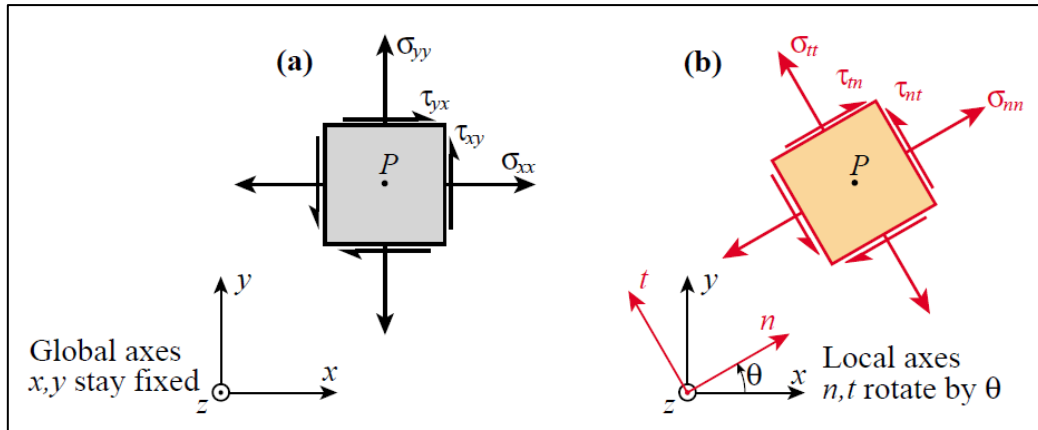


Figure 2-9: Transformation of planar stress state [University of Colorado Boulder]

Normal stress and shear stress equations for the transformed plane at an angle Θ are given as follows in single angle form,

$$\sigma_{mn} = \sigma_{xx} \cos^2 \theta + \sigma_{yy} \sin^2 \theta + 2\tau_{xy} \sin \theta \cos \theta \quad 2-8$$

$$\sigma_{tt} = \sigma_{xx} \sin^2 \theta + \sigma_{yy} \cos^2 \theta + 2\tau_{xy} \sin \theta \cos \theta \quad 2-9$$

$$\tau_{nt} = -(\sigma_{xx} - \sigma_{yy}) \sin \theta \cos \theta + \tau_{xy} (\cos^2 \theta - \sin^2 \theta) \quad 2-10$$

In double angle form these equations can be written as,

$$\sigma_{nm} = \frac{\sigma_{xx} + \sigma_{yy}}{2} + \frac{\sigma_{xx} - \sigma_{yy}}{2} \cos 2\theta + \tau_{xy} \sin 2\theta \quad 2-11$$

$$\tau_{nt} = -\frac{\sigma_{xx} - \sigma_{yy}}{2} \sin 2\theta + \tau_{xy} \cos 2\theta \quad 2-12$$

The maximum values of normal stress acting on the inclined planes are called principal stresses. For two-dimensional planar stress there are 2 principal stresses while for 3D stress state, there are 3 principal stresses.

$$\sigma_{1,2} = \frac{\sigma_{xx} + \sigma_{yy}}{2} \pm \sqrt{\left(\frac{\sigma_{xx} - \sigma_{yy}}{2}\right)^2 + \tau_{xy}^2} \quad 2-13$$

$$\tan 2\theta_p = \frac{2\tau_{xy}}{\sigma_{xx} - \sigma_{yy}} \quad 2-14$$

This gives two solutions $2\theta_1$ and $2\theta_2$ which are 180° s apart. This means there are two planes in range from 0° to 360° s where principal stresses act.

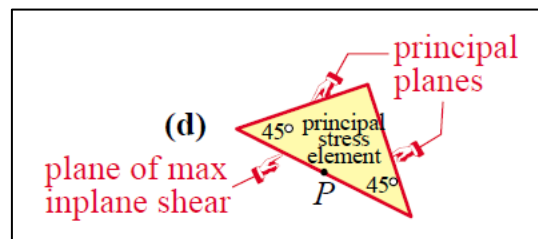


Figure 2-10: Plane of maximum shear [University of Colorado Boulder]

Maximum shear acting in-plane or out-of-plane is also of importance when it comes to fatigue assessments.

Furthermore, normal and shear stress on the inclined planes can be determined using the graphical method of stress and strain Mohr circle.

d. Effects of loading frequencies

In case of a sinusoidal biaxial loading, σ_{xx} and σ_{yy} , may or may not have the same frequency. If the two stresses acting on each other are from independent source, there is a good chance that they will be acting at different frequencies to each other leading to another type of non-proportional loading.

Even if the stresses are from the same source, factors such as shape and geometry of the structure can lead to a difference in the frequency of two stresses.

McDiarmid [29,30,31], was one of the first to test the results of variation of frequency on fatigue of a tubular section, subjected to longitudinal and transverse stresses.

e. Effect of mean stress

The effect of having a mean stress in a biaxially loading in any one or more directions has a direct effect on the fatigue life. While a compressive mean stress improves the fatigue life by decreasing the damage, a compressive mean stress does just the opposite.

This effect was first witnessed by Sines [39] where compressive mean stresses were shown to improve the fatigue life in the material.

Contrary to effects of mean normal stresses, mean shear stresses seem to show no significant effect on the fatigue life. This was shown in through tests conducted by Smith [41]

2. Geometry

The shape of the specimen for which the fatigue life assessment needs to be carried has an impact on the fatigue life. Changes in geometry leads to changes in stress distribution as well as stress localisation might occur depending on the shape.

During the fatigue tests following types of specimen are usually used:

- a. Shaft and pipe specimen
- b. Cruciform specimen
- c. Boxbeam specimen

Types of each are discussed in Figure 2-11, Figure 2-12 and Figure 2-13.

Furthermore, the specimen can have the following additional features depending on the aim of the test:

- a. Welded or seamless specimen
- b. Notched or un-notched specimen
- c. Slotted or un-slotted specimen



Figure 2-11: Types of shaft/pipe specimen [Laboratory Testing Inc.]

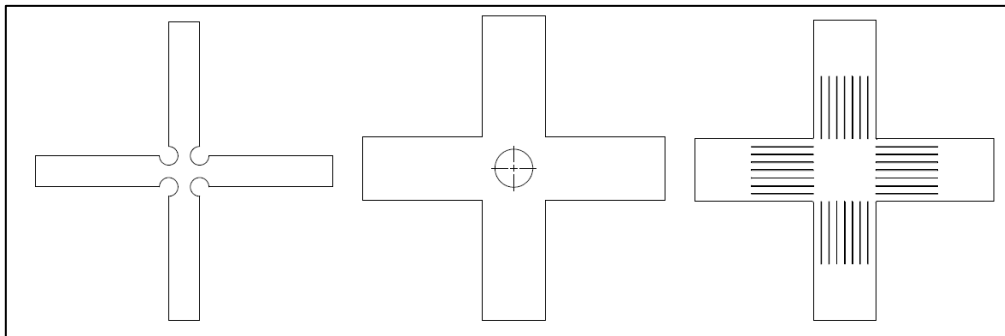


Figure 2-12: Types of cruciform specimen - Left to right – Cut type, Reduced section type and Strip and slop Type [22]

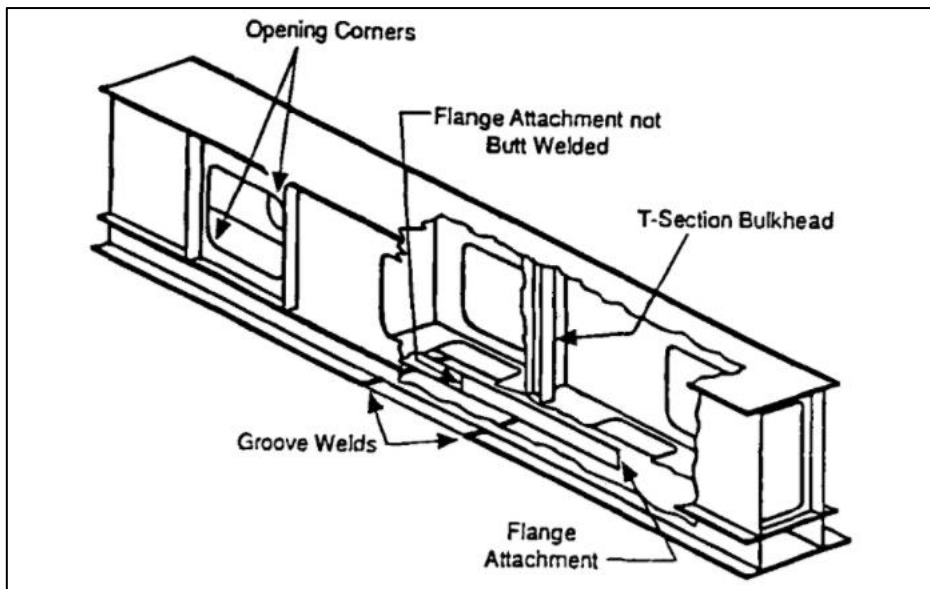


Figure 2-13: Boxbeam specimen details [22]

3. Material

Material has a huge impact on the fatigue life. With the change in material all material related properties change and the material behaviours under multiaxial stress state varies significantly. Challenge in fatigue life prediction model lies in the effort of developing an approach which can be used for the widest range of materials.

4. Others

Environmental conditions, corrosion and erosion effects among others also impact the fatigue life of a component or structure. These are not discussed in this report.

3 LITERATURE REVIEW

Multiaxial fatigue is currently an active area of research in many fields including aerospace, oil and gas, railways, etc due to its complexity and lack of understanding of the concept. Mechanical components and structures often face cyclic stresses which act in more than one direction leading to multiaxial stress state. Many methods have been researched and used till now to address the fatigue issues originating due to this multiaxial stress state.

Though research on fatigue started long back in 1850-1875 with Wohler [44] who tried to determine the endurance limit for train axels, the multiaxial fatigue was first addressed around 1970s when many experiments were carried out on different types of specimen to collect valuable fatigue data.

Fatigue life prediction models can be of various types based on their approach towards fatigue. According to Gustafsson and Saarinen [22], fatigue models can be grouped in following five categories:

1. Stress based models
2. Strain based models
3. Energy based models
4. Fracture mechanics models
5. Methods for welded components

Out of these, emphasis is made on the following approaches and combinations in this project work:

1. Stress based approach
2. Critical plane-based approach
3. Energy based approach
4. Combination of critical plane and energy-based approach

3.1 Stress based models

These fatigue life prediction models are based on the stresses involved in the multiaxial stress state. These stresses are used in one or more ways to determine the fatigue life of the component

or structure. According to Gustafsson and Saarinen [22], the models can further be divided into:

1. Empirical equivalent stress model
2. Stress invariants model
3. Average stress model
4. Critical plane stress model

Each approach has its advantages and disadvantages. Empirical equivalent stress approach is the most accepted approach in engineering practice today. Gough et al. [20] was one of the first to approach the multiaxial fatigue problem by conducting numerous experiments under torsion and bending stresses. Gough et al. [22] proposed ellipse quadrant approach to ductile materials and ellipse arc approach to brittle materials as follows,

$$\left(\frac{S_b}{f_{-1}}\right)^2 + \left(\frac{S_t}{t_{-1}}\right)^2 = 1 \quad 3-1$$

$$\left(\frac{S_t}{t_{-1}}\right)^2 + \left(\frac{S_b}{f_{-1}}\right)^2 \left(\frac{f_{-1}}{t_{-1}} - 1\right) + \left(\frac{S_b}{f_{-1}}\right)\left(2 - \frac{f_{-1}}{t_{-1}}\right) = 1 \quad 3-2$$

where,

S_b, S_t = Bending and torsional stress amplitudes, respectively;

t_{-1}, f_{-1} = Fatigue limits in reversed bending and torsion, respectively

Wang and Yao [46] showed that this approach is not suitable for non-proportional loading. Also, since the tests conducted by Gough et.al. [20] was specific to a material, this approach cannot be applied to all engineering materials or even weld details.

You et al. [50] improved the ellipse quadrant formula by Gough [20] by introducing material constant, phase difference and an empirical constant to address problems associated with Gough [20]'s approach. They used Findley [15]'s formula to further improve his formula which was applicable for both in-phase and out-of-phase loading.

Sines [39] studied failure criteria based on constant stress or stress invariant approach and concluded that octahedral shear stress is best suited. This approach was popular but is considered non-conservative according to Gustafsson and Saarinen [22].

Papadopoulos et. al. [33,34] proposed an approach based on average shear stress amplitude which acts on a critical plane. It addresses the constant amplitude proportional and non-proportional loading in high cycle fatigue. This approach is considered complex and mathematically demanding according to Gustafsson and Saarinen [22].

3.2 Critical plane approach

Critical plane approach is based on defining a plane on which the crack formation is likely to take place. In this approach the main criteria are to select a defined methodology to accurately define and predict the critical plane.

Critical plane selection can be done based on stress or strain and their ranges acting on the material. It has been seen that normal and shear stress and strain based critical planes have usually been selected in this kind of approach. While the stress based critical planes are applicable mainly to the high-cycle fatigue problems, the strain based critical planes are used for low-cycle fatigue life estimations.

3.2.1 Critical plane based on stress

Findley [15] was one of the first to adopt a critical plane-based approach for fatigue life estimation. He developed his approach based on shear and normal stresses which acted on a plane in a biaxial stress state. He adopted a shear plane and studied the influence of normal stresses on this plane. He predicted that the maximum normal stress development on the shear plane would affect the allowable alternating shear stress linearly.

His model was based on maximising the linear combination of shear stress range and the maximum normal stress to determine the critical plane on which fatigue crack growth is expected to initiate. He used a material coefficient (range for ductile 0.2-0.3) on the value of maximum normal stress in his model.

Furthermore, Bäckströms [5] concluded that the effective shear stress equal to the maximised linear combination of shear stress range and maximum normal stress acting on the critical plane would the same fatigue life prediction. He stated that failure shall be determined on a critical plane with the highest effective stress range than the alternating shear stress range.

Findley [15]'s model is found to give good results for in-phase and out-of-phase biaxial stresses.

$$\left[\left[\frac{\Delta\tau}{2} \right] + k \cdot \sigma_n \right]_{max} = \left[\frac{\Delta\tau'}{2} \right] = f \quad 3-3$$

where,

$\Delta\tau$ = Shear stress

σ_n = Normal stress

k = Material dependent coefficient (Normally 0.2-0.3)

$\Delta\tau$ = Effective shear range

f = Fatigue on a certain plane

McDiarmid [29,30,31] conducted numerous experiments on a thin walled tubular specimen under biaxial stress state. The aim of his experiments was to determine the effects of change of frequency, stress amplitude, phase and mean stress on the fatigue life for specimen loaded in biaxial stress state.

McDiarmid [29,30,31], introduced a critical plane approach which related the fatigue strength to the maximum shear stress range and maximum normal stress. The two planes considered for investigation were first proposed by Brown and Miller [7] for their strain based critical plane model. McDiarmid [29,30,31] based his critical plane on the maximum shear stress amplitude. Tubular specimen (Figure 3-1) used in his tests was made of EN24T steel material and had no welds. In 1985, he conducted tests with 8 cases as shown in Table 3-1.

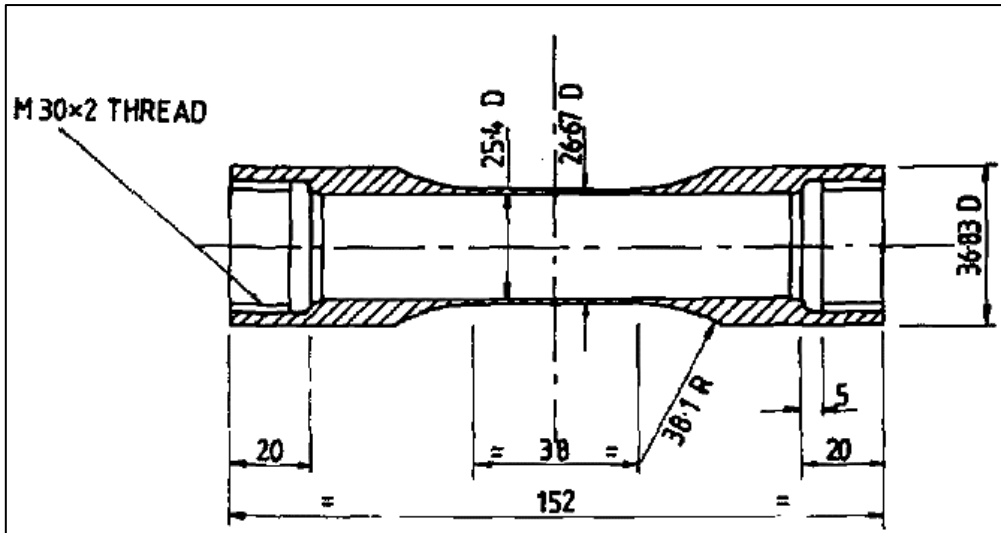


Figure 3-1: Tubular specimen used in fatigue tests, see McDiarmid [29]

Table 3-1: Load cases tested by McDiarmid [29]

Case	$\lambda = \sigma_{2a}/\sigma_{1a}$	$\Phi =$ Phase angle ($^{\circ}$)	$\alpha = \frac{\text{Frequency of } \sigma_{2a}}{\text{Frequency of } \sigma_{1a}}$
1	0	-	
2	0	-	
3	1	0	1
4	1	180	1
5	1	0	2
6	1	90	2
7	1	0	3
8	1	180	3

McDiarmid [29,30,31] concluded that the out of phase stresses acting at different frequencies produced varying maximum shear stress ranges and corresponding normal stress range was also not constant. The in-plane and out-of-plane stresses acting on a material are shown in Figure 3-2.

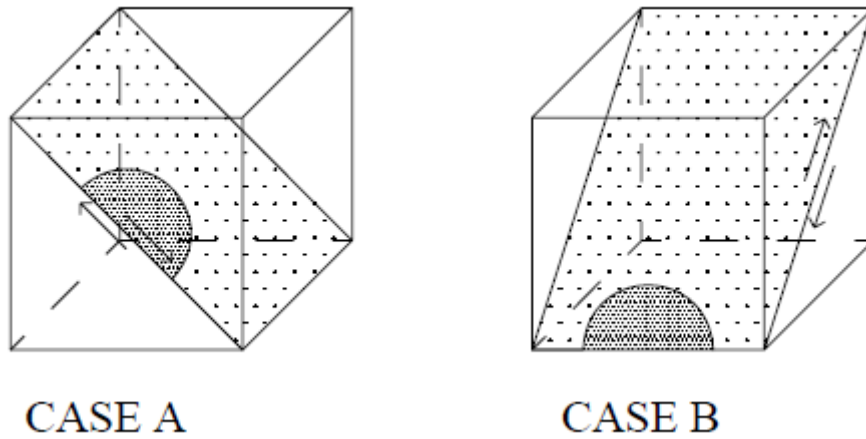


Figure 3-2: In-plane (Case-A) and out-of-plane (Case-B) shear [22]

McDiarmid [29,30,31]'s model can be presented in the form of following equation:

$$\frac{\Delta\tau_{max}}{2t_{A,B}} + \frac{\sigma_{n,max}}{2\sigma_{uts}} = 1 \quad 3-4$$

where,

$\Delta\tau_{max}$ = Shear stress amplitude

σ_{uts} = Ultimate tensile strength

$\sigma_{n,max}$ = Normal stress (acting on the same plane as $\Delta\tau_{max}$)

$t_{A,B}$ = Shear fatigue strength were A and B are two different cases in cracking

Limitations of McDiarmid [29,30,31]'s model can be listed as follows:

1. Model works only when maximum shear stress is in the range of $0.5t$ to t where t is fatigue strength in torsion.
2. Since all his tubular specimen were non-welded type, it is only safe to assume that this criterion works only for the parent metal and not for the welded material.

Dang-Van [10] developed a critical plane criterion for fatigue life that was based on microscopic shear and hydrostatic stresses which were combined in a linear relationship using constants “a” and “b” as follows:

$$\tau(t) + a\sigma_n(t) = b \quad 3-5$$

where,

$\tau(t)$ = Microscopic shear stress

$\sigma_n(t)$ = Microscopic hydrostatic stress

a, b = constants

Dang-Van [10] considered the granular level of the material and the parameters which affected the slip formation i.e. microscopic shear stress and parameter which affected the opening of cracks i.e. microscopic hydrostatic stresses. His approach was well received and is known to give good results for multiaxial stress states according to Gustafsson and Saarinen [22].

3.2.2 Critical plane based on strain

Brown and Miller [7] proposed a critical plane based on plastic deformation slip process which governs the crack initiation. Since the model is based on plastic deformations, it is used mainly for low cycle fatigue life estimation (cycles between 10²-10⁴). The area of focus of this report is elastic deformations and hence Brown and Miller [7]’s criterion is not discussed further in detail.

3.3 Energy-based approach

Energy considered in this approach is the strain energy. It can be of following types based on the type of fatigue:

1. Elastic strain energy for high cycle fatigue when the alternating stresses are well within the elastic limits of the material

2. Plastic strain energy for low cycle fatigue when the alternating stresses are beyond the elastic limits but less than the ultimate strength of the material.
3. Elastic-plastic energy for high cycle and low cycle when the alternating stresses are on the borderline between elastic and plastic limits.

Strain energy defines the damage that takes place in the material which is under a multiaxial stress state.

3.4 Combined critical plane energy-based approach

There has been advancement in critical plane approaches as more test data have shed light on nucleation and growth of cracks. Fatigue life under multiaxial stress state is understood to be either governed by a critical shear plane or a critical tensile plane. Critical plane of maximum shear strain range gives good results as it considers both failure mode and crack initiation mechanism. Guard [16], Brown and Miller [7] and Findley [15] have proposed fatigue parameters for life prediction based on maximum shear stress/strain and maximum normal stress/strain acting on the material.

As stated by Farahani [13,14], these critical plane fatigue parameters have been criticised for lack of adherence to continuum mechanics fundamentals. To overcome this major drawback, Liu [28], Chu et al. [9] and Glinka et al. [19] have used a combination of energy-based approach on the critical plane. In critical plane-energy combined approach normal and shear energies are calculated using different damage models.

Liu [28] considers both elastic and plastic strain energies for damage assessment on the critical plane. These were calculated based on Virtual Strain Energy (VSE) concept. The VSE approach is adopted from the uniaxial energy calculation model.

If VSE is given by ΔW_e and ΔW_p are the elastic and plastic strain energy, respectively, ΔW can be calculated as:

$$\Delta W_e + \Delta W_p = \Delta W \quad 3-6$$

This is approximately equal to $\Delta\sigma\Delta\varepsilon$ in according to Figure 3-3.

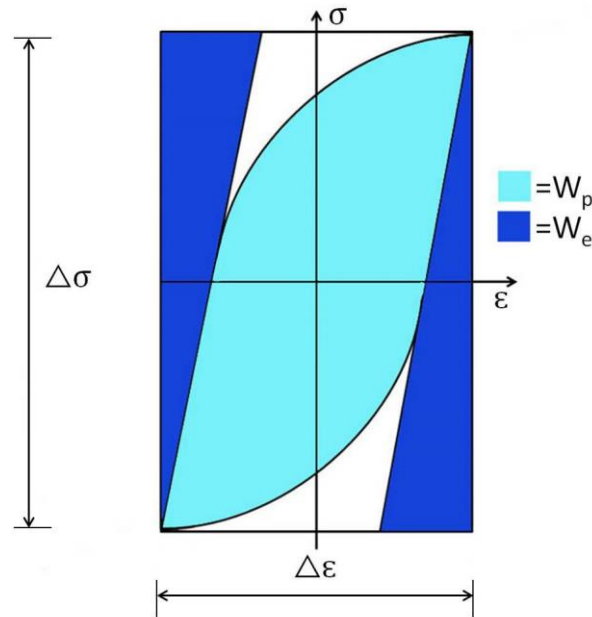


Figure 3-3: Hysteresis graph showing elastic and plastic strain energy regions

Chu et al. [9] approached the problem by using the Smith-Watson-Topper (SMT) parameter. SMT parameter was developed by Smith, Watson and Topper [41] based on maximum normal stress ($\sigma_{n,max}$) and the maximum principal strain range ($\Delta\epsilon_1$) as follows:

$$\sigma_{n,max} \frac{\Delta\epsilon_1}{2} = \frac{\sigma_f'^2}{E} (2N_f)^{2b} + \sigma_f' \epsilon_f' (2N_f)^{b+c} \quad 3-7$$

where,

σ_f' = Axial fatigue strength coefficient

ϵ_f' = Axial fatigue ductility coefficient

N_f = Number of cycles to failure

E = Young's elastic modulus

b, c = Constants

SMT parameter is effective in describing the effect of mean stress and strain hardening on a material regarding its fatigue life.

Parameter proposed by Glinka et al. [19] was based on the sum of the product of shear and normal energies which were acting on a critical plane selected based on shear stress criterion.

3.4.1 Farahani's fatigue parameter

When we consider critical plane based on maximum shear strain or maximum shear stress, fatigue occurs on a surface where one of the principal stresses zero. As a result, multiaxial fatigue problems are usually biaxial in nature.

Farahani [13,14] proposed an energy critical plane parameter for fatigue life assessment of metallic metals under various biaxial loading combinations and stress ranges:

1. In-phase and out-of-phase loading
2. Loading at different frequencies
3. Loading with mean stresses

Biaxial constant amplitude alternating stresses are considered in longitudinal and transverse direction. The critical plane is selected based on the angle of longitudinal stress loading that gives the highest shear strain/stress range according to Mohr circle calculations.

The biaxial loading is grouped into different cases i.e. block loading histories, based on the combination of phase change, frequency change and application of mean stresses.

Each block loading history can have one or more cycles of longitudinal stresses. For each half cycle of longitudinal stress, a critical plane is defined where maximum shear stress/strain is acting. For one cycle of longitudinal stress loading, two such planes are identified. Values of maximum shear stress/strain and corresponding maximum values of normal stress acting on that plane are determined using Mohr circle. An illustration of this method is shown with an example of B1 load history in Figure 3-4 and Figure 3-5.

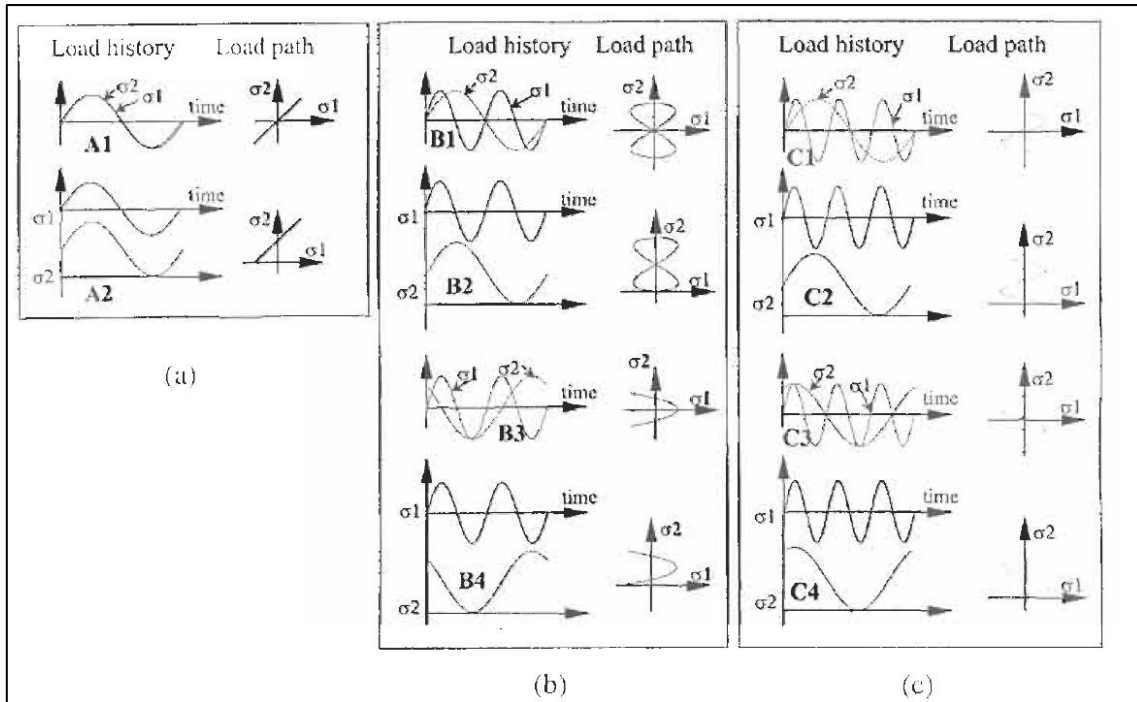


Figure 3-4: Load histories (a) A1-A2; (b) B1-B4; C1-C4 showing change of frequencies (A1, B1, C1), effect of mean stress (A2, B2, B4, C2, C4) and change of phase angle (B3, C3) [29]

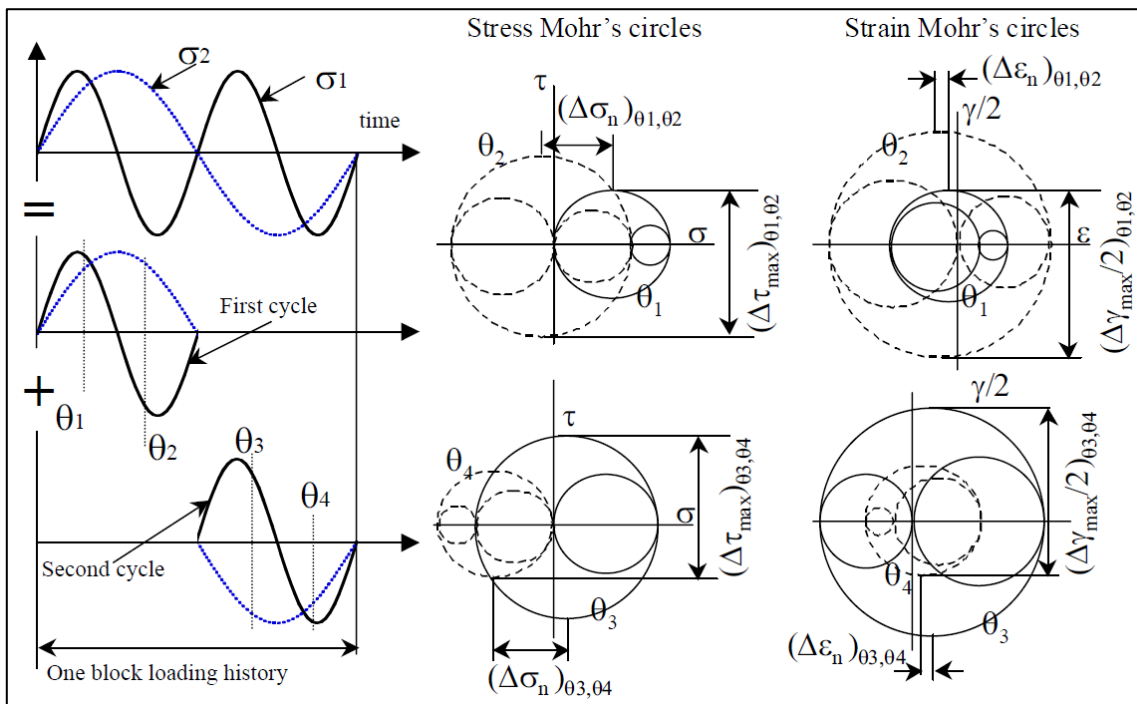


Figure 3-5: Calculation of maximum shear stress range ($\Delta\tau_{max}$), maximum shear strain range ($\frac{\Delta\gamma_{max}}{2}$) and corresponding normal stress range ($\Delta\sigma_n$) and strain range ($\Delta\epsilon_n$) values from Mohr circle for Load History B1 [29]

Thus, for each cycle of longitudinal stress acting in each load history, maximum shear stress and strain range can be calculated. Also, the range of maximum normal stress and strain acting on that plane can be calculated. Shear and normal energies can be obtained as a product of maximum shear strain - maximum shear stress and corresponding maximum normal stress - maximum normal strain, respectively. These shear and normal energies are normalized using the shear and axial material fatigue properties.

In earlier studies by Garud [17], Tipton [45], Andrews [2], Chu et al. [9] used an empirical weight factor that was governed by the material that was being investigated. In other studies, by Liu [28] and Glinka et al. [19], equal weight was given to both normal and shear energies. In Farahani [13,14], these empirical weight factors have been eliminated using shear and axial material fatigue properties. This makes it easier to use this parameter for a range of metals.

Farahani fatigue parameter ($f(N_f)$) for N number of longitudinal cycles in a fatigue loading history is given as a sum of fatigue parameter for each cycle of longitudinal loading as follows:

$$\sum_{i=1}^N \left\{ \frac{1}{\sigma'_f \varepsilon'_f} (\Delta\sigma_n \Delta\varepsilon_n)_i + \frac{\left(1 + \frac{\sigma_n^m}{\sigma'_f}\right)}{\tau'_f \gamma'_f} \left(\Delta\tau_{max} \Delta\left(\frac{\gamma_{max}}{2}\right) \right)_i \right\} = f(N_f) \quad 3-8$$

where,

σ'_f = Axial fatigue strength coefficient

ε'_f = Axial fatigue ductility coefficient

τ'_f = Shear fatigue strength coefficient

γ'_f = Shear fatigue ductility coefficient

$\Delta\sigma_n$ = Range of normal stress range corresponding to maximum shear stress range (MPa)

$\Delta\tau_{max}$ = Range of maximum shear stress range (MPa)

$\Delta\varepsilon_n$ = Range of normal strain range corresponding to maximum shear strain range (mm/mm)

$\left(\frac{\gamma_{max}}{2}\right)$ = Range of maximum shear strain range (mm/mm)

$\left(1 + \frac{\sigma_n^m}{\sigma_f}\right)$ = Mean stress correction factor; calculated for load histories A2, B2, B4, C2, C4

σ_n^m = Normal mean stress acting on critical plane

$f(N_f)$ = Farahani Fatigue Parameter

Farahani [13,14] correlated the results from proposed fatigue parameter to the results from McDiarmid [29,30,31] tests on thin wall tubular member subjected to a biaxial stress state. Value of Farahani [13,14]'s fatigue parameter describes the amount of damage that is accumulated in the critical plane of the material for a given load history.

Table 3-2: Load histories according to Farahani [13,14]

Block Loading Histories	λ	α	f_1	f_2	(σ_{1m})	(σ_{2m})	ϕ
A1	1	1	30	30	0	0	0
A2	1	1	30	30	0	σ_2	0
B1	1	2	30	15	0	0	0
B2	1	2	30	15	0	σ_2	0
B3	1	2	30	15	0	0	90
B4	1	2	30	15	0	σ_2	90
C1	1	3	30	10	0	0	0
C2	1	3	30	10	0	σ_2	0
C3	1	3	30	10	0	0	90
C4	1	3	30	10	0	35	90

where,

σ_1 = Constant amplitude alternating longitudinal stress applied through constant amplitude alternating force using fatigue testing machine (MPa)

σ_2 = Constant amplitude alternating transverse pressure applied across the specimen wall thickness (MPa)

f_1 = Frequency of σ_1 (Hz)

f_2 = Frequency of σ_2 (Hz)

σ_{1a} = Amplitude of σ_1 (MPa)

σ_{2a} = Amplitude of σ_2 (MPa)

σ_{1m} = Mean longitudinal stress (MPa)

σ_{2m} = Mean transverse stress (MPa)

λ = Ratio of stress amplitudes = σ_{1a}/σ_{2a}

α = Ratio of stress frequencies = f_1/f_2

Notes:

1. For A2, B2, B4, C2, C4 a pulsating tensile stress, equal to amplitude of alternating transverse stress (σ_2) is applied in the transverse direction only; $\sigma_{1m} = 0$
2. For B3, B4, C3, C4 - σ_2 always leads σ_1

4 METHODOLOGY

This chapter describes the methodology that is adopted for:

1. 3D model setup using 3D modelling software, Ansys SpaceClaim 17.1, and data from Wang et al. [46] and Zheng et al. [51].
2. Modal analysis using Ansys Workbench 17.1 (Static Structural module, Modal Analysis module & Design Assessment module).
3. VIV response prediction and stress range calculations using DNVGL-RP-F105 (2017 edition) [11].
4. Fatigue assessment and fatigue damage calculation using Farahani [13,14]'s fatigue damage parameter.

The complete methodology is presented in a flow chart (see Figure 4-1). The methodology is divided into the following major stages for an M-shaped rigid jumper:

1. Model setup
2. Modal analysis
3. Mode classification
4. Response model
5. Stress range and response frequency calculation
6. Fatigue damage assessment
 - a. Block loading
 - b. Critical plane selection
 - c. Normal and shear stress and strain range calculation at critical plane
 - d. Fatigue damage assessment

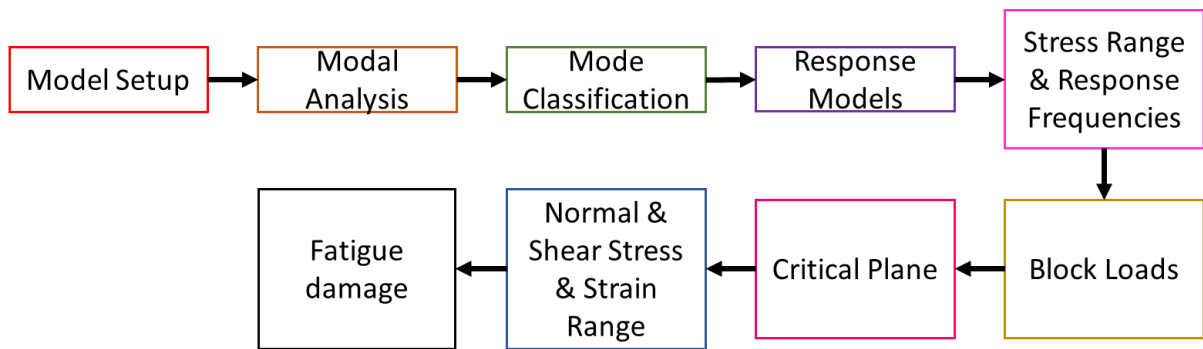


Figure 4-1: Flow Chart for fatigue damage assessment for M-shaped rigid jumper

4.1 3D Model

A rigid M-shaped rigid jumper model (see Figure 4-2) has been selected based on ExxonMobil's Jumper VIV Research Program and data from the subsequent work done by Wang et al. [46] and Zheng et al. [51].

An FE model is prepared using Ansys SpaceClaim 17.1.

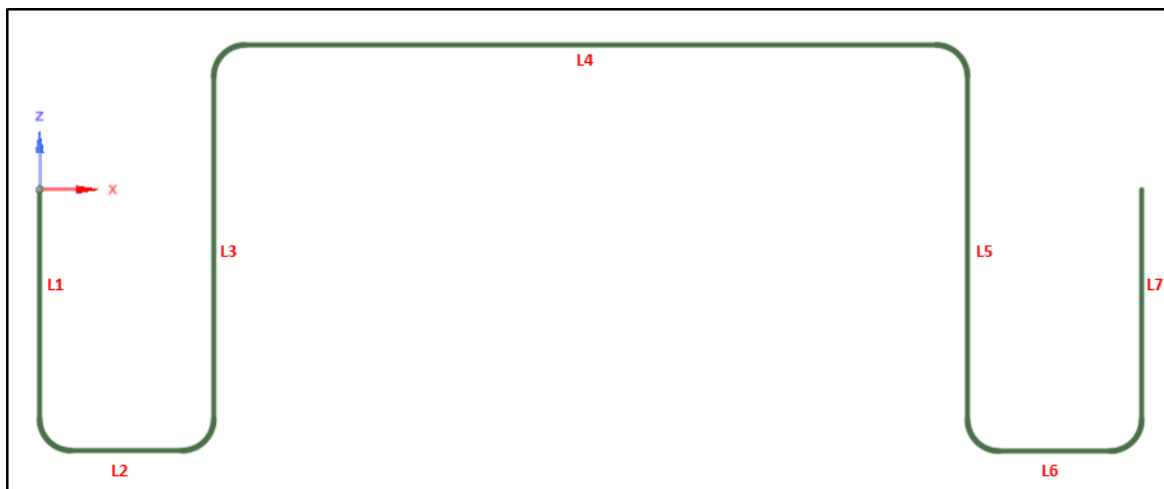


Figure 4-2: M-shaped rigid spool jumper model – ExxonMobil's Jumper VIV Research Program

ExxonMobil conducted a series of model testing experiments in 2012 using an M-shaped rigid jumper as part of its Jumper VIV Research Program. Under this program, a scaled M-shaped rigid jumper, at different orientations with respect to spool run, was exposed to a range of towing speeds in a 200m towing tank located at National Research Council's Ocean, Coastal and River Engineering facility in Canada with the help of support frames (See Figure 4-3).

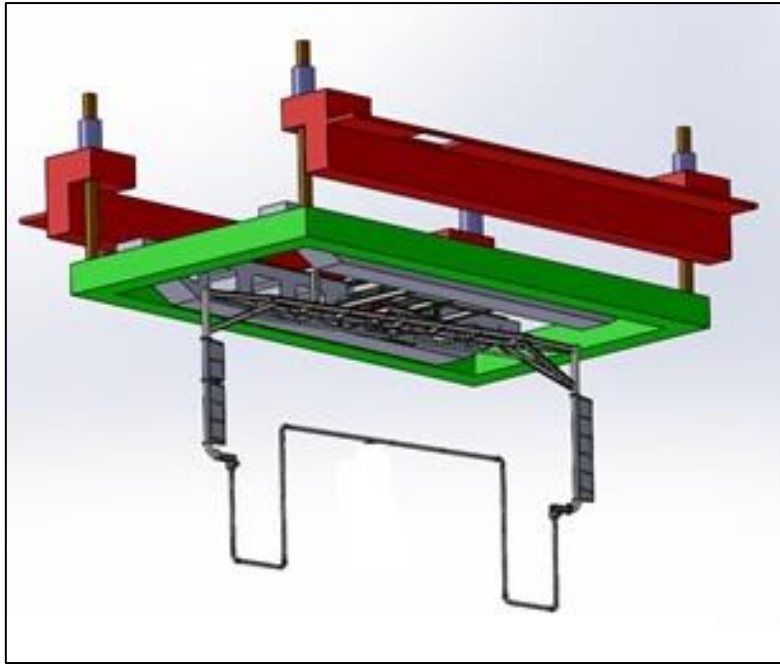


Figure 4-3: Towing experimental setup – ExxonMobil’s Jumper VIV Research Program (Wang et al. [46])

By towing the spool at varying speeds and orientations, current dominant conditions were created in the towing tank, such as those at the seabed. The responses, in the form of accelerations, bending/torsion strain and end connection loads, due to current velocities on the spool were recorded using accelerometers and strain gauges installed on the spool at different locations. The locations of accelerometers and strain gauges are shown in Figure 4-4.

The M-shaped spool is fixed at the two ends where dynamometers (ATI N and ATI P) are installed to measure the end loads. ACC (1-13) refers to the accelerometers and ST1-ST3 refers to the strain gauges in Figure 4-4.

Two configurations, bare and straked, were tested in 3 different orientations - 10° , 45° and 90° with respect to the axis of spool run.

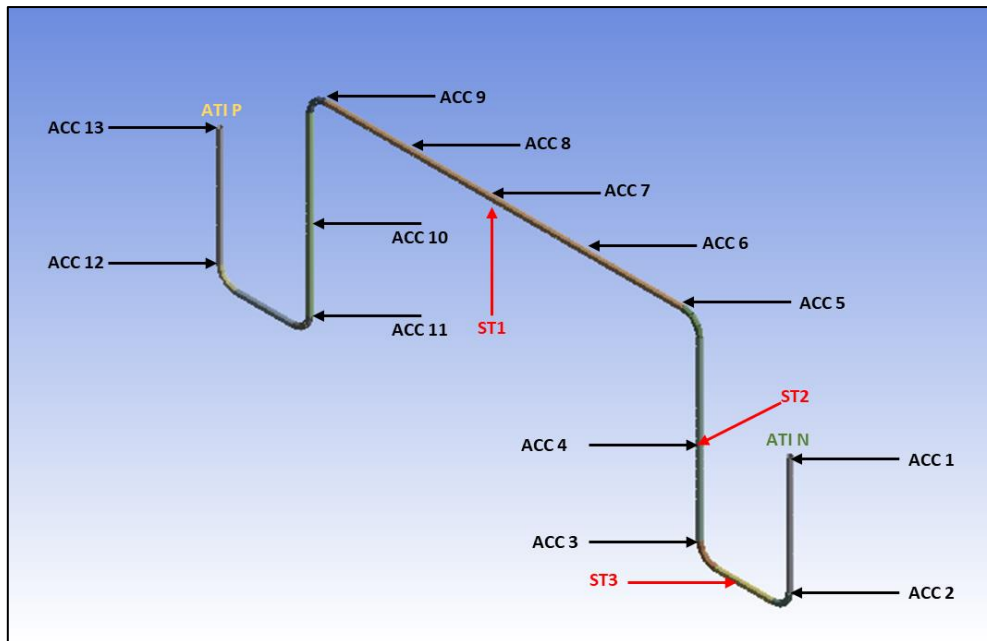


Figure 4-4: Location of accelerometers and strain gauges on spool model

The model was scaled to fit the testing facility capacity. Scaled jumper model properties and dimensions of each segment of jumper are given in Table 4-1 and Table 4-2. Out of the two configurations, bare model tests were carried out to observe and study the initiation of VIV and corresponding loads on the spool exposed to a range of uniform currents. A total of 82 tests were carried out at the 3 orientations with speed varying from 0.05 m/s to 0.98 m/s for 0° and 45° orientations while the upper limit of current speed was limited to 0.79 m/s due to the limitations of load capacity of the dynamometers installed at the fixed ends.

Table 4-1: Jumper model properties

Properties	Value – ExxonMobil Model (Wang et al. [46], Zheng et al. [51])
Total length	13.96 m
Pipe density	2700 kg/m ³
Unit mass in air	3.8 kg/m
Unit mass filled with oil	6.66 kg/m
Mass ratio	2.33
Outer diameter	0.0605 m
Inner diameter	0.055 m
Wall thickness	0.00277
Elastic modulus (E)	6.90 E+10
Bending stiffness (EI)	1.44 E+04
Shear modulus (J)	2.61 E+10
Torsional stiffness (GJ)	1.08 E+04

Table 4-2: Dimensions of segments of jumper model

Segment	Length – ExxonMobil Model (Wang et al. [46], Zheng et al. [51])
L1	1.495 m
L2	1.000 m
L3	2.323 m
L4	4.327 m
L5	2.326 m
L6	1.000 m
L7	1.495 m

4.2 Modal Analysis

A modal analysis is performed to access the vibrational characteristics of a structure to gather information about the natural frequencies of the structure, mode shapes and modal stresses.

For rigid jumper exposed to uniform current velocities, the knowledge of vibrational characteristics is the first and the most important step in determining the VIV response.

Modal analysis is carried out using Ansys Mechanical Workbench's Modal analysis module. The results from Modal analysis such as eigen frequencies, mode shapes and modal stresses are used in the estimation of VIV induced responses according to DNVGL-RP-F105 (2017 edition) [11].

4.2.1 Hydrodynamic parameters

Hydrodynamic parameters are an important input for Modal analysis. Following hydrodynamic parameters are specified using Ansys Mechanical Workbench help document as input for modal analysis:

1. Drag coefficients
2. Added mass coefficients (C_{ay} , C_{az})
3. Inertia coefficients (C_{my} , C_{mz})

In addition to the hydrodynamic parameters, following environmental data is also required:

1. Water depth

2. Sea water density

All parameters are included in the FE model via APDL “ocean loading” command.

4.2.2 Damping and Eigen modes

No damping is considered in the modal analysis to access the full extent of modal deflections as well as flexural and torsional modal stresses.

The maximum number of modes & eigen frequencies to be calculated is set at 9. This value has been selected based on the work done by Igeh [24] in which she conducted a modal analysis using Ansys APDL (Classic) for the same jumper model in line with DNVGL-RP-F105 (2006 edition) [12].

4.2.3 Unit diameter stress amplitude

Unit diameter stress amplitude for a mode j is the modal stress corresponding to the unit outer diameter of the pipe and is calculated by multiplying the modal stress amplitude with a ratio of outer diameter of the pipe and maximum displacement/modal curvature. Unit diameter stress amplitude for in-line or cross-flow directions for a mode j is determined as follows:

$$(A_{IL/CF,j})(x) = \psi_j(x) \times \frac{D_o}{\kappa_{max_j}} \quad 4-1$$

where,

$(A_{IL/CF,j})(x)$ = Unit diameter stress amplitude as a function of x (pipe run) for in-line or cross-flow direction depending on the mode classification of mode j (MPa)

$\psi_j(x)$ = Modal stress amplitude (flexural or torsional) as a function of x (pipe run) for mode j (MPa)

D_o = Outer diameter of pipe (m)

κ_{max_j} = Maximum displacement of mode j (m)

4.3 Mode Classification

A mode is associated with a unique eigen frequency of the structure and gives the modal deflections/modal curvatures as well as the modal stresses. Modes can be classified:

1. Based on multi-mode response of a structure as:
 - a. Active modes
 - b. Participating modes
 - c. Contributing modes
2. Based on flow orientation:
 - a. In-line modes
 - b. Cross-flow modes

It is also important to select between a multimode analysis or a single point analysis for determination of response values for a given structure under VIV.

4.3.1 Mode classification for multi-mode response

1. For straight pipe

According to DNVGL-RP-F105 (2017 edition) [11], for a straight subsea pipeline, modes can be classified as:

Active modes – All modes that may be excited by VIV are considered as active modes.

Participating modes – It is a subset of active modes. A mode, j , is considered participating in the participation interval, $x_{start,j} < x < x_{end,j}$, where the participation interval is defined by the following criteria:

$$|A_{IL/CF,j}(x)| < \frac{A_{IL/CF,j}^{max}}{10} \text{ for } x_{start,j} < x < x_{end,j} \quad 4-2$$

where:

$A_{IL/CF,j}(x)$ = Unit diameter stress amplitude for mode j (in –line or cross flow) depending of mode classification as a function of x ;

$A_{IL/CF,j}^{max}$ = Maximum unit diameter stress amplitude for mode j (in –line or cross flow) depending of mode classification

Contributing modes - It is a subset of participating modes and consists only of those modes which, at a given location x and current velocity, adhere to the following criteria based on the extent of response amplitude or stress range depending on if a given active mode has been classified as cross-flow or in-line:

$$(A_z/D)_j \geq 0.1(A_z/D)_{max} \text{ for cross-flow direction;} \quad 4-3$$

$$S_{IL,j}^P(x) \geq 0.1S_{IL}^{max}(x) \text{ for in-line direction} \quad 4-4$$

where,

$(A_z/D)_j$ = Normalized cross-flow VIV amplitude of mode j

$(A_z/D)_{max}$ = Normalized VIV amplitude for the dominant cross flow mode

$S_{IL,j}^P(x)$ = Preliminary response stress range for the j-th in-line mode

$S_{IL}^{max}(x)$ = Response stress range associated with the dominant in-line mode

2. For non-straight geometries

For non-straight geometries, following additional design criteria are given in DNVGL-RP-F105 (2017 edition) [11] which, where applicable, supersede the criteria given in Section 1.

1. All participating modes for a non-straight geometry shall be considered as contributing i.e. the requirement for determining the contributing modes from the participating modes stands void for non-straight geometries.

4.3.2 Mode classification based on flow orientation

Relative to the flow of current, the displacement in the pipe can be in-line or 90° out of plane. Hence, the modes can be classified as in-line modes and cross-flow modes.

For straight pipes, the modes can be classified distinctly as in-line or cross flow based on the direction of displacement with respect to the direction of current flow.

For non-straight geometry however, the modes classification depends on

1. Direction of run of a segment of pipe (vertical or horizontal);
2. Direction of current flow with respect to direction of pipe run for a given segment of pipe;

Figure 4-5 shows a part of non-straight geometry with two pipe segments – a vertical segment (V1) and a horizontal segment (H1). Two possible modes are also shown which may exist for this given geometry – Mode 1 (in XZ plane) and Mode 2 (in XY plane). Furthermore, three cases of current flow directions are given - $U_{\Theta 1}$ (in direction of Y-axis), $U_{\Theta 2}$ (at an angle to Y and Z-axis) and $U_{\Theta 3}$ (in direction of negative Z-axis).

According to DNVGL-RP-F105 (2017 edition) [11],

1. Case-1

For $U_{\Theta 1}$, Mode 1 is distinctly cross-flow and Mode 2 is distinctly in-line for V1 and H1

2. Case-2

For $U_{\Theta 2}$, For V1, Mode 1 and 2 are both in-line and cross-flow. For H1, Mode 1 is cross-flow and Mode 2 is in-line.

3. Case-3

For $U_{\Theta 3}$, For V1, Mode 1 is in-line and Mode 2 is cross-flow. For H1, no mode is in-line or cross-flow.

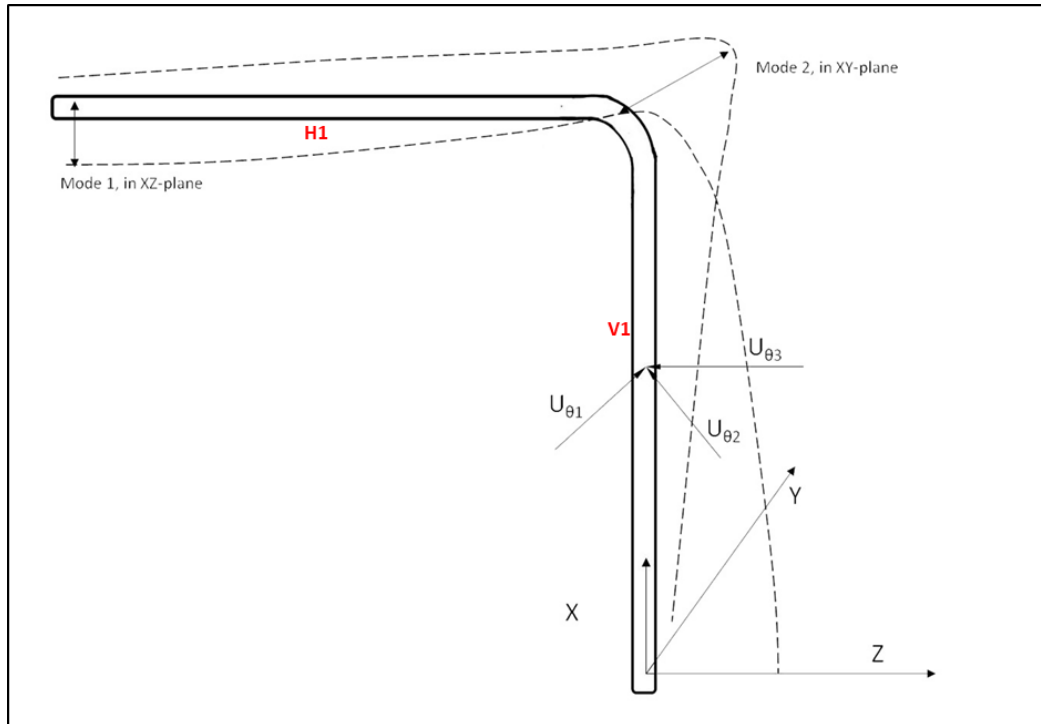


Figure 4-5: Non-straight pipe geometry showing two modes (Mode 1 and 2) and three directions of current flow ($U_{\theta 1}$, $U_{\theta 2}$ and $U_{\theta 3}$) [Recreated from DNVGL-RP-F105 (2017 edition) [11]]

4.3.3 Selection of critical point for single point analysis

Criteria for selection of a single critical point for response calculation and fatigue damage assessment is not clearly defined in DNVGL-RP-F105 (2017 edition) [11]. In the absence of such a selection criterion, Design Assessment module of Ansys Mechanical Workbench has been used to combine the active IL and CF modes for at 10° and 90° flow to assess the maximum unit amplitude stresses (flexural and torsional) at all points along the rigid jumper. From this, two critical points selected for fatigue damage assessment are considered based on following criteria:

Location A: Location over the arc length of the rigid jumper at which the combined unit amplitude flexural stress is maximum.

Location B: Location over the arc length of the rigid jumper at which the combined unit amplitude torsional stress is maximum.

4.4 Response Model based on DNVGL-RP-F105 (2017 edition) [11]

The response models described in DNVGL-RP-F105 (2017 edition) [11] are empirical models which uses hydrodynamic and structural parameters to determine the maximum steady state VIV amplitude response of a structure. The hydrostatic parameters are extremely important in establishing the response model from environmental loads.

4.4.1 General

This response model is a well-established method of estimating the VIV response for a structure for following cases:

1. In-line VIV in steady current and current dominated conditions
2. Cross-flow VIV induced in-line motion
3. Cross-flow VIV in steady current and combined wave and current conditions
4. Cross-flow VIV in wave dominated low Keulegan-Carpenter flow regimes

Since the towing tests conducted under the Exxon Mobil's Jumper VIV Research Program represented pure current dominated conditions, we shall only consider the case for In-line VIV and Cross-flow VIV in steady and uniform current conditions for this study.

A step wise process for construction of response model and calculation of response stress range and response frequency is given in Figure 4-6.

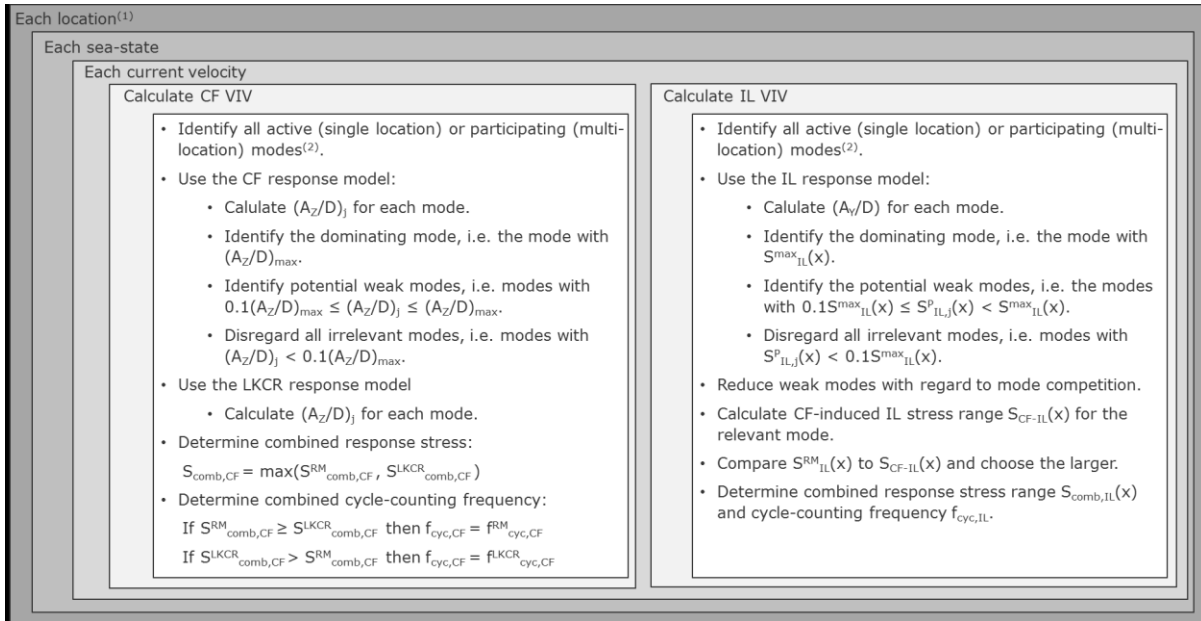


Figure 4-6: Calculation process for multi-mode response [DNVGL-RP-F105 (2017 edition) [11]]

4.4.2 Hydrodynamic Parameters

Some of the hydrodynamic parameters and dimensionless numbers used in construction of the response models are given as follows:

1. Reduced velocity (V_r and V_{rd})

Reduced velocity is defined as following:

$$V_R = \frac{U_c + U_w}{f_j D} \quad 4-5$$

where,

f_j = Still-water eigen frequency for the j-th mode

U_c = Mean current velocity normal to the pipe

U_w = Significant wave-induced flow velocity

D= Outer pipe diameter

Design value of reduced velocity (V_{rd}) is used for all response model calculations and is defined as follows:

$$V_{rd} = V_R \gamma_{f,IL/CF} \quad 4-6$$

where,

V_r = Reduced velocity

$\gamma_{f,IL/CF}$ = Safety factor for in-line or cross-flow natural frequency (See

Table 4-4)

It may be noted that for non-straight pipes, reductions in flow velocity due to angle of attack/flow angle (Θ_{rel}) is not to be considered for modes which are excited for both in-line and cross-flow conditions.

2. Keulengan-Carpenter number (KC)

Keulengan-Carpenter number is defined as following:

$$KC = \frac{U_w}{f_w D} \quad 4-7$$

where,

$f_w = 1/T_u$ is the significant wave frequency.

For a current dominant condition, $KC = 0$

3. Current velocity ration (α)

Current velocity ratio is defined as following:

$$\alpha = \frac{U_c}{U_c + U_w} \quad 4-8$$

where,

U_c = Mean current velocity normal to the pipe

U_w = Significant wave-induced flow velocity

For a current dominant condition, $U_w = 0$, and therefore $\alpha = 1$

4. Turbulence intensity (I_c)

Turbulence intensity is defined as following:

$$I_c = \frac{\sigma_c}{U_c} \quad 4-9$$

where,

σ_c = Standard deviation of the velocity fluctuations

U_c = 10 min or 30 min average (mean) velocity at 1 Hz sampling rate

In the absence of available information, I_c can be considered as 5%.

5. Flow angle (Θ_{rel})

It is defined as the angle between the flow and the pipeline direction. In case of the rigid jumper, it is the angle between the flow direction and the plane of rigid jumper.

6. Stability parameter (K_s and K_{sd})

Stability parameter is defined as following:

$$K_s = \frac{4\pi m_e \zeta_T}{\rho_w D^2} \quad 4-10$$

where,

ρ_w = Water density

ζ_T = Total modal damping ratio which is the sum of structural damping (ζ_{str}), soil damping (ζ_{soil}) and hydrodynamic damping (ζ_h)

ζ_{str} = Assumed 0.01 in the absence of information

ζ_{soil} = Assumed zero considering no pipe-soil interaction.

ζ_h = Assumed zero for VIV lock-in region

m_e = Effective mass per unit length which is the sum of structural mass (m_{st}), mass of internal fluid (m_c) and added mass (m_a)

Design value of stability parameter (K_{sd}) is used for all response model calculations and is defined as follows:

$$K_{sd} = \frac{K_s}{\gamma_k} \quad 4-11$$

where,

K_s = Stability parameter

γ_k = Safety factor for stability parameter (See Table 4-3)

4.4.3 In-line response model

The inline-response model gives the inline VIV steady state response amplitude for a range of reduced velocities.

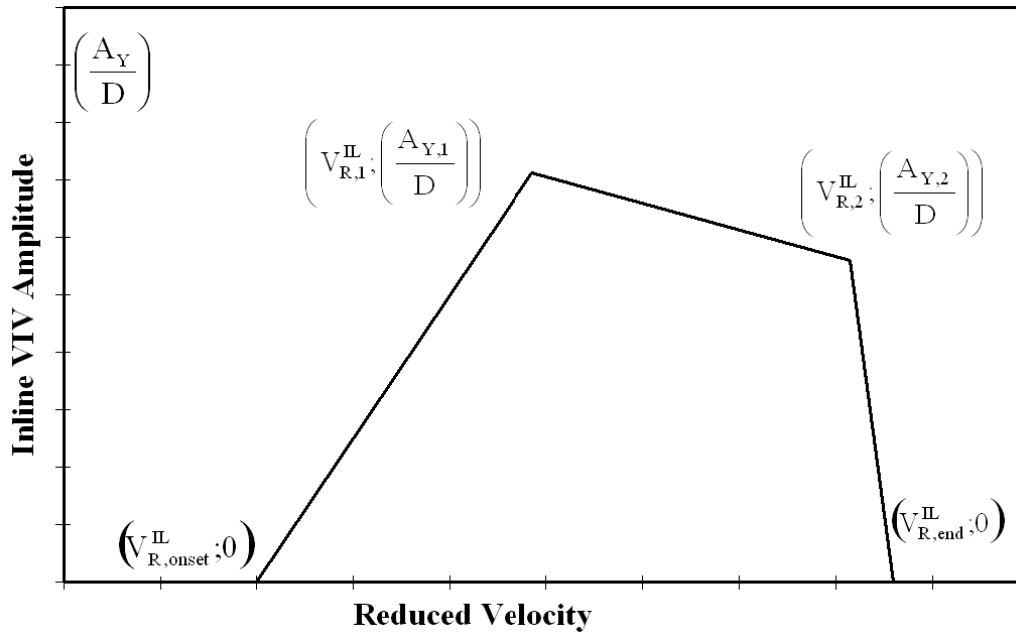


Figure 4-7: In-line response model [DNVGL-RP-F105 (2017 edition) [11]]

The in-line response model is constructed according to Figure 4-7 from the following set of empirical equations:

$$V_{R,onset}^{IL} = \begin{cases} \frac{1}{\gamma_{on,IL}} & \text{for } K_{sd} < 0.4 \\ \frac{0.6 + K_{sd}}{\gamma_{on,IL}} & \text{for } 0.4 \leq K_{sd} < 1.6 \\ \frac{2.2}{\gamma_{on,IL}} & \text{for } K_{sd} \geq 1.6 \end{cases} \quad 4-12$$

$$V_{R,1}^{IL} = 10 \cdot \frac{A_{Y,1}}{D} + V_{R,onset}^{IL} \quad 4-13$$

$$V_{R,2}^{IL} = V_{R,end}^{IL} - 2 \cdot \frac{A_{\gamma,2}}{D} \quad 4-14$$

$$V_{R,end}^{IL} = \begin{cases} 4.5 - 0.8 \cdot K_{sd} & \text{for } K_{sd} < 1.0 \\ 3.7 & \text{for } K_{sd} \geq 1.0 \end{cases} \quad 4-15$$

$$\frac{A_{\gamma,1}}{D} = \max \left(0.18 \left(1 - \frac{K_{sd}}{1.2} \right) \cdot R_{1\theta,1}; \frac{A_{\gamma,2}}{D} \right) \quad 4-16$$

$$\frac{A_{\gamma,2}}{D} = 0.13 \left(1 - \frac{K_{sd}}{1.8} \right) \cdot R_{1\theta,2} \quad 4-17$$

where,

$\gamma_{on,IL}$ = safety factor for onset value for in-line or cross-flow V_R . It can be taken from Table 4-3.

$R_{I\theta,1}$ and $R_{I\theta,2}$ = Reduction functions which are calculated from turbulence intensity (I_c) and flow angle (Θ_{rel}) and account for the effects of turbulence and angle of attack of the current for the flow. These can be read from Figure 4-8 and calculated from the following equations:

$$R_{I\theta,1} = 1 - \pi^2 \left(\frac{\pi}{2} - \sqrt{2 \cdot \theta_{rel}} \right) (I_c - 0.03) \quad 0 \leq R_{I\theta,1} \leq 1 \quad 4-18$$

$$R_{I\theta,2} = 1.0 - \frac{(I_c - 0.03)}{0.17} \quad 0 \leq R_{I\theta,2} \leq 1 \quad 4-19$$

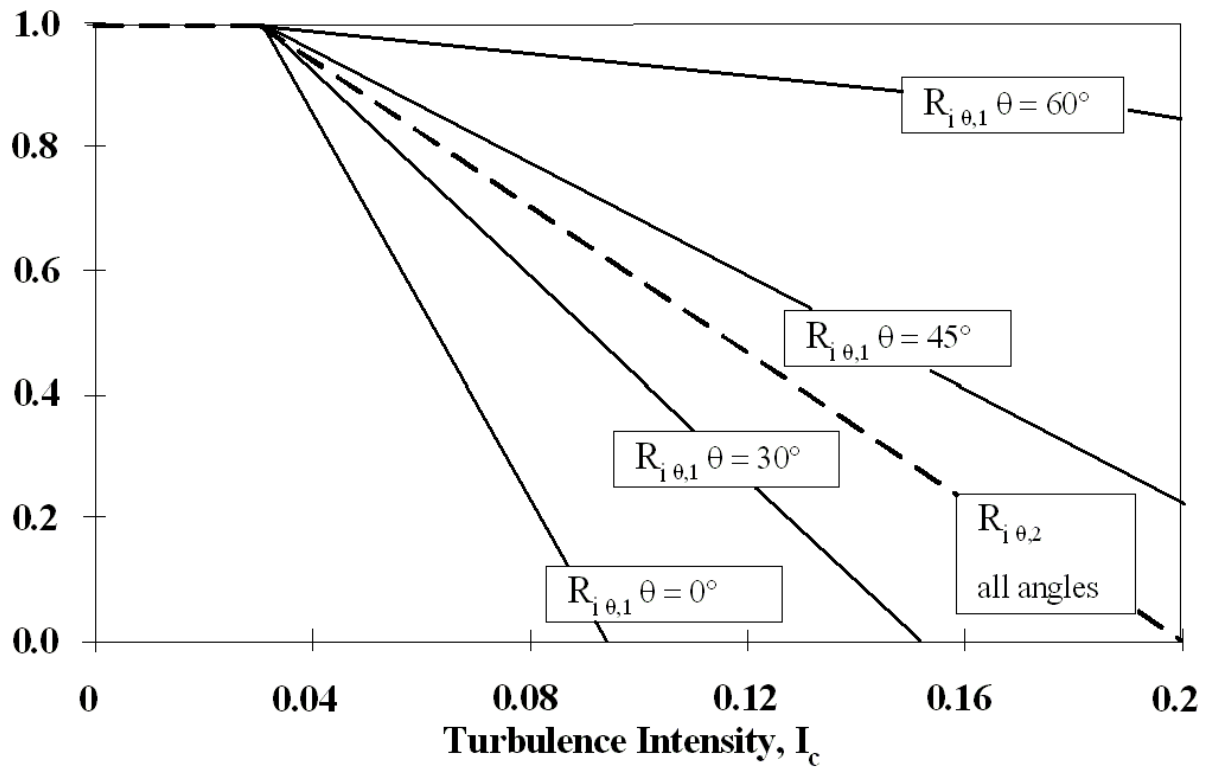


Figure 4-8: Reduction functions ($R_{I\theta,1}$ and $R_{I\theta,2}$) as a function of Turbulence Intensity (I_c) [DNVGL-RP-F105 (2017 edition) [11]]

4.4.4 Cross-flow response model

The cross-flow response model gives the cross-flow VIV steady state response amplitude for a range of reduced velocities.

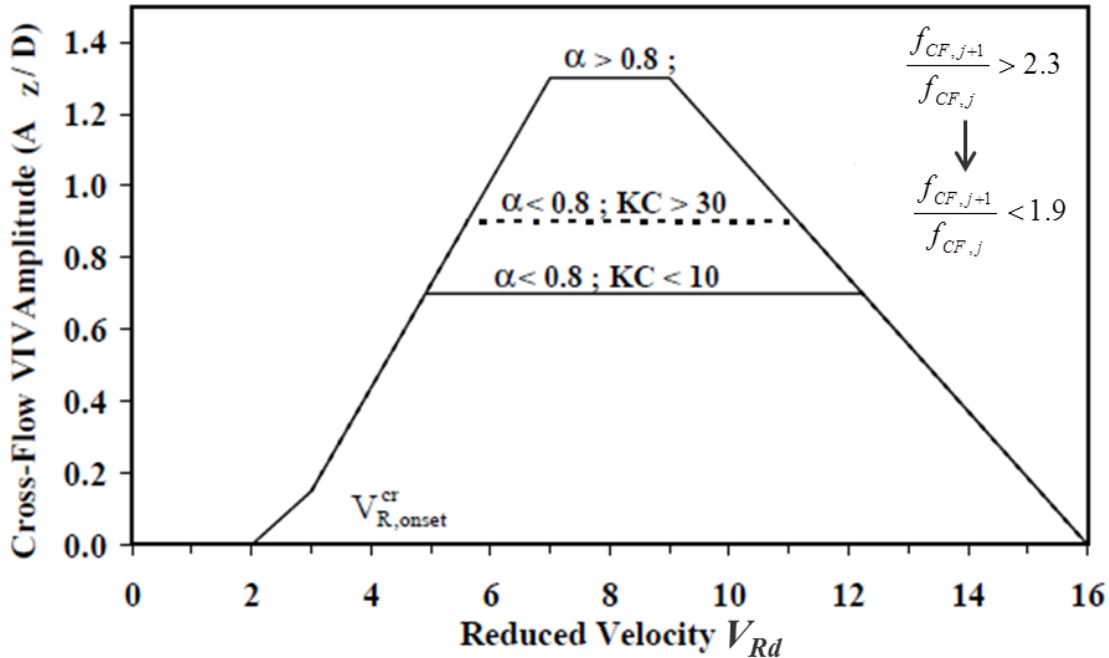


Figure 4-9: Cross-flow response model based on different α , KC and fratio values [DNVGL-RP-F105 (2017 edition) [11]]

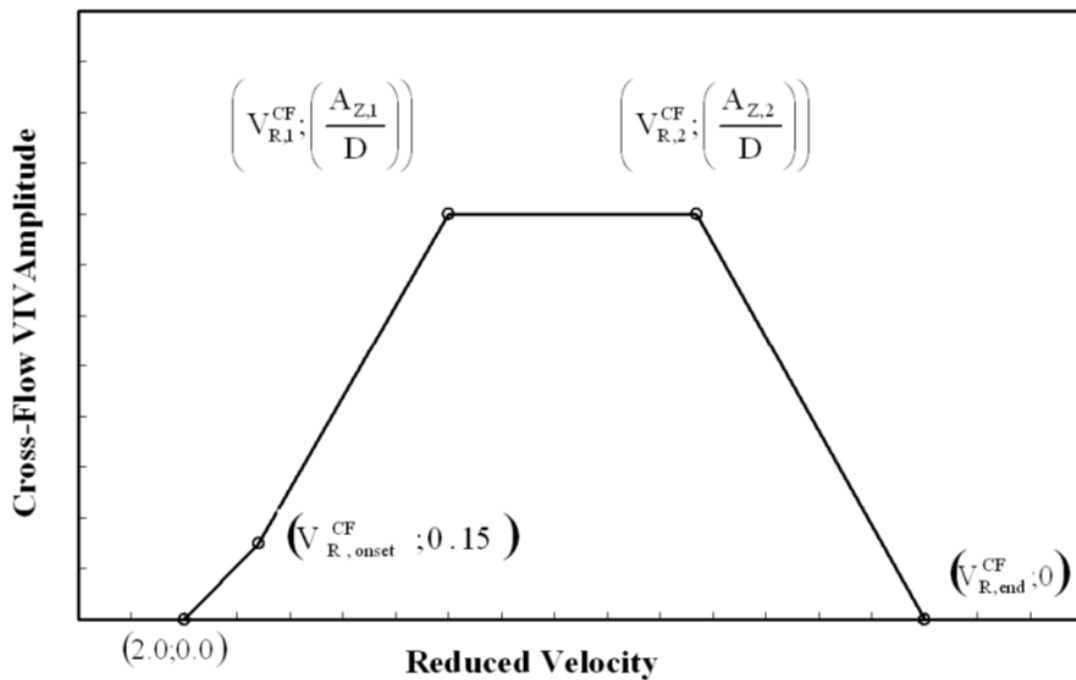


Figure 4-10: Cross-flow response model [DNVGL-RP-F105 (2017 edition) [11]]

Figure 4-9 shows how the cross-flow response model changes with different values of current velocity ratio (α) and Keulegan-Carpenter number (KC).

The in-line response model is constructed according to Figure 4-10 from the following set of empirical equations:

$$V_{R,onset}^{CF} = \frac{3 \cdot \Psi_{proxi,onset} \cdot \Psi_{trench,onset}}{\gamma_{on,CF}} \quad 4-20$$

$$V_{R,1}^{CF} = 7 - \frac{V_{R,onset}^{CF}}{1.15} \cdot \left(1.3 - \frac{A_{z,1}}{D}\right) \quad 4-21$$

$$V_{R,2}^{CF} = V_{R,end}^{CF} - \left(\frac{7}{1.3}\right) \cdot \left(\frac{A_{z,1}}{D}\right) \quad 4-22$$

$$V_{R,end}^{CF} = 16 \quad 4-23$$

$$\left(\frac{A_{z,1}}{D}\right) = \begin{cases} 0.9 & a > 0.8 & f_{ratio} < 1.5 \\ 0.9 + 0.5(f_{ratio} - 1.5) & a > 0.8 & 1.5 \leq f_{ratio} \leq 2.3 \\ 1.3 & a > 0.8 & f_{ratio} > 2.3 \\ 0.9 & a \leq 0.8 & 30 \leq KC \leq 40 \\ 0.7 + 0.01(KC - 10) & a \leq 0.8 & KC \leq 30 \\ 0.7 & a \leq 0.8 & KC < 10 \end{cases} \quad 4-24$$

$$\frac{A_{z,2}}{D} = 0.13 \left(1 - \frac{K_{sd}}{1.8}\right) \cdot R_{1\theta,2} \quad 4-25$$

where,

f_{ratio} = is cross-flow frequency ratio for two consecutive (participating) cross-flow modes, taken as the minimum of $\frac{f_{CF,j}}{f_{CF,j-1}}$ and $\frac{f_{CF,j+1}}{f_{CF,j}}$.

$\Psi_{proxi,onset}$ is defined as a correction factor for seabed proximity at the onset of response and given by following expression:

$$\Psi_{proxi,onset} = \begin{cases} \frac{1}{5} \left(4 + 1.25 \frac{e}{D} \right) & \text{for } \frac{e}{D} < 0.8 \\ 1 & \text{for } \frac{e}{D} \geq 0.8 \end{cases} \quad 4-26$$

where,

$\frac{e}{D}$ is defined as the ratio between the seabed proximity of pipe to the outside diameter of the pipe.

$\Psi_{trench,onset}$ is defined as a correction factor that incorporates the effect of a pipe running in or over a trench and is given by the following expression:

$$\Psi_{trench,onset} = 1 + 0.5 \frac{\Delta}{D} \quad 4-27$$

where,

$\frac{\Delta}{D}$ is the relative trench depth (see Figure 4-11) and defined as given below:

$$\frac{\Delta}{D} = \frac{1.25d - e}{D} \quad 4-28$$

$\frac{\Delta}{D}$ has value between 0 to 1.

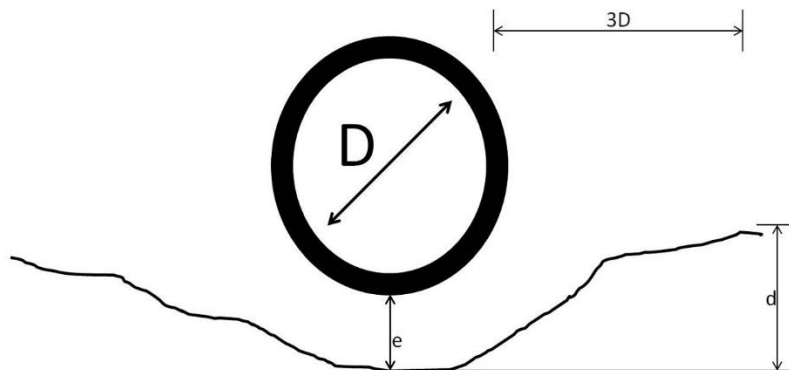


Figure 4-11: Trench proximity/factor [Recreated from DNVGL-RP-F105 (2017 edition) [11]]

4.4.5 Safety factors

Safety factors used in response model calculations are given in DNVGL-RP-F105 (2017 edition) [11] and tabulated as follows for use:

Table 4-3: General Safety factors for fatigue (DNVGL-RP-F105 (2017 edition) [11])

Safety Factor	Safety Class		
	Low	Medium	High
η	1.0	0.5	0.25
γ_k	1.0	1.15	1.30
γ_s	1.3		
$\gamma_{on,IL}$	1.1		
$\gamma_{on,CF}$	1.2		

Table 4-4: Safety factors for natural frequencies (DNVGL-RP-F105 (2017 edition) [11])

Free Span Classification	Safety Class					
	Low		Medium		High	
	$\gamma_{f,IL}$	$\gamma_{f,CF}$	$\gamma_{f,IL}$	$\gamma_{f,CF}$	$\gamma_{f,IL}$	$\gamma_{f,CF}$
Very well defined	1.0	1.0	1.0	1.0	1.0	1.0
Well to very well defined	1.0	1.05	1.0	1.1	1.0	1.15
Well defined	1.05	1.05	1.1	1.1	1.15	1.15
Not well defined	1.1	1.1	1.2	1.2	1.3	1.3

4.5 Stress Range calculation

Stress range is calculated separately for each flow direction (in-line and cross-flow) at each value of current velocity according to DNVGL-RP-F105 (2017 edition) [11] at the critical locations (A and B).

4.5.1 Mode classification for stress range calculation

Out of the contributing modes, only modes classified as dominant and weak are considered for stress range calculations while rest are disregarded. Contributing CF and IL modes are classified as follows:

1. Dominant modes

Dominant CF mode is defined as that contributing mode which has the highest $\left(\frac{A_{z,1}}{D}\right)$ response for a uniform flow velocity satisfying the following criteria:

$$\left(\frac{A_{z,1}}{D}\right)_i = \left(\frac{A_{z,1}}{D}\right)_{max} \quad 4-29$$

where, mode-i is the dominant mode having the highest response among n contributing modes.

Dominant IL mode is defined as that contributing mode which has the maximum in-line VIV induced stress range at a given point for a given uniform flow velocity satisfying the following criteria:

$$S_{IL,k}^P = S_{IL}^{max} \quad 4-30$$

where, mode-k is the dominant mode having the maximum in-line VIV induced stress range among n contributing modes.

For non-straight geometries, stress range is determined by considering all participating modes as dominant.

2. Weak modes

Weak CF mode is defined as a set of contributing modes which do not include the dominant mode and whose cross-flow VIV amplitude are equal or higher than 10% of the cross-flow VIV amplitude of the dominant mode. Weak modes shall satisfy the following criteria:

$$0.1(A_z/D)_{max} \leq (A_z/D)_j \leq (A_z/D)_{max} \quad 4-31$$

where, mode-j is a weak mode having its cross-flow VIV amplitude equal or higher than 10% of cross-flow VIV amplitude of dominant mode but less than the cross-flow VIV amplitude of the dominant mode.

Weak IL mode is defined as a set of contributing modes which do not include the dominant mode and whose VIV induced stress range at a given point for a given uniform flow velocity are equal or higher than 10% of the VIV induced stress range of the dominant mode. Weak modes shall satisfy the following criteria:

$$0.1.S_{IL}^{max} \leq S_{IL,j}^P < S_{IL}^{max} \quad 4-32$$

where, mode-j is a weak mode having its VIV induced stress range equal or higher than 10% of VIV induced stress range of dominant mode but less than the VIV induced stress range of the dominant mode.

4.5.2 Competing IL contributing modes

Once the modes are classified as CF modes and IL modes for a given direction of current flow and are categorised as contributing, the effects of adjacent IL modes on their contribution to stress range is determined based on the following criteria:

A contributing mode is considered as competing if it satisfied the following condition:

$$\frac{f_{IL,j+1}^{con}}{f_{IL,j}^{con}} < 2 \quad 4-33$$

A contributing mode is considered as non-competing if it satisfied the following condition:

$$\frac{f_{IL,j+1}^{con}}{f_{IL,j}^{con}} \geq 2 \quad 4-34$$

where, mode- j and mode- $j+1$ are adjacent contributing IL modes.

4.5.3 Unit amplitude stress for stress range calculation

The unit amplitude stress (flexural and torsional) from modal analysis is considered for the critical locations A and B for all contributing modes.

This value is unique at the given location on the rigid jumper where the fatigue damage assessment is to be done.

4.5.4 IL VIV induced stress range

The in-line VIV induced stress range (flexural and torsional) for “ m ” contributing modes at the critical locations (A and B) is calculated based on the following criteria:

$$S_{IL,j}^{RM}(x) = S_{IL,j}^P(x) \cdot 0.5\beta_j(x) \quad 4-35$$

where,

$S_{IL,j}^{RM}(x)$ = Effective IL VIV induced stress range for mode- j at location x

$S_{IL,j}^P(x)$ = IL VIV induced stress range for mode- j at location x

$\beta_j(x)$ = Mode competition reduction factor for mode- j

$j \in \{1, \dots, m\}$ i.e. mode- j is one of the contributing modes in a set of m contributing IL modes

The in-line VIV induced stress range ($S_{IL,j}^P(x)$) is calculated for each contributing IL dominant mode at the critical location A and B for the entire range of flow velocities as follows:

$$S_{IL,j}^P(x) = 2A_{IL,j}(x) \cdot \left(\frac{A_\gamma}{D}\right)_j \cdot \Psi_{a,IL} \cdot \gamma_s \quad 4-36$$

where,

$A_{IL,j}(x)$ = Unit amplitude stress for CF mode-j from modal analysis according to Section 4.5.3 at location x

$\left(\frac{A_\gamma}{D}\right)_j$ = IL VIV amplitude response for mode-j as a function of uniform current velocity/design value of reduced velocity (Vrd)

$\Psi_{a,IL}$ = Reduction factor for wave dominant conditions given as a function of velocity ratio (α) as following:

$$\Psi_{a,IL} = \begin{cases} 0.0 & \text{for } \alpha < 0.5 \\ (a - 0.5)/0.3 & \text{for } 0.5 < \alpha < 0.8 \\ 1.0 & \text{for } \alpha > 0.8 \end{cases} \quad 4-37$$

It may be noted that for current dominant condition, $\alpha = 1$ and hence $\Psi_{a,IL} = 1$ i.e. no reduction in IL VIV stress range is made.

γ_s = Safety factor for stress amplitudes from Table 4-3

For an IL mode classified as contributing but weak (according to section 4.5.1) the in-line VIV induced stress range ($S_{IL,j}^P(x)$) is calculated at the critical location A and B for the entire range of flow velocities as follows:

$$S_{IL,j}^P(x) = A_{IL,j}(x) \cdot \left(\frac{A_\gamma}{D}\right)_j \cdot \Psi_{a,IL} \cdot \gamma_s \quad 4-38$$

4.5.4.1 Mode competition reduction factor

A reduction factor based on the mode classification (competing or non-competing according to Section 4.5.2) is included for all contributing competing IL modes.

For mode- j , at each location (x), the mode competition reduction factor ($\beta_j(x)$) can be calculated using the following method:

1. $\beta_j(x)$ is set at 0 initially for mode- j
2. Check if the adjacent modes, mode j and mode $j+1$, are competing or non-competing according to requirements of Section 4.5.2.
3. If adjacent modes are non-competing or if the mode- j is dominant mode, $\beta_j(x) = 0$

If adjacent modes are competing value of $\beta_j(x)$ shall be increases or decreased by one based on the following conditions:

$$\frac{S_{IL,j}^P(x)}{S_{IL,j+1}^P(x)} < 1 \Rightarrow \text{increase } \beta_j(x) \text{ by one} \quad 4-39$$

$$\frac{S_{IL,j}^P(x)}{S_{IL,j+1}^P(x)} > 1 \Rightarrow \text{increase } \beta_{j+1}(x) \text{ by one} \quad 4-40$$

For a non-straight geometry, multimode reductions are considered as void. Conservatively, no mode is considered as competing and no reduction is made to the in-line stress range calculated according to Section 4.5.4.

4.5.5 Cross-flow induced IL VIV stress range

DNVGL-RP-F105 (2017 edition) [11] gives guidance for including stress range from cross-flow induced IL VIV response in the effective IL induced VIV stress range.

The criterion assumes that only the dominant cross-flow mode will contribute to the cross-flow induced IL VIV response.

4.5.5.1 Selection of IL mode

The in-line mode satisfying the following criteria is selected for calculation of cross-flow induced IL VIV stress range:

$$\text{Minimum of } |f_{IL,k}^{part} - 2 \cdot f_{CF-RES,i}| \quad 4-41$$

where,

$f_{IL,k}^{part}$ = participating in-line mode frequency for IL mode-k

$f_{CF-RES,i}$ = dominant cross-flow response frequency for dominant CF mode-i

4.5.5.2 Stress range

Cross-flow induced in-line stress range for all locations (x) and full range of reduced velocities (V_{rd}) is determined based on the following criteria:

$$S_{CF-IL}(x) = 0.8 \cdot A_{IL,k}(x) \cdot \left(\frac{A_z}{D}\right)_{max} \cdot R_k \cdot \gamma_s \quad 4-42$$

where,

$S_{CF-IL}(x)$ = Cross-flow induced in-line stress range

$A_{IL,k}(x)$ = Unit stress amplitude for IL mode-k

$\left(\frac{A_z}{D}\right)_{max}$ = Maximum VIV response amplitude in CF direction for mode-i

R_k = Reduction factor for CF VIV due to damping

γ_s = Safety factor for stress amplitudes from Table 4-3

4.5.6 Effective IL VIV induced stress range

There are two cases based on the in-line frequency chosen to determine the cross-flow induced VIV stress range as follows:

4.5.6.1 Case - 1

If the mode selected for cross-flow induced in-line VIV response is among the contributing modes, the effective value of in-line VIV induced stress range is selected based on following criteria:

$$S_{IL,j}(x) = \begin{cases} S_{IL,j}^{RM}(x) & , j \neq k \\ \max(S_{IL,j}^{RM}(x), S_{CF-IL}(x)) & , j = k \end{cases} \quad 4-43$$

where,

j = Selected in-line mode for cross-flow induced in-line VIV response

k = cross-flow mode corresponding to the dominant cross-flow response frequency

$S_{IL,j}^{RM}(x)$ = In-line VIV induced stress range (See section 4.5.4) for mode- j

$S_{CF-IL}(x)$ = Cross-flow induced In-line VIV stress range (See Section 4.5.5.2)

The corresponding in-line response frequency is then determined as follows:

$$f_{IL,k}^{con} = 2f_{CF-RES,i} \quad 4-44$$

where,

$f_{IL,k}^{con}$ = contributing in-line mode response frequency for IL mode- k

$f_{CF-RES,i}$ = dominant cross-flow response frequency for dominant CF mode- i

4.5.6.2 Case - 2

If the mode selected for cross-flow induced in-line VIV response is not among the contributing modes, the set of contributing stresses and frequencies is increased by one to $m+1$. The effective value of in-line VIV induced stress range is then selected based on following criteria:

$$S_{IL,j}(x) = \begin{cases} S_{IL,j}^{RM}(x) & , j \in \{1, \dots, m\} \\ S_{CF-IL}(x) & , j = m + 1 \end{cases} \quad 4-45$$

where,

j = Selected in-line mode for cross-flow induced in-line VIV response

k = cross-flow mode corresponding to the dominant cross-flow response frequency

$S_{IL,j}^{RM}(x)$ = In-line VIV induced stress range (See section 4.5.4) for mode- j

$S_{CF-IL}(x)$ = Cross-flow induced In-line VIV stress range (See Section 4.5.5.2)

The corresponding in-line response frequency is then determined as follows:

$$f_{IL,m+1}^{con} = 2f_{CF-RES,i} \quad 4-46$$

where,

$f_{IL,k}^{con}$ = contributing in-line mode response frequency for IL mode- $k=m+1$

$f_{CF-RES,i}$ = dominant cross-flow response frequency for dominant CF mode- i

4.5.6.3 Combined IL VIV induced stress range

The combined in-line stress range ($S_{comb,IL}(x)$) at critical location (A and B) for full range of flow velocities is then determined from the following:

$$S_{comb,IL}(x) = \sqrt{\sum_{j=1}^{m_{aug}} (S_{IL,j}(x))^2} \quad 4-47$$

where,

$S_{IL,j}(x)$ = Effective IL VIV induced stress range for contributing mode-j (See section 4.5.6)

m_{aug} = m+1 for Case-2 of Section 4.5.6

= m for Case-1 of Section 4.5.6

4.5.6.4 In-line cycle counting frequency

The inline cycle counting frequency can be determined from the following:

$$f_{cyc,IL}(x) = \sqrt{\sum_{j=1}^{m_{aug}} \left(f_{IL,j}^{con} \cdot \frac{S_{IL,j}(x)}{S_{comb,IL}(x)} \right)^2} \quad 4-48$$

where,

$f_{IL,j}^{con}$ = Eigen frequency for contributing mode-j

j = 1 to m_{aug}

$S_{IL,j}(x)$ = Effective IL VIV induced stress range for contributing mode-j (See section 4.5.6)

$S_{comb,IL}(x)$ = Combined in-line stress range for set of m_{aug} contributing modes (See section 4.5.6.3)

m_{aug} = m+1 for Case-2 of Section 4.5.6

= m for Case-1 of Section 4.5.6

4.5.7 Cross-flow induced VIV stress range

The cross-flow VIV induced stress range (flexural and torsional) for “m” contributing modes at the critical locations (A and B) is calculated based on the following criteria:

$$S_{CF,j}^{RM}(x) = A_{CF,j}(x) \cdot (A_z/D)_j \cdot R_k \cdot \gamma_s \quad 4-49$$

where,

$A_{CF,j}(x)$ = Unit amplitude stress for CF mode-j from modal analysis according to Section 4.5.3 at location x

$\left(\frac{A_z}{D}\right)_j$ = CF VIV amplitude response for CF mode-j as a function of uniform current velocity/design value of reduced velocity (V_{rd})

R_k = Reduction factor for CF VIV due to damping

γ_s = Safety factor for stress amplitudes from Table 4-3

4.5.7.1 Reduction factor for damping

To include the effects of damping in the stress range, a factor is introduced to reduce the values of stress range to make them closer to a realistic value.

The damping reduction factor (R_k) is defined as a function of design value of stability parameter and given as shown below:

$$R_k = \begin{cases} 1 - 0.15K_{sd} & \text{for } K_{sd} \leq 4 \\ 3.2K_{sd}^{-1.5} & \text{for } K_{sd} > 4 \end{cases} \quad 4-50$$

where,

K_{sd} = Design value of Stability parameter (Ks)

4.5.7.2 Combined CF VIV induced stress range

The combined in-line stress range ($S_{comb,CF}^{RM}(x)$) at critical location (A and B) for full range of flow velocities is then determined from the following:

$$S_{comb,CF}^{RM}(x) = \sqrt{\sum_{j=1}^m \left(S_{CF,j}^{RM}(x) \right)^2} \quad 4-51$$

where,

$S_{CF,j}^{RM}(x)$ = CF VIV induced stress range for contributing mode-j (See section 4.5.7)

4.5.7.3 Cross-flow cycle counting frequency

The cross-flow cycle counting frequency can be determined from the following expression:

$$f_{cye,CF}^{RM}(x) = \sqrt{\sum_{j=1}^m \left(f_j \frac{S_{CF,j}^{RM}(x)}{S_{comb,CF}^{RM}(x)} \right)^2} \quad 4-52$$

where,

$S_{CF,j}^{RM}(x)$ = CF VIV induced stress range for contributing mode-j (See section 4.5.7)

$S_{comb,CF}^{RM}(x)$ = Combined in-line stress range for set of m_{aug} contributing modes (See section 4.5.7)

$f_j = f_{CF-RES,j}$ for $j=i$ where mode-i is the dominant cross-flow mode

$f_j = f_{CF,j}$ for $j \neq i$

$f_{CF-RES,j}$ = Cross-flow response frequency

$f_{CF,j}$ = Cross-flow eigen frequency

4.5.7.4 Cross-flow response frequency

During VIV, the added mass changes from the constant value of still water added mass. This further affects the eigen frequencies as eigen frequencies are a function of the added mass. To incorporate this effect to the still water eigen frequency, cross-flow response frequency is calculated, as a function of still water added mass, cross-flow response added mass and specific gravity/mass ratio of the pipe, using DNVGL-RP-F105 (2017 edition) [11] as follows:

$$f_{CF-RES,j} = f_{CF,j} \sqrt{\frac{S_g + C_a}{S_g + C_{a,CF-RES}}} \quad 4-53$$

where:

$S_g = (q+b)/b$ is the specific gravity of the pipe (often referred to as mass ratio in the context of VIV)

q = Submerged weight of the pipe, including content if any

$b = \pi\rho_w g D^2/4$ is the pipe buoyancy

C_a = Added mass coefficient in still water

$C_{a,CF-RES}$ = Added mass coefficient due to cross-flow response

Added mass coefficient due to cross-flow response is determined according to the following graph as a function of design value of reduced velocity (V_{rd}) (See Figure 4-12)

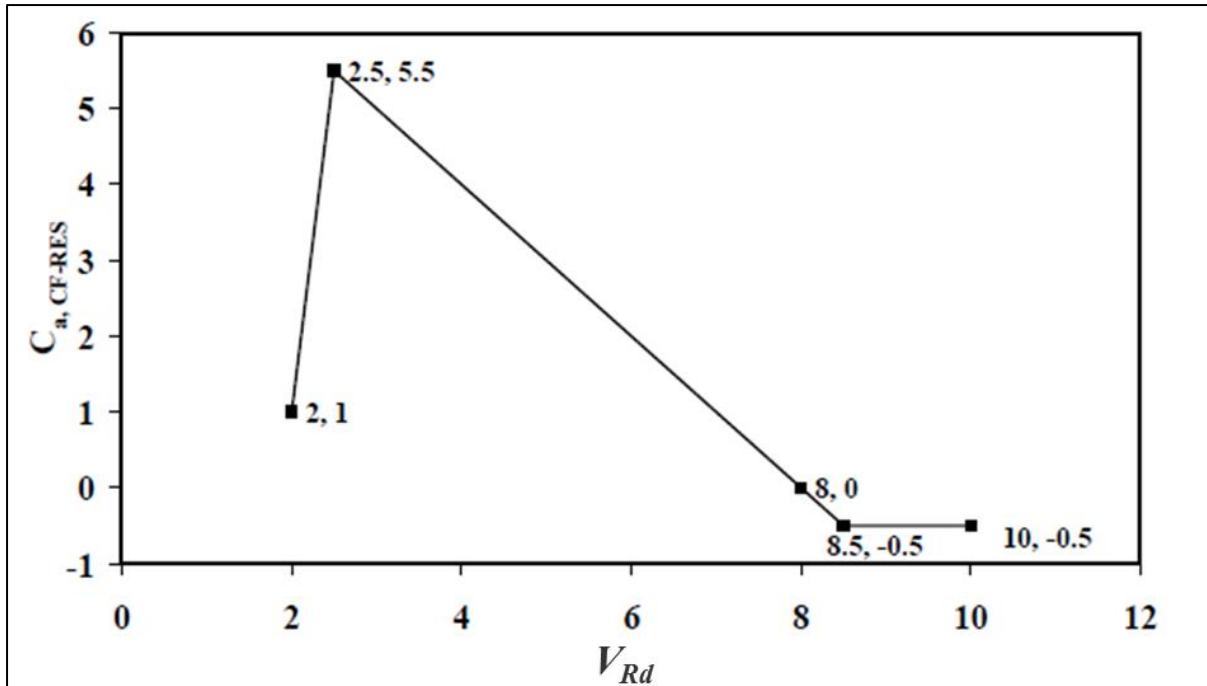


Figure 4-12: Added mass coefficient due to cross-flow response ($C_{a,CF-RES}$) [DNVGL-RP-F105 (2017 edition) [11]]

4.6 Fatigue assessment

Fatigue assessment is carried out by the method described by Farahani [13,14] using a fatigue damage assessment parameter. This fatigue damage parameter is based on a critical plane energy approach. The critical plane is selected for every half cycle of first principal stress loading at a point where the shear strain is maximum. Normal and shear energies are determined at this point for each full cycle by calculating normal and shear stress and strain ranges using Mohr circle. The normal and shear energies are normalised using fatigue properties of the material. To get the full extent of damage, fatigue damage calculated for each cycle of first principal loading is added for a given block loading.

For rigid jumper, exposed to a range of flow velocities and orientations, different cases for each value of flow velocity are obtained as follows:

1. 10° Flow
 - a. Cross-flow response
 - i. At location A
 - ii. At location B

- b. In-line response
 - i. At location A
 - ii. At location B
- 2. 90° Flow
 - a. Cross-flow response
 - i. At location A
 - ii. At location B
 - b. In-line response
 - i. At location A
 - ii. At location B

The methodology discuss hereon, is based flow velocity of 0.25m/s for Case-1(a)(i) mentioned above. The same methodology is followed for each value of flow velocity and each case given above. Following steps are described in detail:

1. Block loading
2. Critical plane selection
3. Normal and shear stress and strain range calculation at critical plane
4. Fatigue damage assessment

4.6.1 Block loading

From DNVGL-RP-F105 (2017 edition) [11] we obtain the stress range for IL and CF response and the corresponding cycle counting frequencies as described in detail in section 4.5. These stress ranges are significant at the critical locations A and B where the fatigue damage is to be assessed.

At the location A, stress range for each value of flow velocity is calculated and utilized to determine the fatigue damage as a function of flow velocity.

For a given flow velocity, and for CF/IL response, the flexural and torsional stress range as well as the cycle counting frequency are different from one another. To be able to determine combined fatigue damage due to flexural and torsional stresses, block loadings are obtained for each flow velocity using the flexural and torsional stress range as well as their corresponding cycle counting frequencies.

4.6.1.1 Principal stresses

The following assumptions are made going forward:

1. Flexural stresses and torsional stresses act in mutually perpendicular directions at all points and at all times.
2. Flexural stresses and torsional stresses are planar stresses and they act along the principal axes.
3. The larger of the two stresses (flexural and torsional) acts along the first principal direction while the smaller acts along the third principal axis while the second principal stress is always zero. i.e.

$$\sigma_{11} = \text{Larger of the flexural and torsional stress}$$

$$\sigma_2 \text{ is zero}$$

$$\sigma_{33} = \text{Smaller of the flexural and torsional stress}$$

4. Cycle counting frequency for the principal stress is the same as that of the flexural stress and the torsional stress.

The flexural and torsional stress range calculated using DNVGL-RP-F105 (2017 edition) [11] gives the full stress range for a complete (360°) cycle of loading. To get the amplitude of this stress range for each half cycle (0°-180° and 180°-360°) we use the half of stress range value.

The principal stresses as a function of time (t) are defined as follows:

$$\sigma_{11} = \sigma_{1a} \sin\left(\frac{360t}{t_1}\right)$$

$$\sigma_2 = 0 \quad 4-54$$

$$\sigma_{33} = \sigma_{3a} \sin\left(\frac{360t}{t_3}\right)$$

where,

σ_{1a} = amplitude of first principal stress defined as follows:

$$\sigma_{1a} = \frac{1}{2}(S_{comb,IL}(x) \text{ flexural}) \quad 4-55$$

σ_{3a} = amplitude of third principal stress defined as follows:

$$\sigma_{3a} = \frac{1}{2}(S_{comb,IL}(x) \text{ torsional}) \quad 4-56$$

t_1 = response time of first principal stress defined as follows:

$$t_1 = \frac{1}{f_{cyc,IL}(x) \text{ flexural}} \quad 4-57$$

t_3 = response time of third principal stress defined as follows:

$$t_3 = \frac{1}{f_{cyc,IL}(x) \text{ torsional}} \quad 4-58$$

t = time on the time axis (second)

4.6.1.2 Length of block loading

Since the principal stresses may act at different frequencies, length of one block loading is obtained from the response time of first (t_1) and third (t_3) principal stresses such that for a block loading of time, t_{block} , “n” and “m” are the number of full cycles of flexural and torsional stresses, respectively such that “n” and “m” are integers.

t_{block} is determined as follows:

$$t_{block} = 10(t_1 \times t_3) \quad 4-59$$

4.6.1.3 Number of principal stress cycles

To obtain the number of full principal stress cycles, n and m , we divide the t_{block} by t_1 and t_3 as shown below:

$$n = \frac{t_{block}}{t_1}$$

$$m = \frac{t_{block}}{t_3}$$
4-60

4.6.2 Critical plane

A critical plane (Θ_{critic}) is defined as the plane at which maximum fatigue damage is assumed to take place. The critical plane, according to Farahani [13,14] is selected based on the maximum shear strain. According to Farahani [13,14], this approach is effective as it based on fracture mode and initiation mechanism of cracks.

Critical plane is calculated for each half cycle of first principal loading at the point when the shear strain is maximum. Maximum shear strain ($\gamma_{max}/2$) for a half cycle, θ_i , can be calculated from strain Mohr circle by using the following equation:

$$\Delta \left(\frac{\gamma_{max}}{2} \right)_i = \left(\frac{\epsilon_{11i} - \epsilon_{33i}}{2} \right)_{\theta_i}$$
4-61

where,

ϵ_{11i} = First principal strain for the i -th half cycle of principal stress loading

ϵ_{33i} = Third principal strain for the i -th half cycle of principal stress loading

θ_i = i -th half cycle of principal stress loading

Value i depends on number of cycles of first principal loading (m) such that,

$$i = 2m$$

4-62

4.6.3 Normal and shear stress and strain range

Normal and shear stress and strain ranges are calculated at the critical angle by the largest stress and strain Mohr circles as follows:

$$\Delta\tau_{maxj} = \left(\frac{\sigma_{11i} - \sigma_{33i}}{2} \right)_{\theta_i} - \left(\frac{\sigma_{11i+1} - \sigma_{33i+1}}{2} \right)_{\theta_{i+1}} \quad 4-63$$

$$\Delta\sigma_{nj} = \left(\frac{\sigma_{11i} + \sigma_{33i}}{2} \right)_{\theta_i} - \left(\frac{\sigma_{11i+1} + \sigma_{33i+1}}{2} \right)_{\theta_{i+1}} \quad 4-64$$

$$\Delta\left(\frac{\gamma_{max}}{2} \right)_j = \left(\frac{\epsilon_{11i} - \epsilon_{33i}}{2} \right)_{\theta_i} - \left(\frac{\epsilon_{11i+1} - \epsilon_{33i+1}}{2} \right)_{\theta_{i+1}} \quad 4-65$$

$$\Delta\epsilon_{nj} = \left(\frac{\epsilon_{11i} + \epsilon_{33i}}{2} \right)_{\theta_i} - \left(\frac{\epsilon_{11i+1} + \epsilon_{33i+1}}{2} \right)_{\theta_{i+1}} \quad 4-66$$

where,

$\Delta\tau_{maxj}$ = Maximum shear stress range for j-th first principal stress cycle

$\Delta\sigma_{nj}$ = Normal stress range for j-th first principal stress cycle (m_1)

$\Delta\left(\frac{\gamma_{max}}{2} \right)_j$ = Maximum shear strain range for j-th first principal stress cycle (m_1)

$\Delta\epsilon_{nj}$ = Normal strain range for j-th first principal stress cycle (m_1)

θ_i = Critical angle for first half of j-th cycle

$\theta_i + 1$ = Critical angle for second half of j-th cycle

σ_{11i} = First principal stress value at θ_i critical angle

σ_{33i} = Third principal stress value at θi critical angle

σ_{11i+1} = First principal stress value at $\theta i + 1$ critical angle

σ_{33i+1} = Third principal stress value at $\theta i+1$ critical angle

ϵ_{11i} = First principal strain value at θi critical angle

ϵ_{33i} = Third principal strain value at θi critical angle

ϵ_{11i+1} = First principal strain value at $\theta i + 1$ critical angle

ϵ_{33i+1} = Third principal strain value at $\theta i+1$ critical angle

Principal strains can be calculated from using elastic-plastic constitutive relation as follows:

$$\epsilon_{ij} = \left[\frac{1 + \nu_e}{E} \sigma_{ij} - \frac{\nu_e}{E} \sigma_{kk} \delta_{ij} \right] + \left[\frac{3}{2} S_{ij} \frac{\epsilon_{eq}^p}{\sigma_{eq}} \right] \quad 4-67$$

In Equation 4-67 the first part describes the elastic strain while the second part describes the plastic strain. Since this thesis is confined to the elastic stress state, we ignore the second part of the equation and the equation can be re-written as follows:

$$\epsilon_{ij} = \left[\frac{1 + \nu_e}{E} \sigma_{ij} - \frac{\nu_e}{E} \sigma_{kk} \delta_{ij} \right] \quad 4-68$$

where,

$$\delta_{ij} = 1 \quad \text{if } i = j$$

$$\delta_{ij} = 0 \quad \text{if } i \neq j$$

σ_{kk} = Summation of principal stresses defined as:

$$\sigma_{kk} = \sigma_{11} + \sigma_{33} \quad 4-69$$

ν_e = Poisson ratio

E = Elastic modulus

4.6.4 Mean stress correction

Mean flexural and torsional stresses may exist in addition to the response stresses induced by VIV. These mean stresses may be due to:

1. The hydrostatic pressure of the sea water above the rigid jumper
2. Inertial stresses due to current velocity
3. Expansion/Contraction due to temperature differences
4. Improper installation of rigid jumper

Mean stresses, in addition to the cyclic stresses, can have a significant impact on the fatigue damage and fatigue life. Sines [39] has shown that compressive mean stresses lead to reduced fatigue damage and an enhanced fatigue life whereas tensile stresses increase the fatigue damage and decrease the fatigue life.

Mean stresses can be incorporated in the Farahani [13,14]'s fatigue damage parameter by adding a mean stress correction factor defined as follows:

$$\text{Mean stress correction factor} = 1 + \frac{\sigma_n^m}{\sigma_f'} \quad 4-70$$

where,

σ_n^m = Mean of maximum and minimum normal stress acting on the critical plane (MPa)

$$\sigma_n^m = \frac{\sigma_{n_i} + \sigma_{n_{i+1}}}{2} \quad 4-71$$

σ_f' = Axial fatigue strength coefficient

It shall be noted that mean stress has not been accounted for in this study and is part of the proposed future work.

4.6.5 Fatigue damage assessment

Farahani [13,14]'s fatigue damage parameter is used to determine the fatigue damage for each full cycle of first principal stress loading. The normal and shear energies ($\Delta\sigma_n\Delta\varepsilon_n$ and $\Delta\tau_{max}\Delta\left(\frac{\gamma_{max}}{2}\right)$) are normalized by normal and shear fatigue properties of the material ($\sigma'_f\varepsilon'_f$ and $\tau'_f\gamma'_f$) and added along with the mean stress correction factor to get the fatigue damage for a given cycle of first principal stress loading.

Farahani [13,14]'s fatigue damage parameter for first cycle of first principal stress loading is given as follows:

$$\frac{1}{\sigma'_f\varepsilon'_f}(\Delta\sigma_n\Delta\varepsilon_n)_j + \frac{\left(1 + \frac{\sigma_n^m}{\sigma'_f}\right)}{\tau'_f\gamma'_f}(\Delta\tau_{max}\Delta\left(\frac{\gamma_{max}}{2}\right))_j = P_j \quad 4-72$$

where,

P_j = Fatigue damage for j-th cycle of first principal stress loading

$(\Delta\sigma_n\Delta\varepsilon_n)_j$ = Normal energy for j-th cycle of first principal stress loading

$(\Delta\tau_{max}\Delta\left(\frac{\gamma_{max}}{2}\right))_j$ = Shear energy for j-th cycle of first principal stress loading

$\left(1 + \frac{\sigma_n^m}{\sigma'_f}\right)$ = Mean stress correction factor for j-th cycle of first principal stress loading

σ'_f = Axial fatigue strength coefficient

ε'_f = Axial fatigue ductility coefficient

τ'_f = Shear fatigue strength coefficient

γ'_f = Shear fatigue ductility coefficient

Since mean stress correction is not considered in this study, Farahani [13,14]'s fatigue damage parameter can be written in the following simplified form:

$$\frac{1}{\sigma'_f \varepsilon'_f} (\Delta \sigma_n \Delta \varepsilon_n)_j + \frac{1}{\tau'_f \gamma'_f} (\Delta \tau_{max} \Delta \left(\frac{\gamma_{max}}{2} \right))_j = P_j \quad 4-73$$

Similarly, fatigue damage is calculated for each cycle of first principal stress in a block loading to determine the total fatigue damage.

$$P_{block} = P_1 + P_2 + P_3 \dots \dots \dots + P_j \quad 4-74$$

where,

$$j = (1, 2, 3 \dots m)$$

Given the length of one block loading, t_{block} , number of block cycles of first principal stress for 1 year (31536000 seconds), m_{1year} , can be calculated as follows:

$$m_{1year} = \frac{31536000}{t_{block}} \quad 4-75$$

Total fatigue damage for a year can be calculated as follows:

$$P_{1year} = P_{block} \times m_{1year} \quad 4-76$$

5 MODAL ANALYSIS

5.1 3D Model

A 3D model is prepared using 3D modelling tool, Ansys SpaceClaim 17.1. Line bodies are used to construct the M-shaped rigid jumper model with dimensions based on Zheng et al. [51] (See Table 5-1 and Table 5-2). Length of L5 segment used Ansys model is slightly different from the ExxonMobil jumper model. This has been done to obtain a symmetric model.

Table 5-1: Jumper model properties comparison

Properties	Value – ExxonMobil Model (Wang et al. [46], Zheng et al. [51])	Value – Ansys Model
Total length	13.96 m	14.1 m
Pipe density	2700 kg/m ³	2700 kg/m ³
Unit mass in air	3.8 kg/m	3.8 kg/m
Unit mass filled with oil	6.66 kg/m	6.66 kg/m
Mass ratio	2.33	2.33
Outer diameter	0.0605 m	0.0605 m
Inner diameter	0.055 m	0.055 m
Wall thickness	0.00277	0.00277
Elastic modulus (E)	6.90 E+10	6.90 E+10
Bending stiffness (EI)	1.44 E+04	1.44 E+04
Shear modulus (J)	2.61 E+10	2.61 E+10
Torsional stiffness (GJ)	1.08 E+04	1.08 E+04

Table 5-2: Comparison of dimensions of segments used for SpaceClaim model

Segment	Length – ExxonMobil Model (Wang et al. [46], Zheng et al. [51])	Length – SpaceClaim Model
L1	1.495 m	1.495 m
L2	1.000 m	1.000 m
L3	2.323 m	2.323 m
L4	4.327 m	4.327 m
L5	2.326 m	2.323 m
L6	1.000 m	1.000 m
L7	1.495 m	1.495 m

A line body only consists of edges having no surface or body. Figure 5-2 shows how cross section data, based on Table 5-1, has been added to the line body in Ansys SpaceClaim model.

In the absence of information regarding the radius of curvature of the bends, a bend with radius 3 time the outer diameter of the pipe (3D bend) has been used.

Figure 5-1 shows jumper model in Ansys SpaceClaim with segments L1 to L7. Dimensions for each segment is given in Table 5-2.

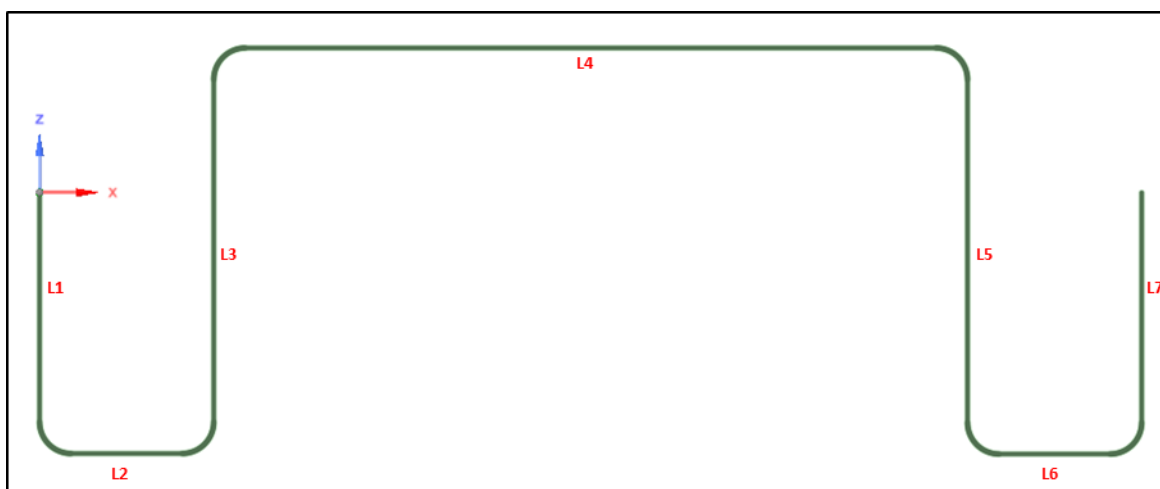


Figure 5-1: Rigid jumper model in Ansys SpaceClaim 17.1

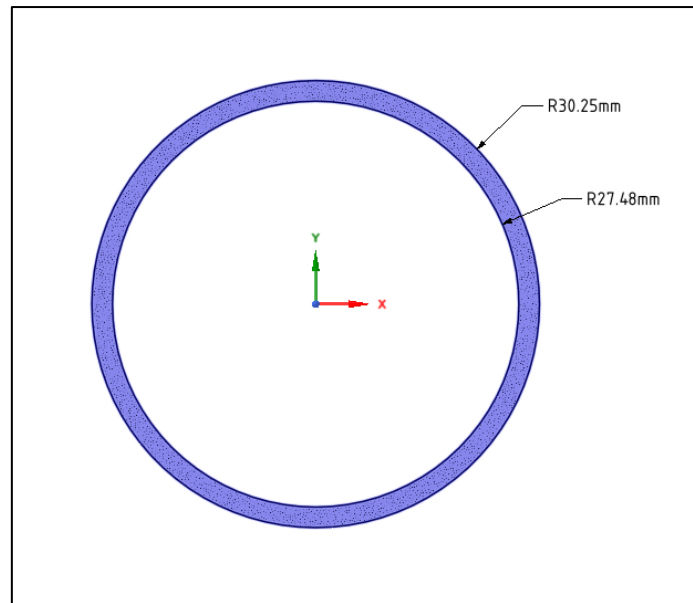


Figure 5-2: Cross-section data for rigid jumper in Ansys SpaceClaim 17.1

5.2 Modal Analysis using FEM

5.2.1 Ansys Project Schematic

Modal Analysis module of Ansys Mechanical Workbench 17.1 has been used to conduct the modal analysis on the jumper model.

Modal analysis can be performed in Ansys either for a pre-stressed or non-pre-stressed structure. Considering the rigid jumper is submerged in water before being exposed to uniform current flow, the structure shall be pre-stressed to include the effects from gravity and hydrostatic head. Pre-stressing is done using Static Structural module by applying uniform gravitational acceleration on the rigid jumper model and selecting Basic Ocean loading via APDL commands. Figure 25 shows how the two modules are setup in Ansys Mechanical Workbench 17.1.

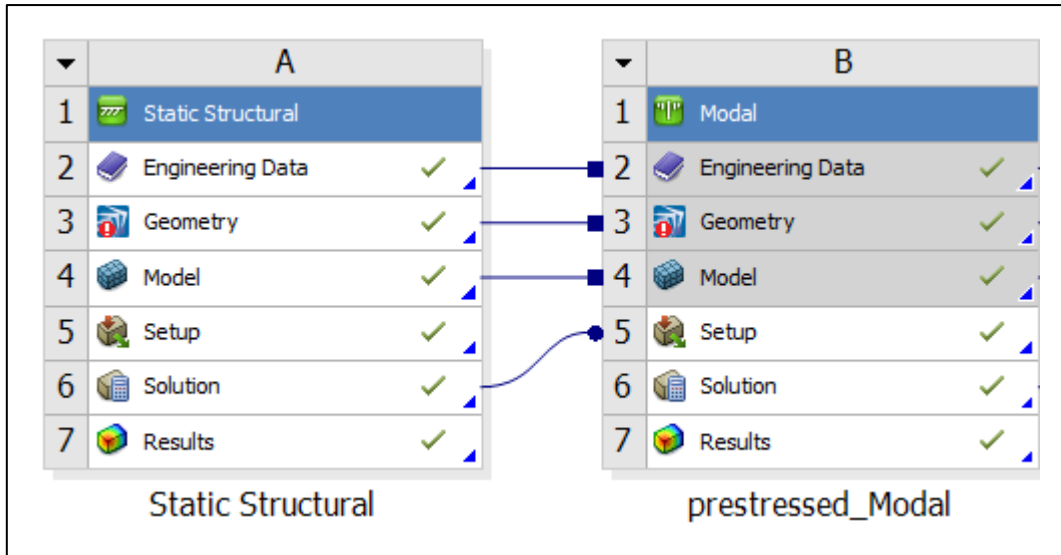


Figure 5-3: Project schematic in Ansys Mechanical Workbench 17.1

Figure 5-4 shows the pre-stressing setup in Static Structural module. Point “A” shows the application of gravitational acceleration at the centre of gravity of the jumper model whereas points “B” and “C” show the location of fixed supports.

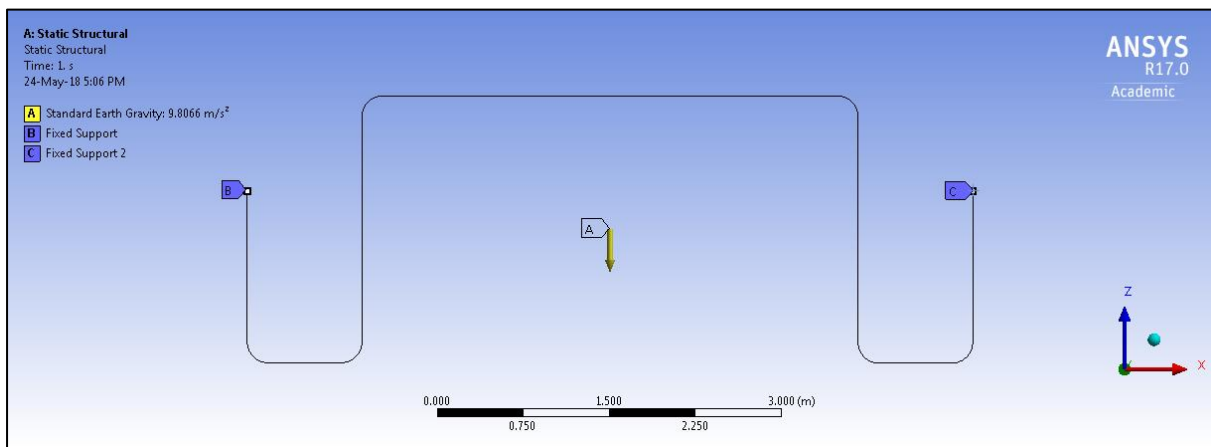
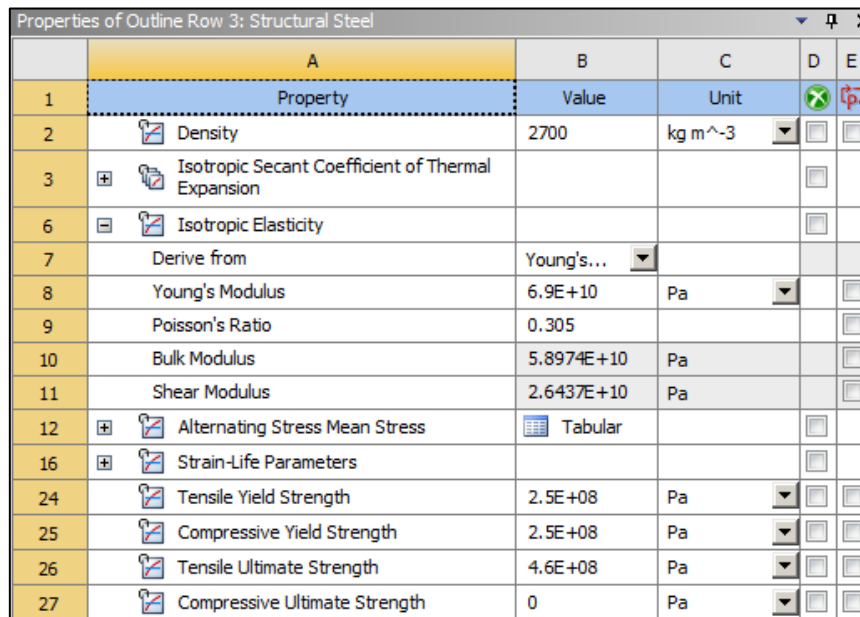


Figure 5-4: Gravitational acceleration & fixed supports in Static Structural module of Ansys Mechanical Workbench 17.1

5.2.2 Rigid jumper properties

As seen in Figure 5-5, material properties such as elastic modulus (E), shear modulus (G), etc. are updated in the Engineering Data of Ansys Mechanical Workbench.

Pipe density (ρ_{pipe}) and fluid content density (ρ_{content}) from Table 4-1 are also included in the pre-processor using APDL commands.



	A	B	C	D	E
1	Property	Value	Unit	<input checked="" type="checkbox"/>	<input checked="" type="checkbox"/>
2	Density	2700	kg m ⁻³	<input type="checkbox"/>	<input type="checkbox"/>
3	Isotropic Secant Coefficient of Thermal Expansion			<input type="checkbox"/>	<input type="checkbox"/>
6	Isotropic Elasticity			<input type="checkbox"/>	<input type="checkbox"/>
7	Derive from	Young's...			
8	Young's Modulus	6.9E+10	Pa	<input type="checkbox"/>	<input type="checkbox"/>
9	Poisson's Ratio	0.305			<input type="checkbox"/>
10	Bulk Modulus	5.8974E+10	Pa		<input type="checkbox"/>
11	Shear Modulus	2.6437E+10	Pa		<input type="checkbox"/>
12	Alternating Stress Mean Stress	Tabular		<input type="checkbox"/>	<input type="checkbox"/>
16	Strain-Life Parameters			<input type="checkbox"/>	<input type="checkbox"/>
24	Tensile Yield Strength	2.5E+08	Pa	<input type="checkbox"/>	<input type="checkbox"/>
25	Compressive Yield Strength	2.5E+08	Pa	<input type="checkbox"/>	<input type="checkbox"/>
26	Tensile Ultimate Strength	4.6E+08	Pa	<input type="checkbox"/>	<input type="checkbox"/>
27	Compressive Ultimate Strength	0	Pa	<input type="checkbox"/>	<input type="checkbox"/>

Figure 5-5: Engineering Data in Ansys Mechanical Workbench

5.2.3 Hydrodynamic parameters and Ocean data

Table 5 gives the ocean data that has been used for modal analysis.

Table 5-3: Ocean data for jumper model

Ocean data	Value	Unit
Ocean water density	1027	Kg/m ³
Water depth	9999	m

Hydrostatic parameters such as drag coefficients, added mass coefficients (C_{ay} , C_{az})^{1,2} and inertia coefficients (C_{my} , C_{mz})^{3,4} are determined based on guidance given in Ansys Mechanical Workbench help document.

¹ If no value of C_{ay} and coefficient of inertia (C_{my}) is specified, both are set to 0; If value of coefficient of inertia (C_{my}) is specified, $C_{ay} = C_{my} - 1$

² If no value is specified and C_{ay} is specified, $C_{az} = C_{ay}$; If no value of C_{az} and coefficient of inertia (C_{mz}) is specified, both are set to 0; If value of coefficient of inertia (C_{mz}) is specified, $C_{az} = C_{mz} - 1$

³ If no value of C_{ay} is specified, C_{my} and C_{ay} are set at 0; If value if C_{ay} is specified, $C_{my} = C_{ay} + 1$

⁴ If no value for C_{mz} is specified but C_{my} is specified, $C_{mz} = C_{my}$; If no value for C_{mz} , C_{my} is specified but C_{az} is specified, $C_{mz} = C_{az} + 1$; If none is specified, $C_{az} = C_{mz} = 0$

Table 5-4: Hydrodynamic parameters used of jumper model

Hydrodynamic Parameter	Value	Unit
Drag coefficient (Normal)	1.1	-
Drag coefficient (Tangential)	1.1	-
Added mass coefficient (Y-axis) (C _{ay})	1 or 0	-
Added mass coefficient (Z-axis) (C _{az})	1 or 0	-

5.2.4 Line body – PIPE288

Once the Ansys SpaceClaim model is imported in Ansys Mechanical Workbench environment, first step is to select the element type which the line body shall represent.

In this model, PIPE288 element has been selected. According to Ansys Mechanical Workbench help [3] document, PIPE288 is suitable for analysing slender structures as well as moderately thick pipe structures. PIPE288 is based on the Timoshenko beam theory which is a first order shear deformation theory. The cross section for PIPE288 remains plane and does not distort due to applied stresses giving constant traverse shear strains at each cross section.

In Figure 5-6, PIPE288 element is shown with pipe run along X-axis of global coordinate system. PIPE288 is a 2-node element where “I” and “J” represent the two nodes. Numbers “4”, “5”, “6”, “7” and “8” represent the different pressure directions for this pipe element.

Direction “4” represents the bending stress direction along negative Y-axis

Direction “5” represents the shear stress direction in Y-Z plane

Direction “6” represents the axial tensile stress direction along negative X-axis

Direction “7” and “8” represents the compressive stress direction along negative X-axis

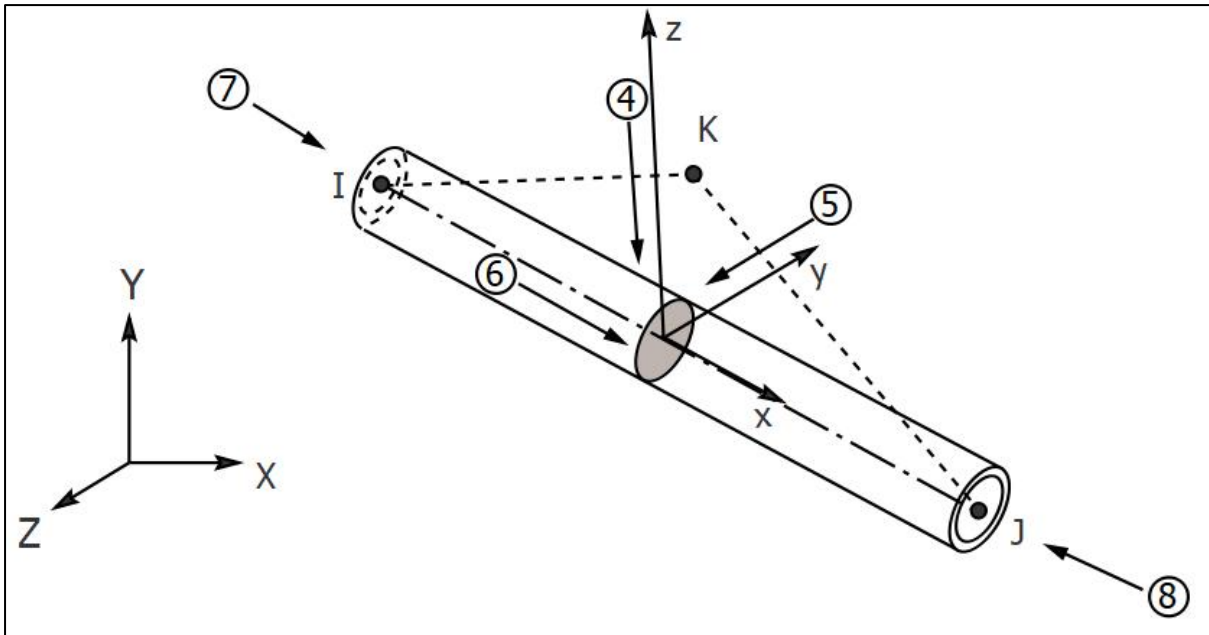


Figure 5-6: PIPE288 geometry [3]

5.2.5 Mesh

Meshing in Ansys Mechanical Workbench is done by considering an element size which is small enough to give good convergence of results and yet requires less computational time.

DNVGL-RP-F105 (2017 edition) [11] recommends using element length of the order of 1 times the outer diameter of the pipe. This has not been adopted as the analysis becomes work intensive and analysis time increases significantly. A mesh size of 0.1m has been selected as it gives good convergence and requires shorter computational time. Figure 5-7 shows the mesh for rigid jumper with node numbers marked.

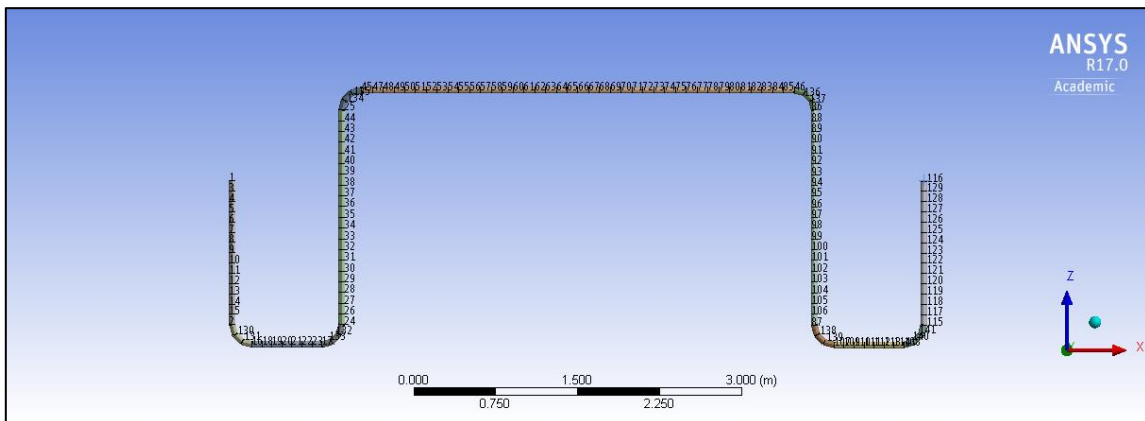


Figure 5-7: Node numbers after meshing in Ansys Mechanical Workbench

5.2.6 Eigen frequencies and mode shapes

As mentioned in Section 4.2.2, a total of nine eigen modes are to be considered for modal analysis.

The predicted eigen frequency values from this study is presented along with those from Igeh [24] and Zheng et al. [51] in Table 5-5. A comparison between the predicted eigen frequencies is also provided showing the difference in the value predicted by this study from those of Igeh [24] and Zheng et al. [51].

Table 5-5: Predicted eigen frequencies from modal analysis

Mode	Eigen Frequencies				Difference (%)	
	Zheng et al. [51]	Igeh [24] (VIVANA)	Igeh [24] (Ansys APDL)	Kapoor (Ansys Mechanical Workbench)	Kapoor Vs. Zheng et al. [51]	Kapoor Vs. Igeh (Ansys APDL)
M1	0.8632	0.8587	0.850	0.850	-1.54	0.00
M2	2.1492	2.1403	2.230	2.230	3.61	0.00
M3	2.1941	2.1741	2.294	2.293	4.33	-0.04
M4	2.5417	2.5457	2.637	2.643	3.84	0.23
M5		3.2669	3.429	3.449		0.58
M6		3.56	3.743	3.758		0.40
M7		3.6218	3.817	3.843		0.68
M8		6.1957	6.397	6.396		-0.02
M9		6.911	7.187	7.196		0.13

The predicted eigen frequencies are shown in a stacked graph for this study along with those done by Igeh [24] and Zheng et al. [51]. Zheng et al. [51] only predicted the first four frequencies while this study and the one conducted by Igeh [24] predicts nine eigen modes and their frequencies. While Igeh [24] has chosen a FEM tools such as VIVANA and Ansys APDL (Classic) to predict the eigen frequencies, this study uses Ansys Mechanical Workbench's modal analysis module.

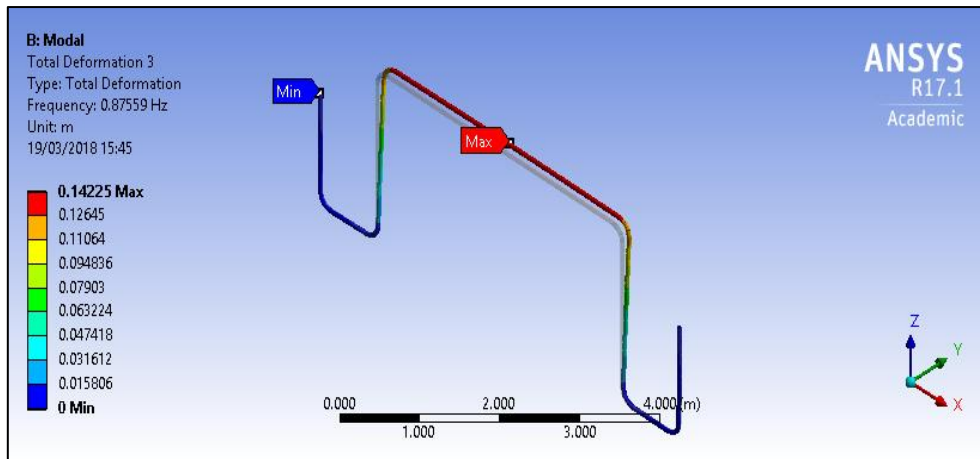


Figure 5-8: Total deformation and mode shape for Mode – 1

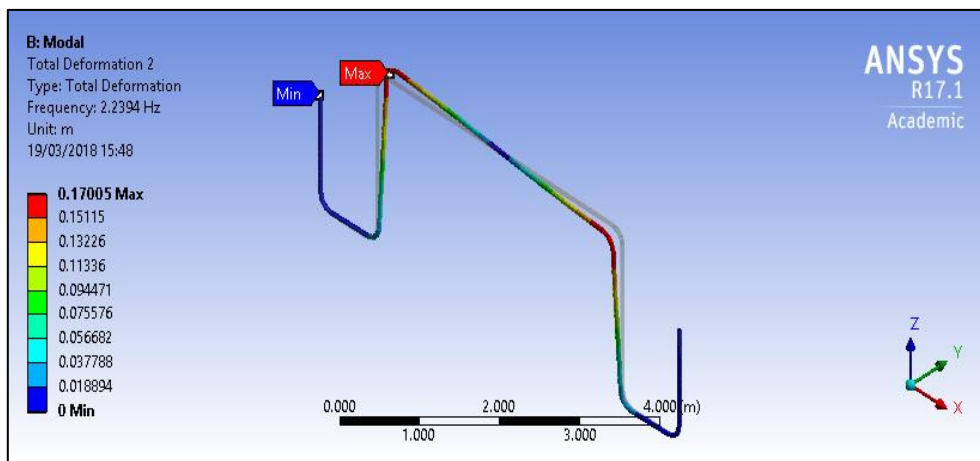


Figure 5-9: Total deformation and mode shape for Mode – 2

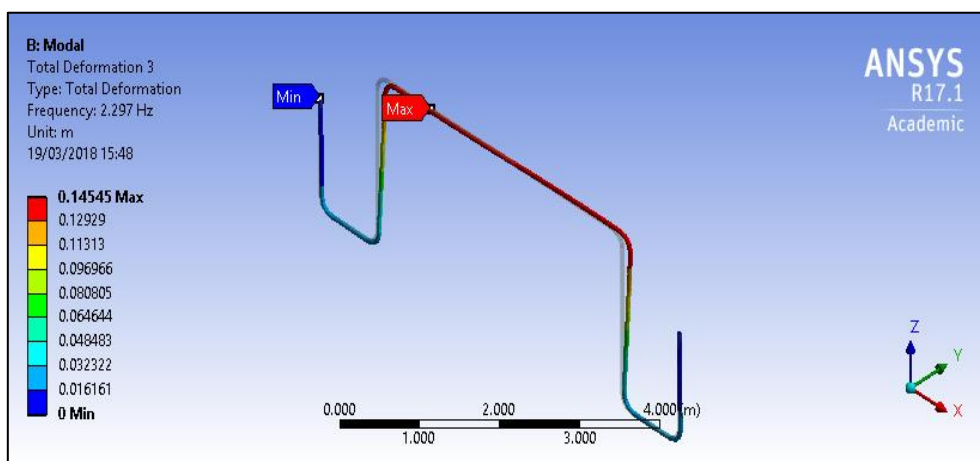


Figure 5-10: Total deformation and mode shape for Mode – 3

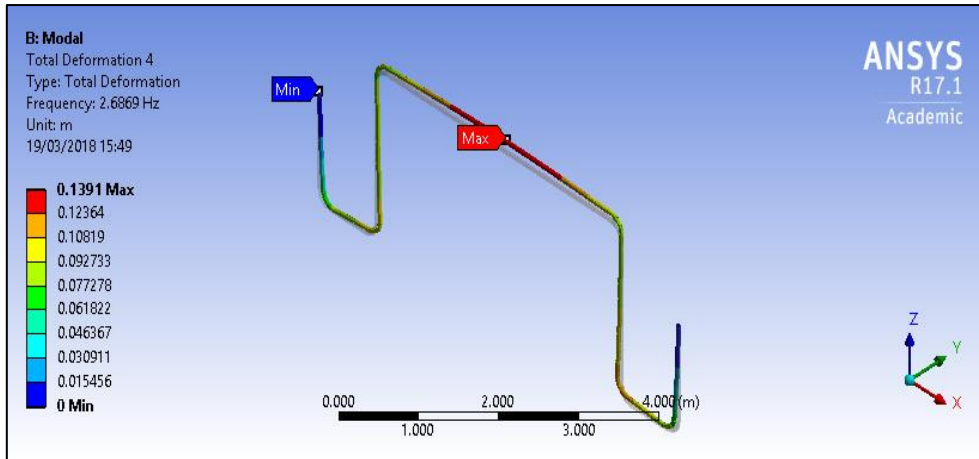


Figure 5-11: Total deformation and mode shape for Mode – 4

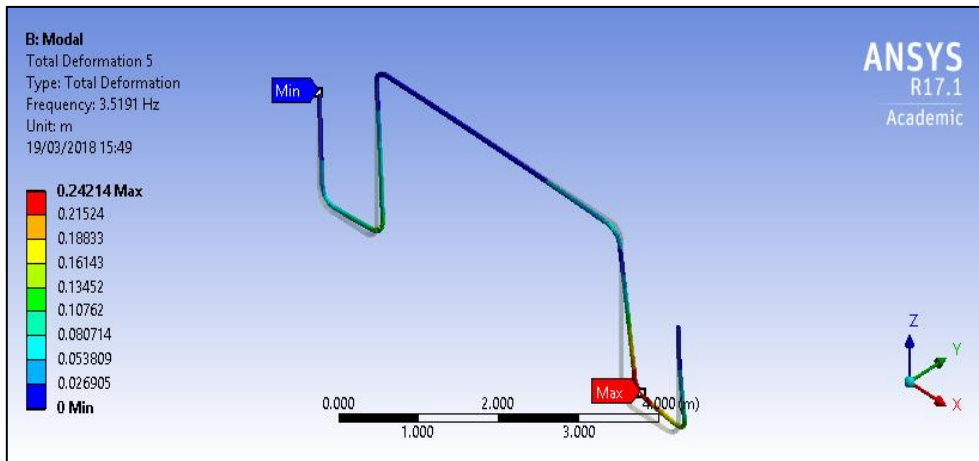


Figure 5-12: Total deformation and mode shape for Mode – 5

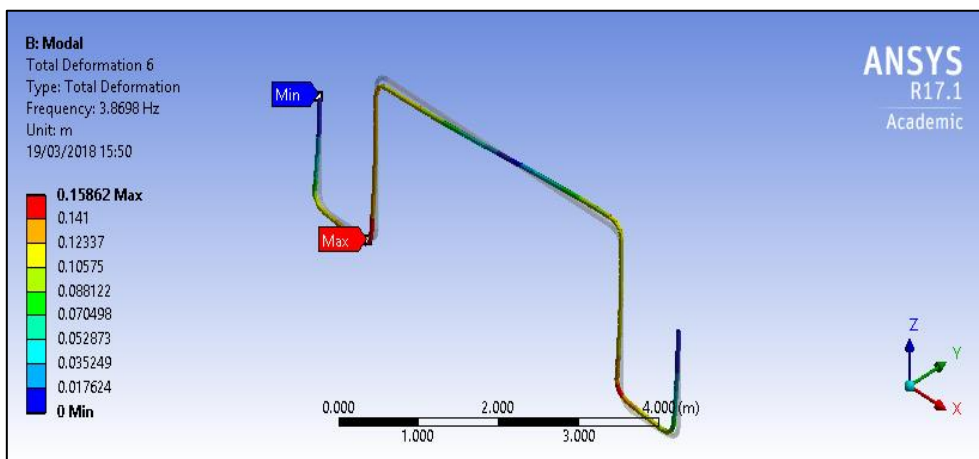


Figure 5-13: Total deformation and mode shape for Mode – 6

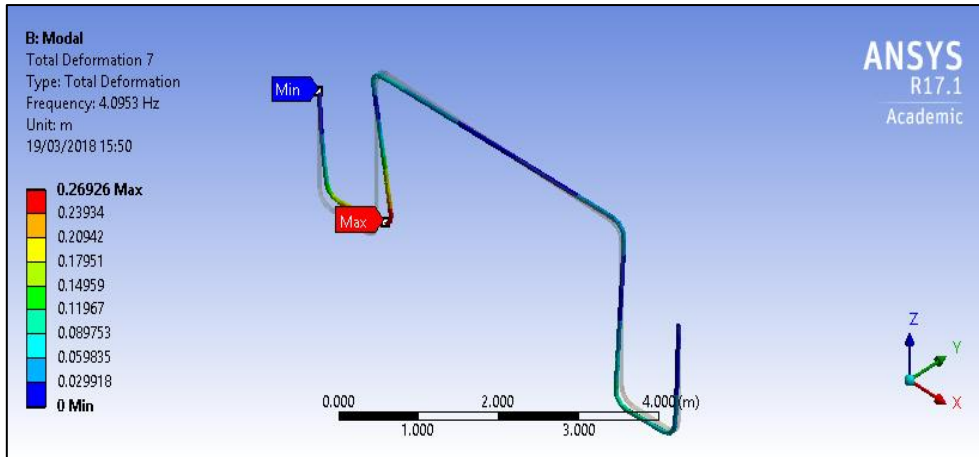


Figure 5-14: Total deformation and mode shape for Mode – 7

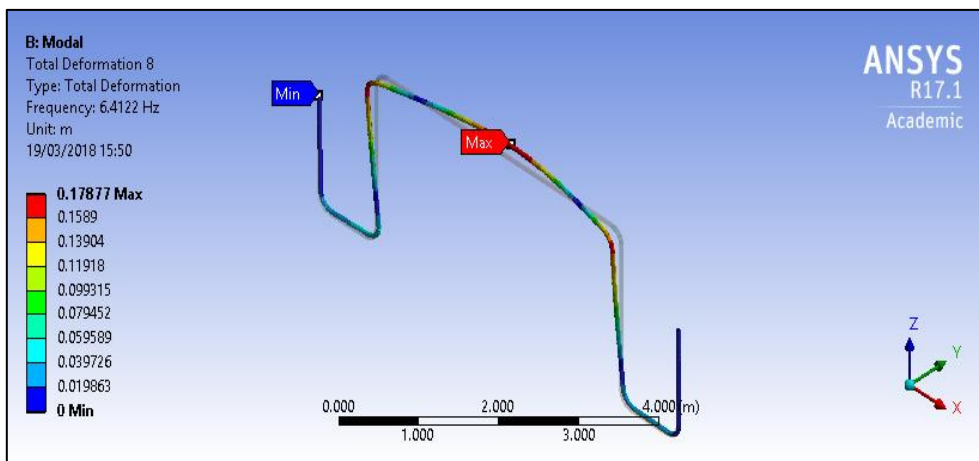


Figure 5-15: Total deformation and mode shape for Mode – 8

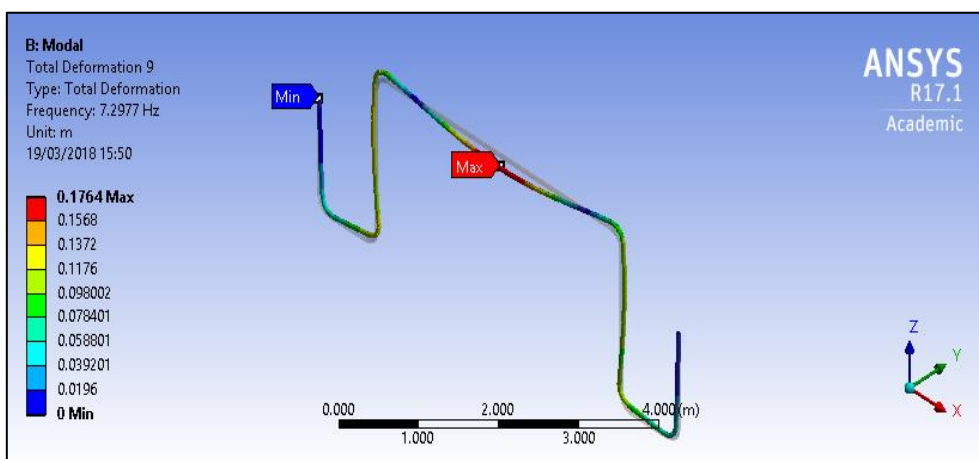


Figure 5-16: Total deformation and mode shape for Mode – 9

5.2.7 Unit amplitude stress

Unit amplitude stress is calculated from flexural modal stresses and shear/torsional modal stresses obtained from Ansys Mechanical Workbench results using the methodology described in section 4.2.3.

Figure 5-17 and Figure 5-18 show the unit amplitude flexural and torsional stresses for all modes along the arc length of the rigid jumper.

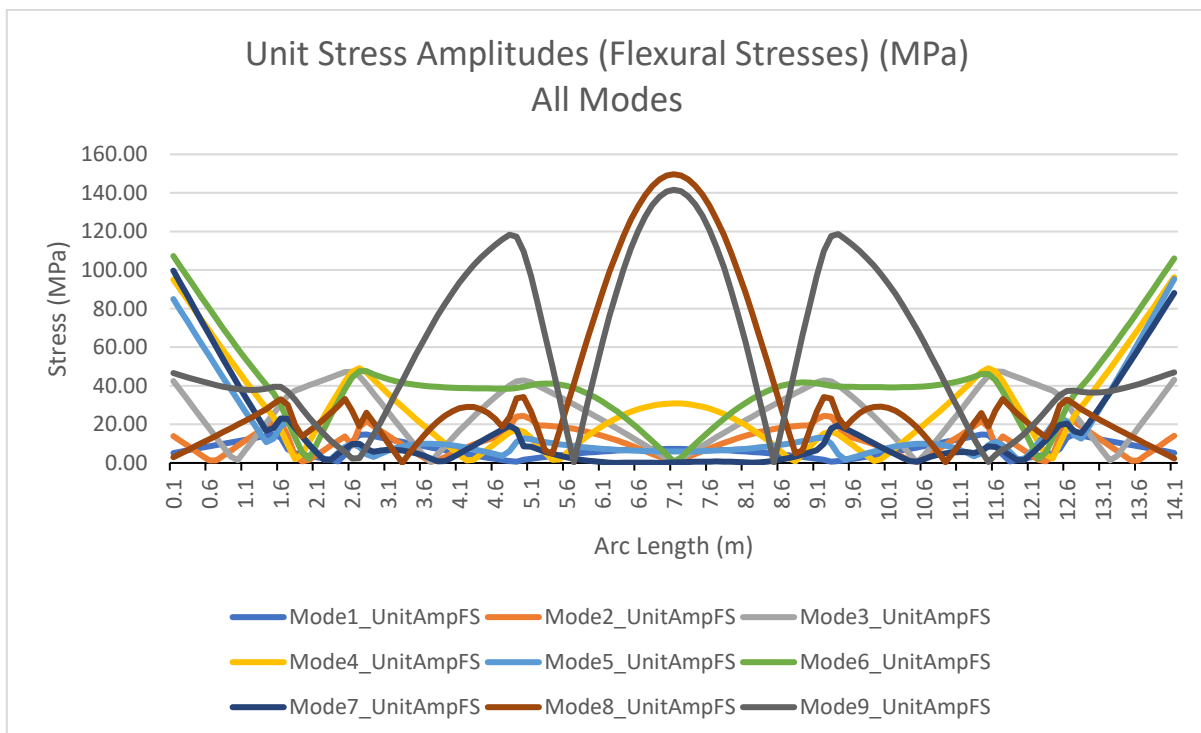


Figure 5-17: Unit amplitude stresses – Flexural stresses – All modes

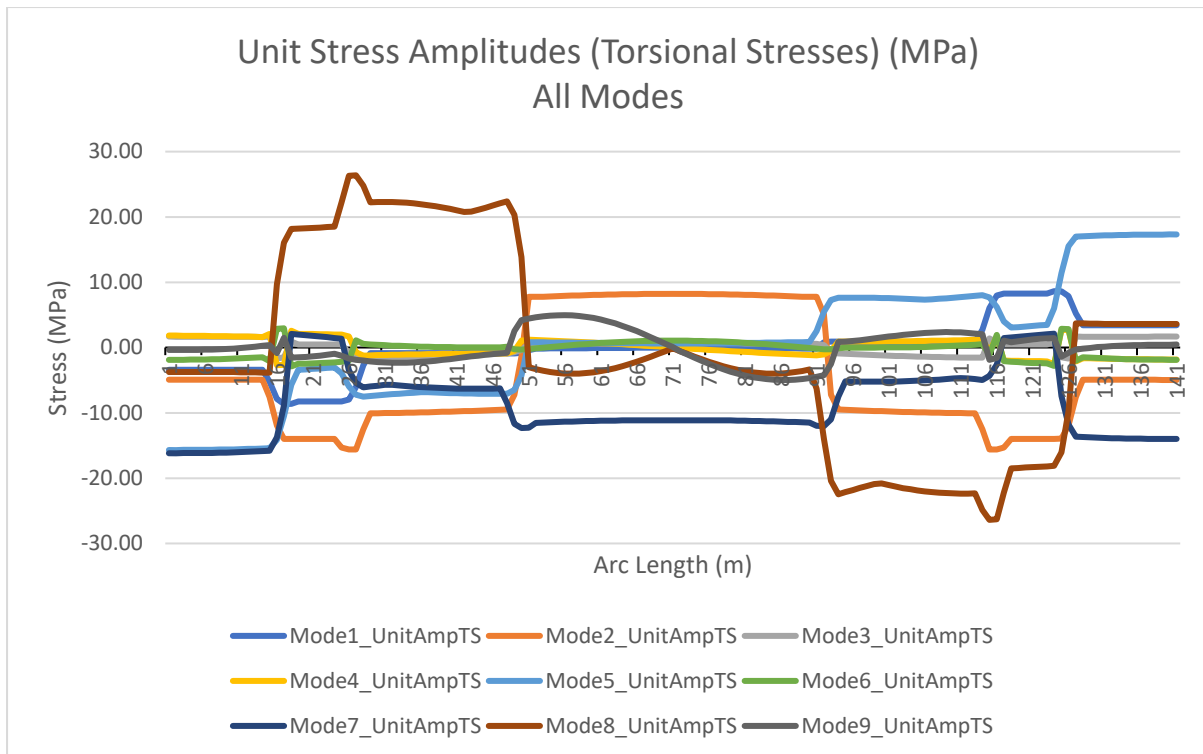


Figure 5-18: Unit amplitude stresses – Torsional stresses – All modes

5.3 Single point analysis

According to DNVGL-RP-F105 (2017 edition) [11], Multiple location analysis gives a more accurate and less conservative fatigue damage but its computationally demanding and hence a time consuming and a complex process. The single point analysis gives less accurate but more conservative results for fatigue damage and is significantly less work intensive.

For non-straight geometries, following additional design criteria are given in DNVGL-RP-F105 (2017 edition) [11] which, as applicable, supersede the criteria given in Section 4.3.3:

“Fatigue damage shall be conservatively calculated at one critical location”

Hence, the single point analysis is preferred over the multiple point analysis for non-straight geometries such as the rigid jumper model.

5.4 Mode classification based on flow orientation

The modes (1-9) obtained from the FEM based modal analysis need to be classified as in-line and cross-flow based on Section 4.3.2.

5.4.1 10° Flow

10° flow represents Case-2 of Section 4.3.2. Since methodology in this thesis is based on a single point analysis according to Section 5.3, the rigid jumper is not divided into horizontal and vertical segments. A conservative approach would be to consider all contributing modes as in-line as well as cross-flow for the whole rigid jumper.

5.4.2 90° Flow

90° flow represents Case-1 of Section 4.3.2. Here, the modes have been distinctively classified for the whole rigid jumper as either in-line or cross-flow depending on the mode shapes. Here, the modes with total deformation along Y-axis are classified as in-line modes while modes with total deformation along X-axis are classified as cross-flow.

The results based on above mentioned criteria are presented in Table 5-6

Table 5-6: Mode classification for 10° and 90° flow into IL and CF for jumper model

Mode	Eigen Frequency [Hz]	Mode Classification	
		10° Flow	90° Flow
1	0.85015	IL & CF	IL
2	2.2297	IL & CF	IL
3	2.2934	IL & CF	CF
4	2.6431	IL & CF	CF
5	3.4486	IL & CF	IL
6	3.7582	IL & CF	CF
7	3.8432	IL & CF	IL
8	6.3956	IL & CF	IL
9	7.1956	IL & CF	CF

5.5 Design assessment

Design assessment module of Ansys Mechanical Workbench is used to evaluate the modal analysis results. This module is used to see the combined effects of flexural and torsional modal stresses according to mode classification shown in Table 5-6. Design assessment project schematic is setup based on the mode classification for flow orientation as shown in Figure 5-19. Following cases of design assessment modules are setup:

1. 10° Flow
 - a. In-line
 - b. Cross-flow
2. 90° Flow
 - a. In-line
 - b. Cross-flow

To determine the critical points for fatigue assessment, the applicable IL and CF modes are combined using design assessment module and two points are selected based on maximum combined flexural stress (point A) and maximum combined torsional stress (point) for each case.

In this section, selection of critical location for 10° Flow – In-line and Cross-flow is explained with results. For 90° Flow – In-line and Cross-flow, same procedure is followed and only results are presented in this section.

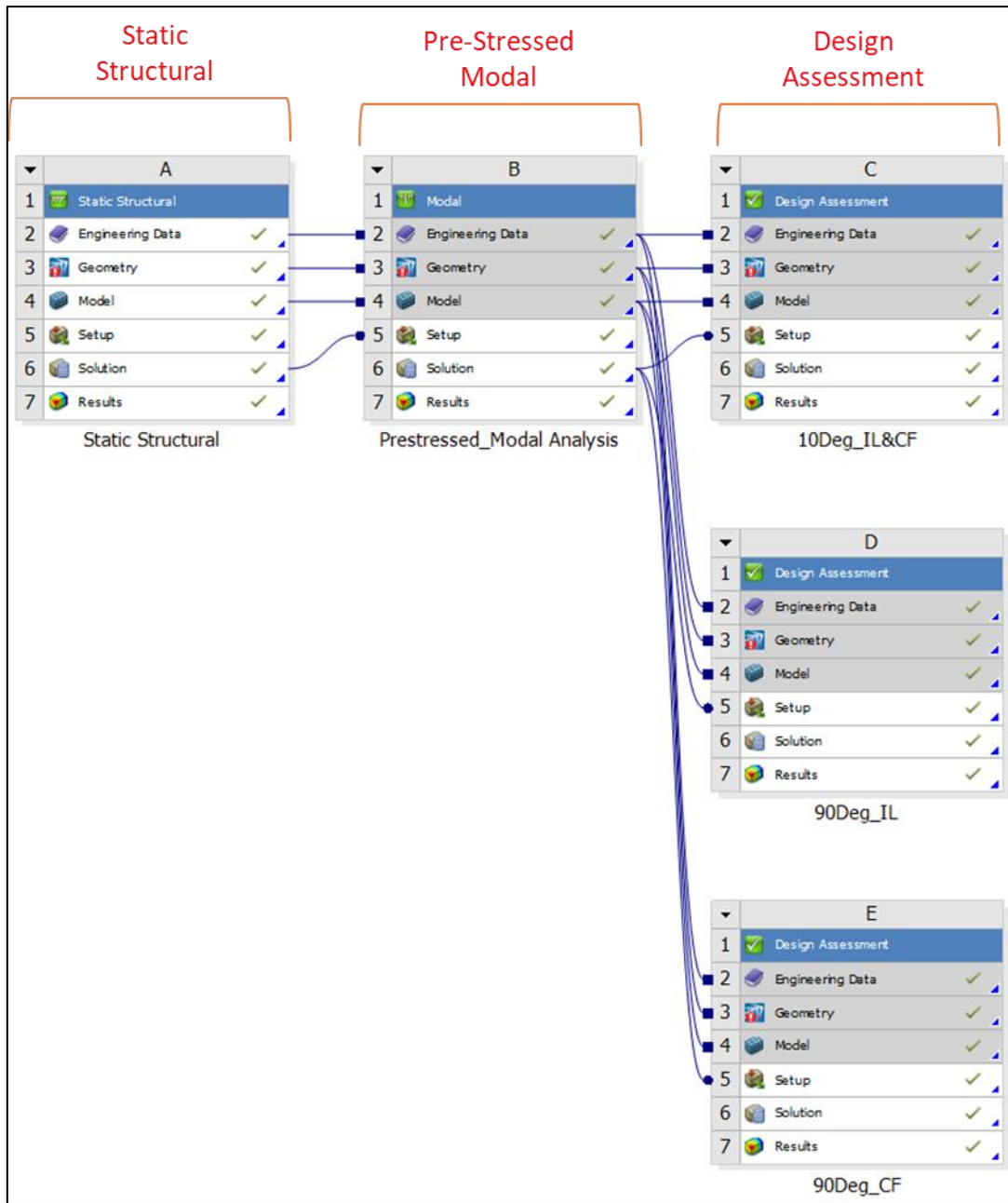


Figure 5-19: Project Schematic – Design assessment module in Ansys Mechanical Workbench 17.1

5.5.1 10° Flow – IL/CF modes

As shown in Table 5-6, for 10° flow, all modes are considered both as in-line and cross-flow. Hence, the design assessment this case is the same for in-line and cross-flow conditions.

Figure 5-20 and Figure 5-21 show the maximum combined flexural stresses (MPa) as a function of arc length (m). From the graph and the figure, we can see that the combined flexural stresses are highest at the fixed ends and lowest near the elbows.

Figure 5-22 and Figure 5-23 show the maximum combined torsional stresses (MPa) as a function of arc length (m). From the graph and the figure, we can see that the combined torsional stresses are high at the left end, but the highest torsional stress occurs near the left end at the elbow. The lowest combined torsional stress occurs at the middle as well as near arc length of 5m from left fixed end of rigid jumper.

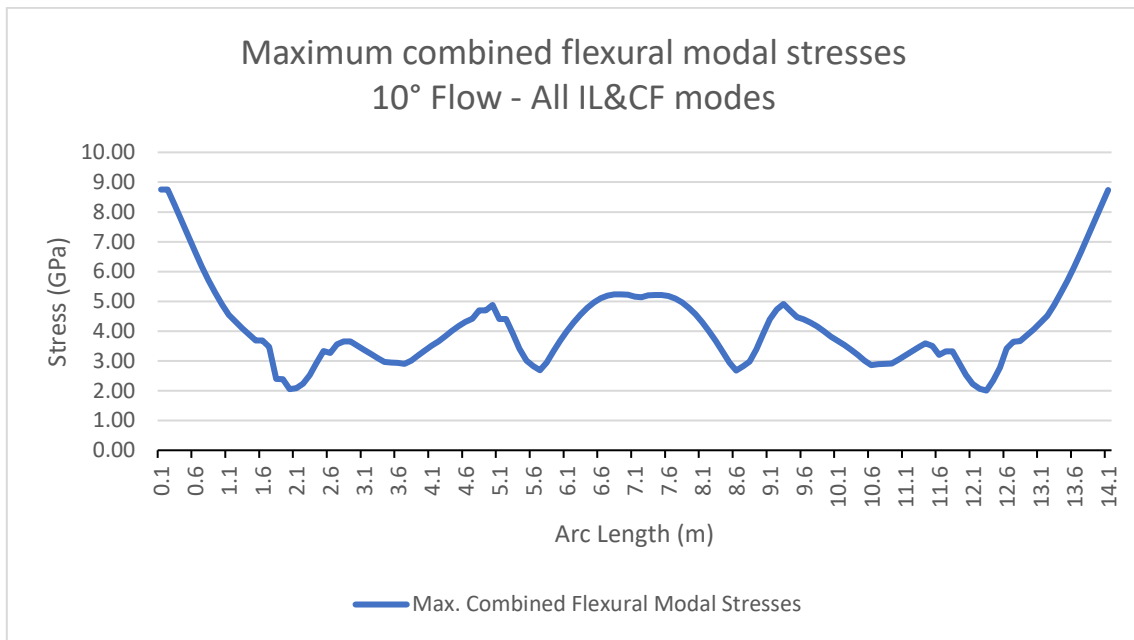


Figure 5-20: Maximum combined flexural modal stresses for 10° Flow - All In-line/Cross-flow modes

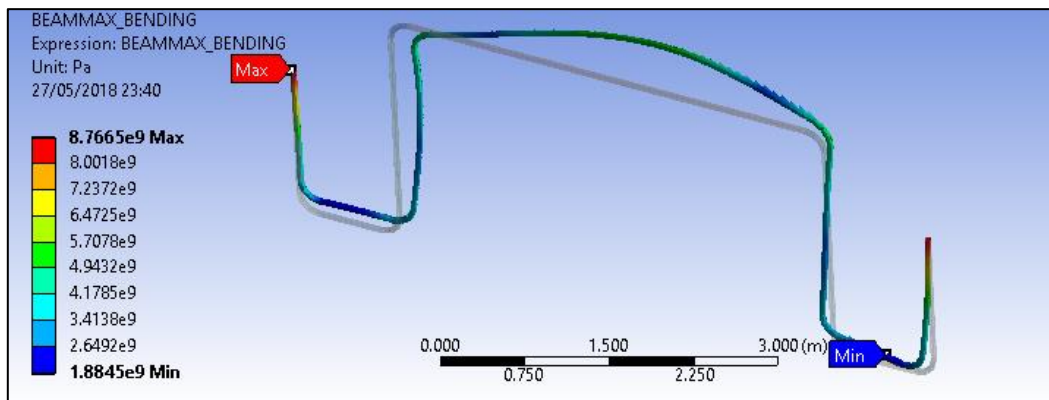


Figure 5-21: Maximum combined flexural modal stresses for 10° Flow - All In-line/Cross-flow modes from Design assessment module

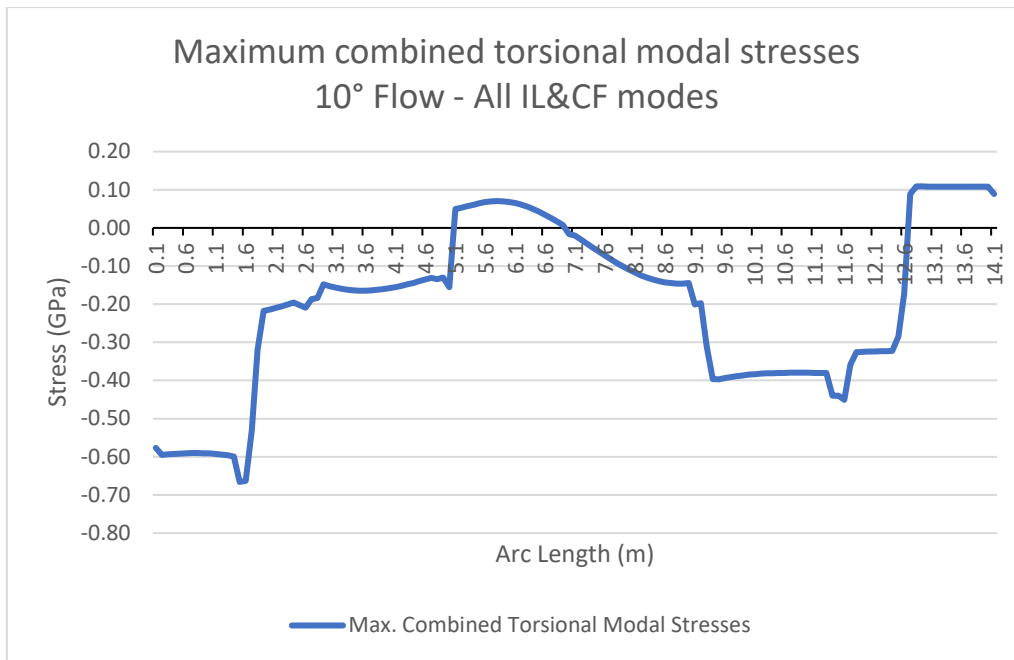


Figure 5-22: Maximum combined torsional modal stresses for 10° Flow - All In-line/Cross-flow modes

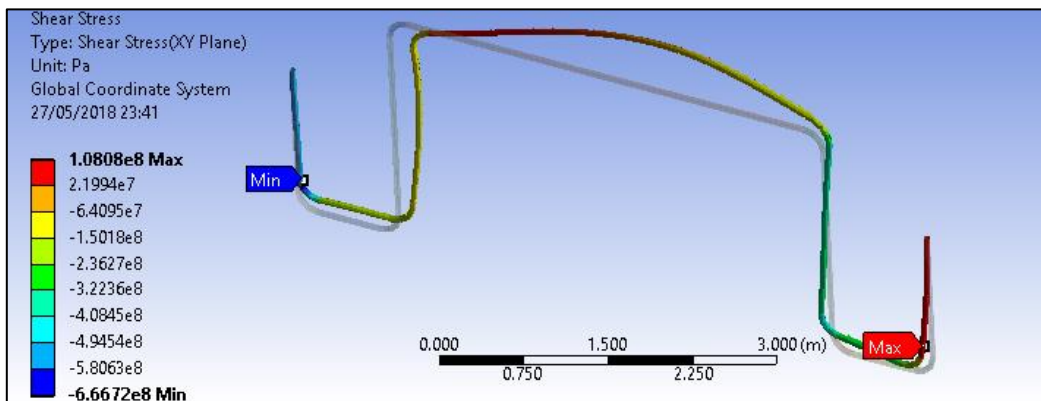


Figure 5-23: Maximum combined torsional modal stresses for 10° Flow - All In-line/Cross-flow modes from Design assessment module

Table 5-7 shows the critical locations (A and B) determined using the procedure explained above for all three cases. The graphs and figures for Case-2(a) and Case-2(b) are presented in section 5.5.2 and 5.5.3.

Table 5-7: Critical location for 10° and 90° in-line and cross-flow cases (measured from left fixed end of rigid jumper)

S. No.	Case	Location A Arc length (m)	Location B Arc length (m)
1 (a)	10° Flow – In-line	0.1 m	1.5 m
1 (b)	10° Flow – Cross-flow	0.1 m	1.5 m
2 (a)	90° Flow – In-line	0.1 m	1.5 m
2 (b)	90° Flow – Cross-flow	14.1 m	5.7 m

Table 5-8 shows the unit amplitude stresses for Case-1 (a) and (b) (10° Flow – In-line and cross-flow) at the critical location A and B. We can also see that more than one mode is active at each of the critical location. Hence, we can conclude that there will be a multimode response at each of the critical location.

Table 5-8: Unit amplitude stresses for 10° Flow – In-line and cross-flow case at the critical locations A and B

Mode	Location A		Location B	
	Unit Amplitude Flexural Stress (MPa)	Unit Amplitude Torsional Stress (MPa)	Unit Amplitude Flexural Stress (MPa)	Unit Amplitude Torsional Stress (MPa)
M1	5.19	-3.40	14.7351111	-5.20
M2	13.96	-4.93	21.5596097	-7.54
M3	42.50	1.67	25.5573489	1.66
M4	95.04	1.82	23.6797	2.10
M5	84.89	-15.69	12.5520762	-15.41
M6	107.28	-1.88	36.2178863	-2.05
M7	99.68	-16.18	18.0565226	-16.18
M8	2.98	-3.72	30.7238913	-3.85
M9	46.57	-0.38	39.440555	0.38

5.5.2 90° Flow – IL modes

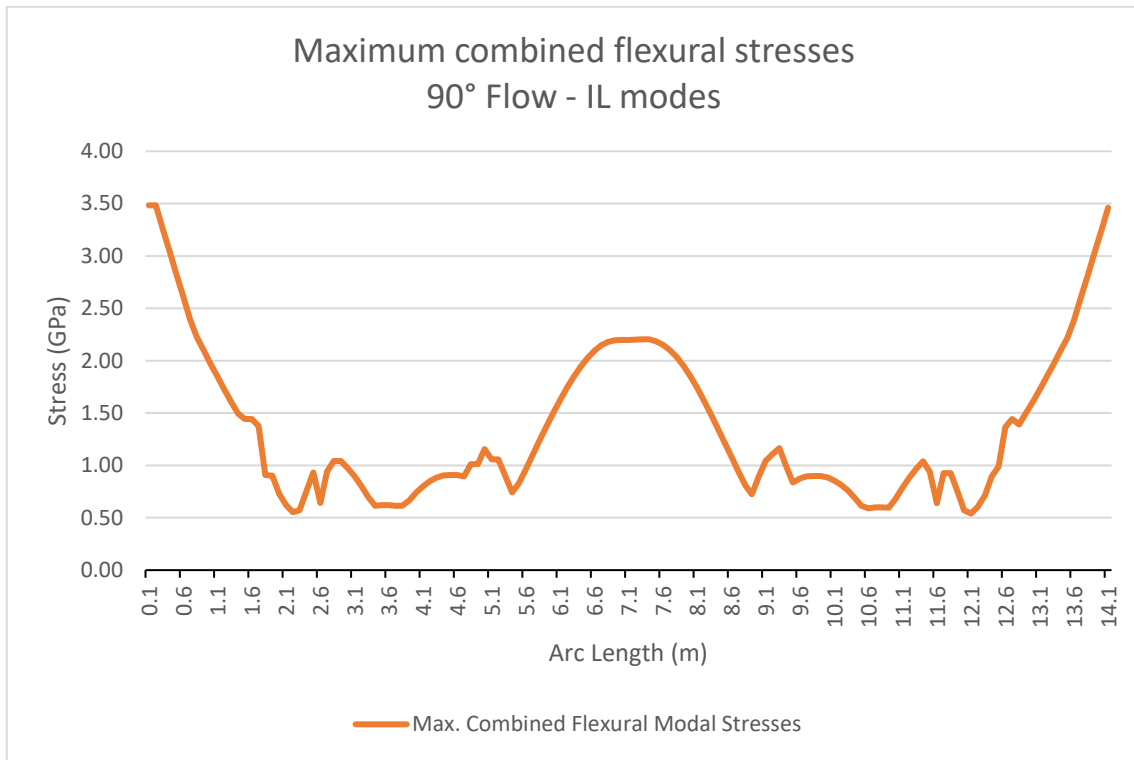


Figure 5-24: Maximum combined flexural modal stresses for 90° Flow - IL modes

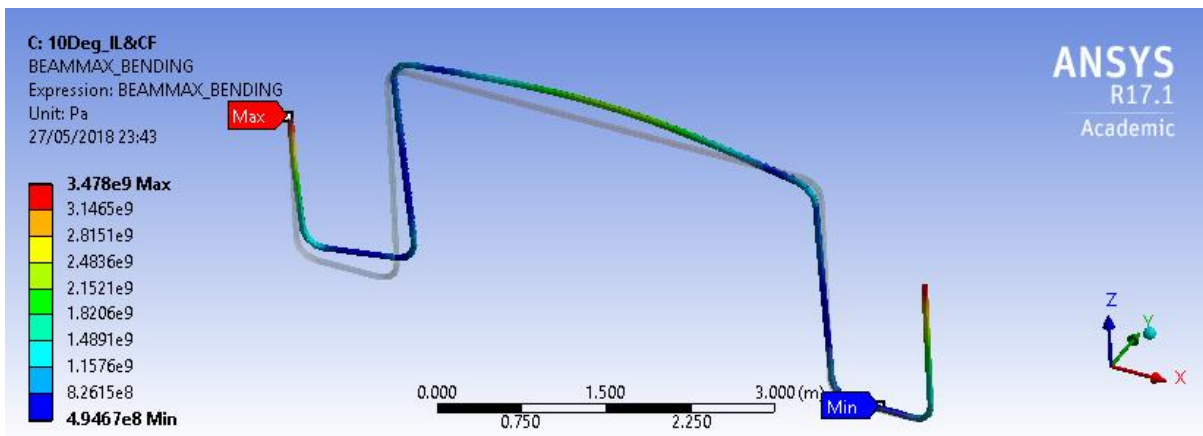


Figure 5-25: Maximum combined flexural modal stresses for 90° Flow - IL modes (Design assessment)

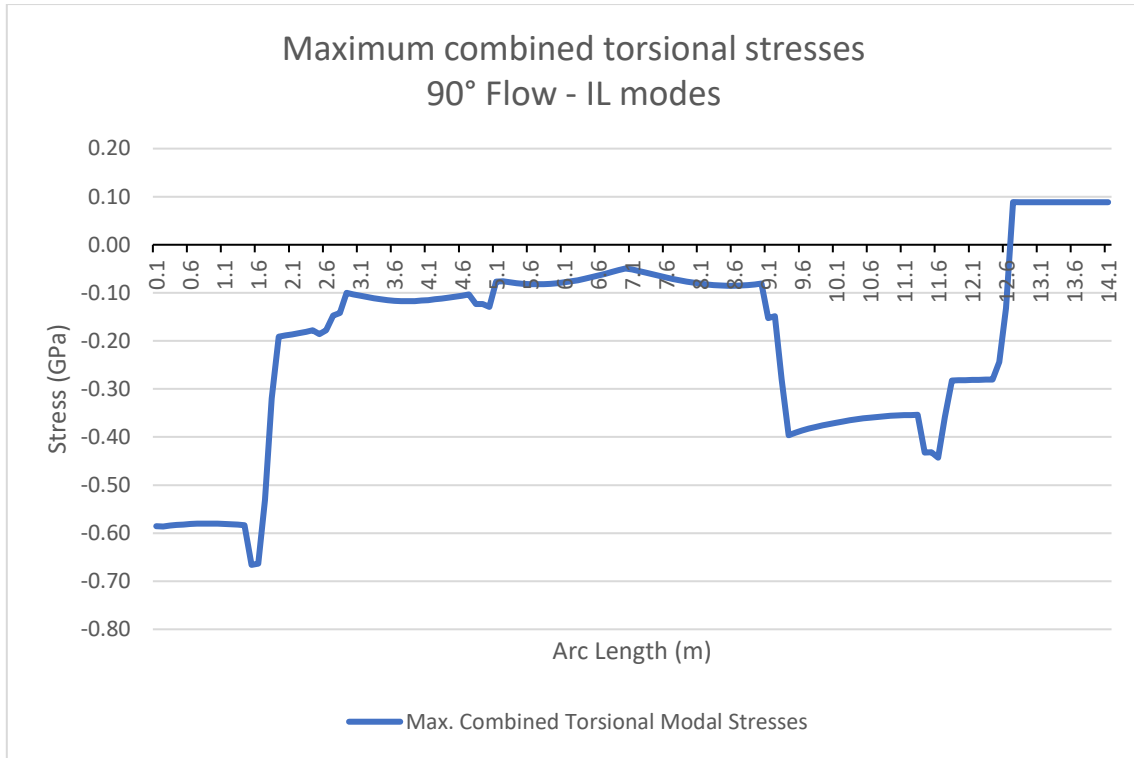


Figure 5-26: Maximum combined torsional modal stresses for 90° Flow - IL modes

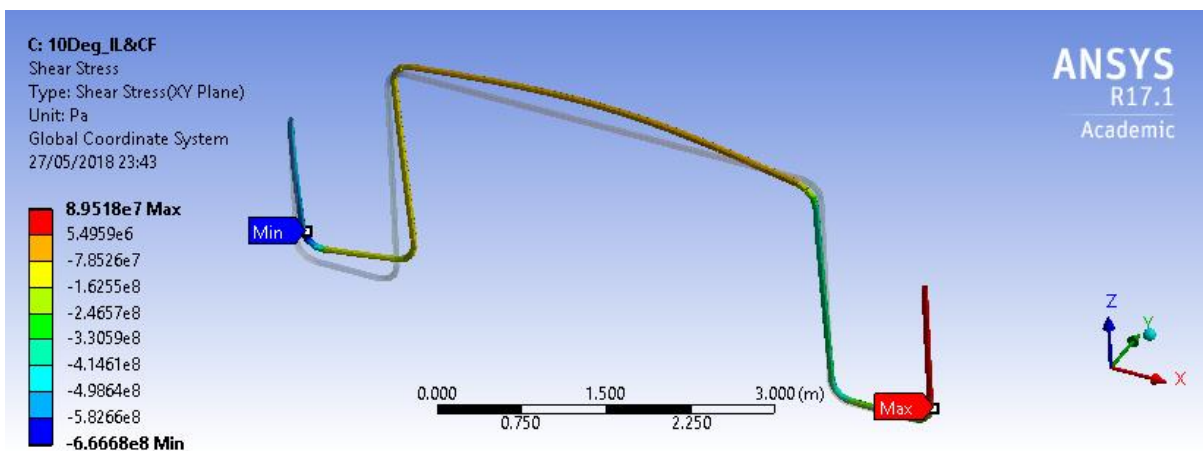


Figure 5-27: Maximum combined torsional modal stresses for 90° Flow - IL modes (Design assessment)

Table 5-9: Unit amplitude stresses for 90° Flow – In-line case at the critical locations A and B

Mode	Location A		Location B	
	Unit Amplitude Flexural Stress (MPa)	Unit Amplitude Torsional Stress (MPa)	Unit Amplitude Flexural Stress (MPa)	Unit Amplitude Torsional Stress (MPa)
M1	5.19	-3.40	14.73511111	-5.20
M2	13.96	-4.93	21.5596097	-7.54
M5	84.89	-15.69	12.5520762	-15.41
M7	99.68	-16.18	18.0565226	-16.18
M8	2.98	-3.72	30.7238913	-3.85

5.5.3 90° Flow – CF modes

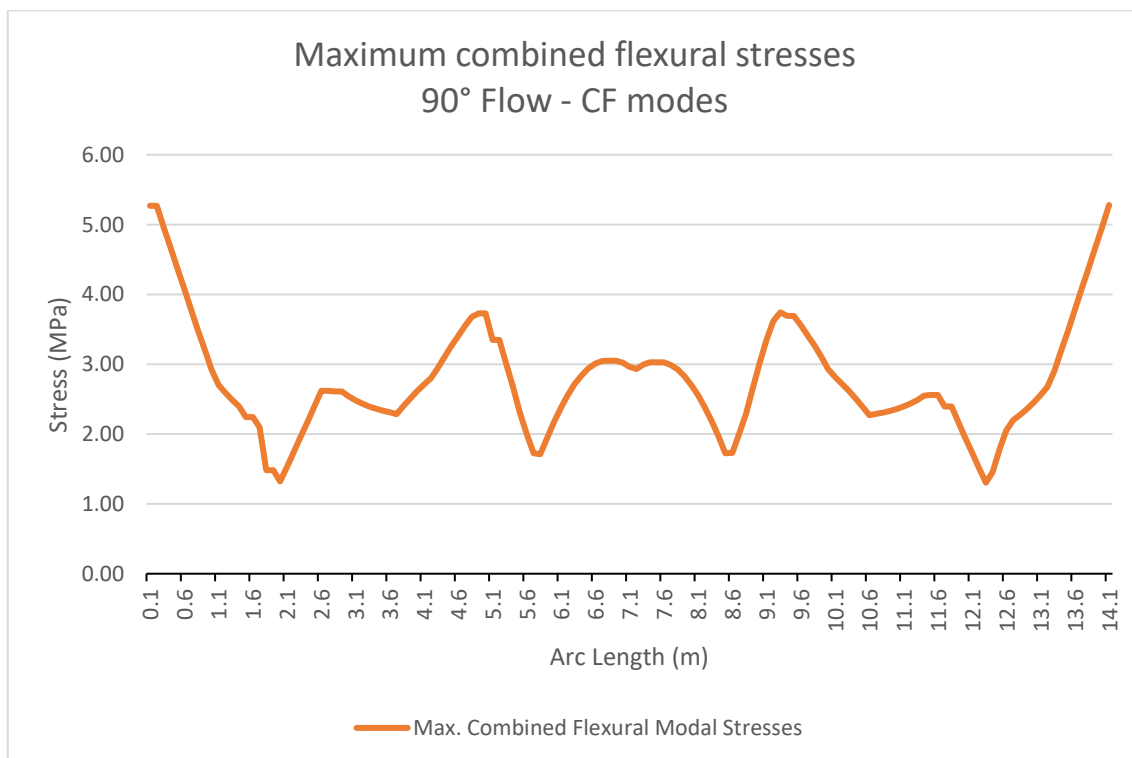


Figure 5-28: Maximum combined flexural modal stresses for 90° Flow - CF modes

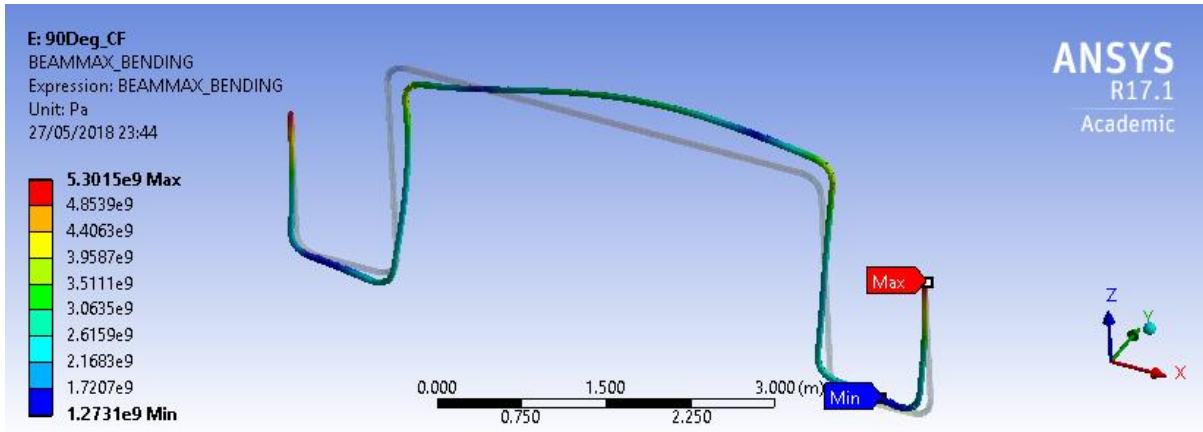


Figure 5-29: Maximum combined flexural modal stresses for 90° Flow - CF modes (Design assessment)

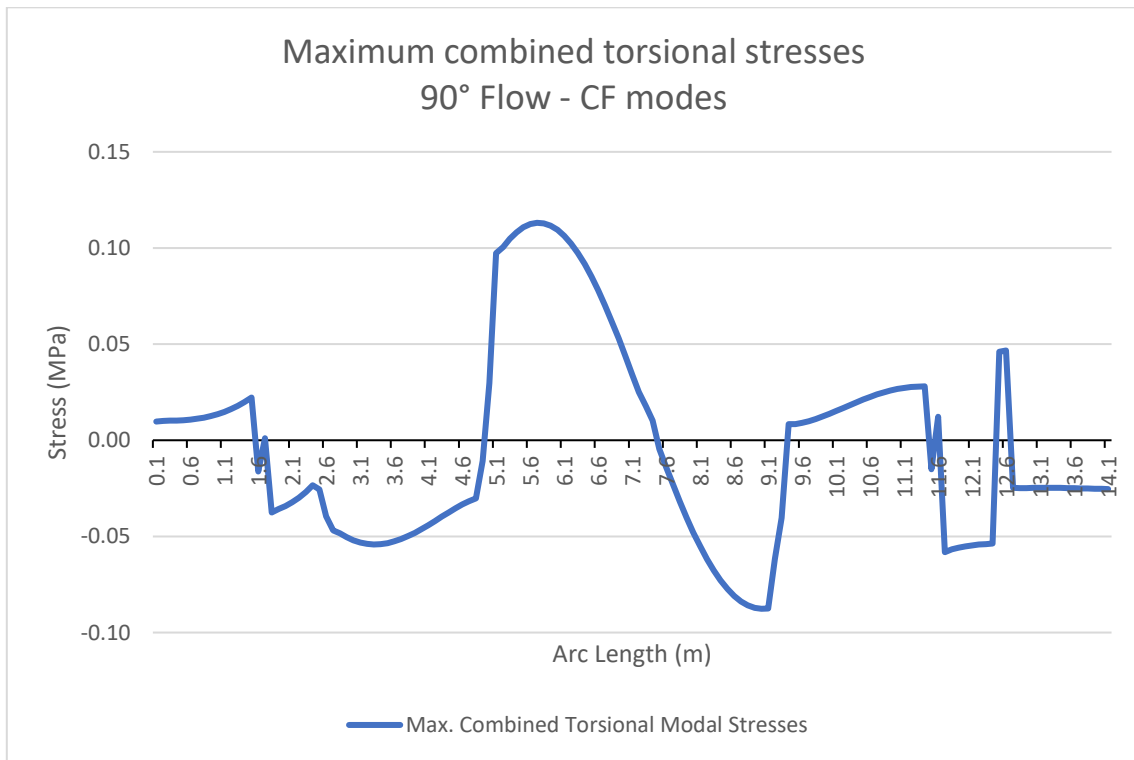


Figure 5-30: Maximum combined torsional modal stresses for 90° Flow - CF modes

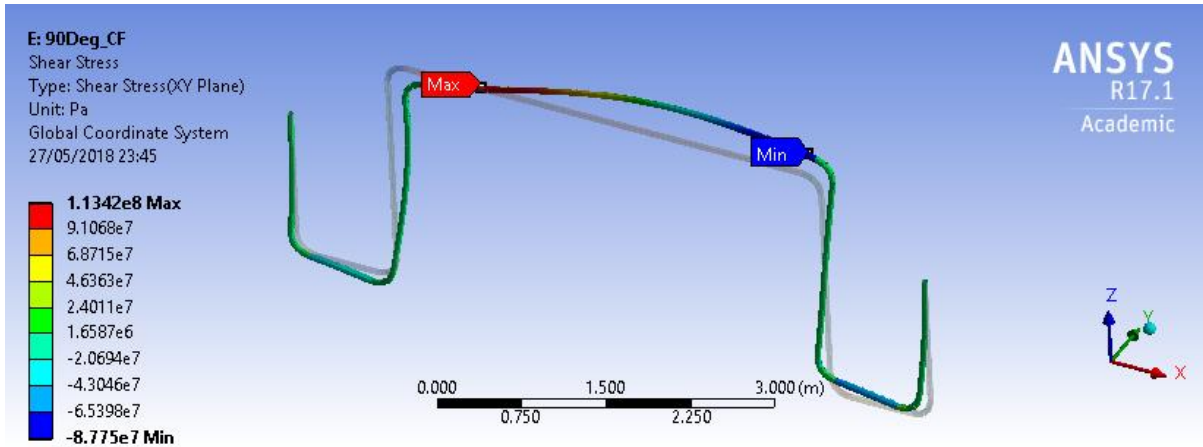


Figure 5-31: Maximum combined torsional modal stresses for 90° Flow - CF modes (Design assessment)

Table 5-10: Unit amplitude stresses for 90° Flow – cross-flow case at the critical locations A and B

Mode	Location A		Location B	
	Unit Amplitude Flexural Stress (MPa)	Unit Amplitude Torsional Stress (MPa)	Unit Amplitude Flexural Stress (MPa)	Unit Amplitude Torsional Stress (MPa)
M1	5.19	-3.40	14.7351111	-5.20
M2	13.96	-4.93	21.5596097	-7.54
M5	84.89	-15.69	12.5520762	-15.41
M7	99.68	-16.18	18.0565226	-16.18
M8	2.98	-3.72	30.7238913	-3.85

5.6 Discussion

5.6.1 Eigen Frequencies and Mode Shapes

From Table 5-5 we can see that the eigen frequencies predicted in this study using Ansys Mechanical Workbench are in close agreement with Igeh [24]’s value that she predicted using Ansys APDL (Classic) interface. Maximum difference of +0.68% occurs for Mode-7 between this study and Igeh [24]. Eigen frequency values for Mode-1 and Mode-2 from this study are in good agreement with Igeh [24]. Difference between the eigen frequency values from this

study and Igeh [24] is less than 1% which shows that Ansys Mechanical Workbench's modal analysis modules gives good results and can be used in place of the Ansys APDL (Classic) interface for modal analysis.

A comparison of the values predicted in this study with the eigen frequencies measured using the Exxon Mobil's rigid jumper setup shows that the eigen frequency of Mode-1 for this study is less as compared to Igeh [24]. The predicted eigen frequency for Mode 2 to Mode-4 are over predicted as compared to Zheng et al. [51]. With a maximum variation of less than 5% between results from this study and Zheng et al. [51], it may be safe to say that the eigen values and mode shapes predicted in this study represent the actual model accurately.

This difference in the predicted eigen frequencies from this study and Zheng et al. [51] may be because of difference in the rigid jumper length. The overall length of the rigid jumper modelled using Ansys SpaceClaim in this study is 14.1m whereas the rigid jumper model using for Exxon Mobil's towing experiments was 13.96m (See Table 5-1).

Normalized displacements from this study are compared with Igeh for all modes as shown in Figure 5-32 to Figure 5-40.

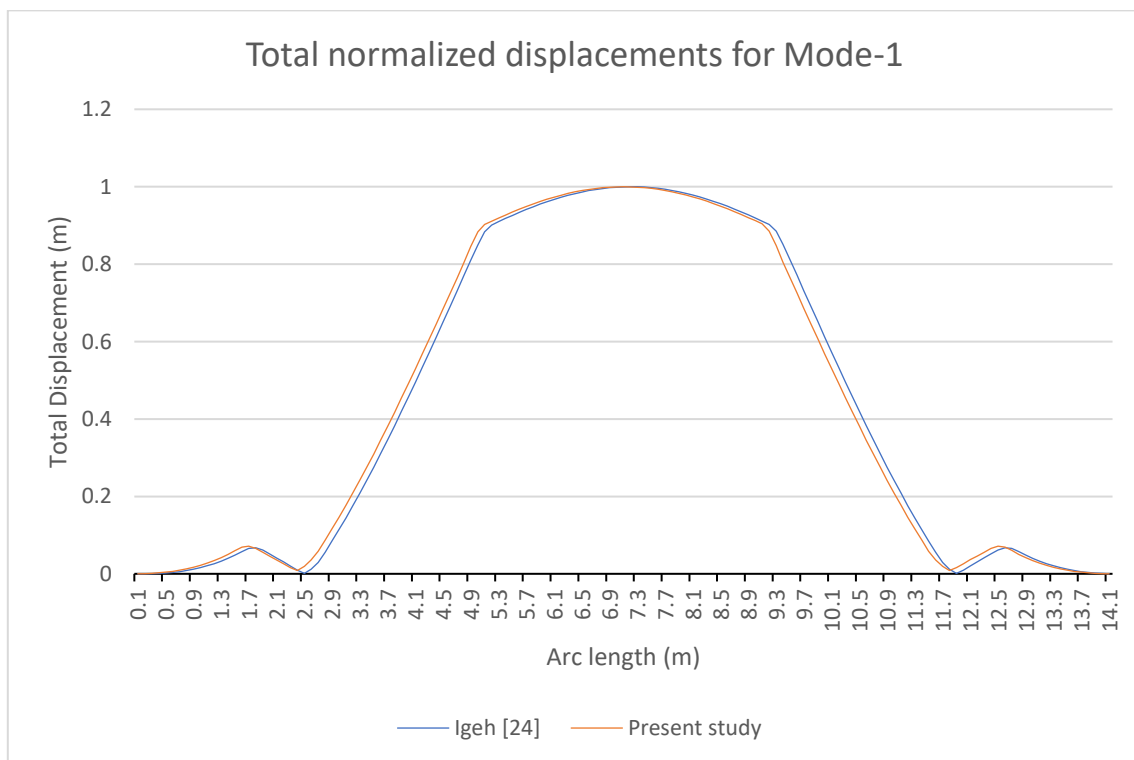


Figure 5-32: Comparison of total normalized displacement for mode-1

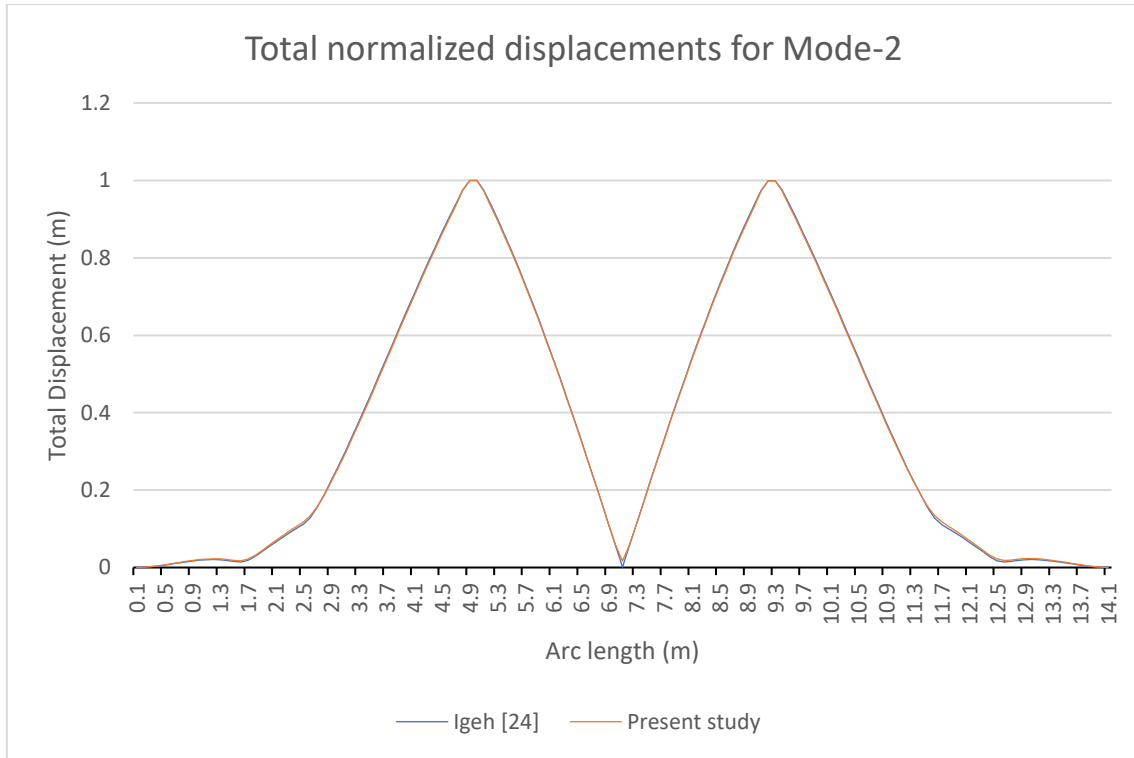


Figure 5-33: Comparison of total normalized displacement for mode-2

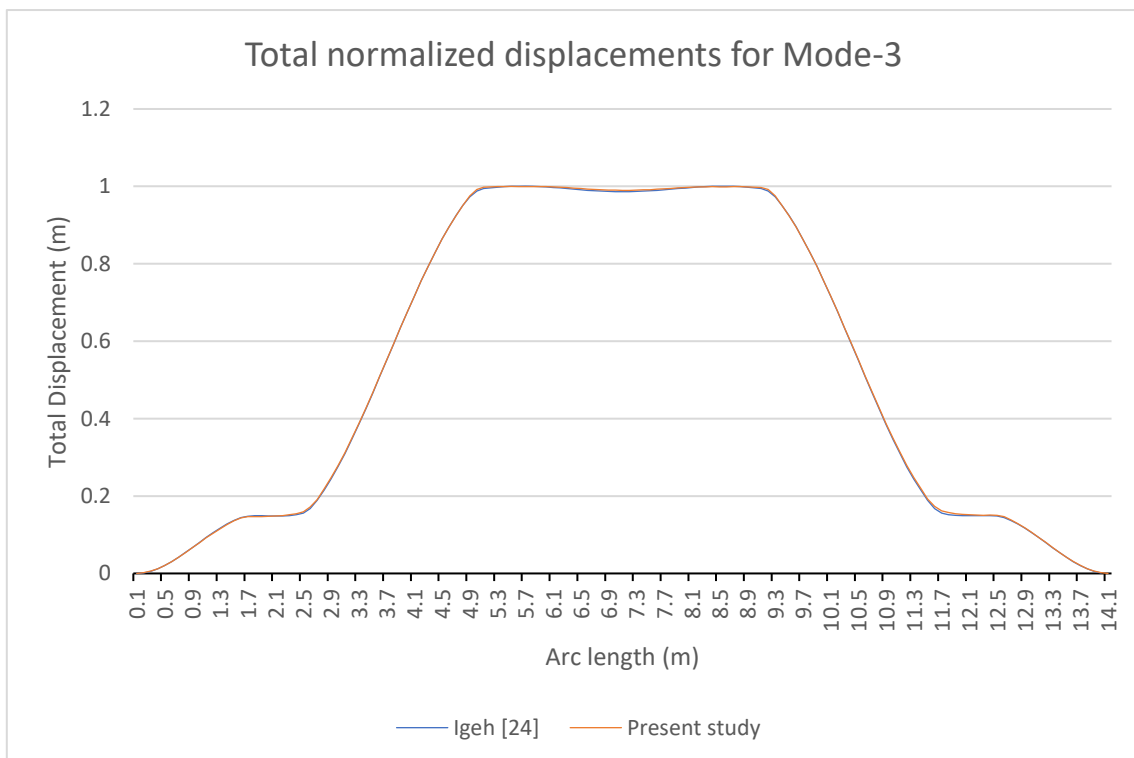


Figure 5-34: Comparison of total normalized displacement for mode-3

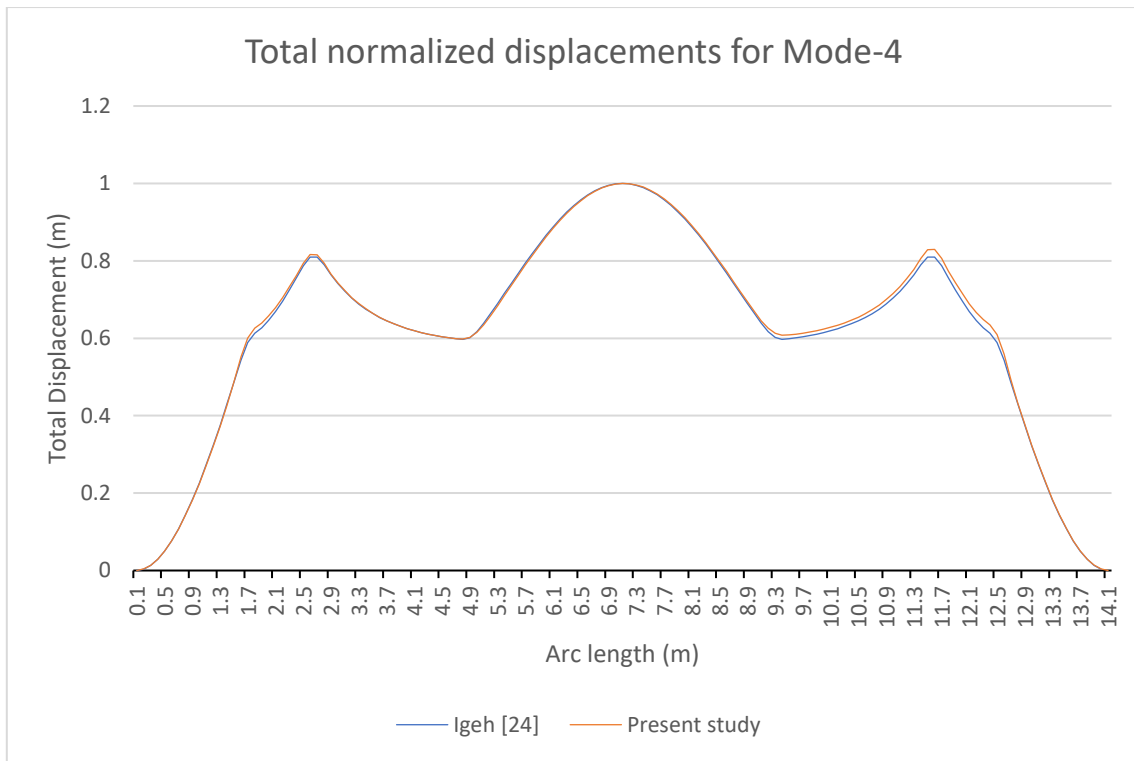


Figure 5-35: Comparison of total normalized displacement for mode-4

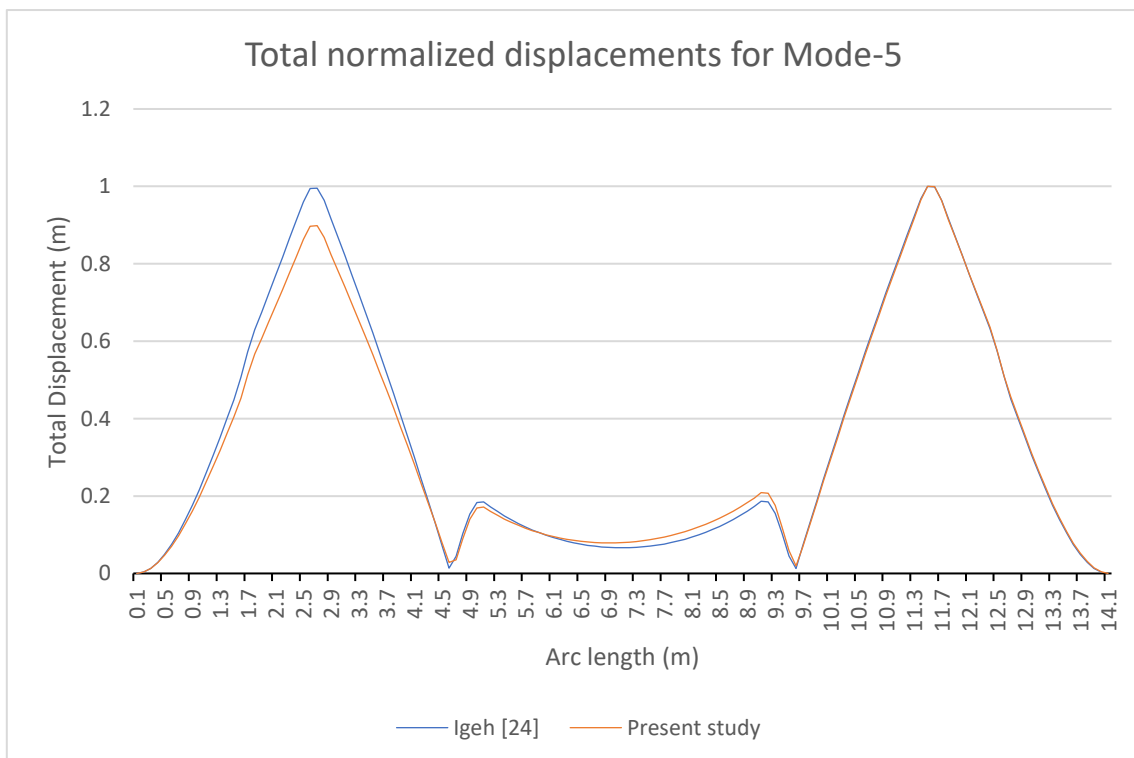


Figure 5-36: Comparison of total normalized displacement for mode-5

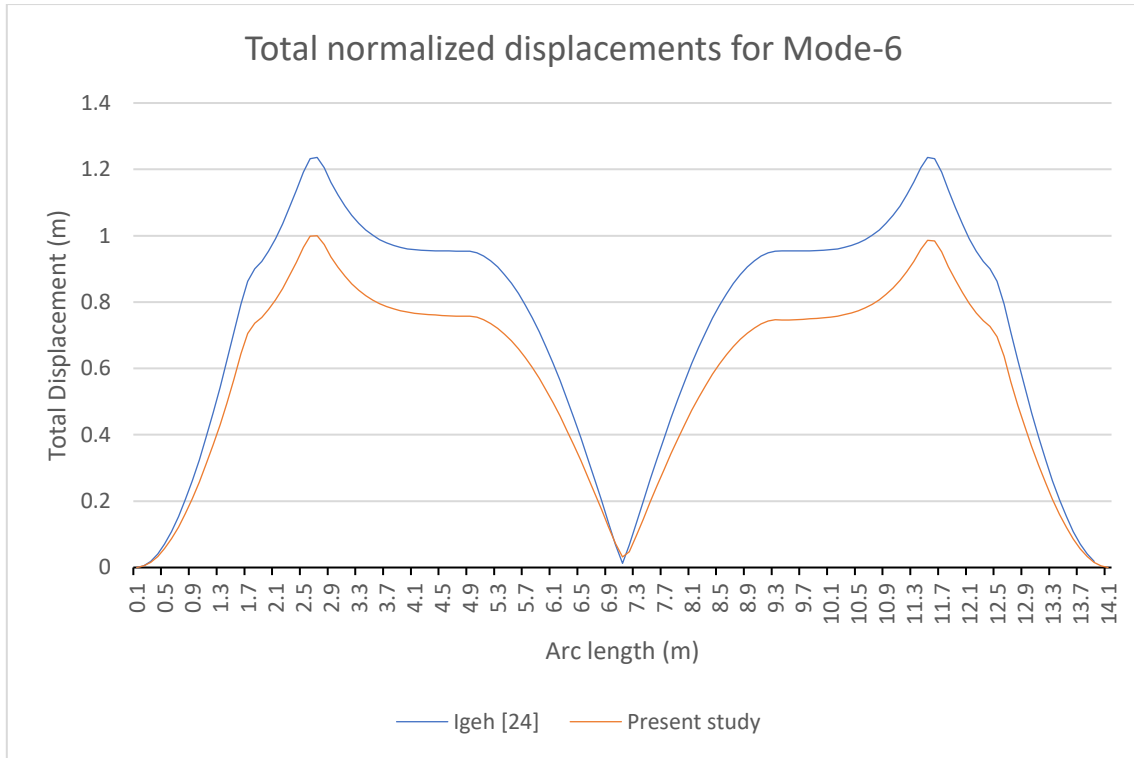


Figure 5-37: Comparison of total normalized displacement for mode-6

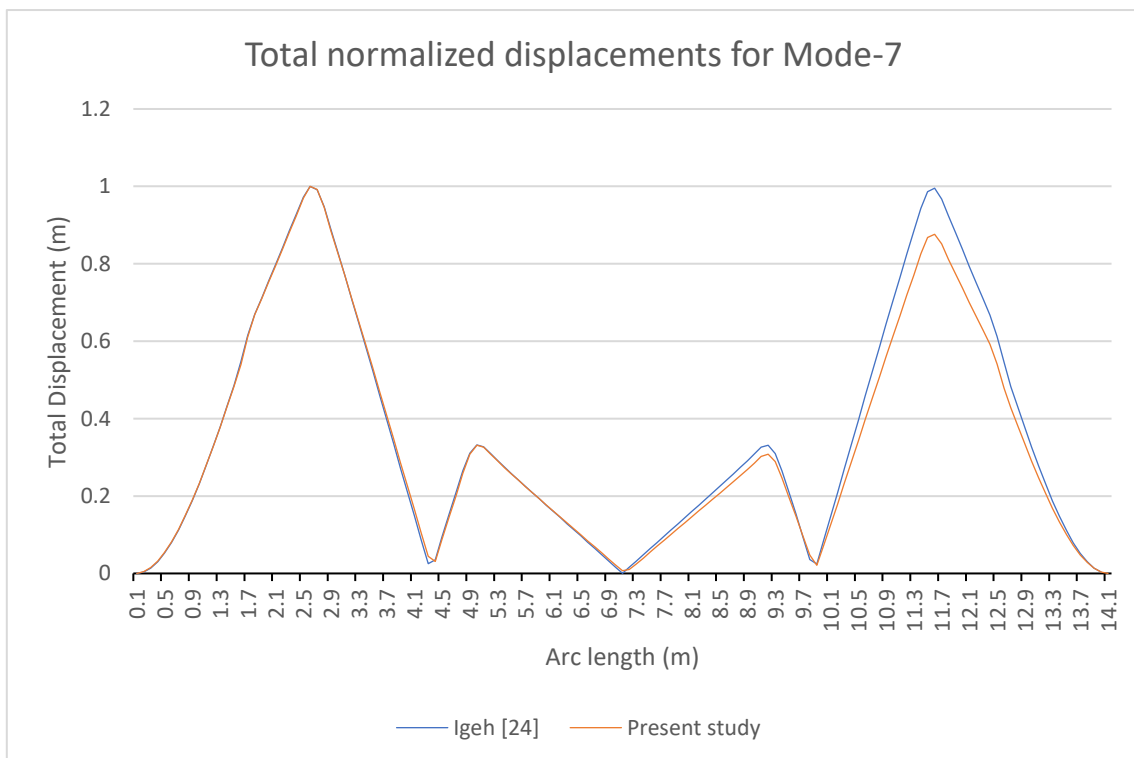


Figure 5-38: Comparison of total normalized displacement for mode-7

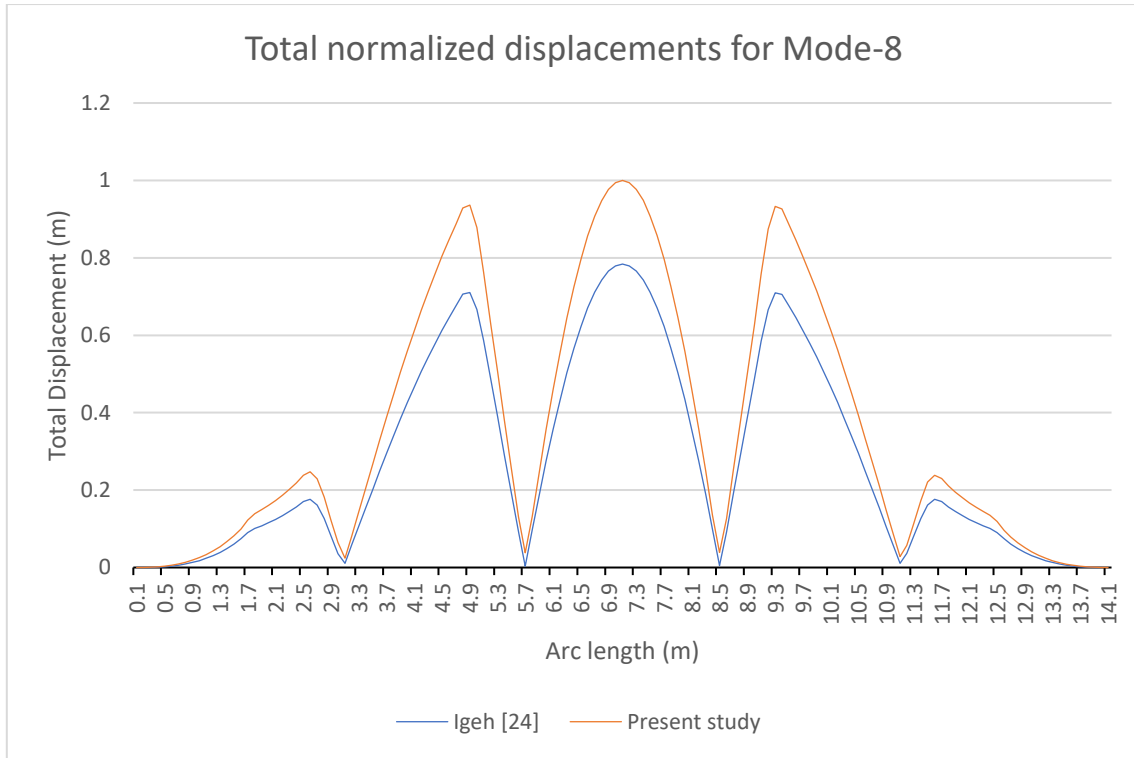


Figure 5-39: Comparison of total normalized displacement for mode-8

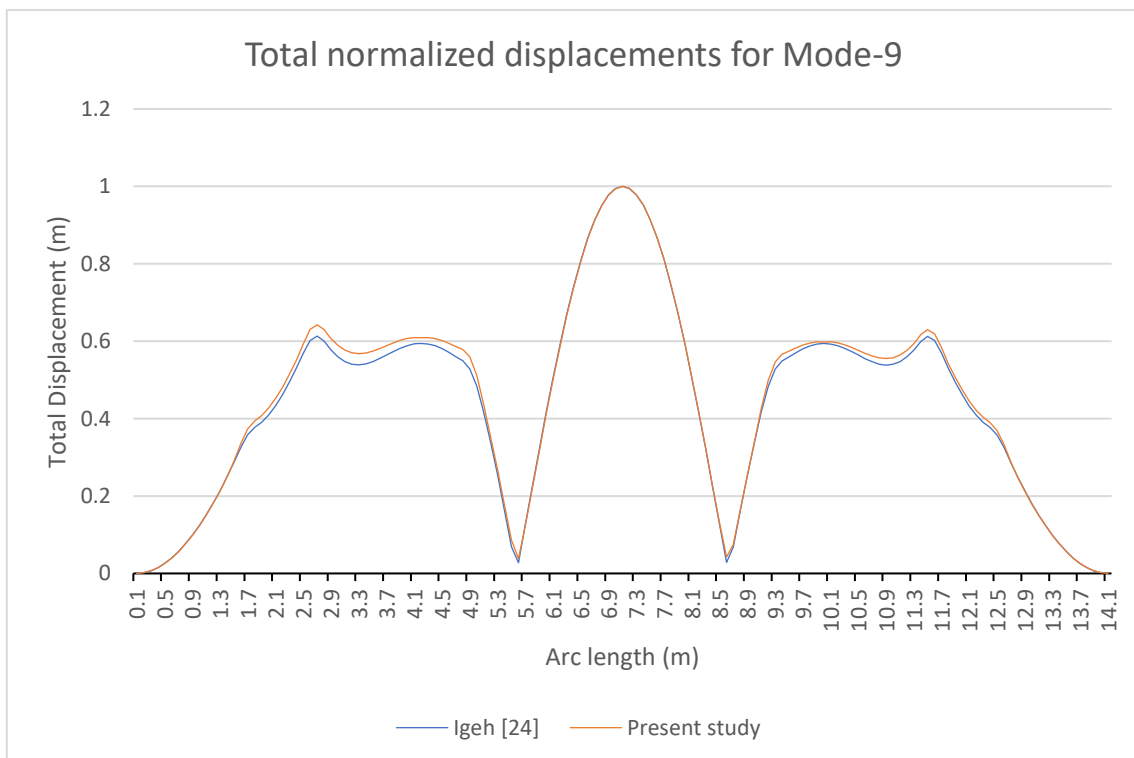


Figure 5-40: Comparison of total normalized displacement for mode-9

The normalized total displacement for mode-6 and mode-8 differ from those predicted in Igeh [24]. While total displacement for mode-6 is underestimated, mode-8 displacements are overestimated by this study. Though the difference is less, this difference may reflect in unit amplitude flexural and modal stresses and hence, in stress range calculations.

5.6.2 Unit amplitude stresses

Figure 5-41 to Figure 5-49 compares the flexural and torsional unit amplitude stresses calculated in this study with those calculated by Igeh [24] for Mode-1 to Mode-9, respectively. The unit amplitude stresses calculated from modal analysis are in close agreement with Igeh [24] for Mode-1,2,7 and 8. For Mode-3,4,5 and 9, the unit amplitude torsional stresses do not match as Igeh [24] considers zero torsional stresses for these modes. Based on the results from modal analysis in this study, we observe non-zero values for unit amplitude torsional stresses for these modes. The value is negligible in comparison to flexural stresses but not zero. For mode-6, there is a significance difference in the unit amplitude flexural stress as compared to Igeh [24]. This corresponds well with the difference in normalized displacement observed earlier.

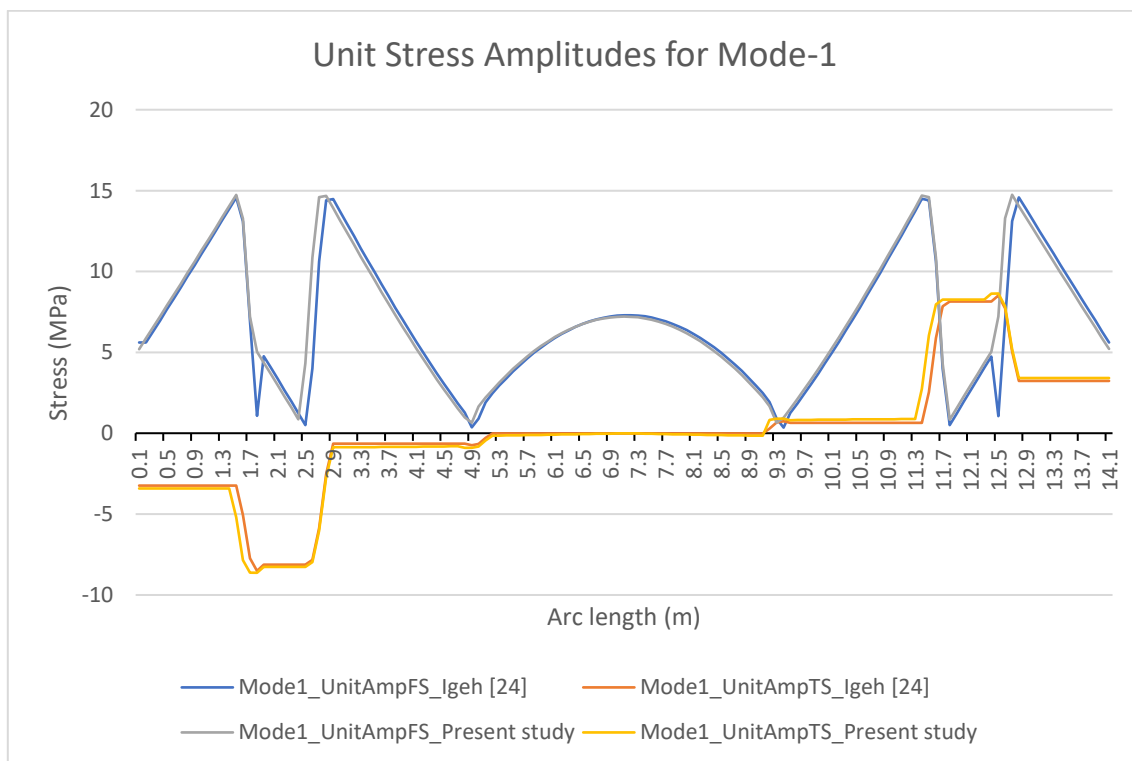


Figure 5-41: Comparison of unit amplitude stress with Igeh [24] for Mode-1

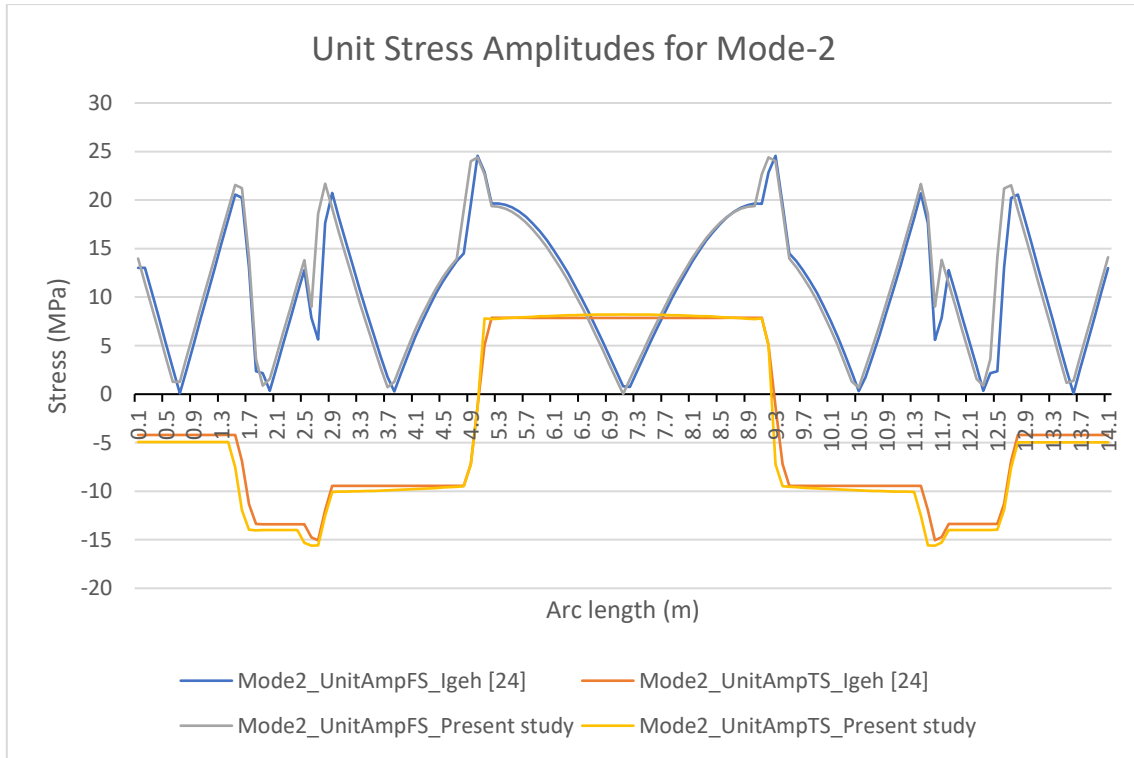


Figure 5-42: Comparison of unit amplitude stress with Igeh [24] for Mode-2

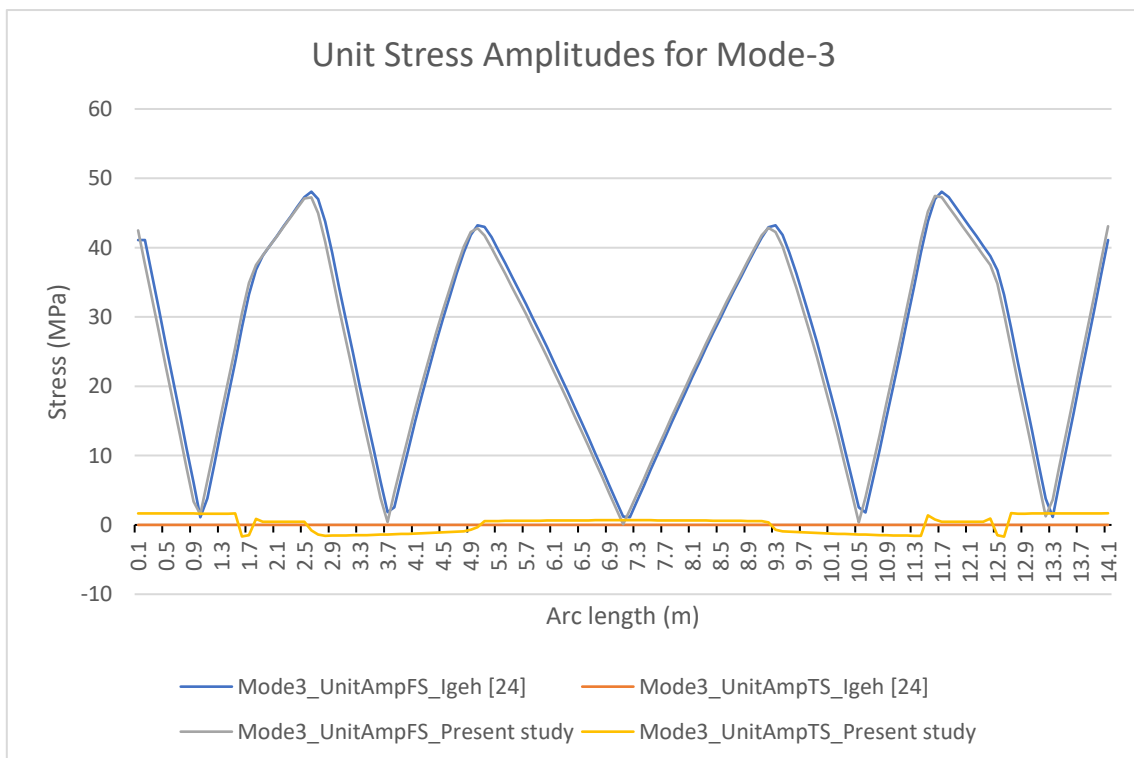


Figure 5-43: Comparison of unit amplitude stress with Igeh [24] for Mode-3

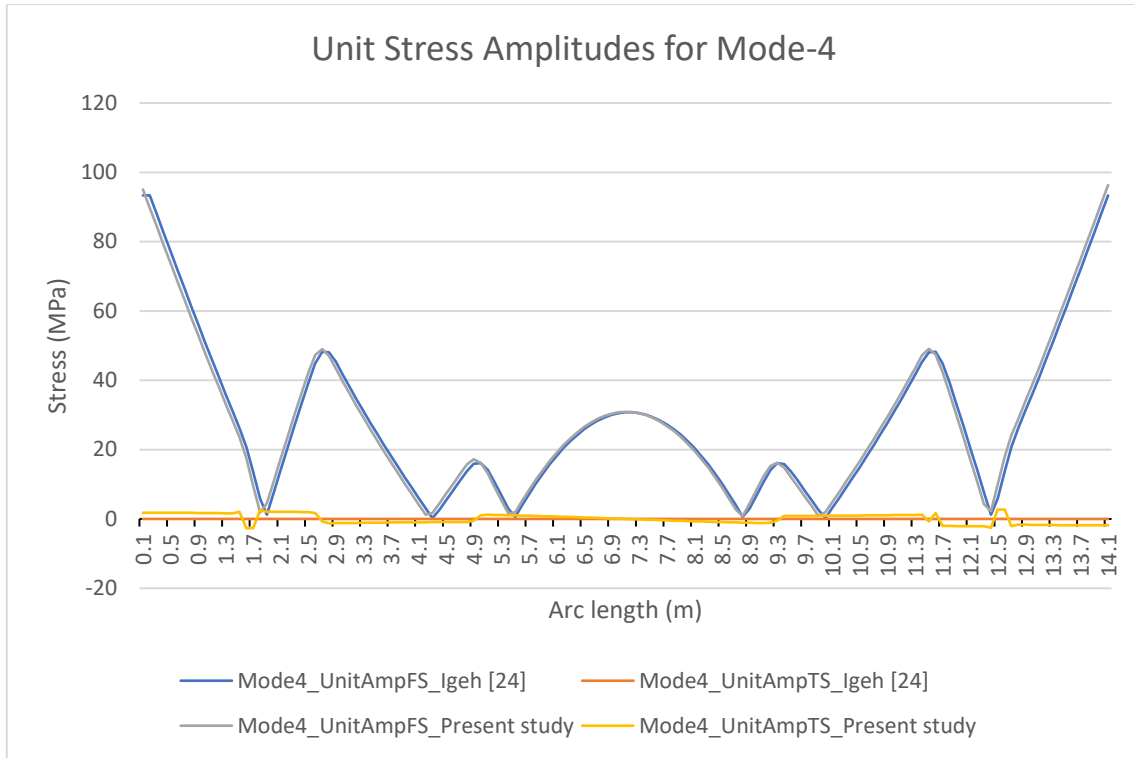


Figure 5-44: Comparison of unit amplitude stress with Igeh [24] for Mode-4

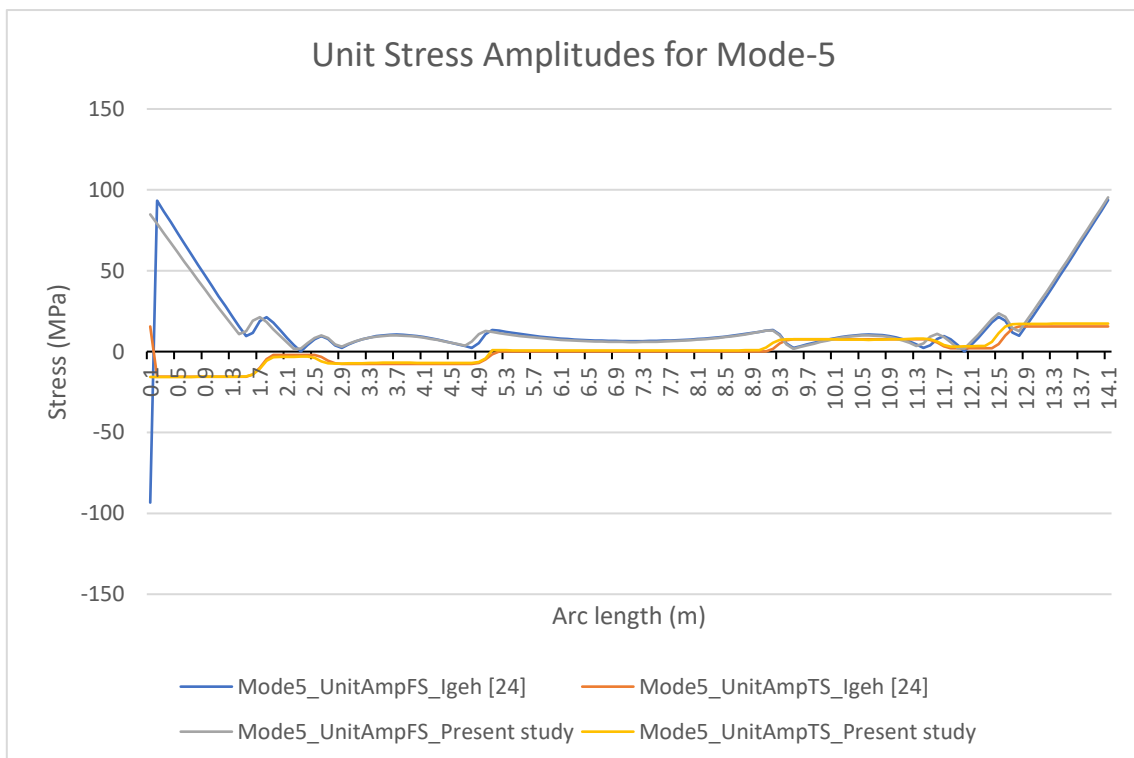


Figure 5-45: Comparison of unit amplitude stress with Igeh [24] for Mode-5

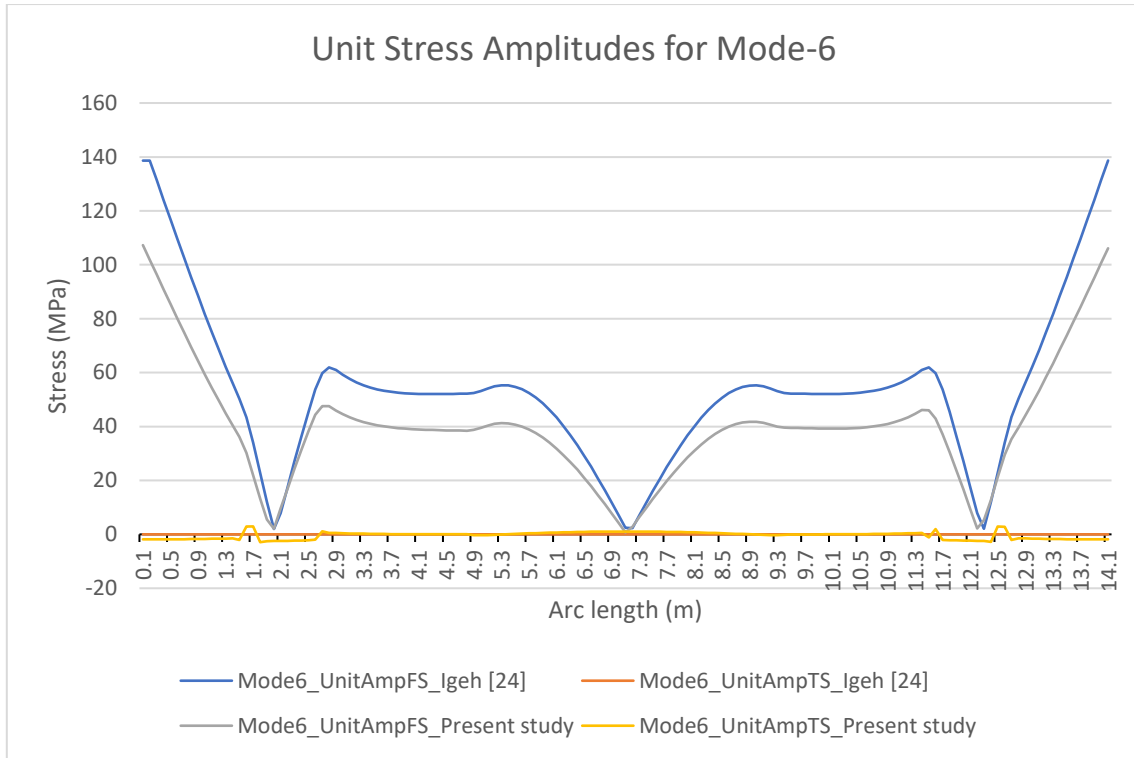


Figure 5-46: Comparison of unit amplitude stress with Igeh [24] for Mode-6

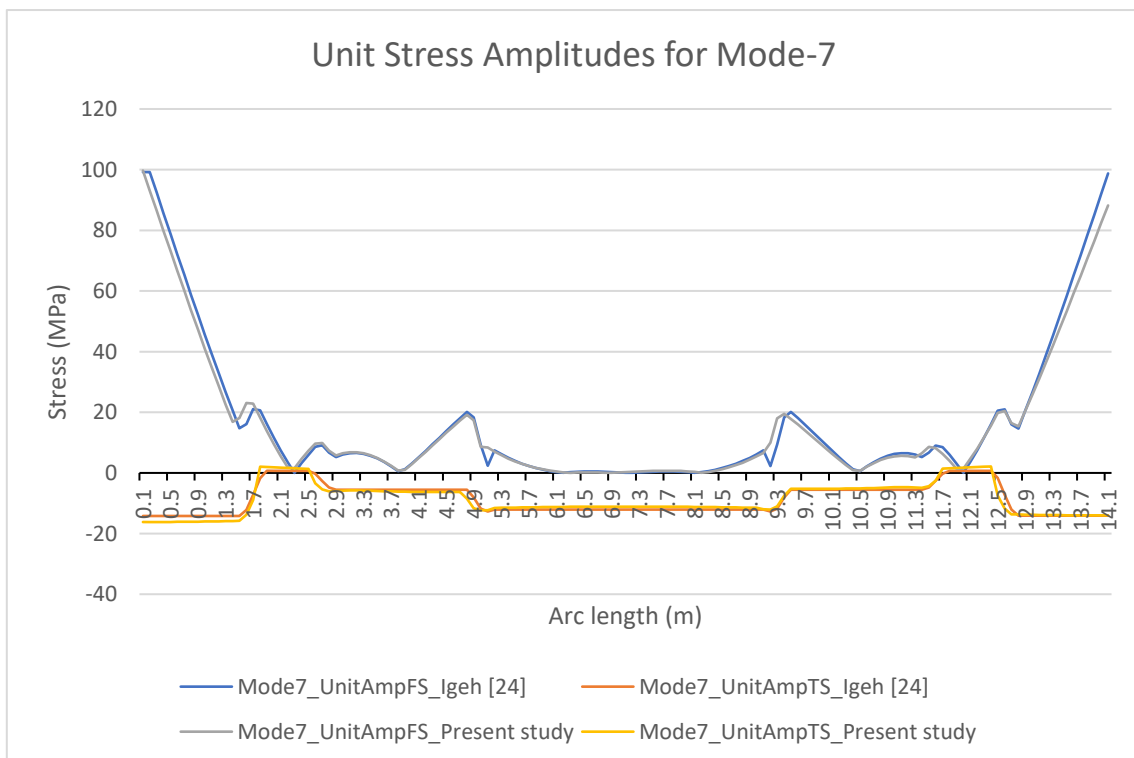


Figure 5-47: Comparison of unit amplitude stress with Igeh [24] for Mode-7

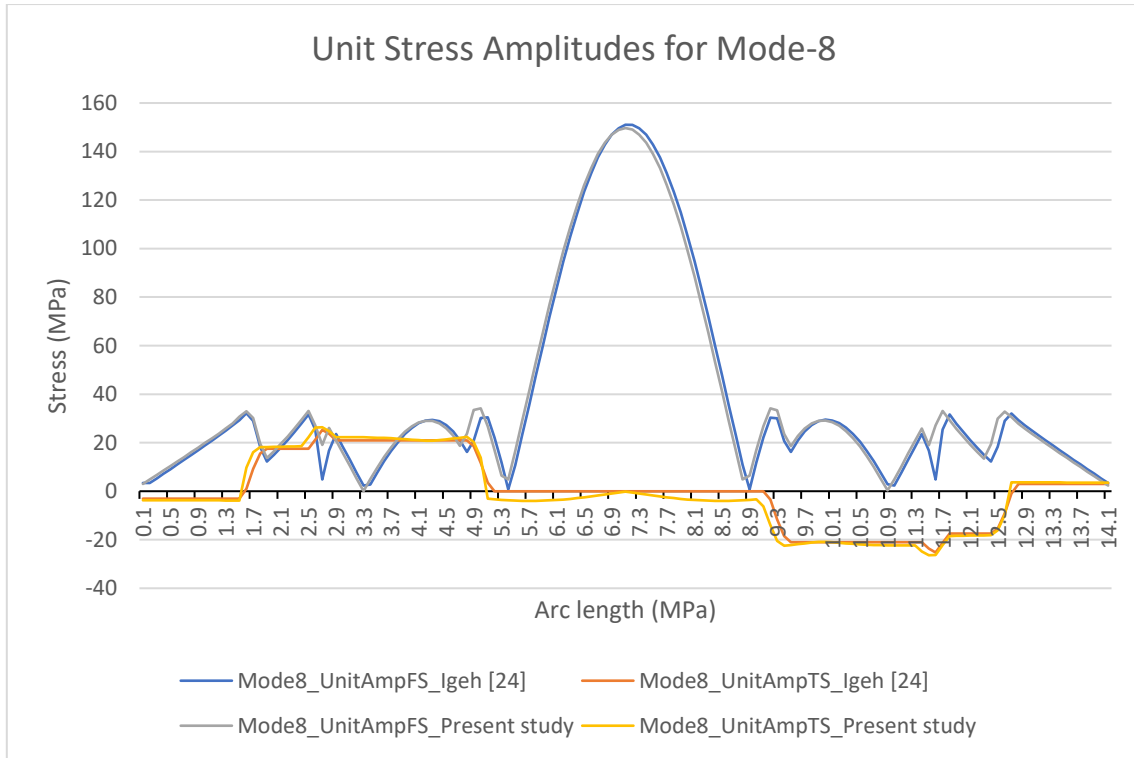


Figure 5-48: Comparison of unit amplitude stress with Igeh [24] for Mode-8

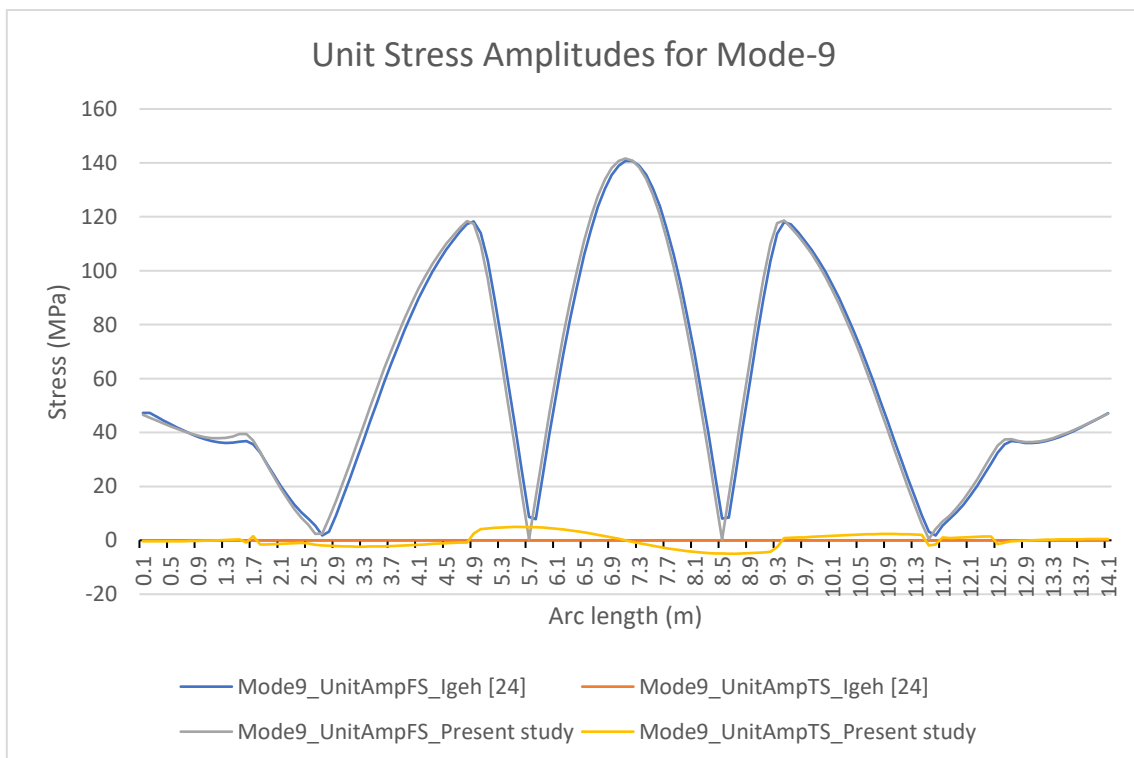


Figure 5-49: Comparison of unit amplitude stress with Igeh [24] for Mode-9

The flexural and torsional unit stress amplitudes from all modes are presented in Figure 5-17 and Figure 5-18. It may be observed that Mode-8 gives the largest flexural and torsional unit stress amplitudes as shown in Figure 5-50 and Figure 5-51.

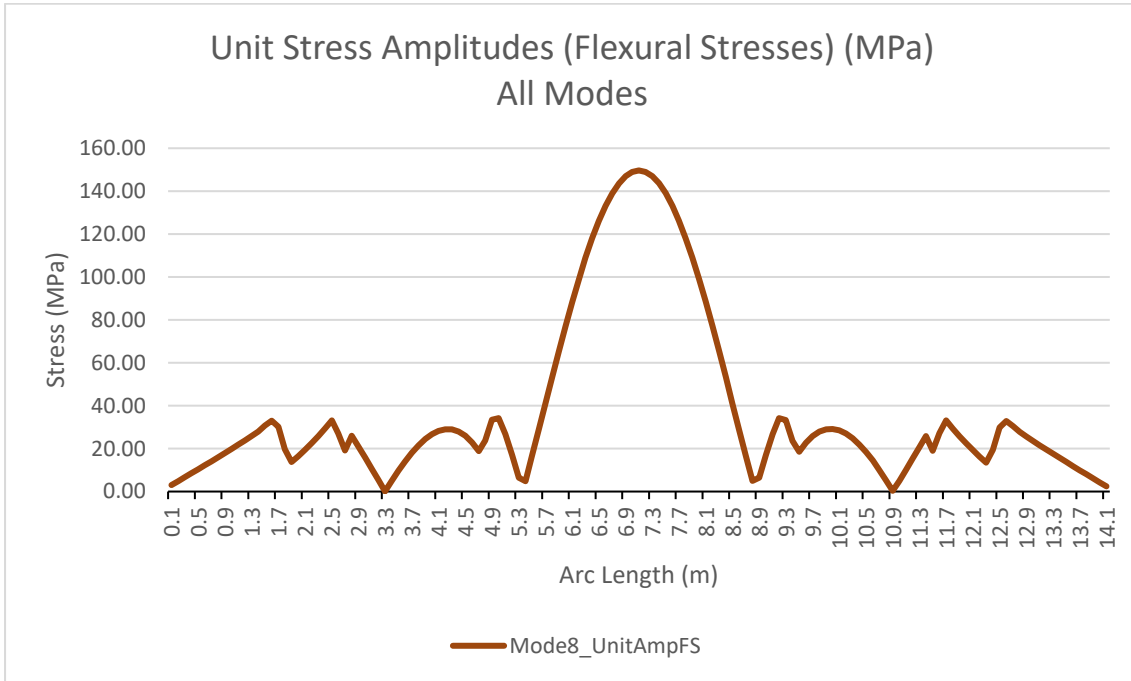


Figure 5-50: Unit amplitude stress (Flexural) for Mode-8

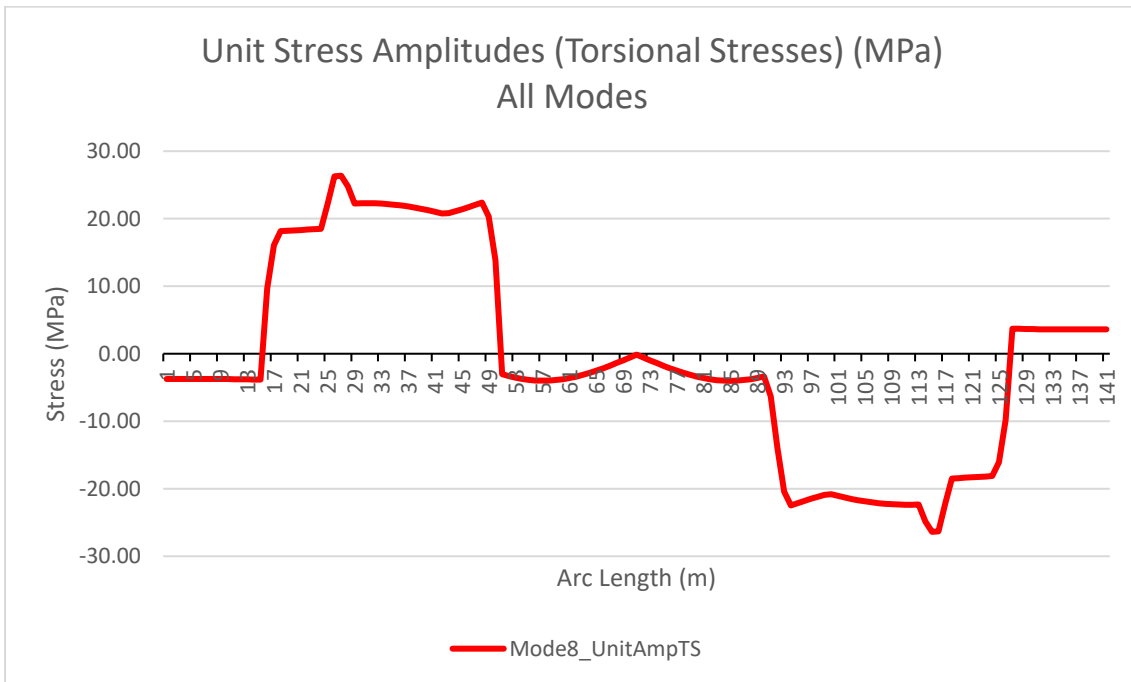


Figure 5-51: Unit amplitude stress (Torsional) for Mode-8

Modes are classified into cross-flow and in-line for 10° and 90° flow as shown in Table 5-6. For 10° flow, all modes are considered as both in-line and cross-flow modes. Figure 5-52, Figure 5-53, Figure 5-54 and Figure 5-24 show the IL and CF modes for 10° and 90° flow orientations.

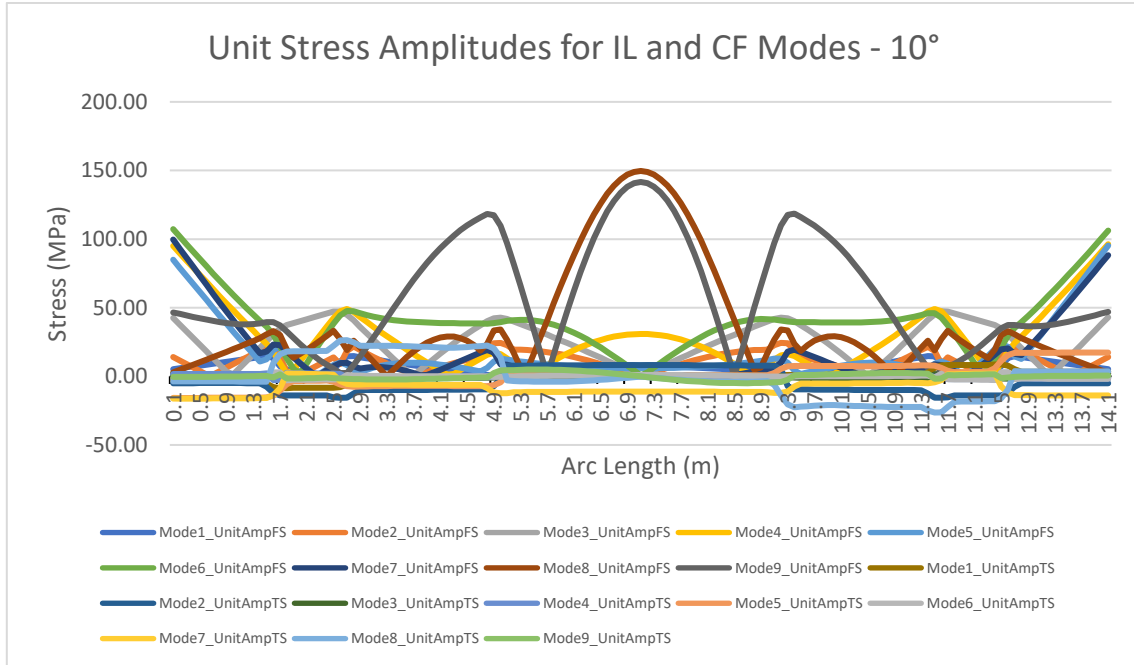


Figure 5-52: Unit amplitude stress (Flexural and Torsional) for 10° IL and CF modes

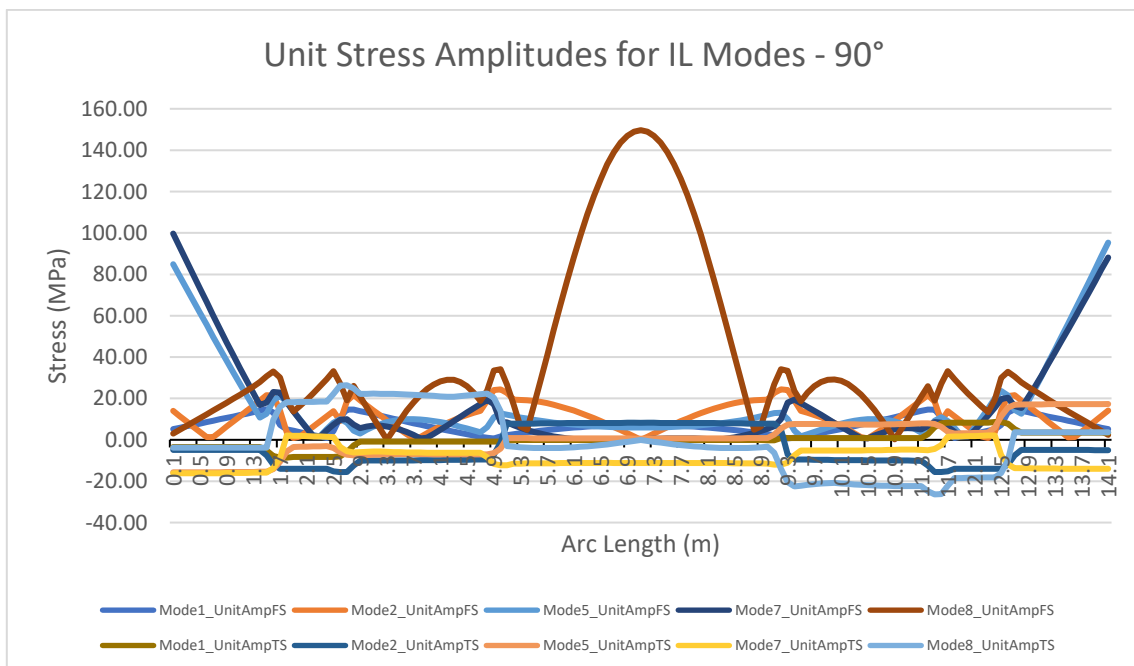


Figure 5-53: Unit amplitude stress (Flexural and Torsional) for 90° IL modes

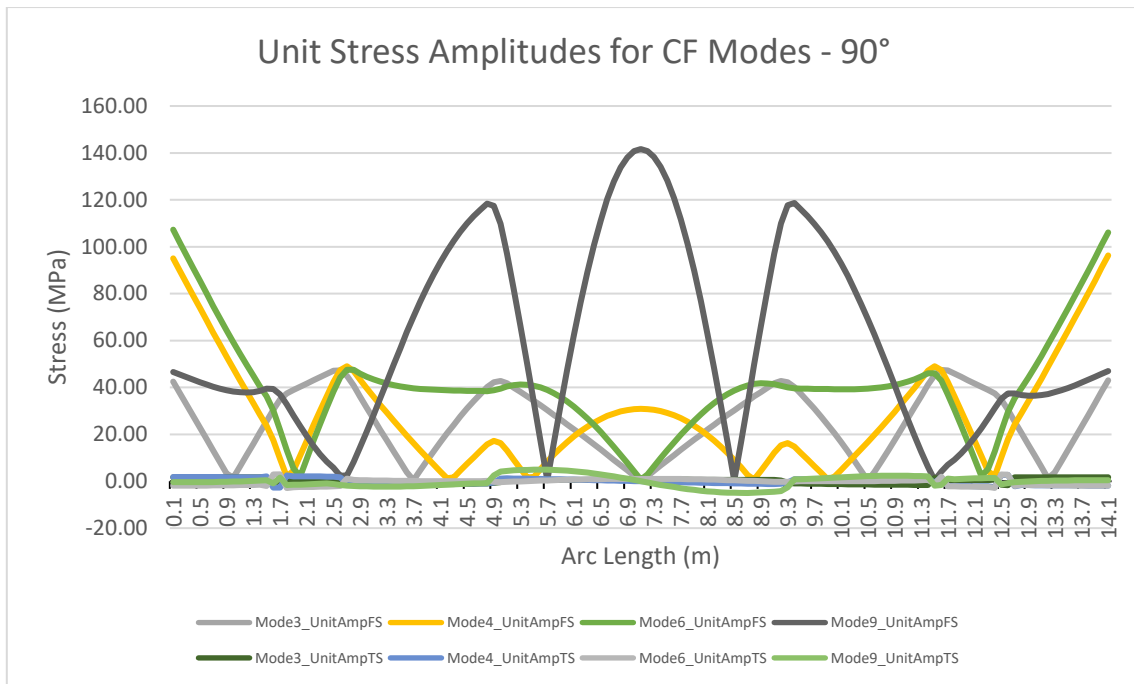


Figure 5-54: Unit amplitude stress (Flexural and Torsional) for 90° CF modes

5.6.3 Selection of Critical location

In the absence of any guidance on selection of critical location for fatigue assessment in DNVGL-RP-F105 (2017 edition) [11], design assessment module of Ansys Mechanical Workbench is in this study used to combine the unit amplitude flexural and torsional stresses for the applicable modes in 10° and 90° cross-flow and in-line modes along the whole arc length of the rigid jumper. Location A is selected as the location with the highest combined unit amplitude flexural stress and Location B is selected as the location for the highest combined unit amplitude torsional stress.

Design assessment results for all cases are presented in section 5.5.1, 5.5.2 and 5.5.3.

In all cases, the maximum combined flexural stress always occurs near the fixed supports. In case of combined torsional stresses, the maximum is seen near the last bend on the rigid jumper along the arc length for 10° IL and CF case as well as the 90° IL case. But for the 90° CF case, we see that the location of maximum combined torsional stresses is near the third bend of the spool jumper along the arc length.

A combined mode shape showing the location on the rigid jumper model can be seen in design assessment module (See Figure 5-25, Figure 5-27, Figure 5-29 and Figure 5-31).

This approach is different from the one followed by Igeh [24] where she considered two locations for each orientation of current flow. In Igeh [24], for 10° flow, location of maximum flexural modal stress from IL mode gives Location A and maximum flexural and torsional modal stresses from CF mode gives Location B. For 90° flow, maximum flexural modal stress from IL mode gives Location C and maximum torsional modal stress from IL mode gives Location B. These locations are selected simply based on visual inference from modal stress graphs.

Table 5-11: Comparison of critical location for 10° and 90° in-line and cross-flow cases (measured from left fixed end of rigid jumper) with Igeh [24]

Case	Location A		Location B	
	Igeh [24]	Kapoor	Igeh [24]	Kapoor
10° IL	Middle of jumper (6.98m)	Left end of jumper (0.1 m)	Right end of jumper (13.95m)	Start of first bend of jumper (1.5 m)
10° CF	Middle of jumper (6.98m)	Left end of jumper (0.1 m)	Right end of jumper (13.95m)	Start of first bend of jumper (1.5 m)
90° IL	Left end of jumper (0.1m)	Left end of jumper (0.1 m)	Right end of jumper (13.95m)	Start of first bend of jumper (1.5 m)
90° CF	Left end of jumper (0.1m)	Right end of jumper (14m)	Right end of jumper (13.95m)	End of third bend of jumper (5.7 m)

Table 5-11 compares the selection of critical location in this study with Igeh [24]. From the above table we see that not all critical locations determined in this study and Igeh [24] are same. For 10° IL and CF case, the difference is due to IL and CF mode classification. While Igeh [24] takes Mode-1,2 and 5 as CF modes and Mode-3,4,6 and 9 as IL modes, this study considers all modes (1 to 9) to be both IL as well as CF. Hence, the location for maximum flexural stress is determined in this study based on the contribution of all modes in CF and IL directions. For 90° IL case, we see that Location A is determined same for both studies i.e. left end of the jumper while Location B is different. For 90° CF case, though location A is determined to be different, we can see from Figure 5-28 that the difference between combined flexural modal stress at left end and right end of the jumper is negligible. Hence, we can say that Location A

for 90° CF case is similar and fatigue results can be compared at this location between this study and Igeh [24].

6 RESPONSE MODEL

Response model for in-line and cross-flow response at 10° flow and 90° flow are constructed in line with the requirements of DNVGL-RP-F105 (2017 edition) [11] according to the methodology given in Section 4.4.

Design value of reduced velocity is calculated using the formulas given in Section 1. Reduction in flow velocity due to angle of attack are not considered for the 10° flow as all modes are excited for both in-line and cross-flow conditions. For 90° flow, full value of current velocity is used as the current velocity is normal to the rigid jumper at along the whole arc length.

Flow velocity range is selected for each case in accordance with the range provided in Zheng et al. [51].

Table 6-1: Flow velocity range for different cases

S. No.	Case	Velocity range (Based on Zheng et al. [51])
1	10° Flow – In-line	0.05 m/s – 0.98 m/s
2	10° Flow – Cross-flow	0.05 m/s – 0.98 m/s
3	90° Flow – In-line	0.05 m/s – 0.75 m/s
4	90° Flow – Cross-flow	0.05 m/s – 0.75 m/s

For sensitivity purposes, an increment of 0.01m/s is considered between each velocity.

6.1 In-line response model

The in-line response model is constructed for the rigid jumper according to the methodology given in Section 4.4.3.

6.1.1 10° Flow

The parameters used construction of 10° in-line response model is presented in Table 6-2 while the hydrodynamic parameters calculated based on these are presented in Table 6-3.

Table 6-2: Parameters for 10° Flow in-line response model

Parameter	Value	Unit	Remarks
ζ_{str}	0.01	-	
ζ_{soil}	0	-	
ζ_{hyd}	0	-	
ζ_{total}	0.01	-	
γ_k	1.3	-	
γ_f	1.15	-	
$\gamma_{on,il}$	1.1	-	
ρ	1027	kg/m ³	
D	0.0605	m	
C_a	1.0	-	$C_a=1$ for $e/D \geq 0.8$ based on section 6.6.7 of F105 (2017 edition)
I_c	5	%	5% assumed based on 3.2.12 of DNV-RP-F105
Θ_{rel}	10	°	
	0.17453	radians	
M_{st+M_c}	6.879	kg/m	From model test data
M_a	$\frac{2.95237}{2}$	kg/m	Calculated from 5.4.3 of DNV-RP-F105
M_e	$\frac{9.83137}{2}$	kg/m	$M_e = M_{st+M_c} + M_a$

Table 6-3: Calculated parameters for 10° Flow in-line response model

Parameter	Value	Unit	Remarks
K_s	0.164328	-	
K_{sd}	0.126407	-	
$R_{i\theta,1}$	0.738659	-	
$R_{i\theta,2}$	0.882353	-	
$A_{y,1}/D$	0.161039	-	
$A_{y,2}/D$	0.120871	-	
$V_{r,onset}^{IL}$	1.04545	-	
$V_{r,1}^{IL}$	2.41341	-	
$V_{r,2}^{IL}$	4.81341	-	
$V_{r,end}^{IL}$	5.05871	-	

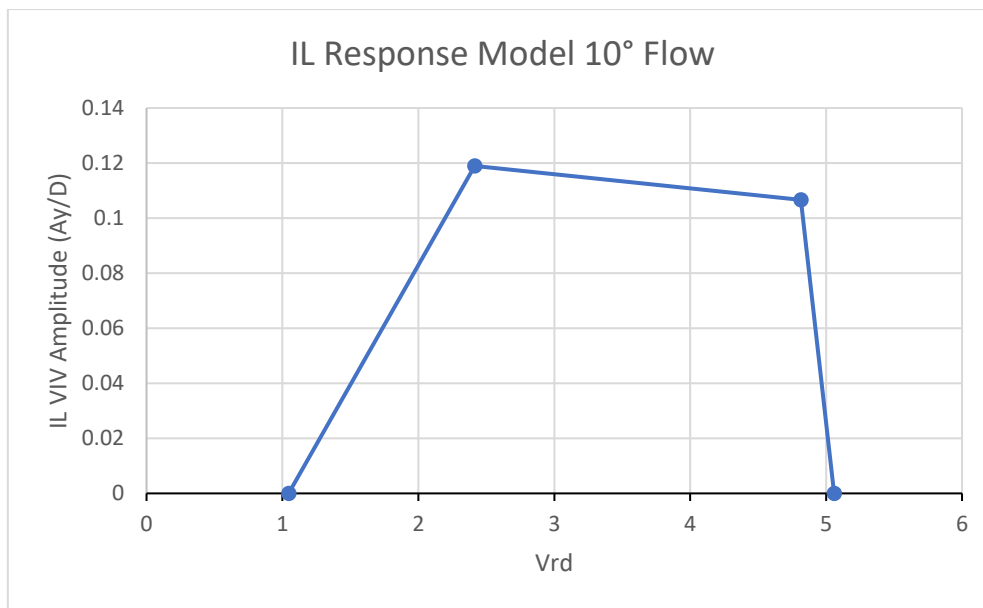


Figure 6-1: In-line response model for 10° Flow

6.1.2 90° Flow

The parameters used construction of 90° ° in-line response model are presented in Table 6-4 while the hydrodynamic parameters calculated based on these are presented in Table 6-5.

Table 6-4: Parameters for 90° Flow in-line response model

Parameter	Value	Unit	Remarks
ζ_{str}	0.01	-	
ζ_{soil}	0	-	
ζ_{hyd}	0	-	
ζ_{total}	0.01	-	
γ_k	1.3	-	
γ_f	1.15	-	
$\gamma_{on,il}$	1.1	-	
ρ	1027	kg/m ³	
D	0.0605	m	
C_a	1.0	-	$C_a=1$ for $e/D \geq 0.8$ based on section 6.6.7 of F105 (2017 edition)
I_c	5	%	5% assumed based on 3.2.12 of DNV-RP-F105
Θ_{rel}	90	°	
	1.57	radians	
$M_{st}+M_c$	6.879	kg/m	From model test data
M_a	2.95	kg/m	Calculated from 5.4.3 of DNV-RP-F105
M_e	9.83	kg/m	$M_e = M_{st}+M_c+M_a$

Table 6-5: Calculated parameters for 90° Flow in-line response model

Parameter	Value	Unit	Remarks
K_s	0.16	-	
K_{sd}	0.12	-	
$R_{i\theta,1}$	1	-	
$R_{i\theta,2}$	0.88	-	
$A_{y,1}/D$	0.11	-	
$A_{y,2}/D$	0.10	-	
$V_{r,onset}^{IL}$	1.04	-	
$V_{r,1}^{IL}$	2.41	-	
$V_{r,2}^{IL}$	4.81	-	
$V_{r,end}^{IL}$	5.05	-	

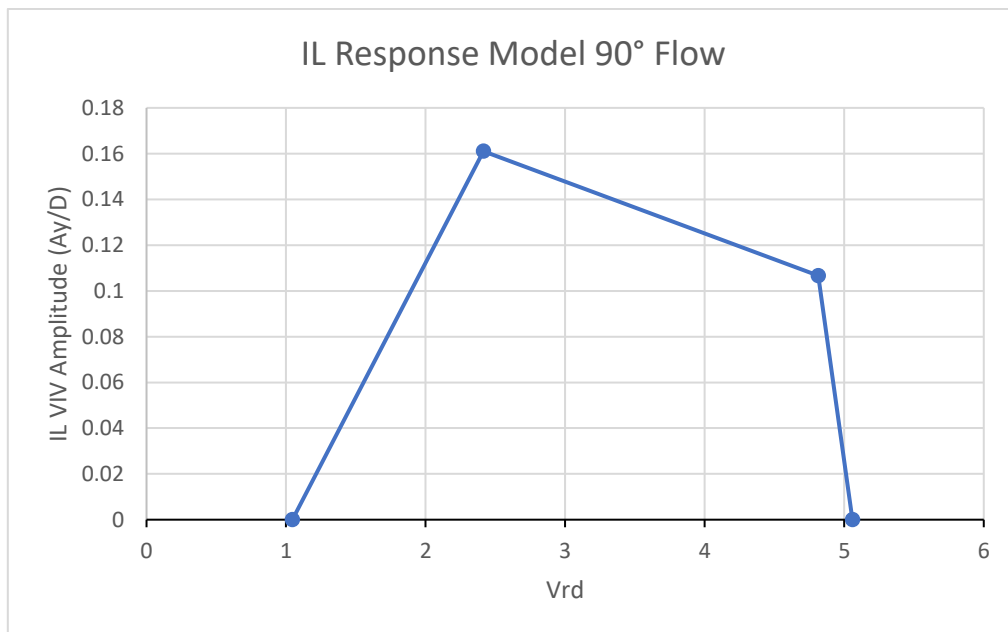


Figure 6-2: In-line response model for 90° Flow

6.2 Cross-flow response model

The cross-flow response model is constructed for the rigid jumper according to the methodology given in Section 4.4.4.

6.2.1 10° Flow

The parameters used construction of 10° ° cross-flow response model is presented in Table 6-6. Table 6-6 while the hydrodynamic parameters calculated based on these are presented in Table 6-7.

Table 6-6: Parameters for 10° Flow cross-flow response model

Parameter	Value	Unit	Remarks
ζ_{str}	0.01	-	
ζ_{soil}	0	-	
ζ_{hyd}	0	-	
ζ_{total}	0.01	-	
γ_k	1.3	-	
γ_f	1.15	-	
$\gamma_{on,cf}$	1.2	-	
ρ	1027	kg/m ₃	
D	0.0605	m	
C_a	1.0	-	$C_a=1$ for $e/D \geq 0.8$ as per section 6.6.7 of F105 (2017 edition)
α	1	-	
f_{ratio}	1.11	-	

Table 6-7: Calculated parameters for 10° Flow cross-flow response model

Parameter	Value	Unit	Remarks
$\Psi_{proxi,onset}$	1	-	
$\Psi_{trench,onset}$	1	-	
$A_{z,1}/D$	0.9	-	
$A_{z,2}/D$	0.9	-	
$V_{r,onset}^{CF}$	2.5	-	
$V_{r,1}^{CF}$	5.43	-	
$V_{r,2}^{CF}$	11.15	-	
$V_{r,end}^{CF}$	16	-	

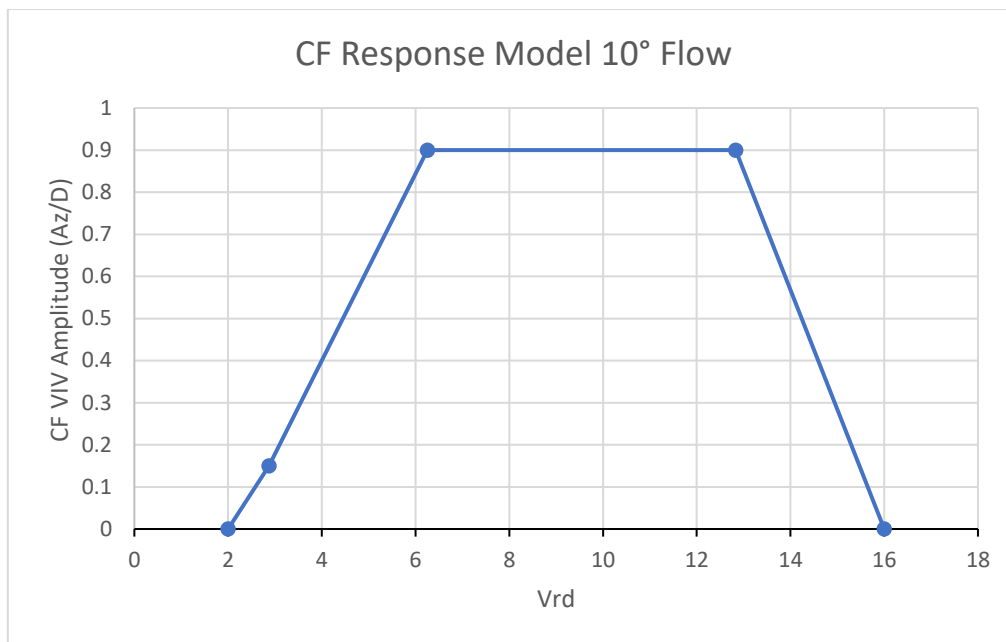


Figure 6-3: Cross-flow response model for 10° Flow

6.2.2 90° Flow

The parameters used construction of 90° ° cross-flow response model is presented in Table 6-8 while the hydrodynamic parameters calculated based on these are presented in Table 6-9.

Table 6-8: Parameters for 90° Flow cross-flow response model

Parameter	Value	Unit	Remarks
ζ_{str}	0.01	-	
ζ_{soil}	0	-	
ζ_{hyd}	0	-	
ζ_{total}	0.01	-	
γ_k	1.3	-	
γ_f	1.15	-	
$\gamma_{on,cf}$	1.2	-	
ρ	1027	kg/m ³	
D	0.0605	m	
C_a	1.0	-	$C_a=1$ for $e/D \geq 0.8$ based on section 6.6.7 of F105 (2017 edition)
α	1	-	
f_{ratio}	1.15	-	

Table 6-9: Calculated parameters for 90° Flow cross-flow response model

Parameter	Value	Unit	Remarks
$\Psi_{\text{proxi,onset}}$	1	-	
$\Psi_{\text{trench,onset}}$	1	-	
$A_{z,1}/D$	0.9	-	
$A_{z,2}/D$	0.9	-	
$V_{r,\text{onset}}^{CF}$	2.5	-	
$V_{r,1}^{CF}$	5.43	-	
$V_{r,2}^{CF}$	11.15	-	
$V_{r,\text{end}}^{CF}$	16	-	

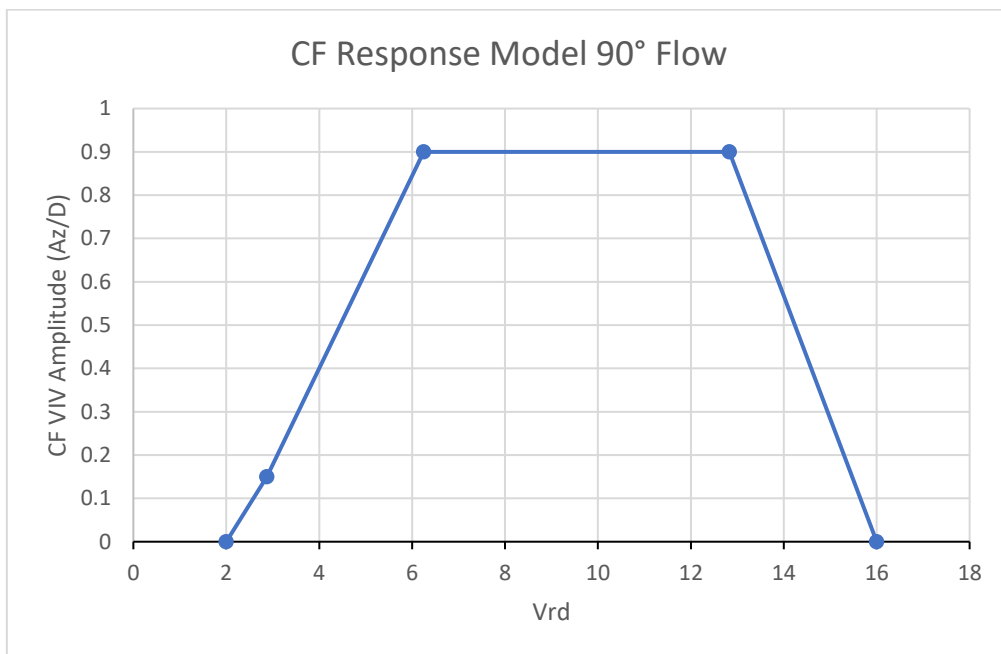


Figure 6-4: Cross-flow response model for 90° Flow

6.3 Mode classification based on multimode response

According to Section 4.3.1 there are four possible cases for which mode classification based on multimode response needs to be done. The cases are presented as follows:

1. For 10° flow
 - a. IL
 - b. CF

2. For 90° flow
 - a. IL
 - b. CF

6.3.1 Active modes

Based on the response models for all four cases, different modes become active at different flow velocities as shown in Table 6-10.

Table 6-10: Flow velocity range for modes to be classified as active modes

Modes	Flow velocity range for active modes			
	10° Flow		90° Flow	
	IL	CF	IL	CF
1	0.05 – 0.22	0.1 – 0.71	0.05 – 0.22	N/A
2	0.13 – 0.59	0.24 – 0.98	0.13 – 0.59	N/A
3	0.14 – 0.60	0.25 – 0.98	N/A	0.25 – 0.75
4	0.16 – 0.70	0.29 – 0.98	N/A	0.29 – 0.75
5	0.21 – 0.91	0.37 – 0.98	0.2 -0.75	N/A
6	0.22 – 0.98	0.41 – 0.98	N/A	0.41 – 0.75
7	0.23 – 0.98	0.42 – 0.98	0.22 – 0.75	N/A
8	0.38 – 0.98	0.69 – 0.98	0.37 – 0.75	N/A
9	0.42 – 0.98	0.77 – 0.98	N/A	0.77 – 0.75

6.3.2 Participating modes

Participating modes are determined for all locations on the rigid jumper based on the criteria given in Section 4.3.1. The criterion is based on the unit amplitude stresses calculated from the modal stress analysis.

Mode participation is then checked for the critical locations (A and B). If the mode is participating at the critical location, it may be contributing, else, the unit stress amplitude for that mode at that critical location is considered as zero as the mode is non-participating.

An example for Case-1 (a) (b) -10° Flow – IL and CF (Case – 1 from Table 5-7) is discussed below in detail. Same procedure is followed for Case -2 (a) (b).

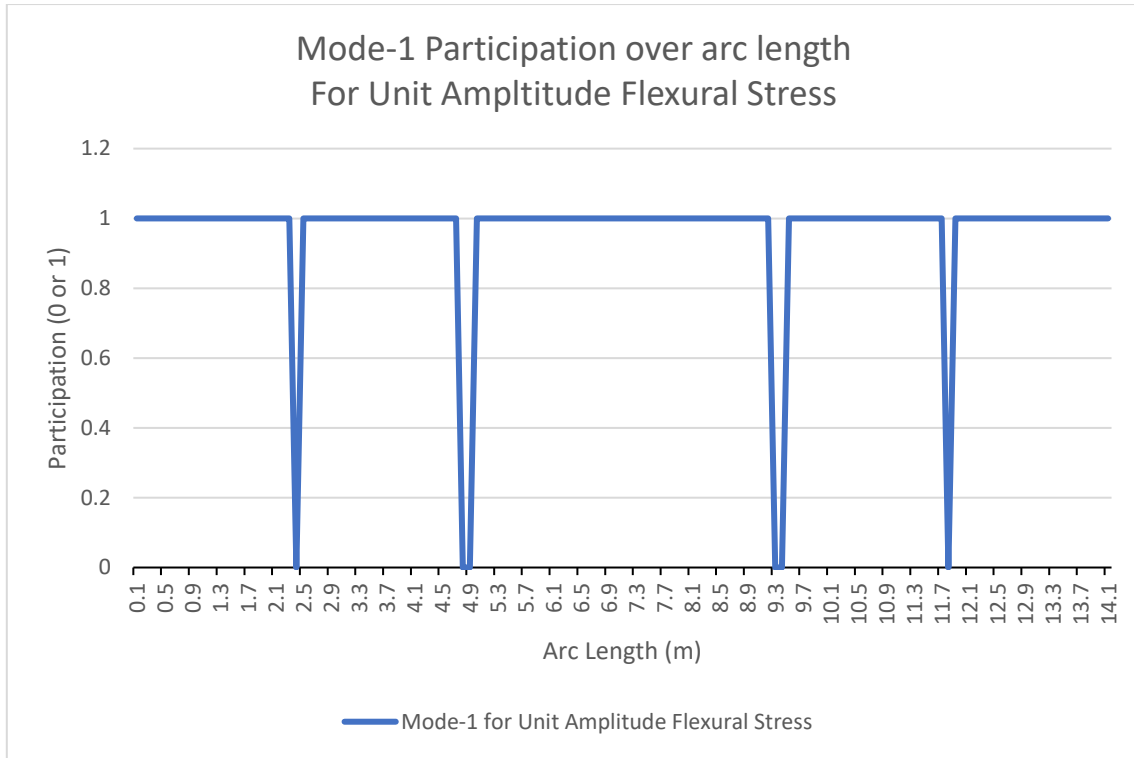


Figure 6-5: Mode-1 participation along the rigid jumper arc length towards unit amplitude flexural stress for 10° flow (In-line and Cross-flow)

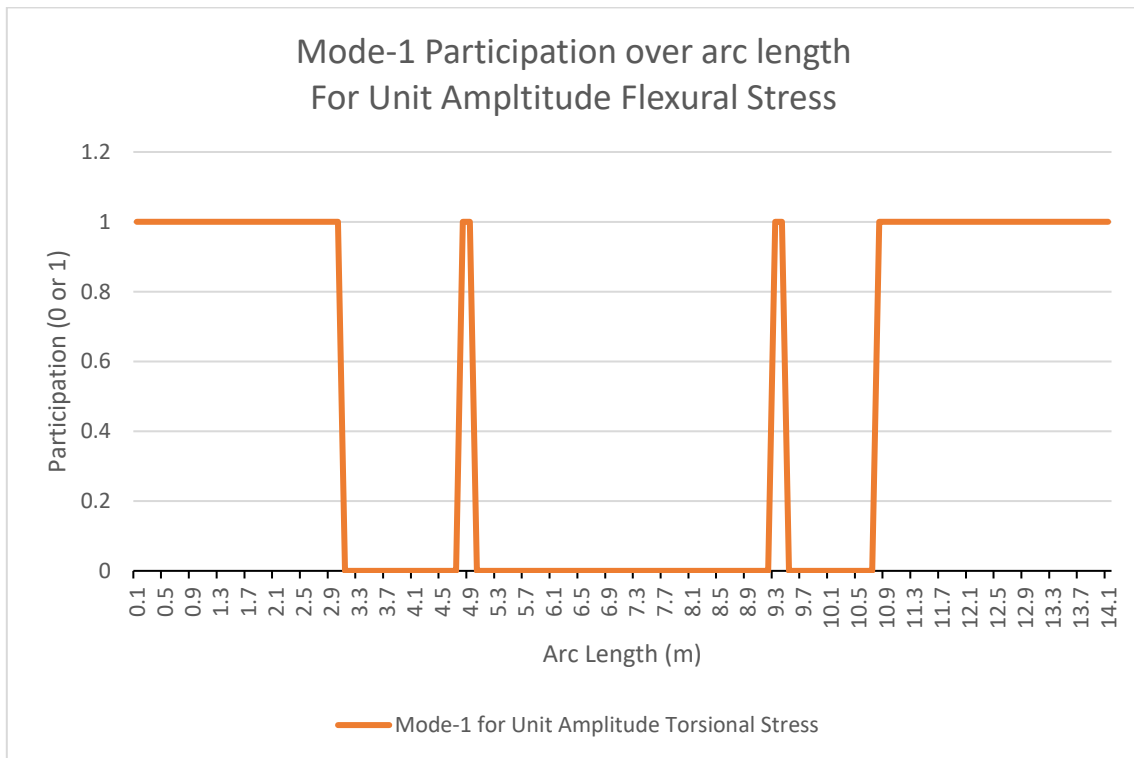


Figure 6-6: Mode-1 participation along the rigid jumper arc length towards unit amplitude torsional stress for 10° flow (In-line and Cross-flow)

Figure 6-5 and Figure 6-6 show the participation of mode-1 toward unit amplitude flexural and torsional stress for 10° flow (in-line and cross-flow) case. “0” represents non-participation while “1” represents participation of mode-1. Same procedure is followed to check the participation of all in-line and cross-flow modes along the rigid jumper arc length.

The participation of a mode at the critical locations (A and B) is of our interest to determine the modes which may be considered as contributing to the stress range and hence to fatigue damage. Therefore, participation of all modes (in-line and cross-flow) is checked at the critical location.

Table 6-11 shows the participation of modes (1-9) for 10° flow (in-line and cross-flow) at critical locations A and B.

Table 6-11: Participating Modes for 10° Flow – In-line and cross-flow case at the critical locations A and B

Mode	Location A		Location B	
	For Unit Amplitude Flexural Stress	For Unit Amplitude Torsional Stress	For Unit Amplitude Flexural Stress	For Unit Amplitude Torsional Stress
M1	1	1	1	1
M2	1	1	1	1
M3	1	1	1	1
M4	1	1	1	1
M5	1	1	1	1
M6	1	1	1	1
M7	1	1	1	1
M8	0	1	1	1
M9	1	0	1	0

The participating modes are determined over the arc length of the rigid jumper within the participating interval. Since fatigue assessment is to be done on the critical locations, the participation of IL and CF modes for 10° and 90° flow is determined. For the 10° IL and CF modes, we see from Table 6-11 that Mode 8 does not participate at Location A for flexural stress range while Mode 9 does not contribute for torsional stress range at Location A and B.

6.3.3 Contributing modes

According to Section 2 all participating modes are considered as contributing modes. Therefore, modes which are non-participating at the critical locations for 10° flow (in-line and cross-flow) are considered non-contributing and not included in the stress range calculations.

Since all participating modes are considered as contributing according to Section 2, stress range for all participating modes is calculated at the Critical Location A and B

6.4 Discussion

6.4.1 Response Models

The response models for 10° and 90° IL and CF are presented in Figure 6-1, Figure 6-2, Figure 6-3 and Figure 6-4.

For the same value of $V_{rd} = 2.1$, 90° IL response model gives a higher amplitude (0.16) as compared to the 10° response model (0.12). This is because in the 90° case, the current velocities are perpendicular to all the segments of the rigid jumpers and all segments respond with the highest in-line amplitudes in the direction of the flow. For the 10° case, the horizontal segments will experience a reduced in-line amplitude deflection as the flow velocity is at a very acute angle (10°) to the pipe run.

The 10° and 90° cross flow response models are the same. The CF model is based primarily on the f_{ratio} which is calculated as 1.11 and 1.15. As both are below 1.5, the maximum amplitude calculated for CF response model is same and equal to 0.9.

For 10° and 90° flow, the IL response starts at V_{rd} of close to 1 while the CF response starts later when the V_{rd} has reached a value close to 2. For V_{rd} 1 to 2, only the IL modes are active and contributing to the stress. On the higher side, the IL response ends when the value of V_{rd} reached 5 while the CF response continues till V_{rd} of 16. Hence for V_{rd} 5 to 16, we have only the CF modes that are active and have the potential to contribute to the stress range. At $V_{rd} = 2.4$, we have the highest response in both IL and CF modes which shall have highest contribution to the stress range at the critical points A and B.

As shown in Table 6-10 different modes become active at different reduced velocities and are potential candidates to contribute to the stress range.

A comparison of IL and CF response models for 10° and 90° flow with Igeh [24] is presented in 9.2.1.

6.4.2 Mode classification

1. Active modes

From Table 6-10 it can be seen that; the higher modes are active at higher flow velocities. The IL response is only between reduced velocity of 1 to 5 and hence most of the IL modes do not contribute to the full extent of the velocity range. The CF response is between reduced velocity of 2 to 16 which gives a wider range than IL modes to be active and potentially participate in the stress range.

2. Participating modes

The participating modes are determined over the arc length of the rigid jumper within the participating interval. Figure 6-5 and Figure 6-6 show the participation of mode-1 over the arc length to flexural stress range and torsional stress range, respectively. Since fatigue assessment is carried out only at the critical locations A and B, the participation of IL and CF modes for 10° and 90° flow is determined at these locations. For the 10° IL and CF modes, we see from Table 6-11 that Mode 8 does not participate at Location A for flexural stress range while Mode 9 does not contribute for torsional stress range at Location A and B.

3. Contributing modes

Since all participating modes are considered as contributing according to Section 2 , stress range for all participating modes is calculated at the Critical Location A and B

7 STRESS RANGE

Stress range (flexural and torsional) and response frequencies are calculated for all cases of 10° flow (in-line and cross-flow) and 90° flow (in-line and cross-flow) based on DNVGL-RP-F105 (2017 edition) [11] according to the methodology described in Section 4.5 for the full range of flow velocities (see Table 6-1) at the critical locations (A and B).

Stress range is calculated at critical location (A and B) for the following cases:

1. 10° Flow
 - a. In-line
 - b. Cross-flow
2. 90° Flow
 - a. In-line
 - b. Cross-flow

For clarity, in this chapter, Stress range response frequency calculation for Case-1(a) - 10° flow (in-line) is explained. Other cases follow the same procedure. Results, along with relevant graphs and figures, are presented in Appendix A for all other cases.

7.1 Unit amplitude stress

Stress range is calculated for all contributing modes for the full range of current velocities for each case. Combined stress range is calculated as the root mean square value from stress ranges of each contributing mode for each value of current velocity.

For Case-1 (a) - 10° flow (in-line) described earlier, the unit amplitude stress (flexural and torsional stresses) for contributing modes at the critical locations (A and B) is determined from Table 6-11 and Table 5-8 by including only the contributing modes (same as participating modes for non-straight geometries).

Table 7-1 lists the unit amplitude stresses that are used for stress range calculation for Case-1(a).

Table 7-1: Unit amplitude stresses for 10° Flow – In-line case at the critical locations A and B (Contributing modes only)

Mode	Location A		Location B	
	Unit Amplitude Flexural Stress (MPa)	Unit Amplitude Torsional Stress (MPa)	Unit Amplitude Flexural Stress (MPa)	Unit Amplitude Torsional Stress (MPa)
M1	5.197323	-3.409989136	14.7351111	-5.20449383
M2	13.96223	-4.938925192	21.5596097	-7.54908338
M3	42.50068	1.671045974	25.5573489	1.66973568
M4	95.0455	1.8242565	23.6797	2.109514
M5	84.89315	-15.69053961	12.5520762	-15.4144354
M6	107.2808	-1.885925073	36.2178863	-2.05836376
M7	99.68952	-16.18519949	18.0565226	-16.1851995
M8	0	-3.72957446	30.7238913	-3.85849123
M9	46.57532	0	39.440555	0

7.2 Unit amplitude response

Unit amplitude response for Case-1 (a) obtained from the response model given in Section 6.1.1 based on Figure 6-1 for each contributing mode at each value of design reduced velocity (V_{rd}) as shown in Figure 7-1 below.

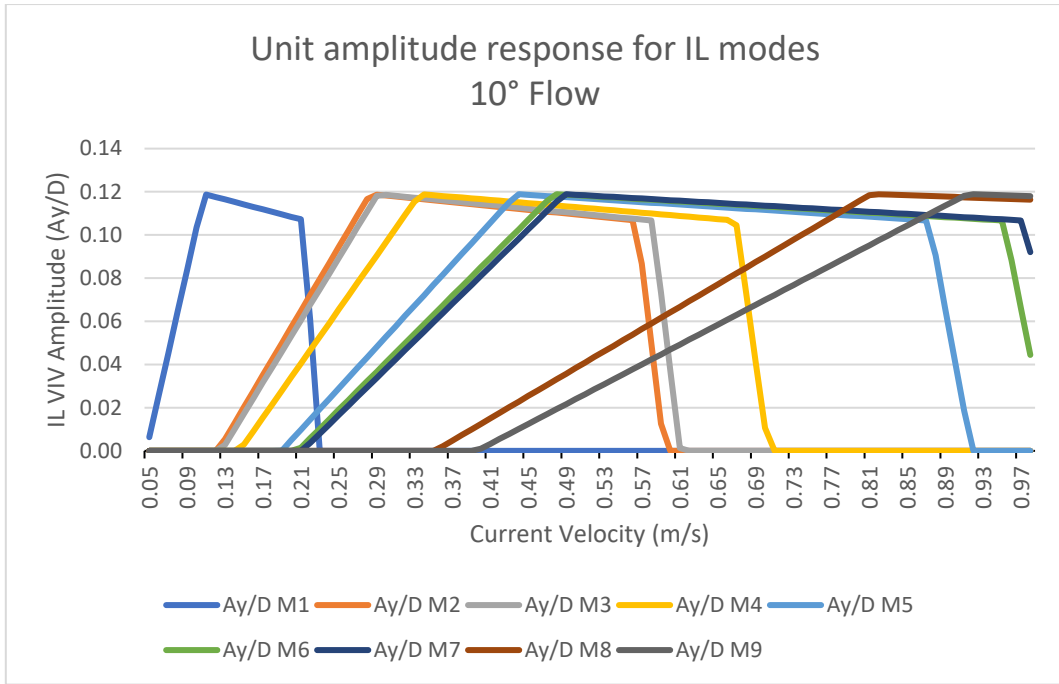


Figure 7-1: Unit amplitude response for contributing IL modes (Case-1(a) - 10° Flow)

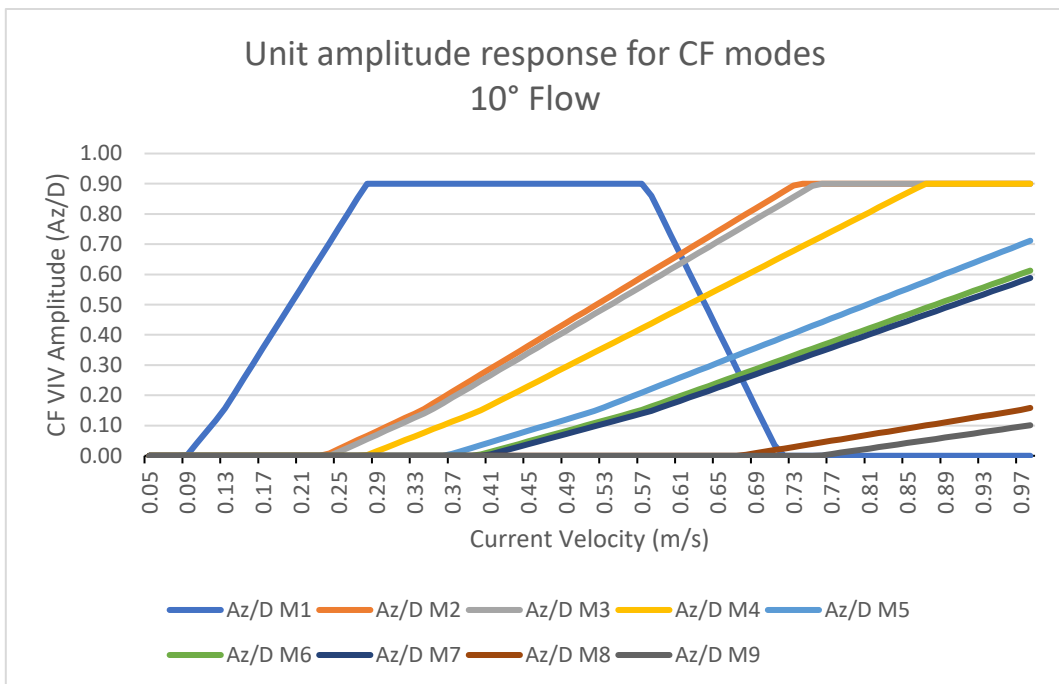


Figure 7-2: Unit amplitude response for contributing CF modes (Case-1(b) - 10° Flow)

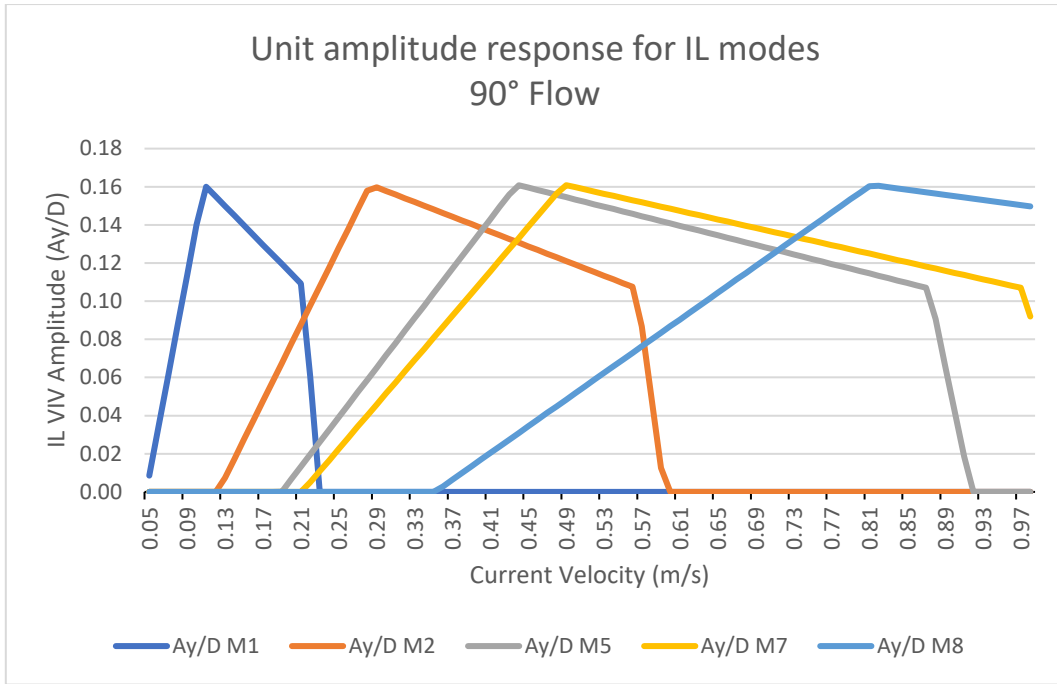


Figure 7-3: Unit amplitude response for contributing IL modes (Case-2(a) - 90° Flow)



Figure 7-4: Unit amplitude response for contributing CF modes (Case-2(b) - 90° Flow)

7.3 Stress range

Flexural and torsional stress range for each contributing mode for Case-1 (a) is calculated at location A and B using the unit stress amplitude from Table 7-1 and unit amplitude response from Figure 7-1.

Flexural and torsional stress range for contributing modes at Location A is show in Figure 7-5 and Figure 7-6 , respectively.

Flexural and torsional stress range for contributing modes at Location B is show in Figure 7-7 and Figure 7-8 , respectively.

Similar figures for all other cases can be found in section 13.

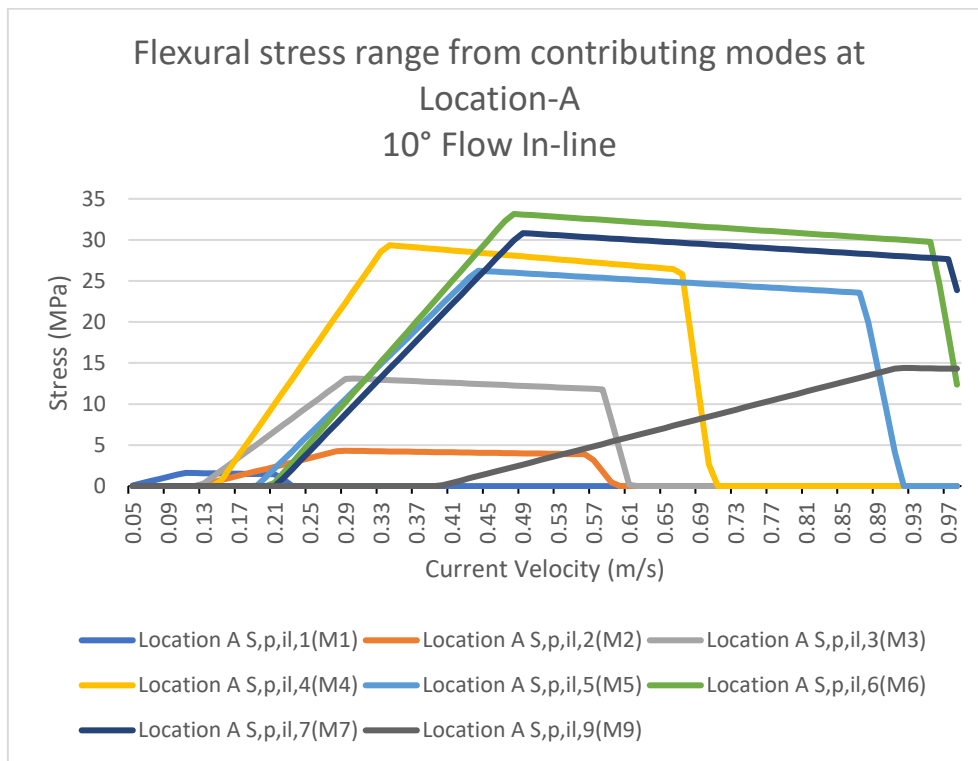


Figure 7-5: Flexural stress range for all contributing modes (Case-1(a) - 10° Flow IL) at Location A

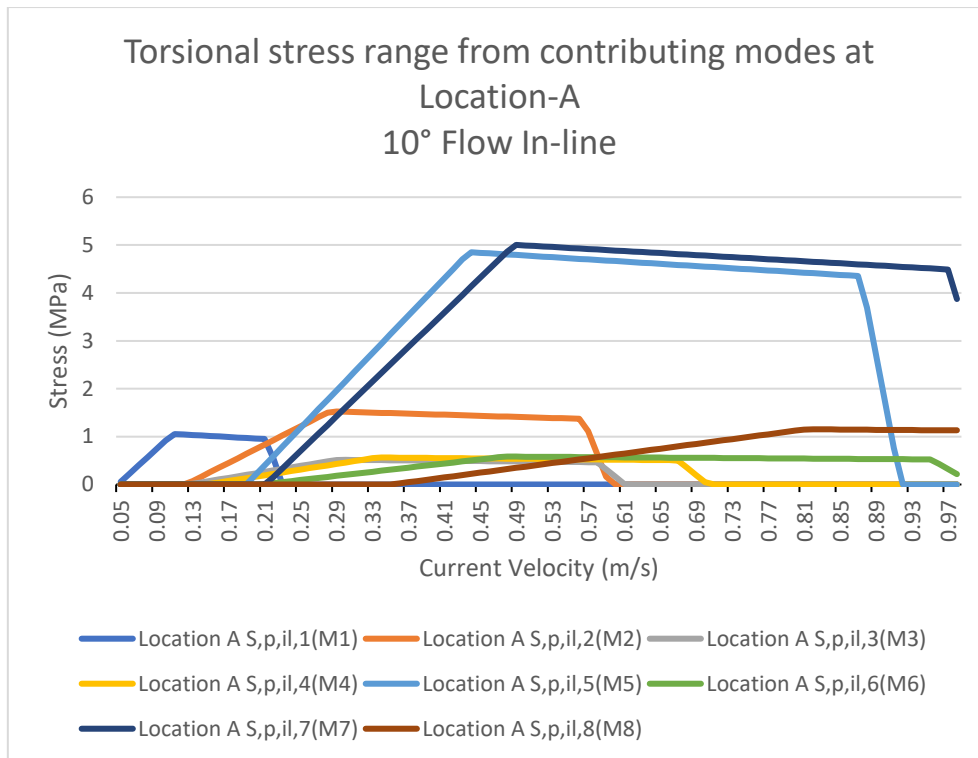


Figure 7-6: Torsional stress range for all contributing modes (Case-1(a) - 10° Flow IL) at Location A

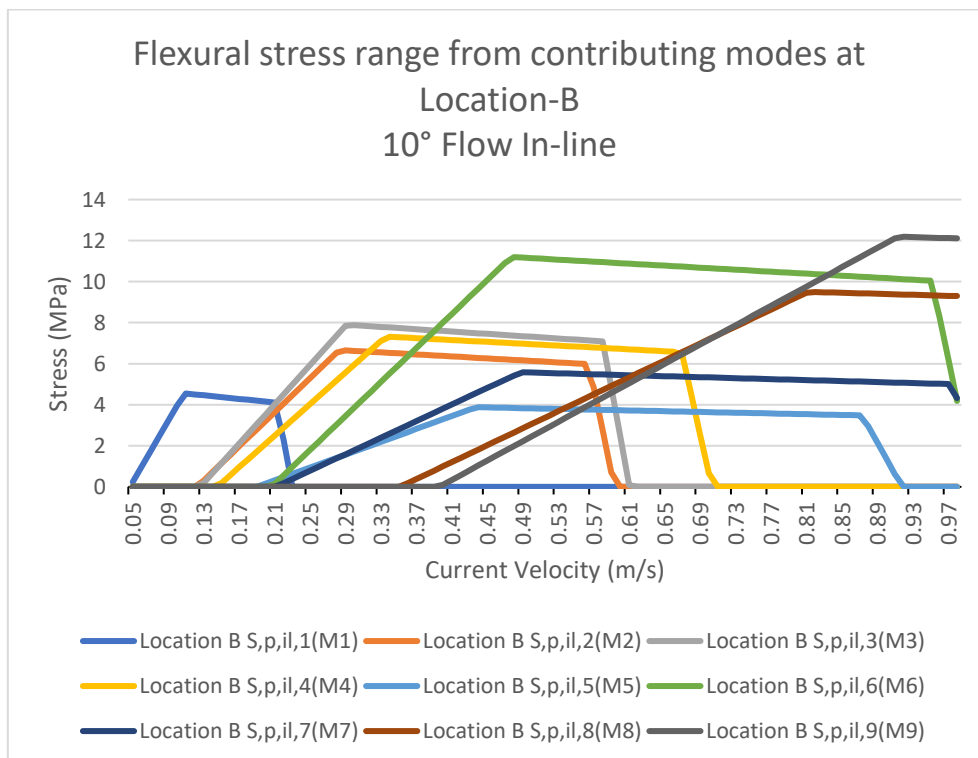


Figure 7-7: Flexural stress range for all contributing modes (Case-1(a) - 10° Flow IL) at Location B

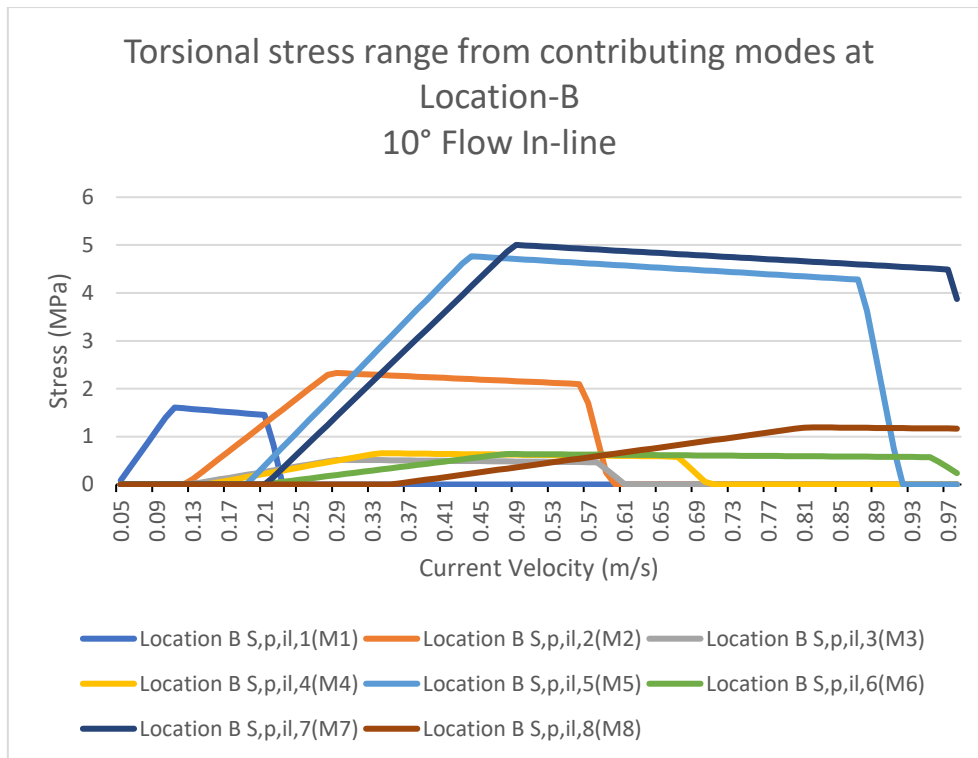


Figure 7-8: Torsional stress range for all contributing modes (Case-1(a) - 10° Flow IL) at Location B

Combined flexural and torsional stress range from each contributing mode for Case-1 (a) is calculated at location A and B using the unit stress ranges shown in Figure 7-5, Figure 7-6 and Figure 7-7, Figure 7-8 , respectively.

Combined flexural and torsional stress at Location A is show in Figure 7-9

Combined flexural and torsional stress at Location B is show in Figure 7-10

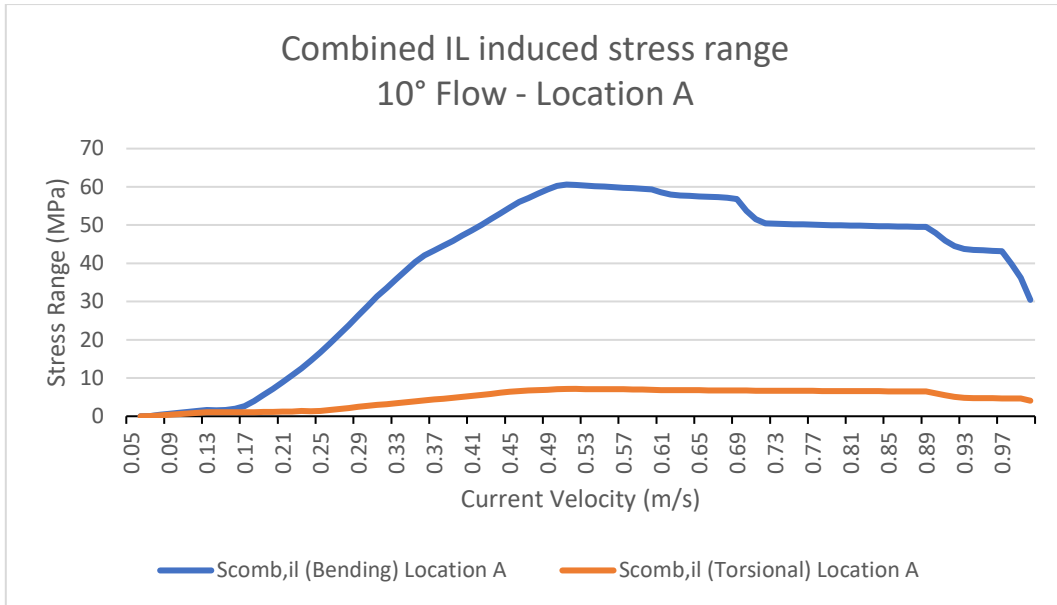


Figure 7-9: Combined flexural and torsional stress range from all contributing modes (Case-1(a) - 10° Flow IL) at Location A

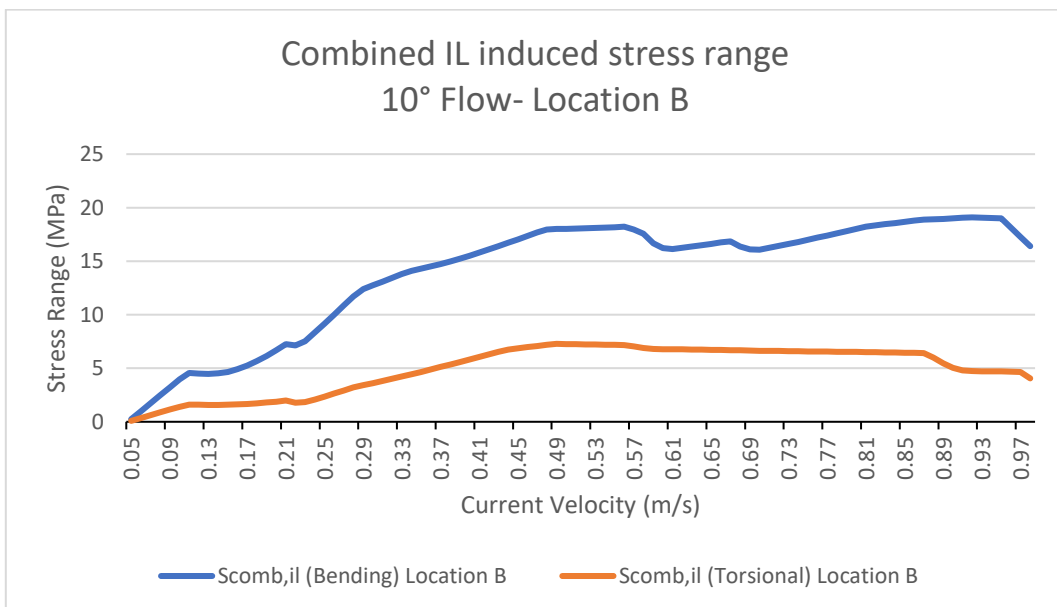


Figure 7-10: Combined flexural and torsional stress range from all contributing modes (Case-1(a) - 10° Flow IL) at Location B

Response frequency of the combined flexural and torsional stress range from each contributing mode for Case-1 (a) is calculated at location A and B and shown in Figure 7-11 and Figure 7-12.

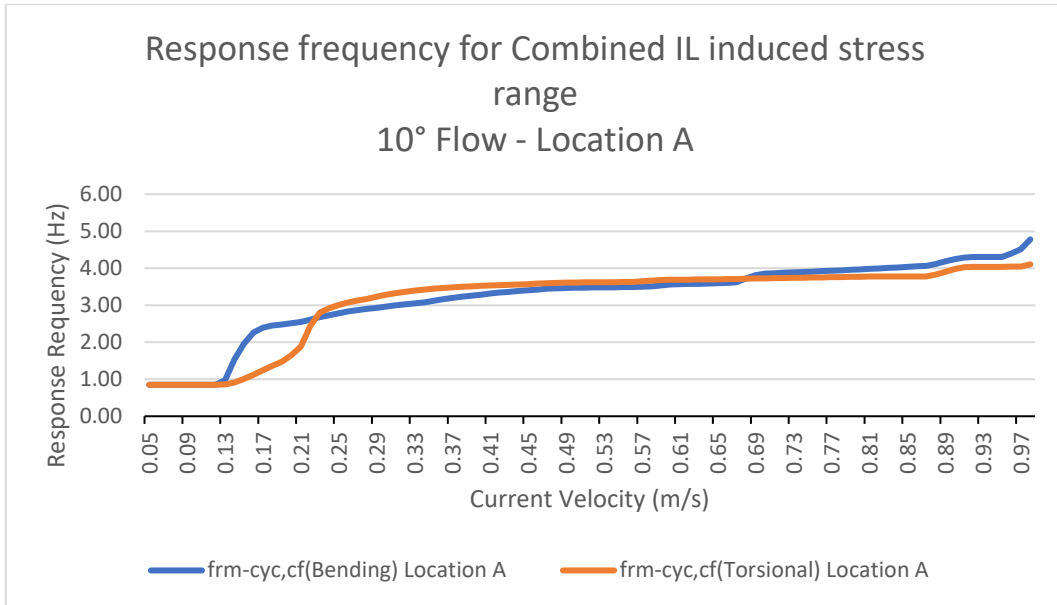


Figure 7-11: Response frequency for combined flexural and torsional stress range from all contributing modes (Case-1(a) - 10° Flow IL) at Location A

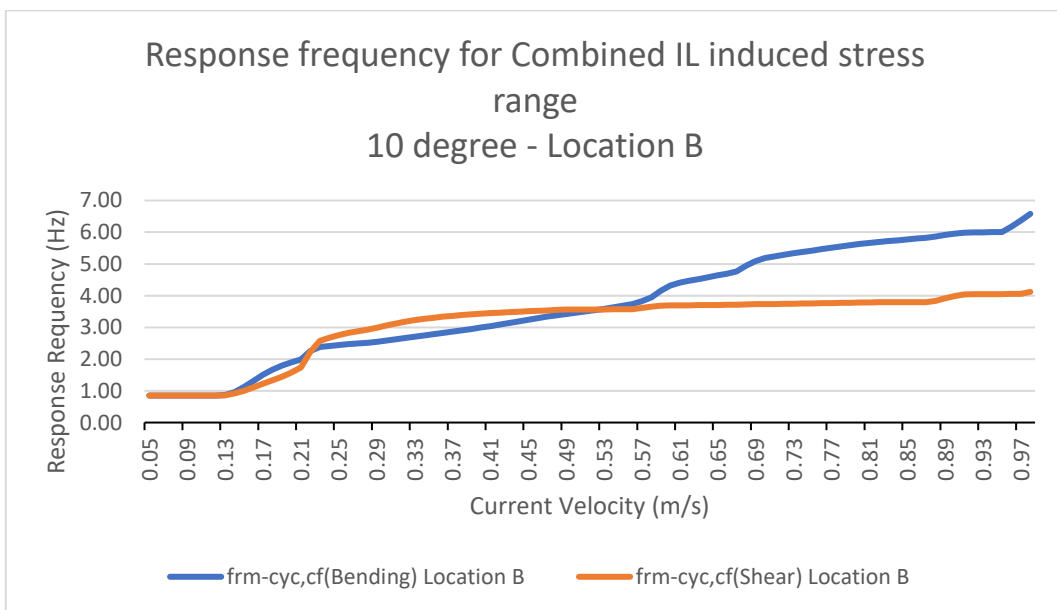


Figure 7-12: Response frequency for combined flexural and torsional stress range from all contributing modes (Case-1(a) - 10° Flow IL) at Location B

7.4 Discussion

7.4.1 Unit stress amplitude

Unit stress amplitude to be considered for stress range calculation is based on the contributing modes only. Hence, the non-contributing mode's unit stress amplitude is not considered.

Table 7-1 shows the flexural and torsional unit stress amplitude for all contributing modes at location A and B for Case 1(a) - IL 10° flow. As we see from Table 6-11, some of the modes are non-participating (hence non-contributing) at critical locations A and B, the unit amplitude stress for these modes has not been considered for stress range calculation.

7.4.2 Stress Range

From Figure 7-5, Figure 7-6, Figure 7-7 and Figure 7-8 we see that the stress range contribution is applicable only for the contributing modes in the flow velocity range for which the response model is applicable. Stress range is primarily depending on the response amplitude for the applicable range of reduced velocity for a given mode as well as the unit stress amplitude value at the critical location A and B.

From Figure 7-9, we see that the flexural stress range is much higher than the torsional stress range at Location A. This correlates well with our criteria for selection of Location A as the location for highest combined flexural modal stresses. Also, we see that the flexural stress range is highest at flow velocity of 0.49 m/s at 60.5 MPa after which we see a decline in the flexural stress range. At the highest point ($U=0.54$ m/s), maximum IL modes are contributing to the combined stress range. As the current velocity increases, some of the IL modes fall out of the limit of the response model and hence do not contribute. We can see a similar trend for the combined torsional stress range. Maximum value of combined torsional stress range is seen at $U=0.49$ m/s at 7.14 MPa. Hence both the flexural and torsional peak values are obtained at the same flow velocity of $U=0.49$ m/s

From Figure 7-10, we see that torsional stress range is comparative to the flexural stress range at Location B. This is because our criterion for selection of Location B is the maximum

combined torsional modal stress. Flexural stress range reaches the highest value of 19.1 MPa at $U=0.92$ m/s while the highest value of torsional stress range, 7.28 MPa, is achieved at $U=0.49$ m/s. Even though less IL modes are contributing at $U=0.92$ m/s, the amplitude response at $U=0.92$ m/s for Mode-9 is highest at that velocity. For location B, unit amplitude flexural stress is highest for Mode-9 at 39.44 MPa as compared to other modes. Contribution of Mode-9 is highest at $U=0.92$ m/s which leads to higher combined flexural stress range at this flow velocity. Hence the combined flexural stress is highest at 0.92 m/s even when less modes are contributing at that velocity.

7.4.3 Correlation with Igeh [24]

A comparison with results from Igeh [24] of flexural and torsional stress range for 10° and 90° flow (IL and CF) at location A and B is provided in Figure 7-13 to Figure 7-20. Igeh [24] used DNV-RP-F105 (2016) [12] to determine the stress range while this study uses DNVGL-RP-F105 (2017 edition) [11]. The latest edition provides guidance for stress calculation of non-straight geometries such as the rigid jumper while the 2006 edition does not provide any such guidance.

1. 10° Flow

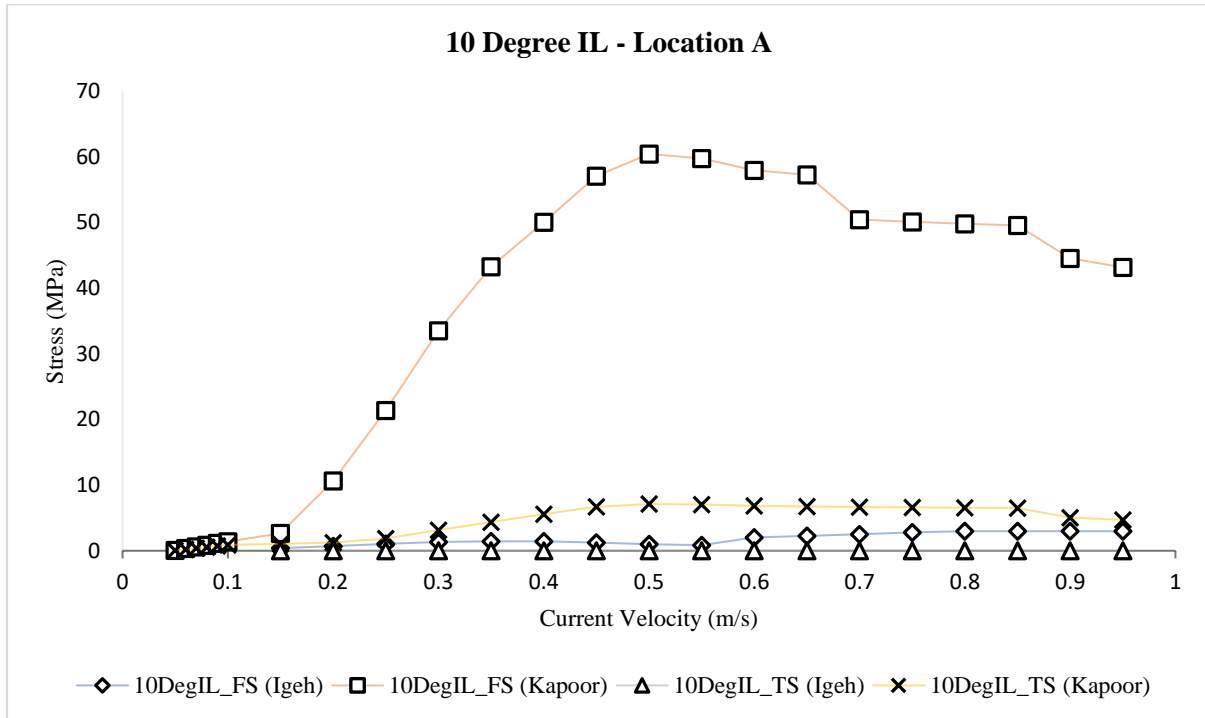


Figure 7-13: Comparison of torsional and flexural stress range with Igeh [24] for 10° Flow - IL at Location A

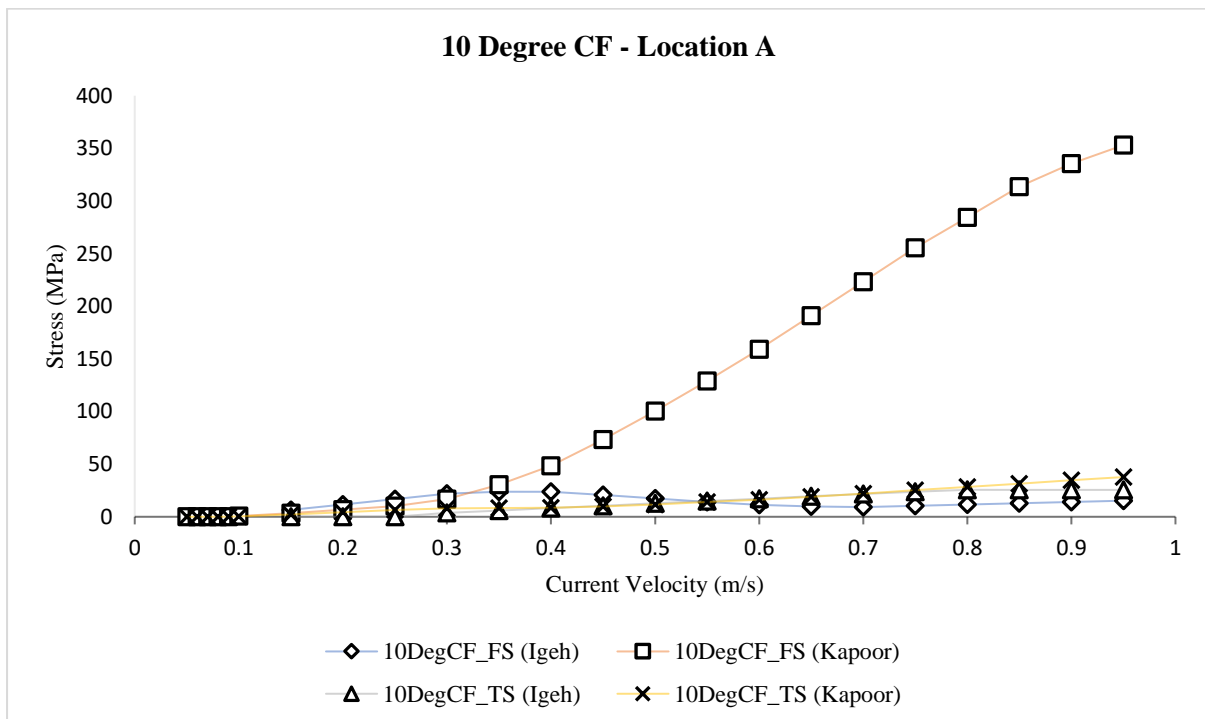


Figure 7-14: Comparison of torsional and flexural stress range with Igeh [24] for 10° Flow - CF at Location A

From the above two graphs, we can see that flexural stress range for 10° flow (IL and CF) at location A is highly overestimated in this study as compared to Igeh [24]. This is primarily due to difference mode classification. Igeh [24] classified Mode-3,4,6 and 9 as IL and Mode-1,2,5,7 and 8 as CF for 10° flow in line with DNV-RP-F105 (2006 edition) [12]. In this study, on the other hand, all modes are classified as both IL and CF in line with DNVGL-RP-F105 (2017 edition) [11]. Hence, more modes are considered contributing leading to higher stress range values. Moreover, CF stress range is higher than IL stress range for 10° flow. Since only 17.36 % of the velocity acts perpendicular to the rigid jumper, stress range in IL direction is much less than CF direction.

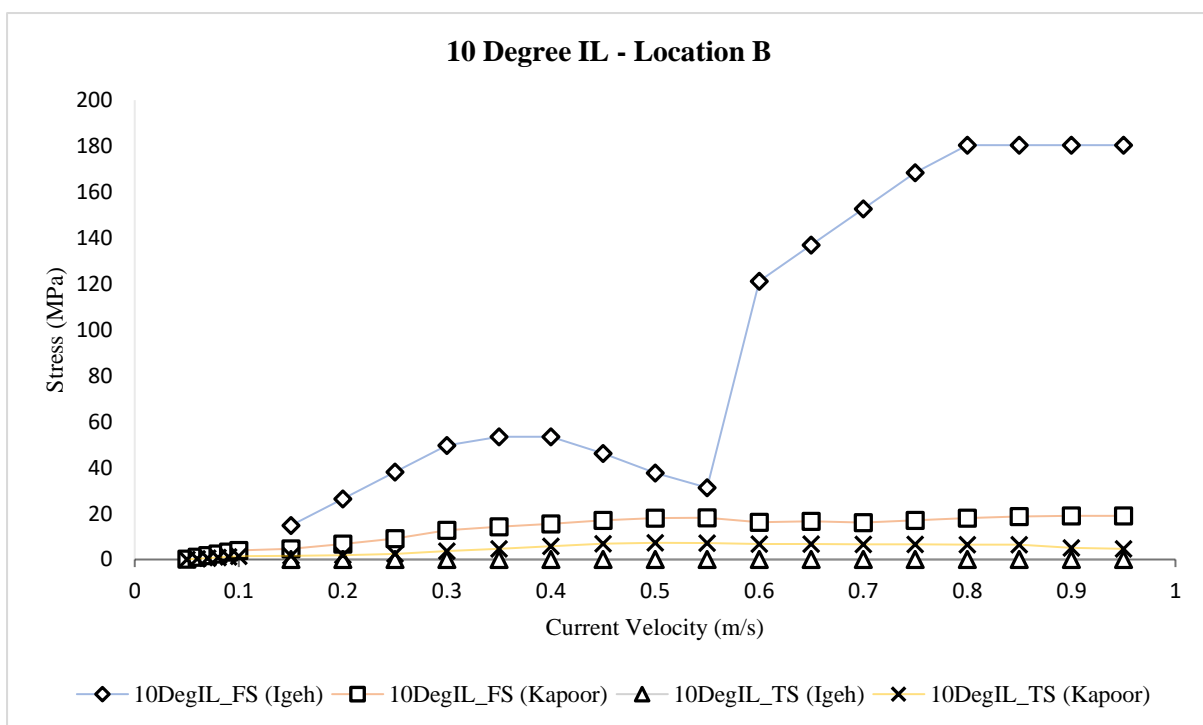


Figure 7-15: Comparison of torsional and flexural stress range with Igeh [24] for 10° Flow - IL at Location B

For 10° flow (IL), at location B, we see that flexural stress range is lower than Igeh [24] while the torsional stress range is higher. The difference in flexural stress range is due to the selection criteria for the critical location B. In this study, selection of location B is based on the maximum combined torsional modal stress from active modes while Igeh [24]’s selection criteria for location B was peak flexural and torsional modal stress.

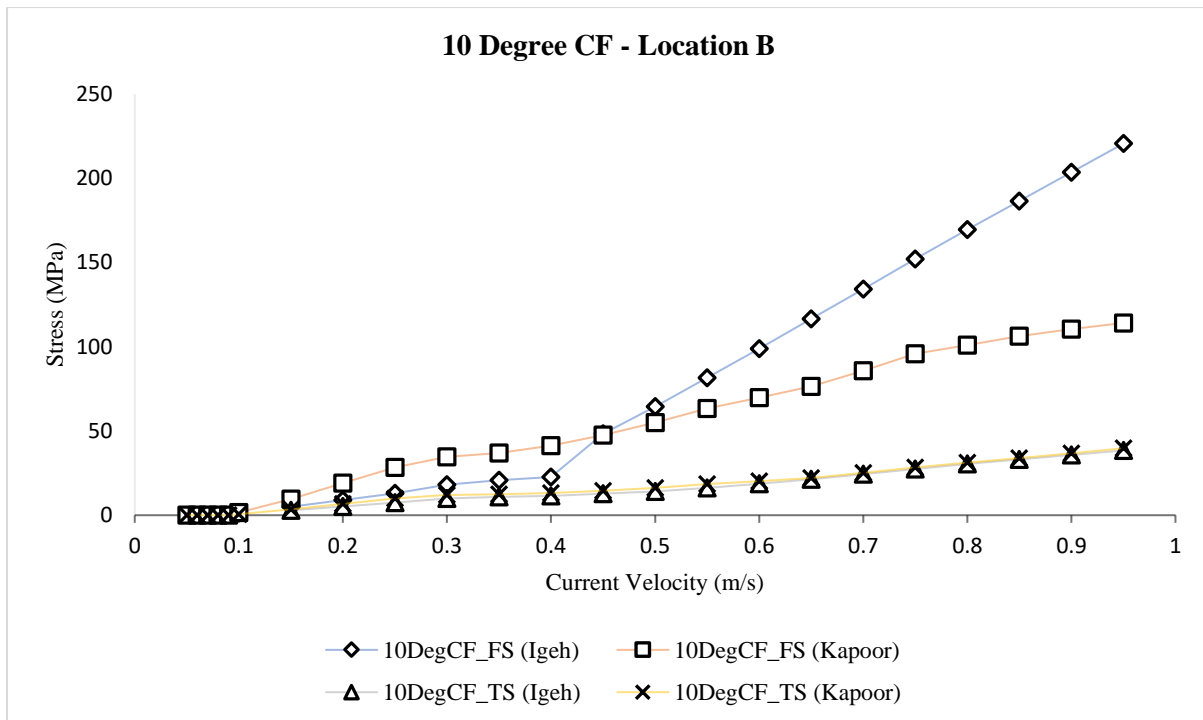


Figure 7-16: Comparison of torsional and flexural stress range with Igeh [24] for 10° Flow - CF at Location B

For 10° flow (CF), at location B, the flexural stress range is higher than Igeh [24] for lower velocities. As the velocity increases beyond 0.4 m/s, Igeh [24]’s stress range becomes higher. At current velocity of 0.95 m/s, Igeh [24]’s flexural stress is highest at 220 MPa which is 92% higher than that calculated in this study. On the other hand, the torsional stress range correlates well with Igeh [24].

2. 90° Flow

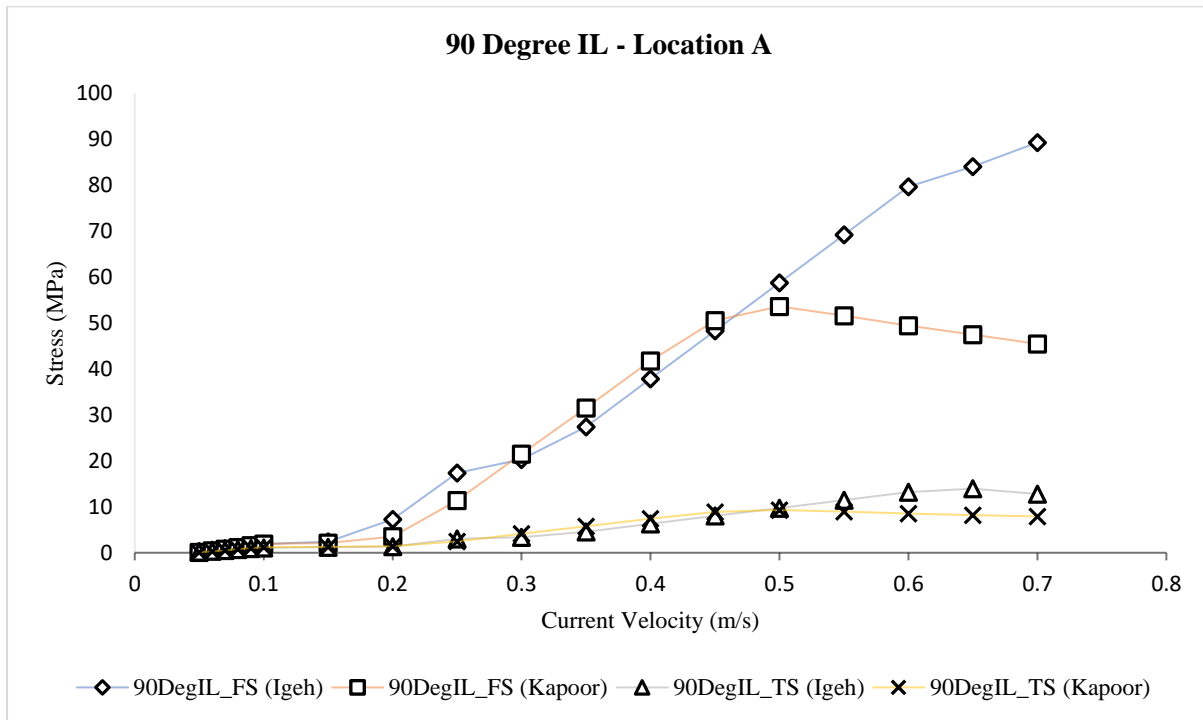


Figure 7-17: Comparison of torsional and flexural stress range with Igeh [24] for 90° Flow - IL at Location A

For 90° flow (IL), at location A, the flexural stress range correlates well with Igeh [24] till the current velocity reaches 0.45 m/s. Flexural stress range calculated in this study decreases after reaching a peak value of 54 MPa at 0.49 m/s current velocity while Igeh [24]’s flexural stress range increases continuously. The difference is due to different IL response models for 90° flow. In this study, after current velocity of 0.49 m/s, the response amplitude of contributing modes 5 and 7 start to decline leading to reduced combined flexural stress range (See Figure 7-3). On the other hand, torsional stress range correlates well till current velocity of 0.5 m/s beyond which contribution from the highest contributor mode, Mode-7, starts to decrease as Mode-7 response amplitude starts declining (See Figure 7-3).

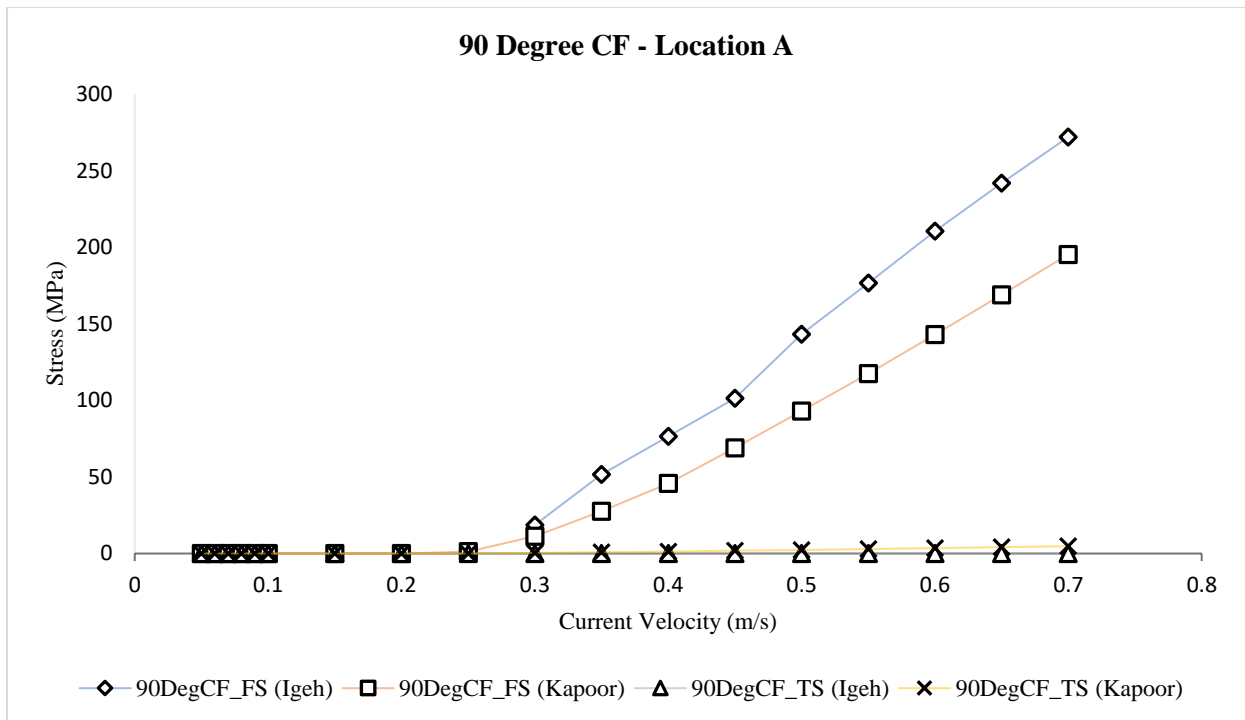


Figure 7-18: Comparison of torsional and flexural stress range with Igeh [24] for 90° Flow – CF at Location A

For 90° flow (CF), at location A, flexural stress range calculated in this study gives lower values than Igeh [24]. At current velocity of 0.7 m/s, Igeh [24]’s value is around 40% higher. This difference is due to the higher slope CF response model for 90° flow of Igeh [24] as compared to CF response model in this study. Due to the higher slope, the response amplitude rises quicker for Igeh [24] leading to higher flexural stress range (See Figure 9-3 and Figure 9-4). On the other hand, torsional stress range in Igeh [24] is considered zero as no torsional unit stress amplitude is considered. In this study, non-zero torsional unit stress amplitude is obtained from modal analysis and hence torsional stress range is determined.

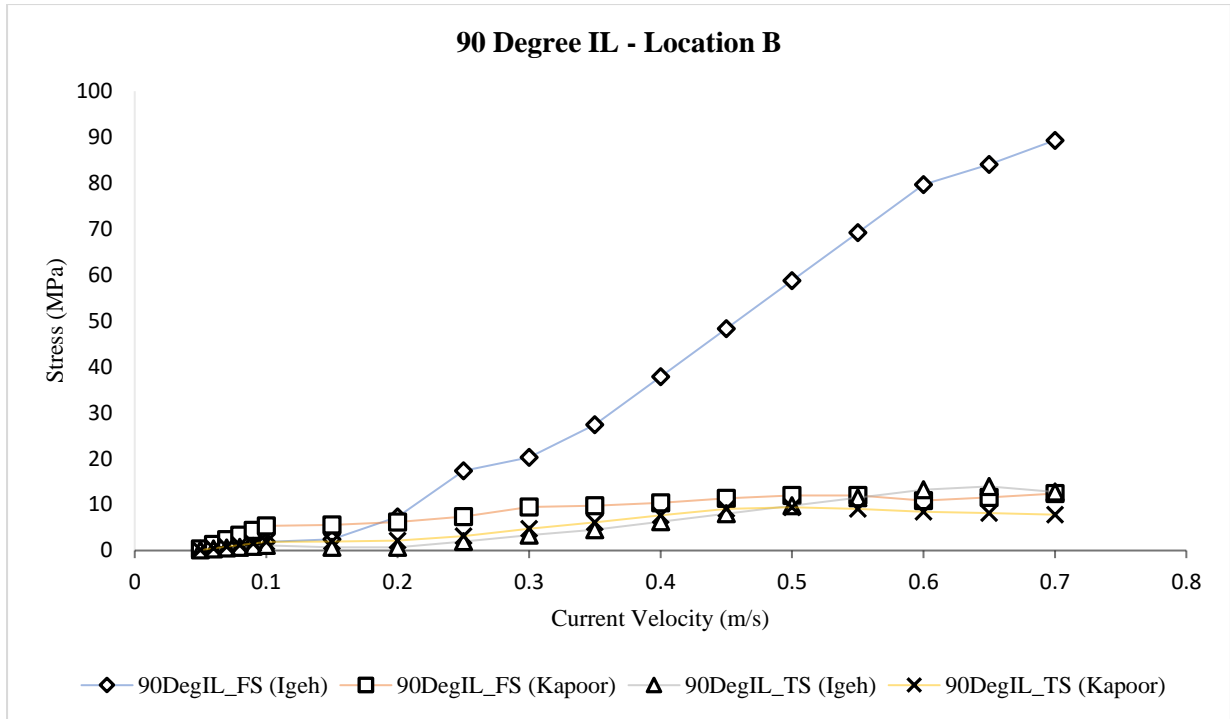


Figure 7-19: Comparison of torsional and flexural stress range with Igeh [24] for 90° Flow IL at Location B

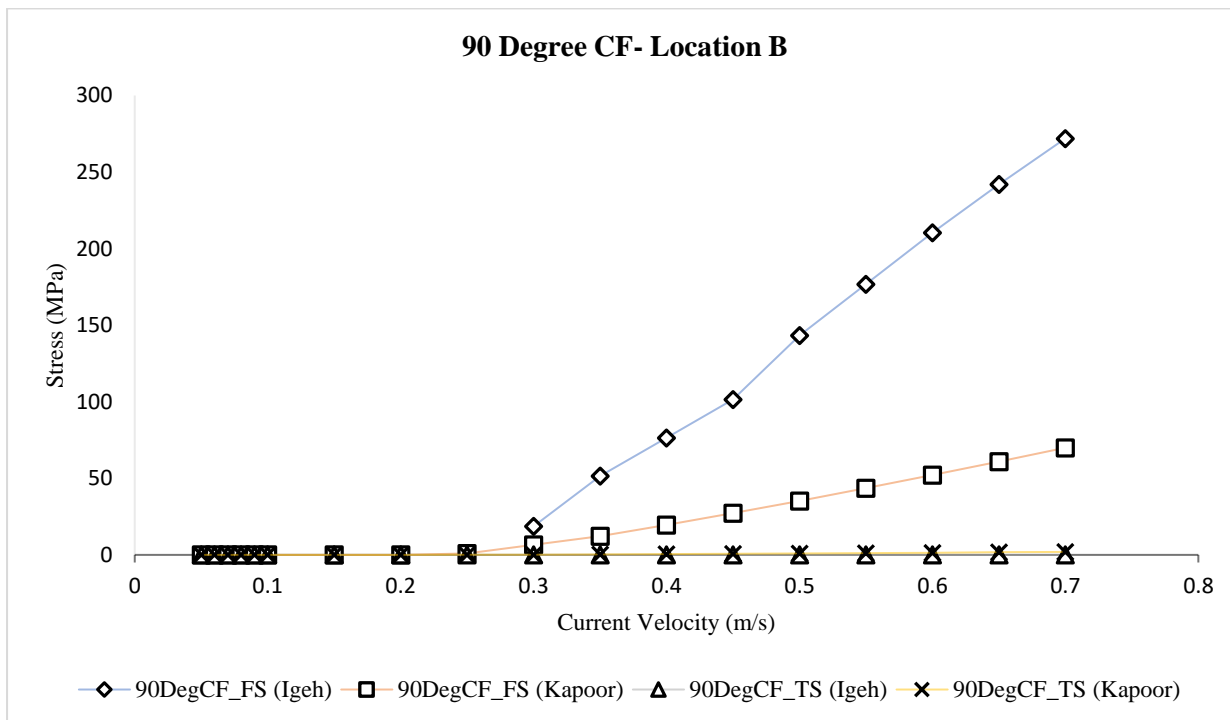


Figure 7-20: Comparison of torsional and flexural stress range with Igeh [24] for 90° Flow – CF at Location B

For 90° flow (IL and CF), at location B, Flexural stress range in Igeh [24] is much higher than that calculated in this study. The difference is purely because of difference in selection of location B in the two studies as mentioned earlier. Torsional stress range on the other hand correlates well with Igeh [24].

8 FATIGUE ASSESSMENT

Fatigue assessment is carried by using the Farahani [13,14] fatigue damage parameter based on Section 4.6.

Fatigue assessment is carried out at critical location (A and B) for the following cases:

1. 10° Flow
 - a. In-line
 - b. Cross-flow
2. 90° Flow
 - a. In-line
 - b. Cross-flow

To show the steps in detail, fatigue assessment method for following case has been described in this chapter:

1. Case-1(a) - 10° flow (in-line) at Location A at current velocity of 0.14 m/s

All other cases follow the same procedure for each value of current velocity. Fatigue damage results for the above-mentioned cases, along with relevant graphs, are presented in Section 8.4. The correlation to fatigue damage data from Igeh [24] is presented in section 8.5

8.1 Block Loading

First step in fatigue analysis using Farahani [13,14]'s fatigue damage parameter is to create block loading for each current velocity using the combined stress range and response frequency of flexural and torsional stresses based on the methodology given in Section 4.6.1.

For Case-1(a) - 10° flow (in-line) at Location A at current velocity of 0.14 m/s, amplitude of first principal stress (σ_{11}) and third principal stress (σ_{33}) are obtained from combined flexural and combined torsional stress range as half of the stress range value. Value of second principal stress is considered zero ($\sigma_{22} = 0$) as the jumper is assumed to in biaxial planar stress state. No mean stress is considered in either first or third principal stress direction, hence the cycling

loading of the two principal stresses is considered about the X-axis as shown in Figure 8-1 and Figure 8-2.

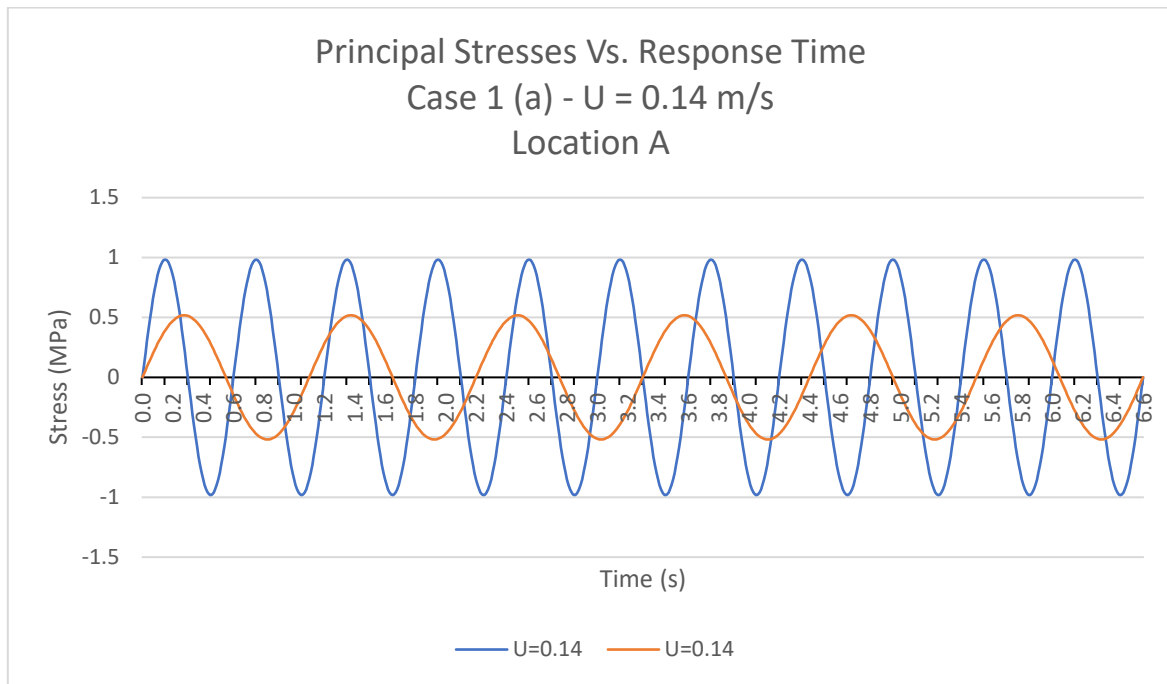


Figure 8-1: Principal Stress (σ_{11} , σ_{33}) variation with time (s) for Case-1 (a) at Location – A for U=0.14 m/s

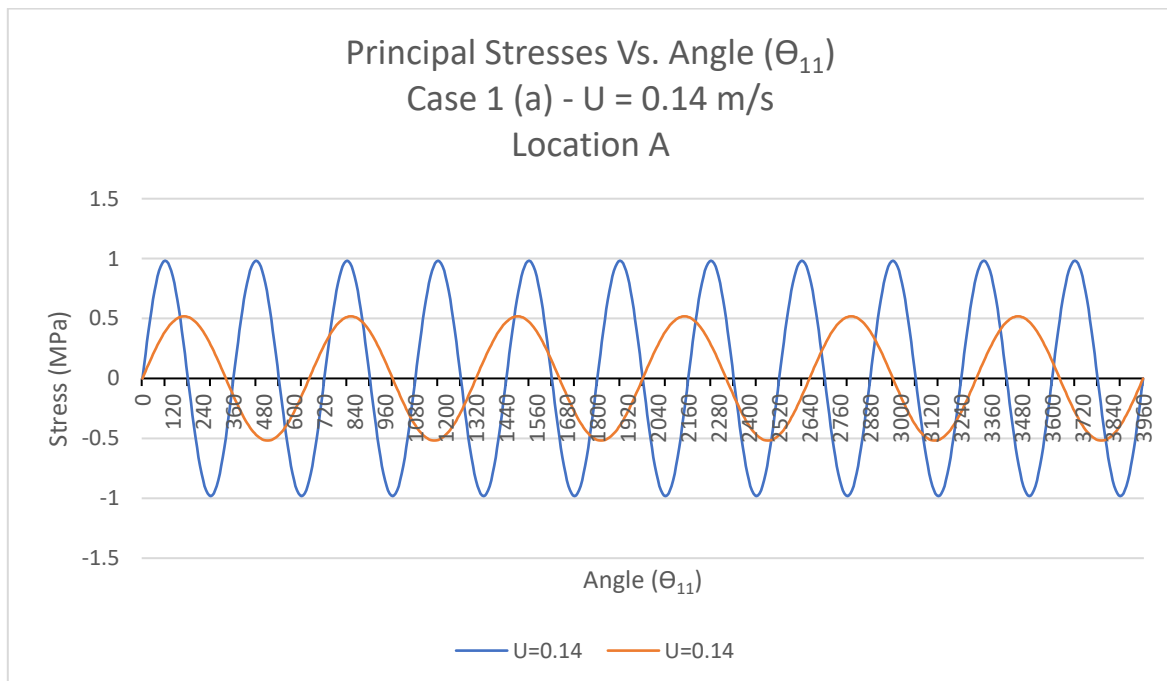


Figure 8-2: Principal Stress (σ_{11} , σ_{33}) variation with angle (θ_{11}) for Case-1 (a) at Location – A for U=0.14 m/s

The above figures show the variation of principal stresses with time (Figure 8-1) and with angle of first principal stress loading (θ_{11}) (Figure 8-2) for the block loading of Case-1(a) - 10° flow (in-line) at Location A at current velocity of 0.14 m/s. We notice a difference in stress amplitudes and frequency between the first and third principal stress (See Table 8-1) which is well captured in formation of block loading.

The block loading calculation for Case-1(a) - 10° flow (in-line) at Location A at current velocity of 0.14 m/s is given in Table 8-1 below:

Table 8-1: Block loading calculation for Case-1(a) - 10° flow (in-line) at Location A at current velocity of 0.14 m/s

Combined Stress Range (MPa)		Principal Stress Amplitude (MPa)		Response Frequency (Hz)		Response Time (s)		Duration of block loading (s)
Flexural	Torsional	σ_{11}	σ_{33}	Flexural	Torsional	Flexural	Torsional	
1.96	1.04	0.98	0.52	1.54	0.92	0.6	1.1	6.6

From the above table, we see that the principal stress amplitudes are taken as half of the combined stress range for flexural and torsional stresses. Also, to obtain a complete block loading, duration of block loading is determined from the response times of flexural and torsional stresses.

Block loading for all cases showing first principal stress (σ_{11}) and third principal stress (σ_{33}) are given in section 13

8.2 Critical plane

Critical plane is selected as the plane at which shear strain is maximum for every half cycle of first principal stress (σ_{11}) loading according to the methodology described in Section 4.6.2.

For Case-1(a) - 10° flow (in-line) at Location A at current velocity of 0.14 m/s, block loading for first principal stress (σ_{11}) (Flexural stress) and third principal stress (σ_{33}) (Torsional stress)

are used to determine first and third principal strains ($\epsilon_{11}, \epsilon_{33}$) based on formulas given in section 4.6.2 (see Figure 8-3).

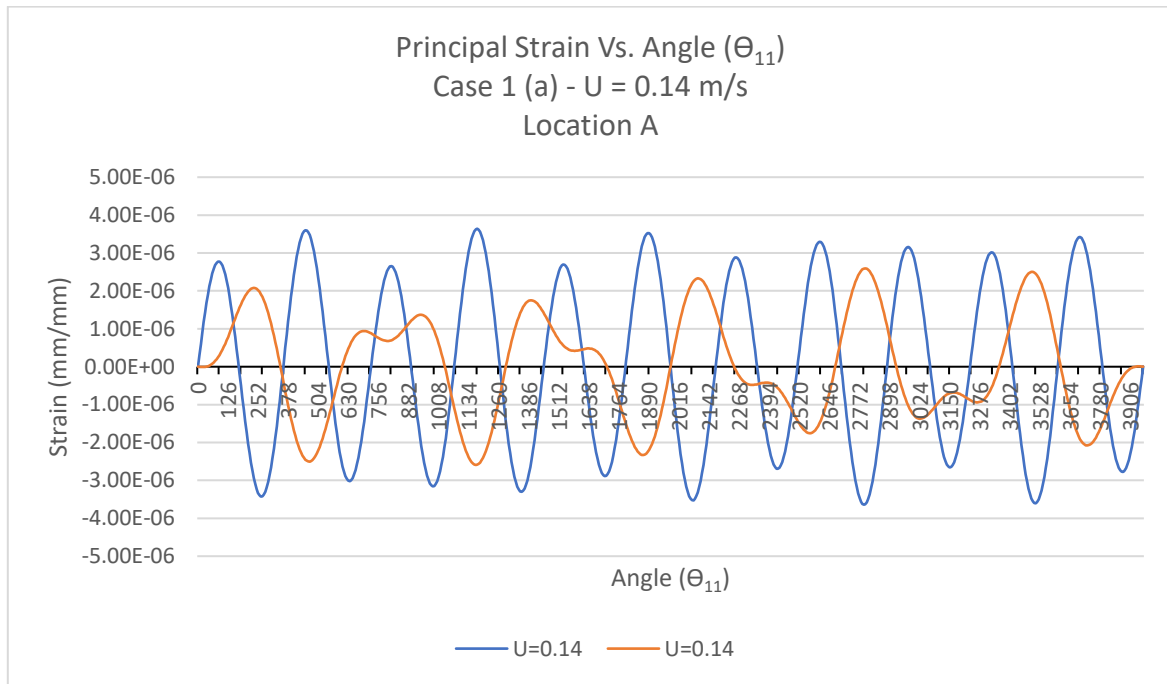


Figure 8-3: Principal Strains ($\epsilon_{11}, \epsilon_{33}$) variation with angle (θ_{11}) for Case-1 (a) at Location – A for U=0.14 m/s

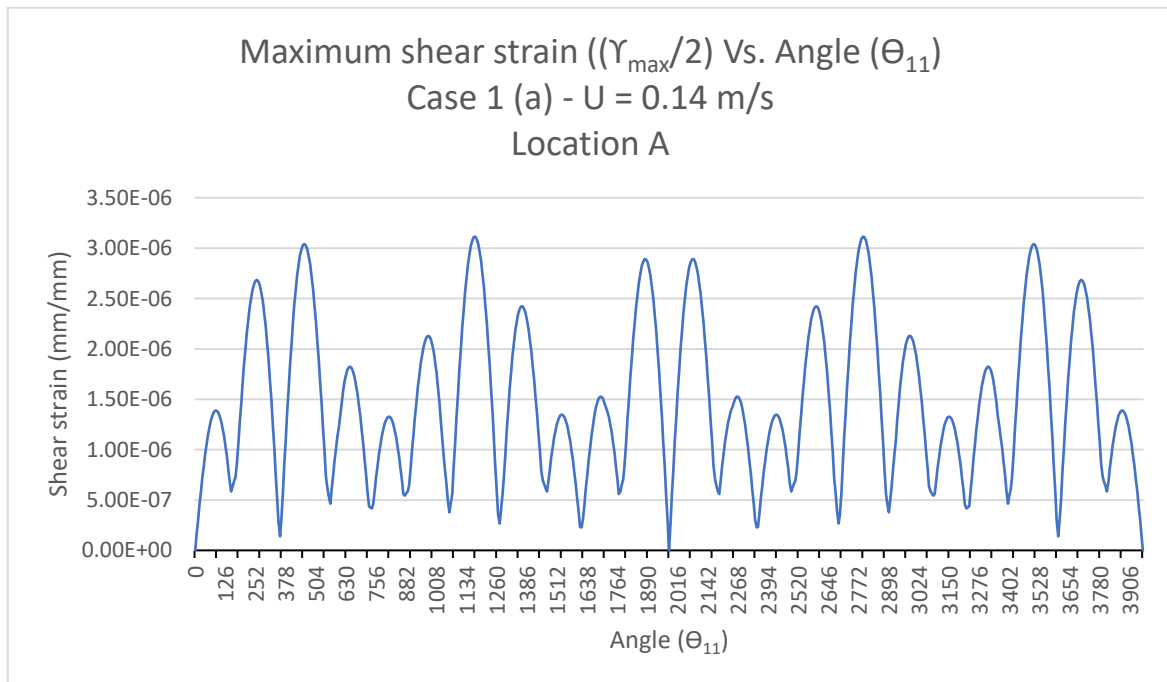


Figure 8-4: Maximum shear strain ($\frac{\gamma_{max}}{2}$) variation with angle (θ_{11}) for Case-1 (a) at Location – A for U=0.14 m/s

Principal strains values are used to determine the maximum shear strain for each half cycle of first principal stress loading angle (θ_{11}). Figure 8-4 shows the maximum shear strain variation with first principal stress loading angle (θ_{11}).

Table 8-2: Critical planes for each half cycle of σ_{11} for Case-1(a) - 10° flow (in-line) at Location A at current velocity of 0.14 m/s

Half Cycle	$\theta_{11,start}$	$\theta_{11,end}$	Critical Plane (θ_{cric})
	(°)	(°)	(°)
Cycle-1	0	180	84
Cycle-2	180	360	258
Cycle-3	360	540	456
Cycle-4	540	720	648
Cycle-5	720	900	810
Cycle-6	900	1080	972
Cycle-7	1080	1260	1170
Cycle-8	1260	1440	1368
Cycle-9	1440	1620	1530
Cycle-10	1620	1800	1692
Cycle-11	1800	1980	1878
Cycle-12	1980	2160	2082
Cycle-13	2160	2340	2268
Cycle-14	2340	2520	2430
Cycle-15	2520	2700	2592
Cycle-16	2700	2880	2790
Cycle-17	2880	3060	2988
Cycle-18	3060	3240	3150
Cycle-19	3240	3420	3312
Cycle-20	3420	3600	3504
Cycle-21	3600	3780	3702
Cycle-22	3780	3960	3876

Plane of maximum shear strain is determined in terms of the angle of first principal stress loading (θ_{11}) at which the maximum shear strain occurs as shown in Table 8-2 above. For Case-1(a) - 10° flow (in-line) at Location A at current velocity of 0.14 m/s, 22 half cycles of (θ_{11}) are present for this block loading and θ_{11} angle at which shear strain is maximum is determined as the critical angle (θ_{cric}).

Maximum shear strain and critical planes (θ_{cric}) for all cases are presented in section 13.

8.3 Normal and Shear Stress and Strain Range

The normal stress range ($\Delta\sigma_n$) and maximum shear stress range ($\Delta\tau_{max}$) are calculated from first and third principal stresses using the largest stress Mohr's circle for each full cycle of first principal stress (θ_{11}) loading at the critical angle (θ_{critic}) for Case-1(a) - 10° flow (in-line) at Location A at current velocity of 0.14 m/s according to the methodology given in Section 4.6.3 (See Figure 8-5)

Similarly, normal strain range ($\Delta\epsilon_n$) and maximum shear strain range ($\Delta\gamma_{max}/2$) are calculated from first and third principal strains using the largest strain Mohr's circle for each full cycle of first principal stress (θ_{11}) loading at the critical angle (θ_{critic}) for Case-1(a) - 10° flow (in-line) at Location A at current velocity of 0.14 m/s according to the methodology given in Section 4.6.3 (See Figure 8-6).

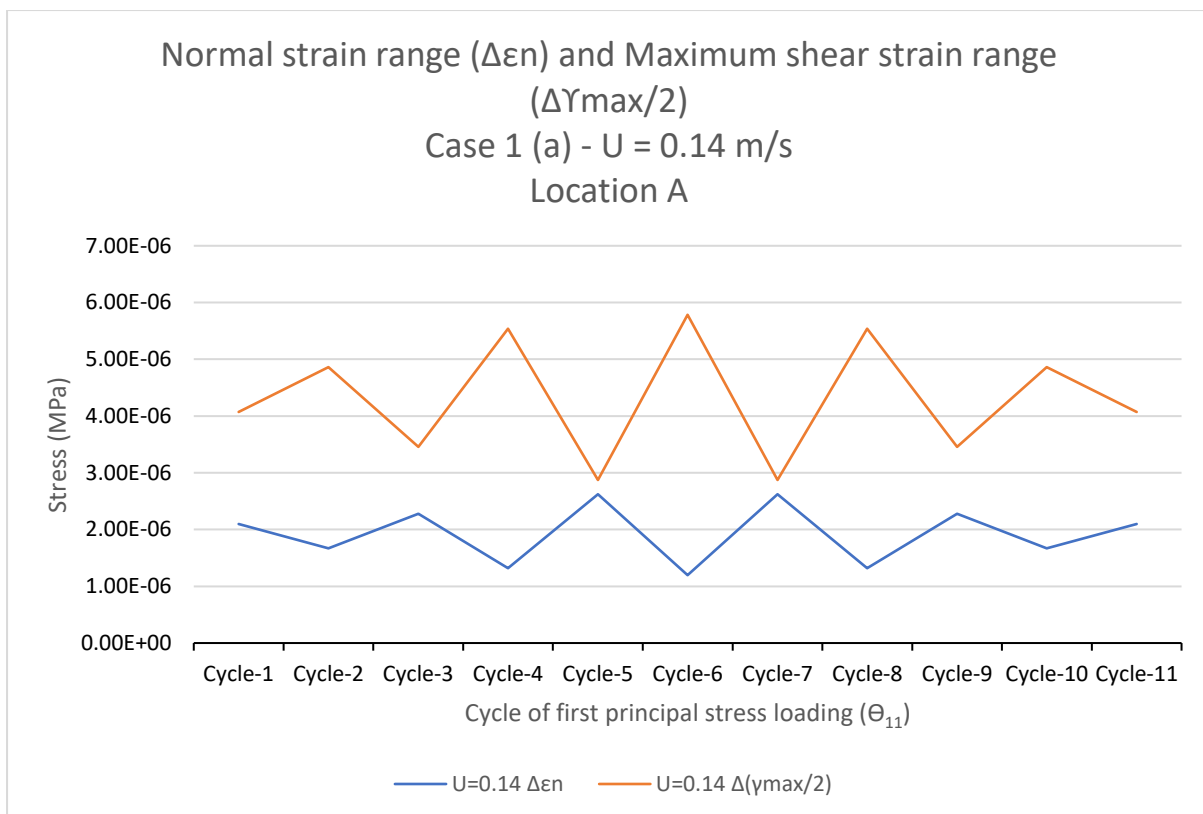


Figure 8-5: Normal stress range ($\Delta\sigma_n$) and maximum shear stress range ($\Delta\tau_{max}$) for each full cycle of (θ_{11}) for Case-1 (a) at Location – A for U=0.14 m/s

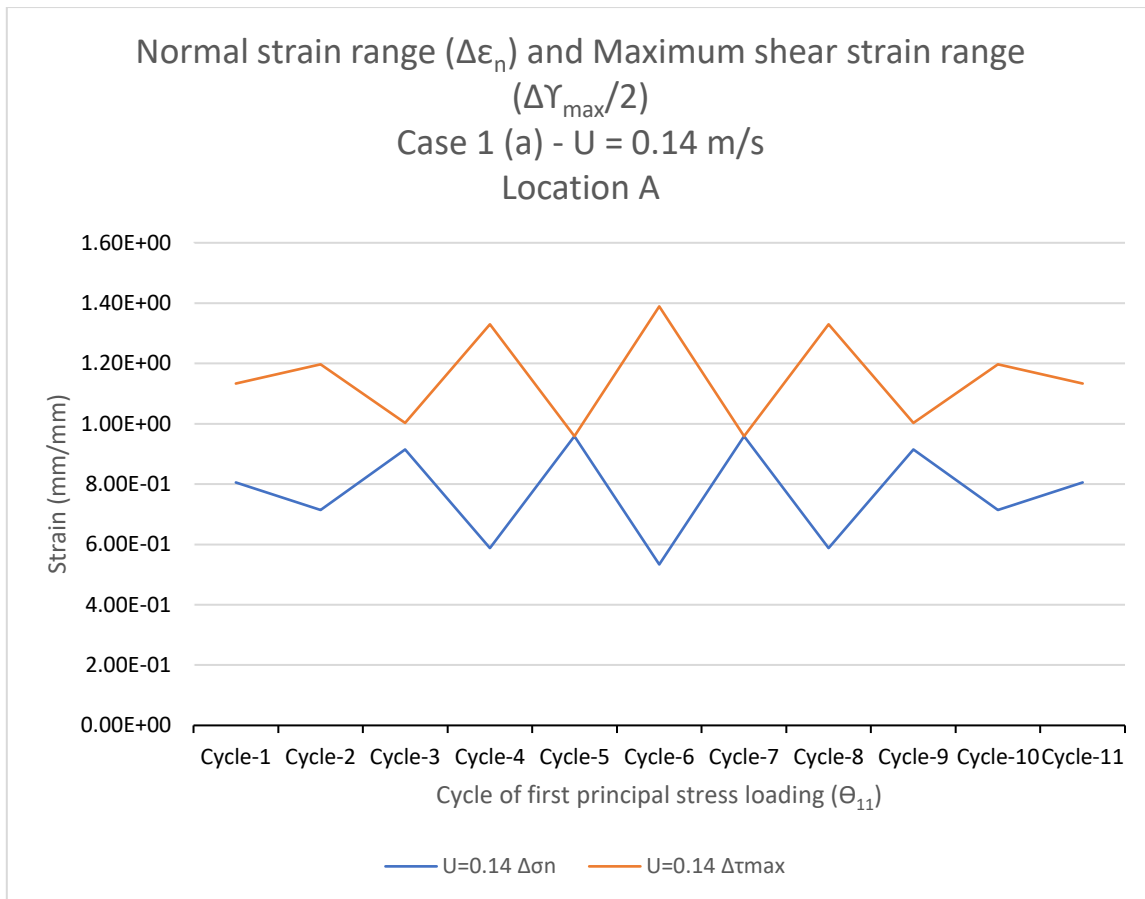


Figure 8-6: Normal strain range ($\Delta\varepsilon_n$) and maximum shear strain range ($\Delta\frac{\gamma_{max}}{2}$) for each full cycle of (θ_{11}) for Case-1 (a) at Location – A for U=0.14 m/s

Values for Normal and shear stress and strain ranges ($\Delta\sigma_n$, $\Delta\tau_{max}$, $\Delta\varepsilon_n$, $\Delta\frac{\gamma_{max}}{2}$) at the critical angle (θ_{cric}) have been tabulated in Table 8-3.

Table 8-3: Normal and shear stress and strain ranges ($\Delta\sigma_n, \Delta\tau_{max}, \Delta\varepsilon_n, \Delta\frac{\gamma_{max}}{2}$) at each full cycle of θ_{11} for Case-1(a) - 10° flow (in-line) at Location A at current velocity of 0.14 m/s

Full Cycle of θ_{11}	$\Delta\sigma_n$	$\Delta\tau_{max}$	$\Delta\varepsilon_n$	$\Delta(\gamma_{max}/2)$
Cycle-1(θ_1 - θ_2)	8.05E-01	1.13E+00	2.10E-06	4.07E-06
Cycle-2(θ_3 - θ_4)	7.15E-01	1.20E+00	1.67E-06	4.86E-06
Cycle-3(θ_5 - θ_6)	9.15E-01	1.00E+00	2.28E-06	3.46E-06
Cycle-4(θ_7 - θ_8)	5.88E-01	1.33E+00	1.32E-06	5.54E-06
Cycle-5(θ_9 - θ_{10})	9.59E-01	9.59E-01	2.62E-06	2.87E-06
Cycle-6(θ_{11} - θ_{12})	5.34E-01	1.39E+00	1.20E-06	5.78E-06
Cycle-7(θ_{13} - θ_{14})	9.59E-01	9.59E-01	2.62E-06	2.87E-06
Cycle-8(θ_{15} - θ_{16})	5.88E-01	1.33E+00	1.32E-06	5.54E-06
Cycle-9(θ_{17} - θ_{18})	9.15E-01	1.00E+00	2.28E-06	3.46E-06
Cycle-10(θ_{19} - θ_{20})	7.15E-01	1.20E+00	1.67E-06	4.86E-06
Cycle-11(θ_{21} - θ_{22})	8.05E-01	1.13E+00	2.10E-06	4.07E-06

Normal and shear stress and strain ranges ($\Delta\sigma_n, \Delta\tau_{max}, \Delta\varepsilon_n, \Delta\frac{\gamma_{max}}{2}$) for all cases are presented in section 13.

8.4 Fatigue

Farahani [13,14]'s simplified fatigue damage parameter is used to predict the damage for each full cycle of first principal stress loading (θ_{11}) at the critical angles (θ_{critic}) for Case-1(a) - 10° flow (in-line) at Location A at current velocity of 0.14 m/s according to methodology provided in section 4.6.5 (See Figure 8-7).

Table 8-4 shows the fatigue damage for each full cycle of first principal stress loading (θ_{11}) calculated at critical angle (θ_{critic}). The total fatigue damage for the block loading is taken as a sum of fatigue damage from each cycle.

Table 8-4: Fatigue damage for each full cycle of Θ_{11} for Case-1(a) - 10° flow (in-line) at Location A at current velocity of 0.14 m/s

P_i	Full Cycle of Θ_{11}	Fatigue damage
P ₁	Cycle-1(Θ_1 - Θ_2)	1.45E-09
P ₂	Cycle-2(Θ_3 - Θ_4)	1.61E-09
P ₃	Cycle-3(Θ_5 - Θ_6)	1.28E-09
P ₄	Cycle-4(Θ_7 - Θ_8)	1.87E-09
P ₅	Cycle-5(Θ_9 - Θ_{10})	1.22E-09
P ₆	Cycle-6(Θ_{11} - Θ_{12})	1.99E-09
P ₇	Cycle-7(Θ_{13} - Θ_{14})	1.22E-09
P ₈	Cycle-8(Θ_{15} - Θ_{16})	1.87E-09
P ₉	Cycle-9(Θ_{17} - Θ_{18})	1.28E-09
P ₁₀	Cycle-10(Θ_{19} - Θ_{20})	1.61E-09
P ₁₁	Cycle-11(Θ_{21} - Θ_{22})	1.45E-09
P_{block}		1.68E-08

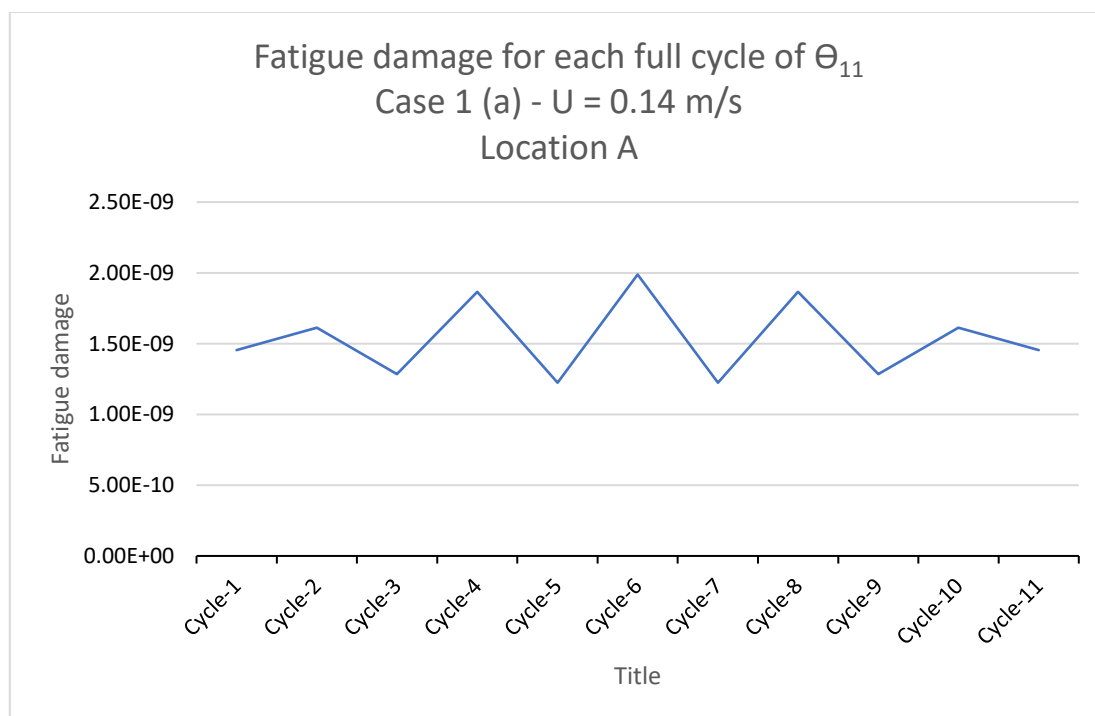


Figure 8-7: Fatigue damage for block loading for Case-1 (a) at Location – A for U=0.14 m/s

Table 8-5: Fatigue damage (1/year) for Case-1(a) - 10° flow (in-line) at Location A at current velocity of 0.14 m/s

Fatigue damage for 1 block loading (P_{block})	Duration of block loading (s)	Number of block loading cycles in 1 year	Fatigue damage (1/Year)
1.68E-08	6.6	4778181	0.080

Table 8-5 shows how fatigue damage is calculated for 1 year using the fatigue damage of one block loading.

No benchmark data could be found for normal and shear fatigue properties of aluminium pipes. Hence, the values for fatigue properties were assumed based on EN24 material used by Farahani [13,14] in his work.

Table 8-6: Normal and shear fatigue properties of Aluminium pipe

Axial fatigue strength coefficient (σ'_f)	Axial fatigue ductility coefficient (ϵ'_f)	Shear fatigue strength coefficient (τ'_f)	Shear fatigue ductility coefficient (γ'_f)
2475	1.71	1725	2.535

To determine the fatigue damage for the full range of current velocity, 0.05 m/s to 0.98 m/s, same procedure is followed for each case of current velocity to obtain fatigue damage (1/year) for 10° In-line case at location A as shown in Figure 8-8. When calculating the same at Location B, everything will change from section 8.1 to 8.4 as the stress range calculation and response frequencies are different at this location.

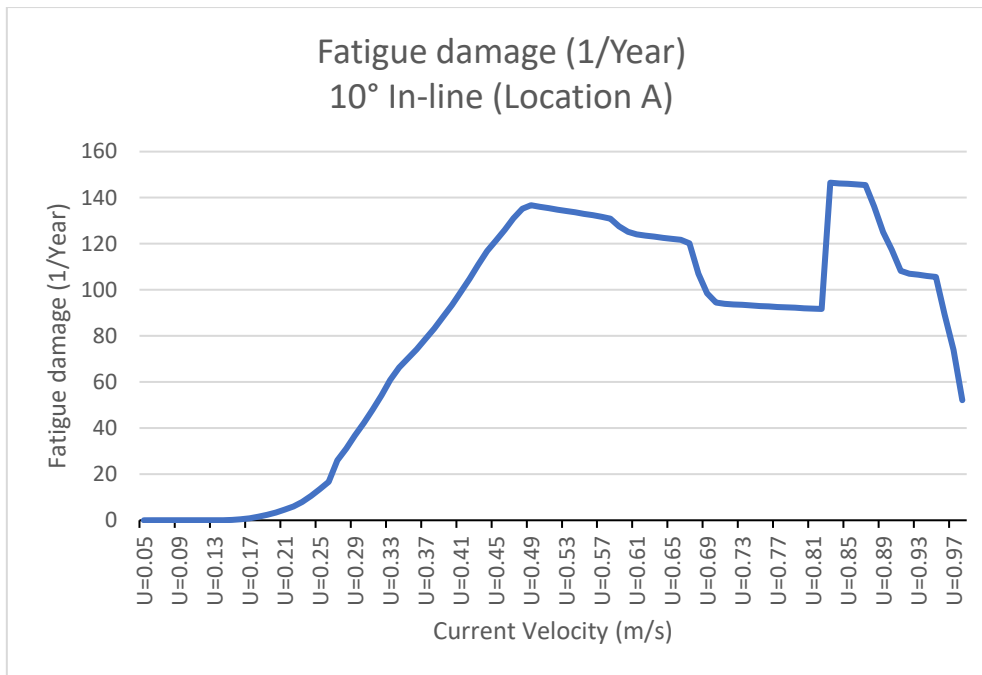


Figure 8-8: Fatigue damage per year for (Case-1(a) - 10° Flow IL) at Location A

Fatigue damage from all cases is presented in Appendix B.

8.5 Discussion

Fatigue damage is not calculated separately for flexural and torsional stresses as done by Igeh [24]. In this study, the flexural and torsional stress ranges are combined by creating block loading based on Section 4.6.1 based on their response frequencies. Hence, we get the combined fatigue damage for flexural and torsional stresses at the critical locations A and B.

8.5.1 Correlation with Igeh [24]

Fatigue damage predicted by this study is correlated with Igeh [24] and presented in Figure 8-9 to Figure 8-12. She used VIVANA and DNV's first principal method for fatigue evaluation.

1. 10° Flow

Figure 8-9 and Figure 8-10 show correlation of fatigue damage at 10° flow for critical location A and B. For a given location (A or B), fatigue damage calculated IL and CF are added to get total fatigue damage at that location.

From Figure 8-9 we can see that fatigue damage is highly over predicted for location A. This may be due to the following reasons:

1. The stress range calculated for IL and CF flow at Location A is much higher than Igeh [24] as shown in Figure 7-13 and Figure 7-14.
2. Farahani [13,14]'s fatigue parameter incorporates the effects of difference in response frequency between flexural and torsional stresses which results in higher fatigue damage prediction.

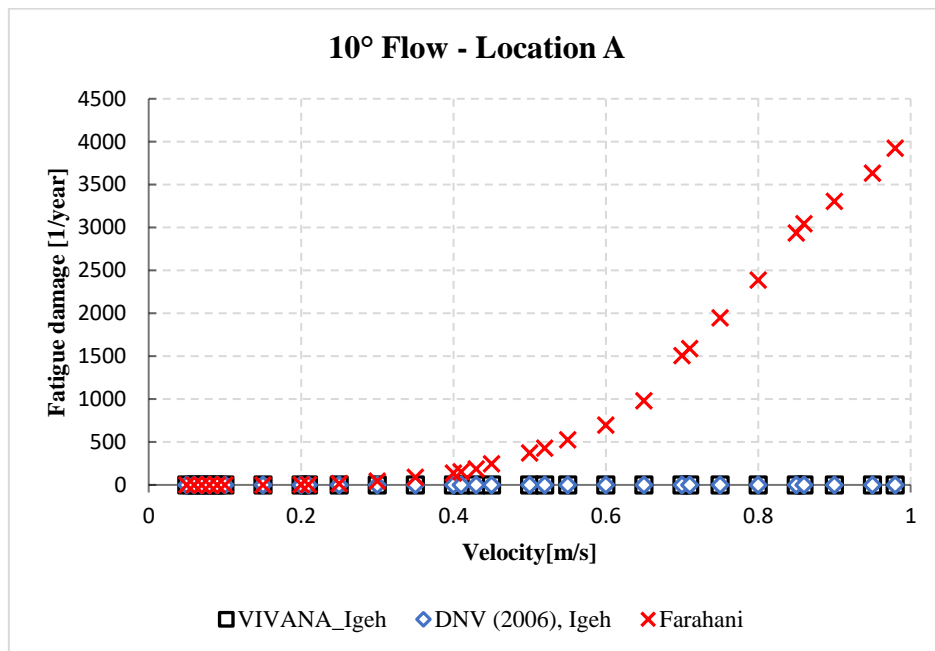


Figure 8-9: Combined fatigue damage per year for 10° Flow at Location A

From Figure 8-10 we can see that fatigue damage correlates well with Igeh [24]'s DNV based prediction for location A but is much higher than prediction based on VIVANA.

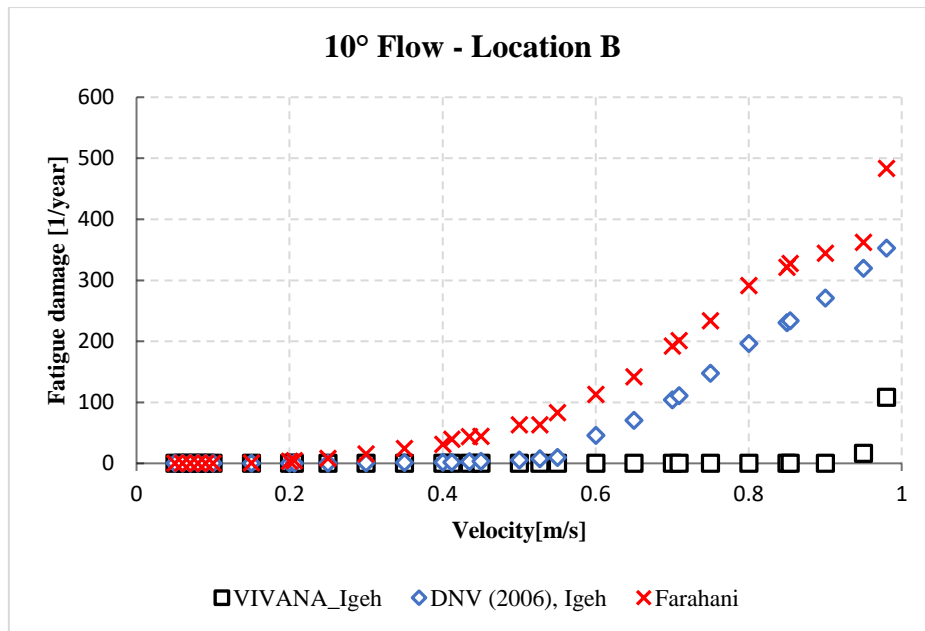


Figure 8-10: Combined fatigue damage per year for 10° Flow at Location B

2. 90° Flow

Figure 8-11 and Figure 8-12 show correlation of fatigue damage at 90° flow for critical location A and B. For a given location (A or B), fatigue damage calculated IL and CF are added to get total fatigue damage at that location.

From Figure 8-11 and Figure 8-12, we see that fatigue damage at location A is over predicted in this study. Figure 8-10 Even though the stress range prediction shows good correlation with Igeh [24] (See Figure 7-17, Figure 7-18, Figure 7-19 and Figure 7-20), fatigue damage is predicted to be higher. This may be because of difference in response frequencies between the flexural and torsional stresses.

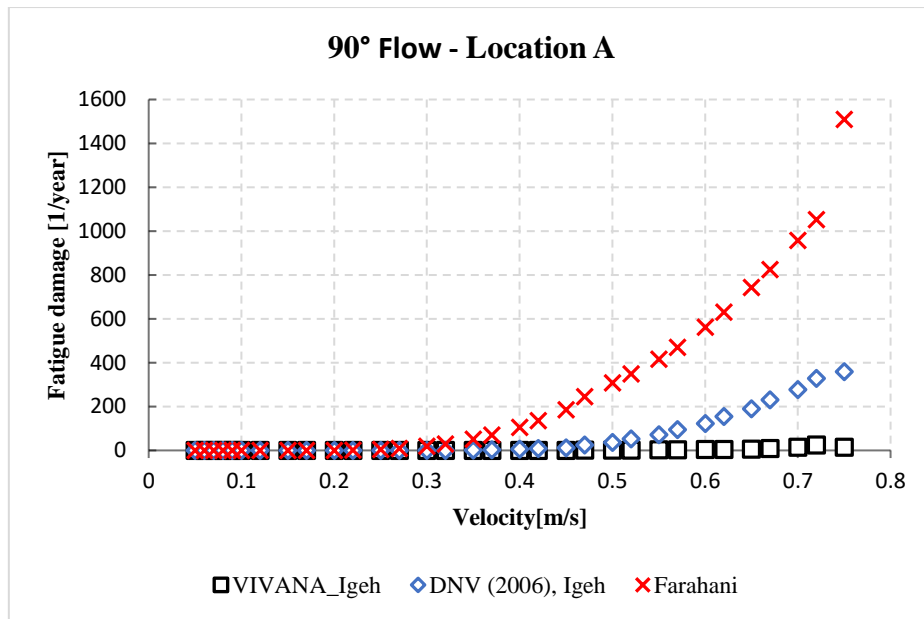


Figure 8-11: Combined fatigue damage per year for 90° Flow at Location A

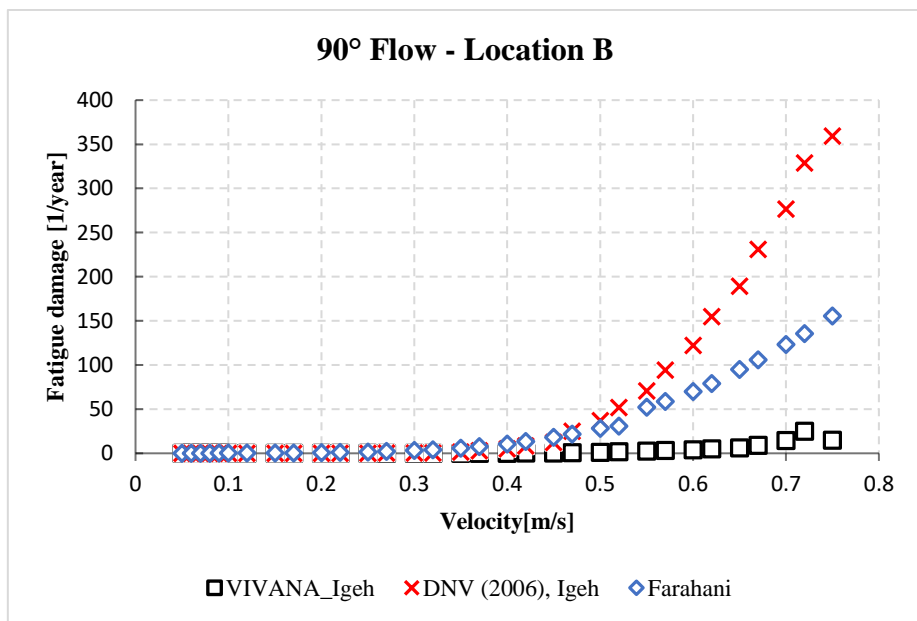


Figure 8-12: Combined fatigue damage per year for 90° Flow at Location B

8.5.2 Effect of difference in response frequencies

Fatigue damage and stress range calculations for Case-1(a) - 10° flow at location A is discussed in this section to understand the Farahani [13,14]’s fatigue damage parameter’s ability to include the effect of change of response frequencies between flexural and torsional stresses in fatigue assessment.

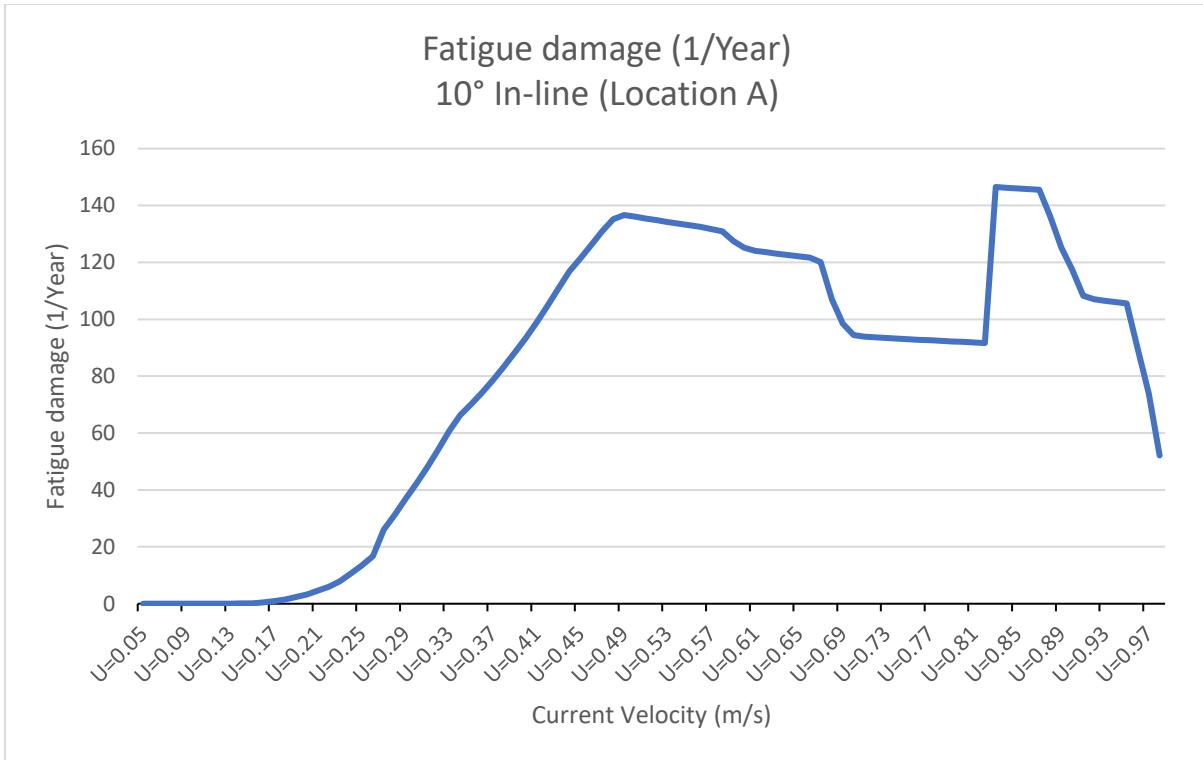


Figure 8-13: Fatigue damage per year for (Case-1(a) - 10° Flow IL) at Location A

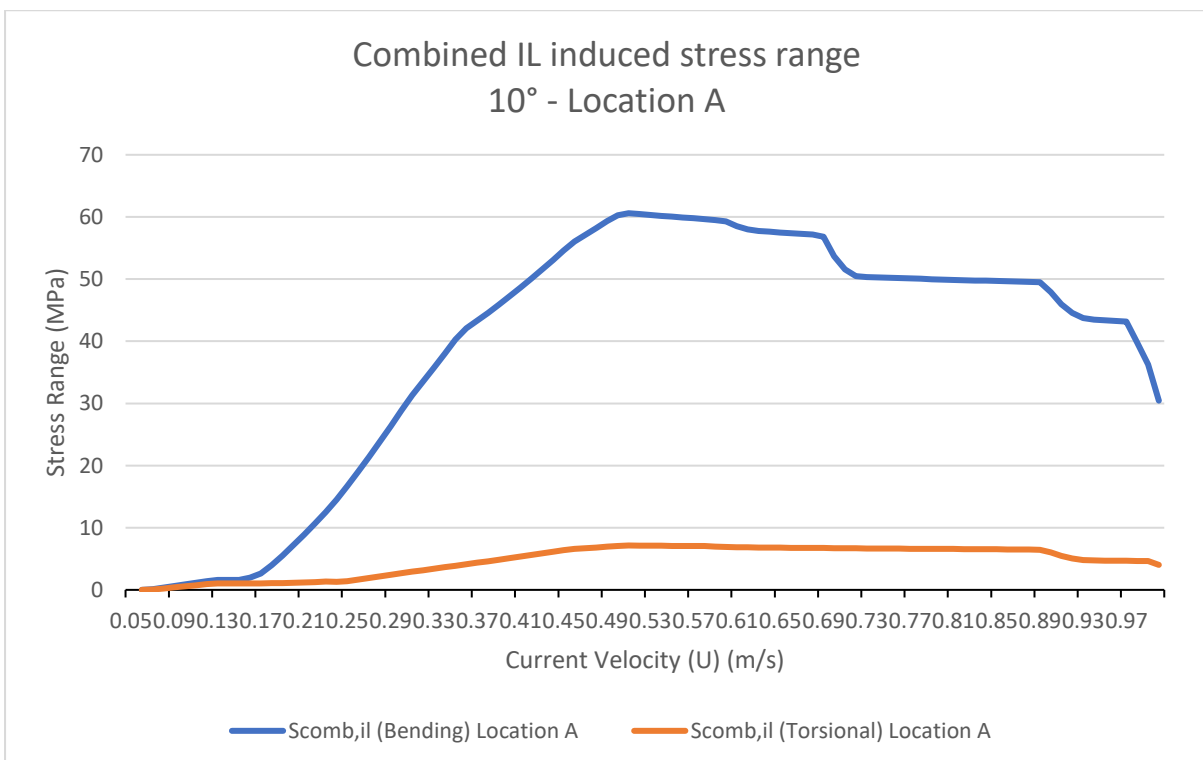


Figure 8-14: Stress range (Case-1(a) - 10° Flow IL) at Location A

From Figure 8-13 and Figure 8-14 we observe the following:

1. The fatigue damage varies according to the flexural and torsional stress range for current velocity from 0.05 m/s to 0.82 m/s. Fatigue damage and flexural stress range first increases and peaks at current velocity of 0.50 m/s. After 0.50 m/s, both decline till 0.82 m/s.
2. As the flow velocity increases from $U = 0.82$ m/s to $U=0.83$ m/s, the fatigue damage increases suddenly from 91.6 (1/Year) to 146.5 (1/Year) despite a negligible change in flexural and torsional stresses. This is an increase of 59.7%. This happens purely because of change of frequency between $U = 0.82$ m/s and $U=0.83$ m/s. At $U = 0.82$ m/s we observe only 1 cycle of flexural loading with a time period of 0.3 seconds while at $U=0.83$ m/s this decreases to 0.2 seconds, thus increasing the number of flexural stress cycles by 66.66% which can be seen as proportional to the percentage rise in fatigue damage.

9 COMPARISON WITH DNV-RP-F105 (2006 edition) [12]

The response model and stress range calculation in this study are based on DNVGL-RP-F105 (2017 edition) [11]. A similar work done by Igeh [24] is based on DNV-RP-F105 (2006 edition) which is the previous edition to the 2017 edition.

The 2006 edition is based only on straight pipelines whereas the 2017 edition has guidance for non-straight geometries such as rigid jumper in addition to the straight pipelines.

In this section, some major differences in 2006 and 2017 edition of DNVGL-RP-F105 have been highlighted and discussed by comparing results from this study to Igeh [24].

9.1 Modal analysis

9.1.1 Flow velocity reduction

In 2006 edition, a reduction in the flow velocities is recommended for flow velocities which are at an angle to the pipe run. The reduction considers only the velocity component perpendicular to the pipe run.

In 2017 edition, it has been recommended that reduction in flow velocities do not apply for modes which are classified as both IL and CF. This is applicable for 10° flow as all modes are classified as IL and CF.

9.1.2 CF and IL mode classification

In the 2006 edition, CF and IL mode classification is based only on the straight pipelines. No criteria are given for classification for non-straight geometries.

In 2017 edition, CF and IL mode classification criterion includes the non-straight geometries such as rigid jumper. The difference is mainly for flows which are at an angle to the pipe run. In this study, for the 10° flow case, all modes have been classified as both IL modes and CF modes.

Table 9-1: Comparison of mode classification for 10° and 90° flow (IL and CF) with Igeh [24]

Mode	Eigen Frequency [Hz]	Mode Classification			
		10°		90°	
		Kunal	Igeh	Kunal	Igeh
1	0.85015	IL & CF	CF	IL	IL
2	2.2297	IL & CF	CF	IL	IL
3	2.2934	IL & CF	IL	CF	CF
4	2.6431	IL & CF	IL	CF	CF
5	3.4486	IL & CF	CF	IL	IL
6	3.7582	IL & CF	IL	CF	CF
7	3.8432	IL & CF	CF	IL	IL
8	6.3956	IL & CF	CF	IL	IL
9	7.1956	IL & CF	IL	CF	CF

9.1.3 Eigen modes

In 2006 edition, guidance was given for the number of eigen modes which need to be calculated from the finite element modal analysis. According to the DNG-RP-F105 (2006 edition) [12], “three contributing cross-flow and four contributing in-line modes were sufficient to capture the underlying physics and provide accurate engineering estimate of fatigue damage”

In 2017 edition, no guidance on number of modes is provided.

9.2 Response Model

9.2.1 CF Response model

In 2006 edition, criteria for calculation of $\frac{A_{z,1}}{D}$ is based on the ratio of frequencies of two consecutive contributing CF modes (f_{ratio}). This criterion is not clear as different sets of consecutive contributing CF modes will give different values. Igeh [24] has selected the maximum of these values as the criteria for calculation of $\frac{A_{z,1}}{D}$ in the CF response model.

In 2017 edition, the criterion for selection calculation of f_{ratio} has been stated as the minimum value of all f_{ratio} values.

A comparison of the CF response models can be seen in Figure 9-1, Figure 9-2, Figure 9-3, Figure 9-4.

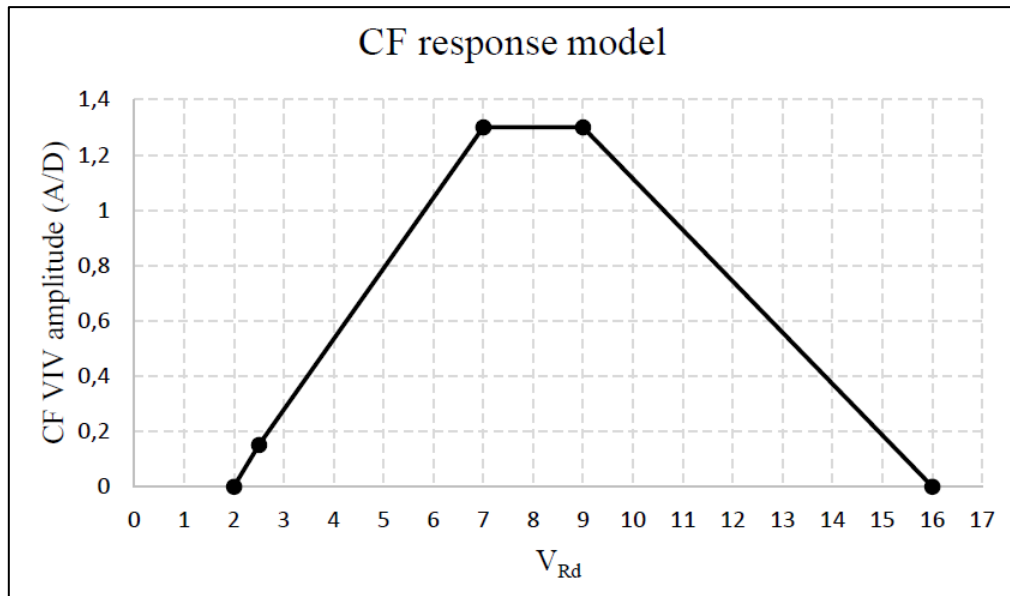


Figure 9-1: CF response model for 10-° flow (Igeh [24]) [According to DNV-RP-F105 (2006 edition)]

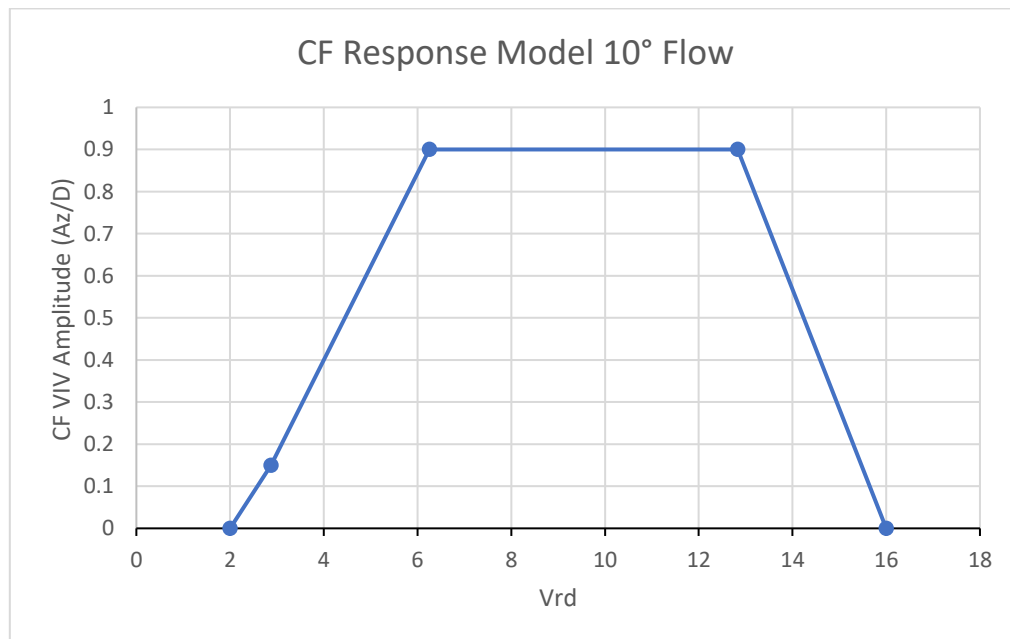


Figure 9-2: CF response model for 10-° flow [According to DNVGL-RP-F105 (2017 edition) [11]]

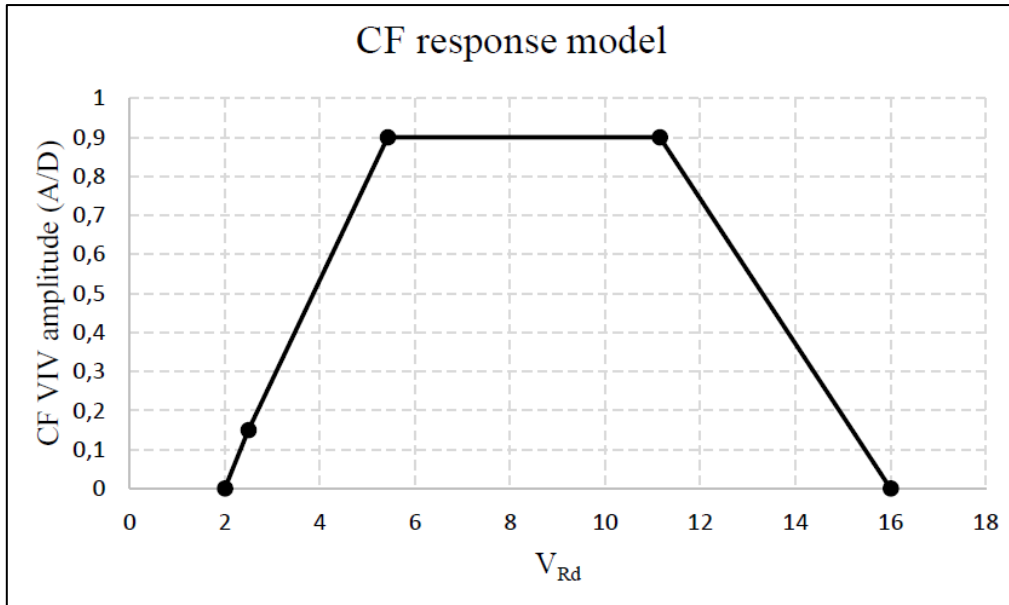


Figure 9-3: CF response model for 90-° flow (Igeh [24]) [According to DNV-RP-F105 (2006 edition)]

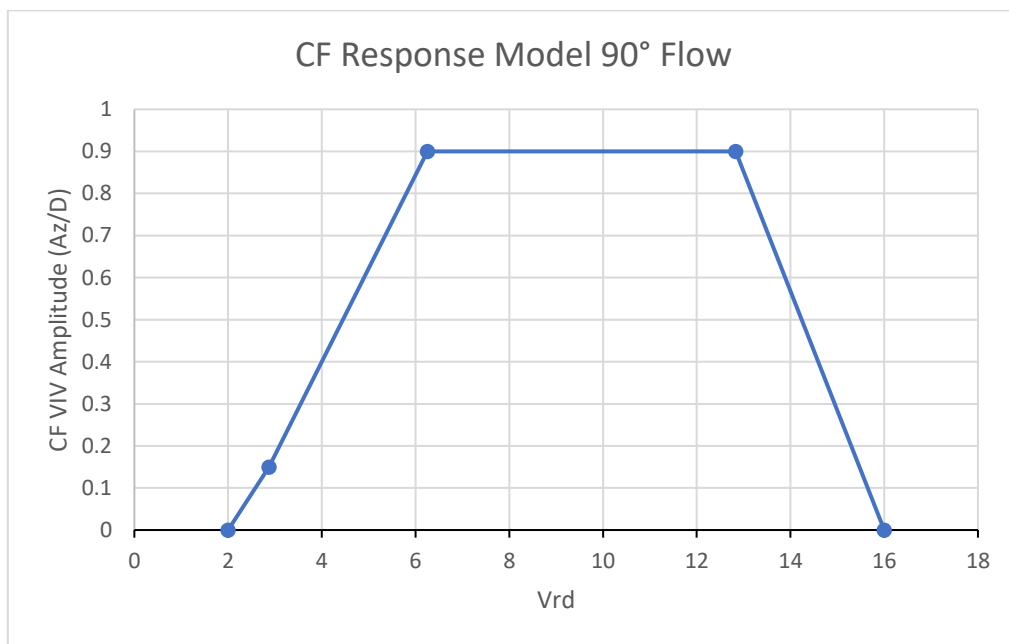


Figure 9-4: CF response model for 90-° flow [According to DNVGL-RP-F105 (2017 edition) [11]]

9.3 Stress Range Calculation

9.3.1 Contributing Modes

In the 2006 edition, cross-flow participating modes with response amplitude less than 10% of the response amplitude of dominant mode are not considered as contributing. Furthermore, modes with response amplitude greater than 10% but less than the response amplitude of dominant mode are considered as weak contributing mode. For in-line, the same criteria are used but in place of response amplitude, response stress range is considered. For stress range calculation purpose, the stress range for weak contributing modes is considered as half of the stress range for dominant mode. This criterion is given for straight pipes and applied by Igeh [24] for non-straight geometries such as the rigid jumper.

In the 2017 edition, a separate over-riding criterion is given for the non-straight geometries such as rigid jumper. For a non-straight geometry, all participating modes for both in-line and cross-flow, are considered as contributing. Also, no reduction of stress range is considered as all contributing modes are treated as dominating and full value of stress range is calculated for each of them.

9.3.2 CF induced IL response stress range

In the 2006 edition, the stress range for CF induced IL response is calculated for the 40% of the cross-flow induced VIV amplitude. The effective IL stress range is selected as the maximum of the CF induced IL stress range and IL stress range.

In the 2017 edition, the effective IL VIV induced stress range and response frequency are calculated based on the condition if the candidate mode selected for CF induced IL response is already among the contributing IL modes or not (See Case-1 and Case-2 in section 4.5.6)

10 CONCLUSION

10.1 Modal analysis

1. Modal analysis using Ansys Mechanical Workbench 17.1 gives good correlation of results with Igeh [24] and Zheng et al. [51]. This FEM method can be used to model similar rigid jumpers to determine the eigen frequencies, mode shapes and stress distribution with good accuracy and better visualization.
2. In the absence of any guidance on selection of critical location for fatigue assessment in DNVGL-RP-F105 (2017 edition) [11], design assessment module of Ansys Mechanical Workbench used to determine the critical locations for stress assessment gives good results for location A. The results for location B prove to be less conservative as compared to Igeh [24].
3. With the use of design assessment module, points on the rigid jumper with maximum flexural and maximum torsional modal stress can be identified with good accuracy. These results can be used to further develop a criterion for critical point selection over the rigid jumper which can be used for similar problems in future.

10.2 Response Model

1. IL response model predicts the amplitude response for 10° and 90° flow with good accuracy.
2. CF response model is the same for 10° and 90° flow. It appears, the CF response model is unable to capture the change in response with the change in flow direction or one of the two cases is highly conservatively constructed.

10.3 Stress Range calculation

1. Number of contributing modes at a given critical location (A or B) is not the sole governing criteria for a higher stress range at that location. Stress range is determined dynamically for a given location and current velocity by considering the number of contributing modes, unit stress amplitude (for each contributing mode) as well as the response the contributing mode is getting from the response model.

2. Torsional stress range can be determined using the same procedure as for the flexural stress range from DNVGLRP-F105 (2017 edition) [11].
3. The response frequencies for flexural and torsional stresses can be estimated using DNVGL-RP-F105 (2017 edition) [11] which can be used to estimate the block loading for the full range of current velocities for fatigue assessment.
4. Selection of critical location B based on maximum combined torsional modal stress criterion gives less conservative results according to this study. On the other hand, criterion adopted by Igeh [24] is subjective and cannot be used universally for other rigid jumper problems. Selection criterion for critical location B needs to be studied. One possible criterion may be based on the largest range (difference) of flexural and torsional modal stresses.
5. Stress range calculated for 10° flow based on DNVGL-RP-F105 (2017 edition) [11] gives very conservative results for rigid jumper. The stress range predicted for 10° flow includes stresses from all modes which have been classified as both IL and CF.

10.4 Fatigue assessment

1. Using block loading methodology, the flexural and torsional stress and response frequencies at every current velocity can be successfully combined to represent a combined effect.
2. Farahani [13,14]'s fatigue damage parameter is successfully able to consider the difference in response frequencies between the flexural and torsional stresses and its impact on the fatigue damage.
3. Fatigue assessment using Farahani [13,14]'s fatigue damage parameter gives higher fatigue damage compared to the fatigue damage assessed by Igeh [24]
4. Changes in frequency of stress loading for the full range of current velocity has been successfully incorporated in the fatigue assessment.
5. Fatigue parameter successfully describes the critical planes and can be used to determine the fatigue damage at the critical plane.

10.5 Comparison between 2017 edition and 2006 edition of DNVGL-RP-F105

1. CF response model in 2017 edition tends to give lower peak amplitude response value as the requirement of taking the minimum value of f_{ratio} has been clarified in this edition. The 2006 edition left it to the discretion of the designer to take the minimum or the maximum value of f_{ratio} leading to chances of a higher peak amplitude response calculation during CF response model construction. This can be seen in the CF response model for 10° flow in this study that gives a lower peak amplitude response as compared to Igeh [24].
2. Requirements given for non-straight geometries (such as rigid jumper) in 2017 edition differentiates the design approach for a rigid jumper from a straight pipeline. It has impact on the following design parameters:

- a. Mode classification

Modes are no longer classified strictly in-line or cross-flow. It can be both in-line and cross-flow

- b. Stress range calculation

Stress range calculation from all contributing modes is done assuming they all are dominant modes. This leads to double stress contribution from otherwise weak contributing modes. Thus, increases the combined stress range significantly.

- c. Amplitude response

No reduction in velocity, hence higher V_{rd} , resulting early prediction of response from response model.

11 FUTURE WORK

Following are some recommendations for future work that can be carried out:

1. Inclusion of mean stress and its effects on the fatigue damage can be assessed.
2. Effects of variation of internal pressure and its effect on the fatigue damage in the multiaxial stress state can be accessed.
3. The Farahani [13,14]'s fatigue parameter can be used to access the fatigue damage in non-planar rigid jumper designs.

12 REFERENCES

1. Achenbach E. and Heinecke E. (1981), "On vortex shedding from smooth and rough cylinders in the range of Reynolds numbers 6×10^3 to 5×10^6 ", *Journal of Fluid Mechanics*, 109, page. 239-251
2. Andrews R.M. (1986). "High temperature fatigue of AISI 316 stainless steel under complex biaxial loading.", PhD thesis, University of Sheffield, UK, 1986.
3. ANSYS Inc. (2017 edition). ANSYS Mechanical [Software], version 17.1
4. ANSYS Inc. (2017 edition). ANSYS Mechanical APDL Structural Analysis Guide. Canonsburg, PA 15317.
5. Bäckström M. (2003). "Multiaxial fatigue life assessment of welds based on nominal and hot-spots stresses", Ph.D. Thesis. VTT publications no. 502, Espoo, Finland, 2003.
6. Blevins R.D. (2001), "Flow-induced vibrations", Second edition, Krieger Publishing Company, Malabar, Florida, USA
7. Brown, M.W., and Miller, K.J. (1973), "A Theory for Fatigue Under Multiaxial Stress-Strain Conditions," *Proceedings of the Institute of Mechanical Engineers*, Vol. 187, 1973, page. 745-756
8. Carpinteri A. and Spagnoli A. (2001), "Multiaxial high-cycle fatigue criterion for hard metals.", *Int. J. Fatigue*, 23 (2), page. 135-145.
9. Chu C.C., Conle F.A. and Bonnen J.F. (1993). "Multiaxial stress-strain modelling and fatigue life prediction of SAE axle shafts.", In: McDowell DL, Ellis R, editors. *Advances in multiaxial fatigue*, ASTM STP 1191. Philadelphia: American Society for Testing and Materials, 1993: page. 37-54.
10. Dang-Van K. (1993), "Macro-Micro Approach in High-Cycle Multiaxial Fatigue", *Advances in Multiaxial Fatigue*, ASTM STP 1191, D.L. McDowell and R. Ellis, Eds., American Society for Testing and Materials, Philadelphia, page. 120-130.
11. DNVGL-RP-F105 Free spanning pipelines (2017 edition). DNV, Norway.
12. DNV-RP-F105 Free spanning pipelines (2006 edition). DNV, Norway.
13. Farahan A.V. (2003). "Critical Plane-Energy Based Approach For Assessment Of Biaxial Fatigue Damage where The Stress-Time Axes Are At Different Frequencies.", *Biaxial and Multiaxial Fatigue and Fracture*, ESIS Publication, page. 203-221.
14. Farahani A.V. (2000). "A new energy-critical plane parameter for fatigue life assessment of various metallic materials subjected to in-phase and out-of-phase

- multiaxial fatigue loading conditions”, *International Journal of Fatigue* 22, page. 295-305.
15. Findley W. N. (1959). “A theory for the effect of mean stress on fatigue of metals under combined torsion and axial load or bending”. *Journal of Engineering for Industry*. Vol. 81, 1959, page. 301-306.
 16. Garud Y.S. (1979). “A new approach to the evaluation of fatigue under multiaxial loadings.”, In: Ostergren WJ, Whitehead JR, editors. *Proceedings of the Symposium on Methods for Predicting Materials Life in Fatigue*. New York: American Society of Mechanical Engineers, 1979: page. 247–63.
 17. Garud Y.S. (1981). “A new approach to the evaluation of fatigue under multiaxial loadings.”, *Trans ASME* 1981;103: page.118–25.
 18. Gentilcore M.L. and Dexter R.J. (1997), " Ductile Tearing of Welded Structural Details " in Piascik R.S., Newman J.C. and Dowling N.E., “Fatigue and Fracture Mechanics”, STP1296, 27th Volume, ASTM International
 19. Glinka G, Shen G. and Plumtree A. (1995). “A multiaxial fatigue strain energy density parameter related to the critical plane.”, *Fatigue Fract Eng Mater Struct* 1995;18:page. 37–46.
 20. Gough H.J., Pollard H.V. and Clenshaw W.J. (1951) “Some Experiments on the Resistance of Metals Under Combined Stress”, Ministry of Supply, Aeronautical Research Council Reports and Memoranda No. 2522, HMSO, London, 1951
 21. Govardhan R.N. and Williamson C.H.K. (2006 edition), “Defining the Modified Griffin Plot in Vortex-Induced Vibration: Revealing the Effect of Reynolds Number Using Controlled Damping”, *Journal of Fluid Mechanics* 561, page. 147-180
 22. Gustafsson J. and Saarinen J. (2007). “Multi-axial fatigue in welded details.”, Master’s Thesis in the Master Degree Programme Civil Engineering, Chalmers University Of Technology
 23. Ibrahim A., Ryu Y. and Saidpour M. (2015) “Stress Analysis of Thin-Walled Pressure Vessels”, Scientific Research Publishing Inc.
 24. Igeh L.A. (2016). “VIV Fatigue Investigation for Subsea Planar Rigid Spools and Jumpers”, Master Thesis, University of Stavanger.
 25. ISO/R 373 (1964). “General principles for fatigue testing of metals” .ISO/TC 164/SC 5 Fatigue testing

26. Klamo J.T, Leonard A. and Roshko, A. (2005), "On the Maximum Amplitude of a Freely Vibrating Cylinder in Cross-Flow", *Journal of Fluids and Structures* 21, page. 429-434
27. Lienhard J. H. (1966), "Synopsis of life, drag and vortex frequency data for rigid circular cylinder", Bulletin 300, Washington State University, College of Engineering, Research Division.
28. Liu K.C. (1984). "A method based on virtual strain–energy parameters for multiaxial fatigue." In: McDowell DL, Ellis R, editors. ASTM STP 1191. Philadelphia: American Society for Testing and Materials, 1993: page. 67–84.
29. McDiarmid D.L. (1985). "Fatigue under out-of-phase biaxial stresses of different frequencies". Miller, K.J. and Brown, M.W., (Eds). *Multiaxial Fatigue*, ASTM STP 853 Philadelphia: American Society for Testing and Materials, page. 606-621.
30. McDiarmid D.L. (1989). "The effect of mean stress on biaxial fatigue where the stresses are out-of-phase and at different frequencies". Brown, M.W. and Miller, K.J., (Eds). *Biaxial and Multiaxial Fatigue*, EGF3. London, page. 605-619.
31. McDiarmid D.L. (1991). "Mean stress effects in biaxial fatigue where the stresses are out-of-phase and at different frequencies". ESIS 10, Kussmual, K., McDiarmid, D. And Socie, D. (Eds), London, page. 321-335.
32. Norway. Inquiry Commission For The "Alexander L. Kielland" Accident (1981), "Norwegian Public Reports - the "Alexander L. Keilland" Accident"
33. Papadopoulos I. V. (2001). "Long life fatigue under multiaxial loading". *International Journal of Fatigue*, Vol. 23, 2001, page. 839-849.
34. Papadopoulos I. V., Davoli P., Gorla C., Filippini M. and Bernasconi A. (1997). "A comparative study of multiaxial high-cycle fatigue criteria for metals". *International Journal of Fatigue*. Vol.19, 1997, page. 219-235.
35. Pipeline Accident Number: DCA-00-MP-004 "Pipeline Accident Brief (2001) - Marathon Ashland Pipe Line LLC, Winchester, Kentucky", National Transportation Safety Board Washington, D.C. 20594
36. Ramberg S. (1983). "The effects of yaw and finite length upon the vortex wakes of stationary and vibrating circular cylinders", *Journal of Fluid Mechanics*, 128, page. 81-107
37. Resvanis T.L., Jhingran V., Vandiver J.K. and Liapis S. (2012), "Reynolds Number Effects on The Vortex-Induced Vibration Of Flexible Marine Risers", *Proceedings of*

- the ASME 2012 31st International Conference on Ocean, Offshore and Arctic Engineering OMAE2012 July 1-6, 2012, Rio de Janeiro, Brazil
38. Roger K. (1977), "A review of vortex shedding research and its application", *Ocean Engineering*, Volume 4, Issue 3, page. 141-171
 39. Sines G. (1961). "The prediction of fatigue fracture under combined stresses at stress concentrations.", *Bull Jpn SOC Mech Eng.* 4(15), page. 443-453.
 40. Smith J.O. (1942) "Effect of range of stress on fatigue strength of metals.", University of Illinois, Engineering Experiment Station, Bul no. 334,39(26).
 41. Smith R.N., Watson P. and Topper T.H. (1970), "A Stress-Strain Parameter for the Fatigue of Metals", *Journal of Materials*, Vol. 5, No. 4, page. 767-778
 42. Socie D. (1987) "Multiaxial fatigue damage models.", *J Eng Mater Technol*, 109, page. 293-298.
 43. Socie D. and Marquis G. (2000), "Multiaxial Fatigue", Society of Automotive Engineers SAE International, 2000.
 44. Suresh S. (1991). "Fatigue of materials", Cambridge University Press
 45. Tipton S.M. (1984). "Fatigue behaviour under multiaxial loading in the presence of a notch: methodologies for the prediction of life to crack initiation and life spent in crack propagation.", PhD thesis, Mechanical Engineering Department, Stanford University, Stanford, CA, 1984.
 46. Wang Y.Y. and Yao W.X. (2003), "Evaluation and comparison of several multiaxial fatigue criteria", *International Journal of Fatigue*, Vol. 26, 2004, page.17-25.
 47. Wang, H., Huang, J., Lee, S., Gioielli, P., Kan, W., Spencer, D., & Islam, M. (2013). VIV Response of a Subsea Jumper in Uniform Current. Paper presented at the ASME 2013 32nd International Conference on Ocean, Offshore and Arctic Engineering(OMAE2013-11417), Nantes, France.
 48. Xiao R., Li X., Lang L., Chen Y. and Ge Y. (2015), "Design Of Biaxial Tensile Cruciform Specimen Based On Simulation Optimization", 2nd International Conference on Machinery, Materials Engineering, Chemical Engineering and Biotechnology.
 49. Yoshio K. and Hideo K. (1980), "Capsize of Offshore Oil Drilling Platform", Japan Crane Association and Tokyo Institute of Technology
 50. You B.R. and Lee S.-B. (1995). "A critical review on multiaxial fatigue assessments of metals", *International Journal of Fatigue*. Vol. 18, No. 4, 1996, page. 235-244.

51. Zheng, H., Slocum, S. T., Huang, J. Z., Srivastava, V., Lee, S., & Wang, H. H. (2015). Numerical Analysis of Experimental Data of Subsea Jumper Vortex Induced Vibrations. Paper presented at the ASME 2015 34th International Conference on Ocean, Offshore and Arctic Engineering(OMAE2015-41224), Newfoundland, Canada.
52. Carruth A.L. and Cerkovnik M.E. (2007), “Jumper VIV – New Issues for New Frontiers”, Proceedings of the Sixteenth (2007) International Offshore and Polar Engineering Conference, Lisbon, Portugal, July 1-6, 2007
53. Guo B., Song S., Chacko J. and Ghalambor A. (2005), “Offshore Pipelines”, 1st Edition, Imprint: Gulf Professional Publishing, Published Date: 25th April 2005, Elsevier
54. Masilamani V. (2015), “Vortex Induced Vibration (VIV) Analysis of Subsea Rigid jumpers”, Master Thesis, University of Stavanger, Norway
55. Cesareo de La Rosa Siqueira, Wikipedia, Source: <http://www.mcef.ep.usp.br/staff/jmeneg/casareo/vort2.gif>
56. NTNU course material. Source: <http://www.ivt.ntnu.no/imt/courses/tmr7/resources/>

13 APPENDIX A

Appendix A contains stress range results from following cases for location A and B:

1. 10° Flow
 - a. In-line VIV
 - b. Cross-flow VIV
2. 90° Flow
 - a. In-line VIV
 - b. Cross-flow VIV

10° Flow In-line

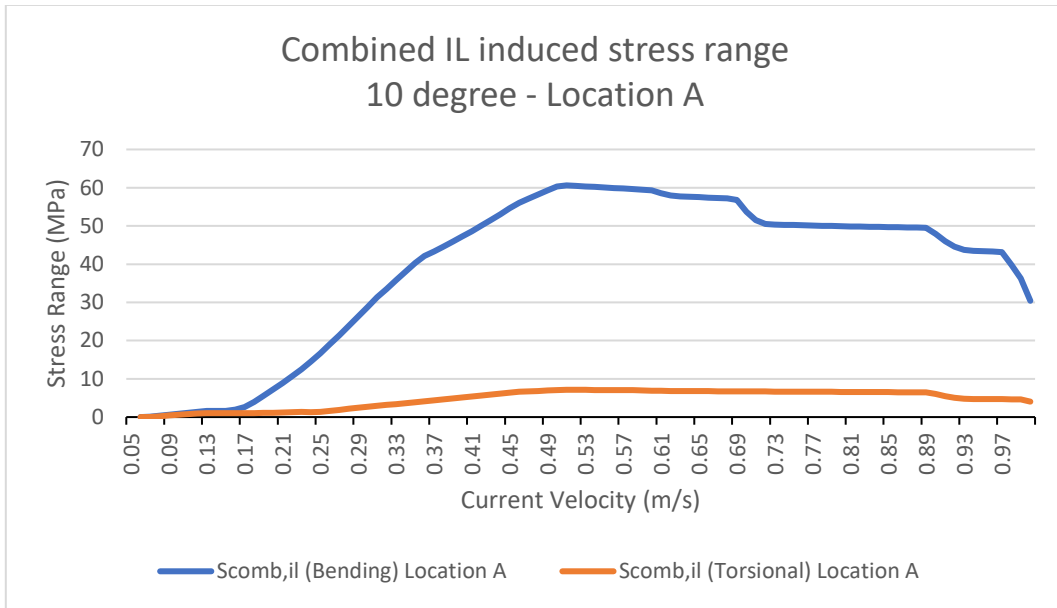


Figure 13-1: Combined flexural and torsional stress range from all contributing modes (Case-1(a) - 10° Flow IL) at Location A

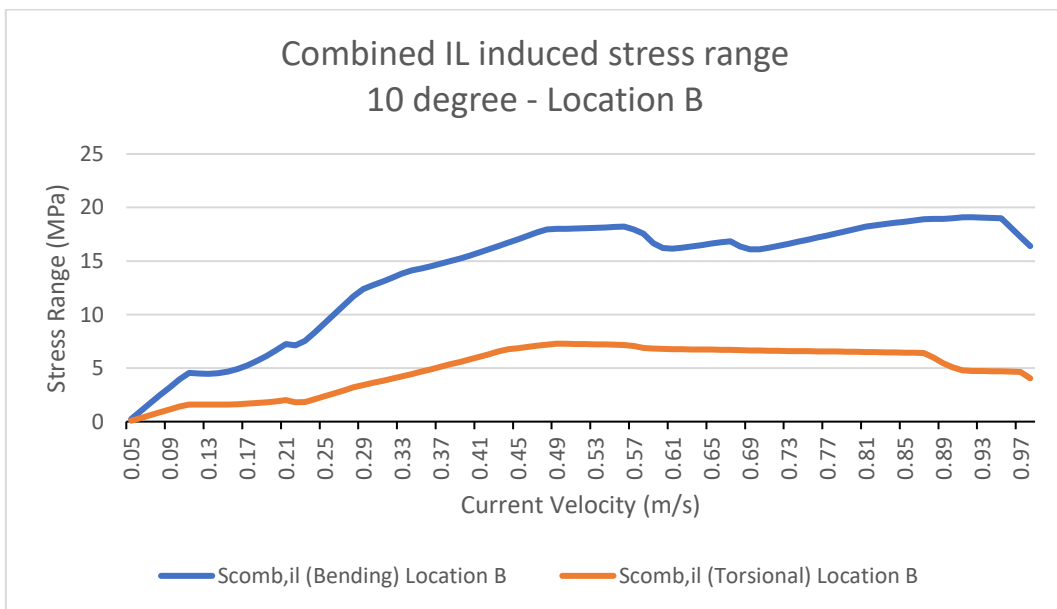


Figure 13-2: Combined flexural and torsional stress range from all contributing modes (Case-1(a) - 10° Flow IL) at Location B

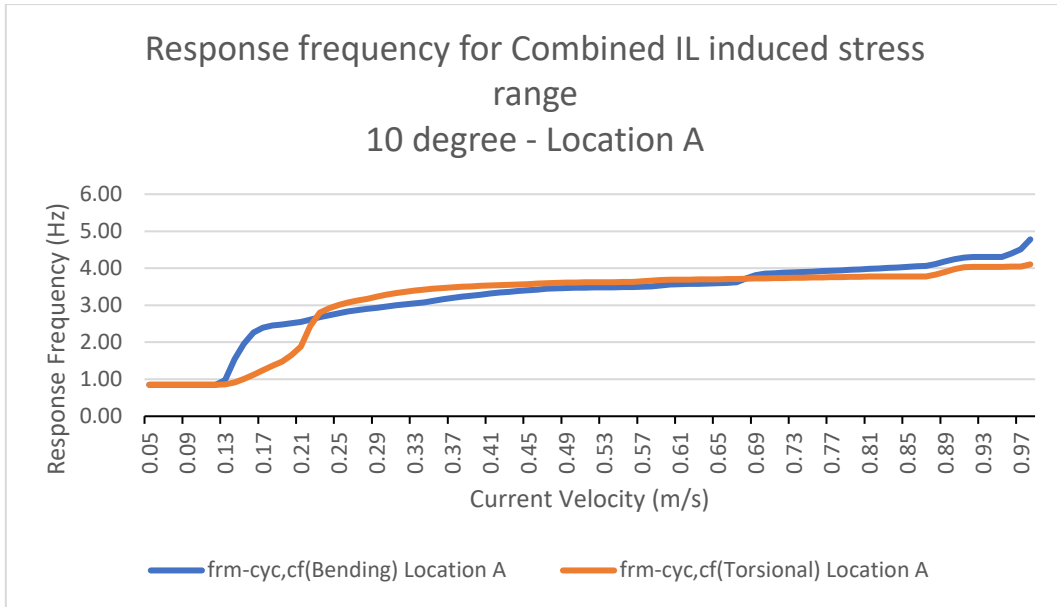


Figure 13-3: Response frequency for combined flexural and torsional stress range from all contributing modes (Case-1(a) - 10° Flow IL) at Location A

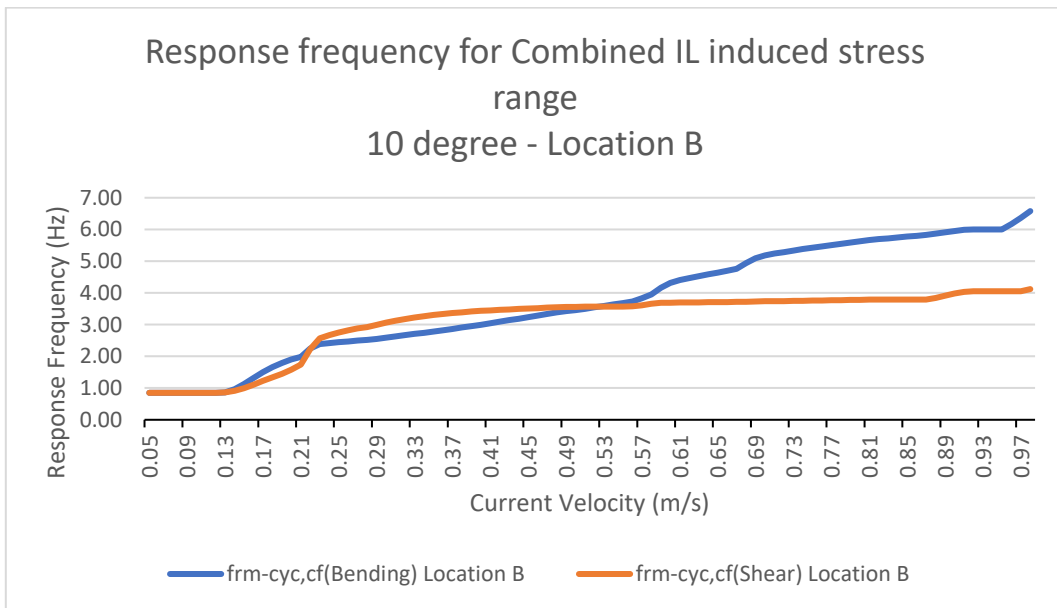


Figure 13-4: Response frequency for combined flexural and torsional stress range from all contributing modes (Case-1(a) - 10° Flow IL) at Location B

10° Flow Cross-flow

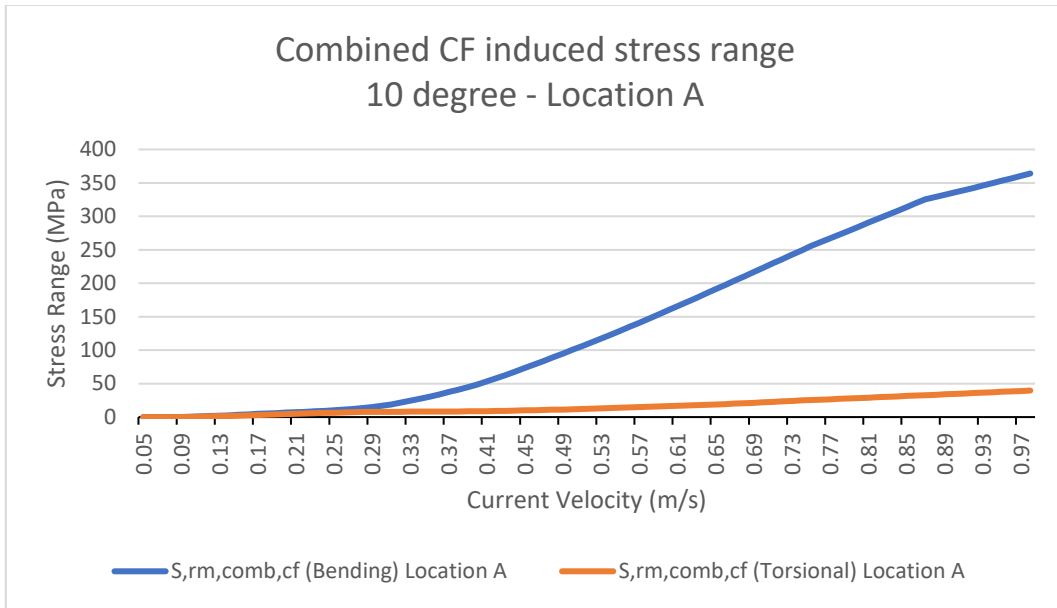


Figure 13-5: Combined flexural and torsional stress range from all contributing modes (Case-1(b) - 10° Flow CF) at Location A

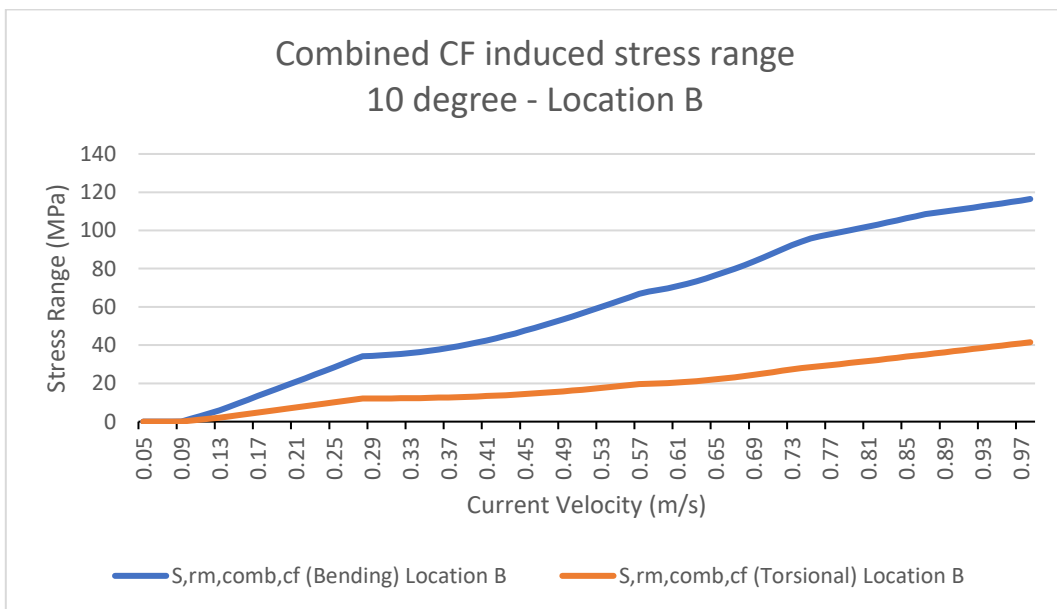


Figure 13-6: Combined flexural and torsional stress range from all contributing modes (Case-1(b) - 10° Flow CF) at Location B

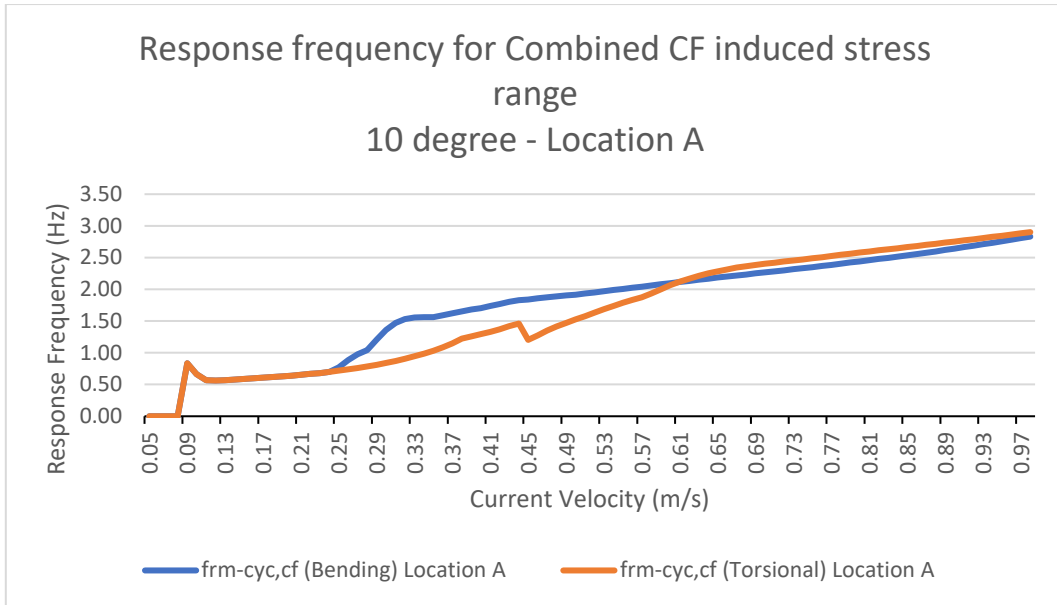


Figure 13-7: Response frequency for combined flexural and torsional stress range from all contributing modes (Case-1(b) - 10° Flow CF) at Location A

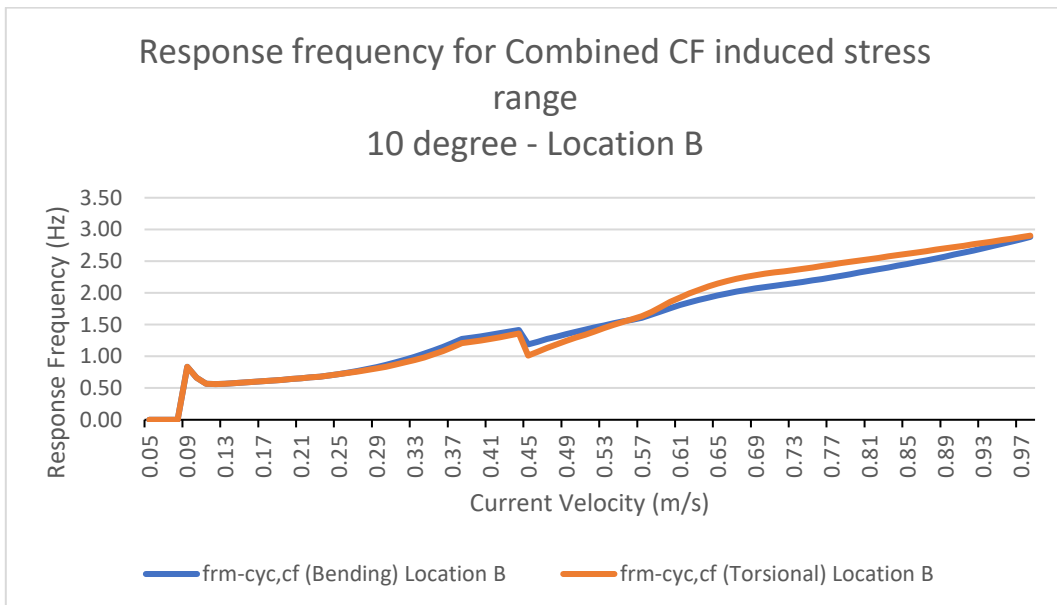


Figure 13-8: Response frequency for combined flexural and torsional stress range from all contributing modes (Case-1(b) - 10° Flow CF) at Location B

90° Flow In-line

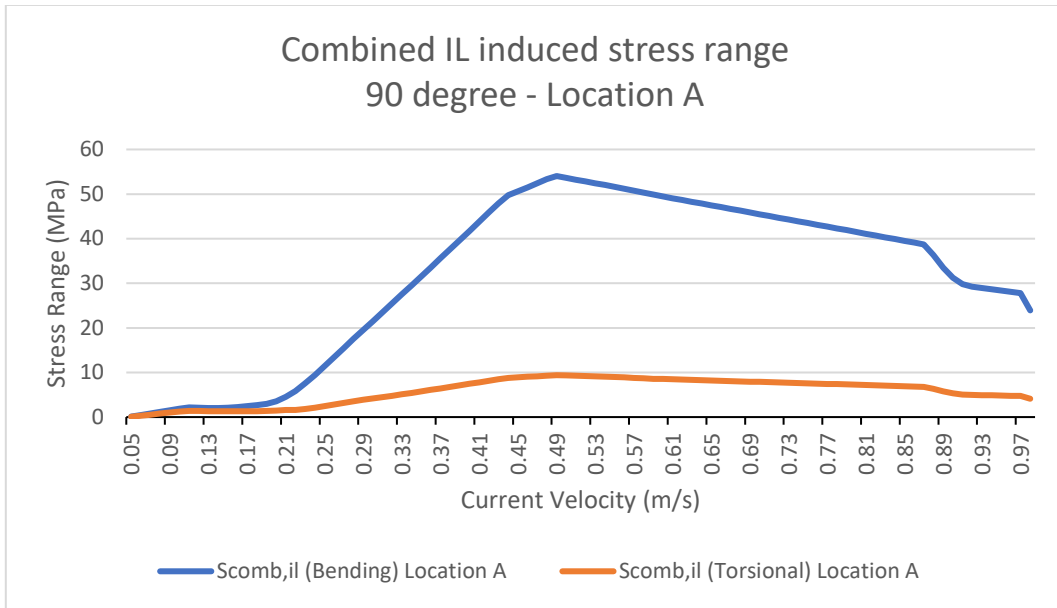


Figure 13-9: Combined flexural and torsional stress range from all contributing modes (Case-2(a) - 90° Flow IL) at Location A

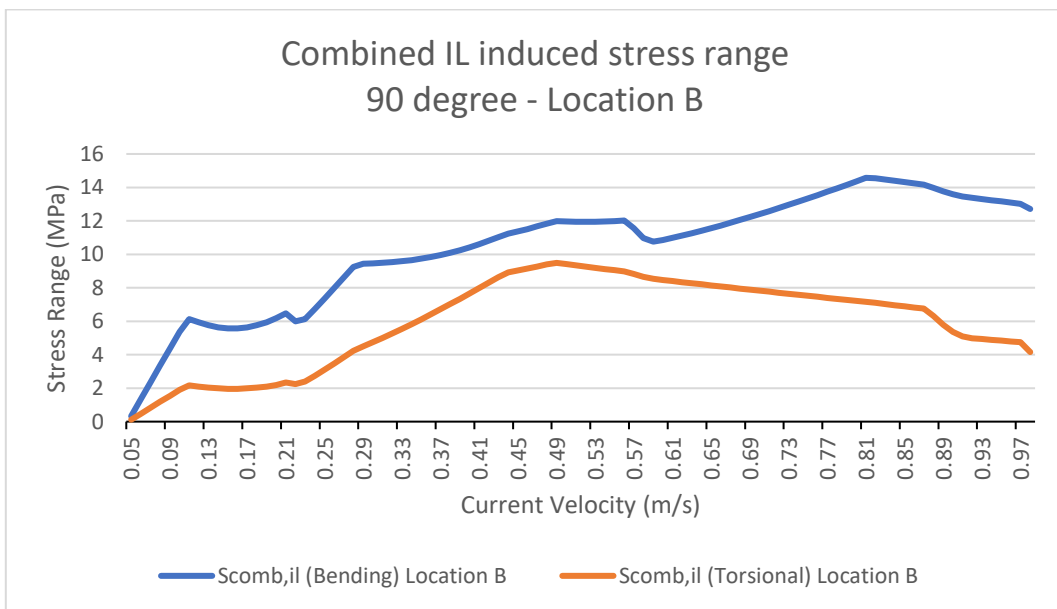


Figure 13-10: Combined flexural and torsional stress range from all contributing modes (Case-2(a) - 90° Flow IL) at Location B

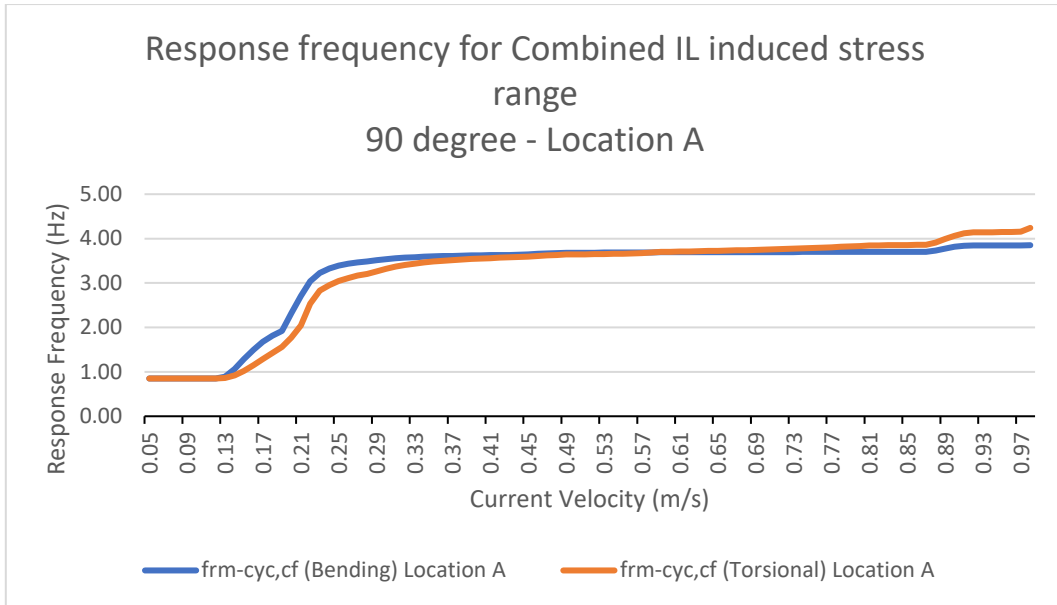


Figure 13-11: Response frequency for combined flexural and torsional stress range from all contributing modes (Case-2(a) - 90° Flow IL) at Location A

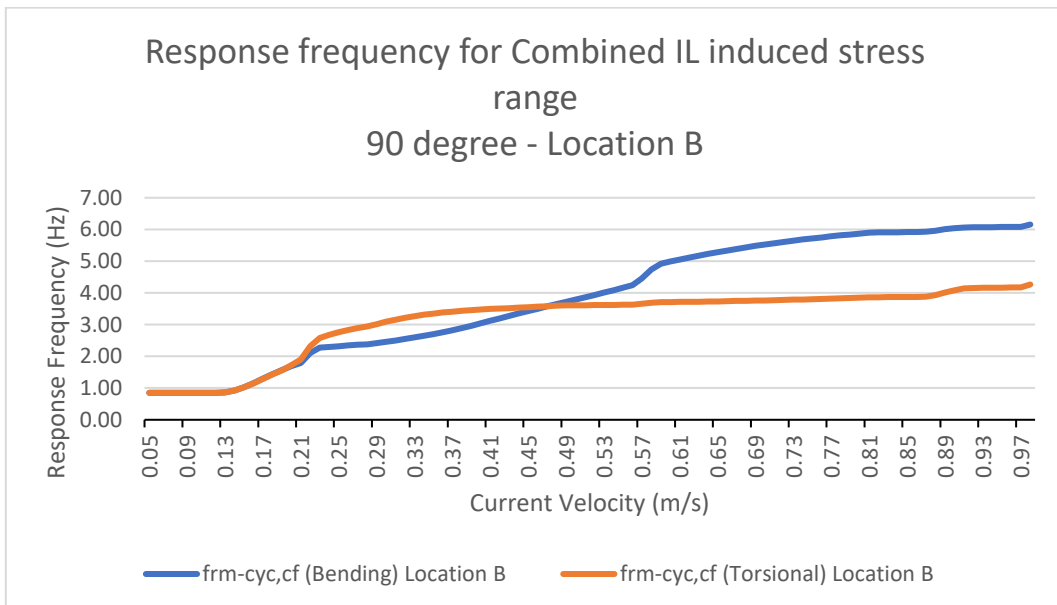


Figure 13-12: Response frequency for combined flexural and torsional stress range from all contributing modes (Case-2(a) - 90° Flow IL) at Location A

90° Flow Cross-flow

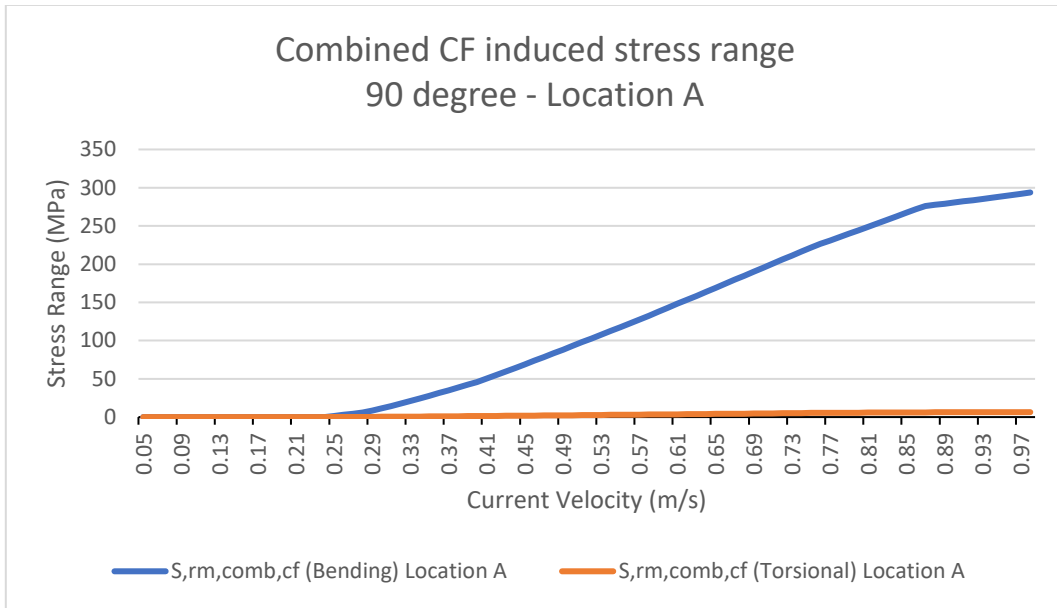


Figure 13-13: Combined flexural and torsional stress range from all contributing modes (Case-2(b) - 90° Flow CF) at Location A

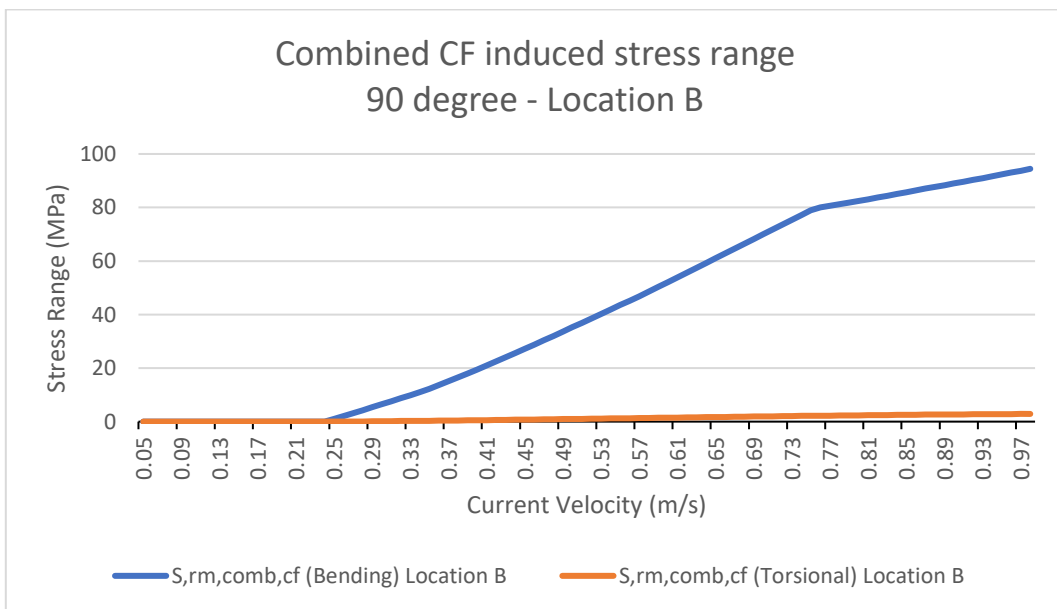


Figure 13-14: Combined flexural and torsional stress range from all contributing modes (Case-2(b) - 90° Flow CF) at Location B

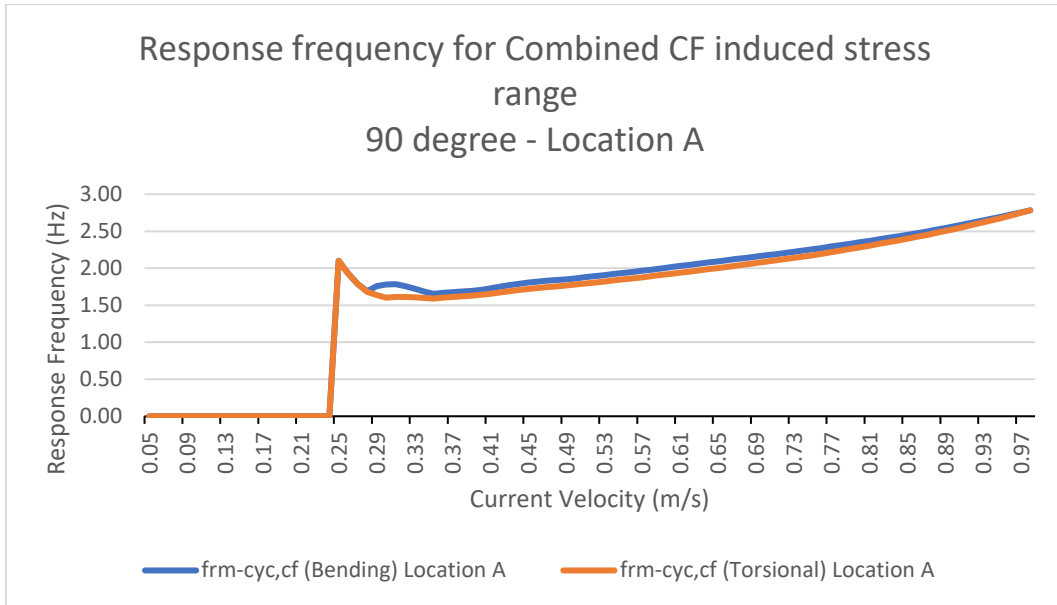


Figure 13-15: Response frequency for combined flexural and torsional stress range from all contributing modes (Case-2(b) - 90° Flow CF) at Location A

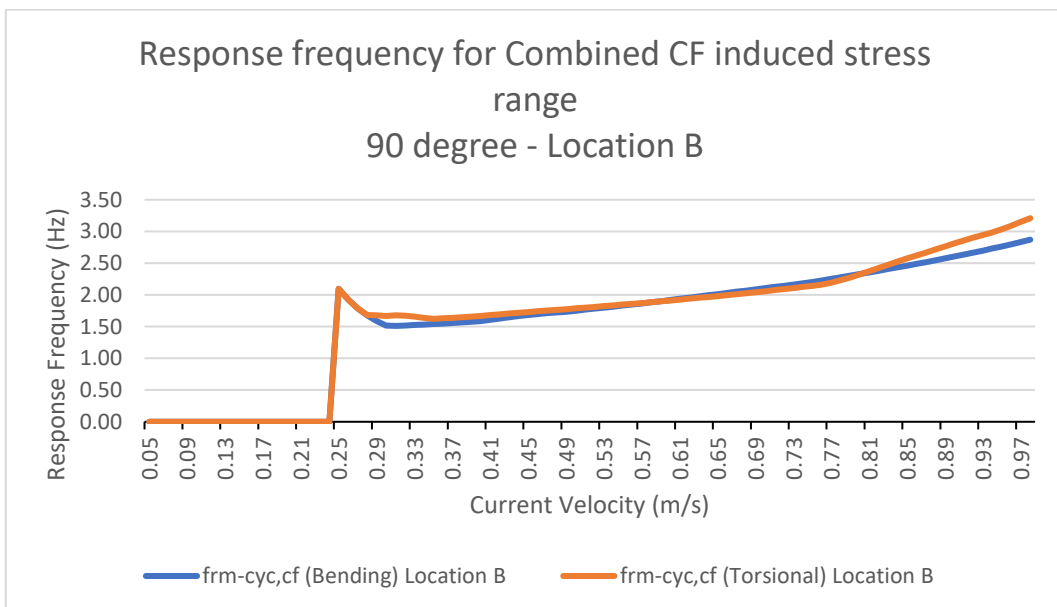


Figure 13-16: Response frequency for combined flexural and torsional stress range from all contributing modes (Case-2(b) - 90° Flow CF) at Location B

14 APPENDIX B

Appendix B contains fatigue damage assessment results from following cases for location A and B:

1. 10° Flow
 - a. In-line VIV
 - b. Cross-flow VIV
2. 90° Flow
 - a. In-line VIV
 - b. Cross-flow VIV

Case-1 (a) – 10° IL Location A

1. Principal Stress and Strains

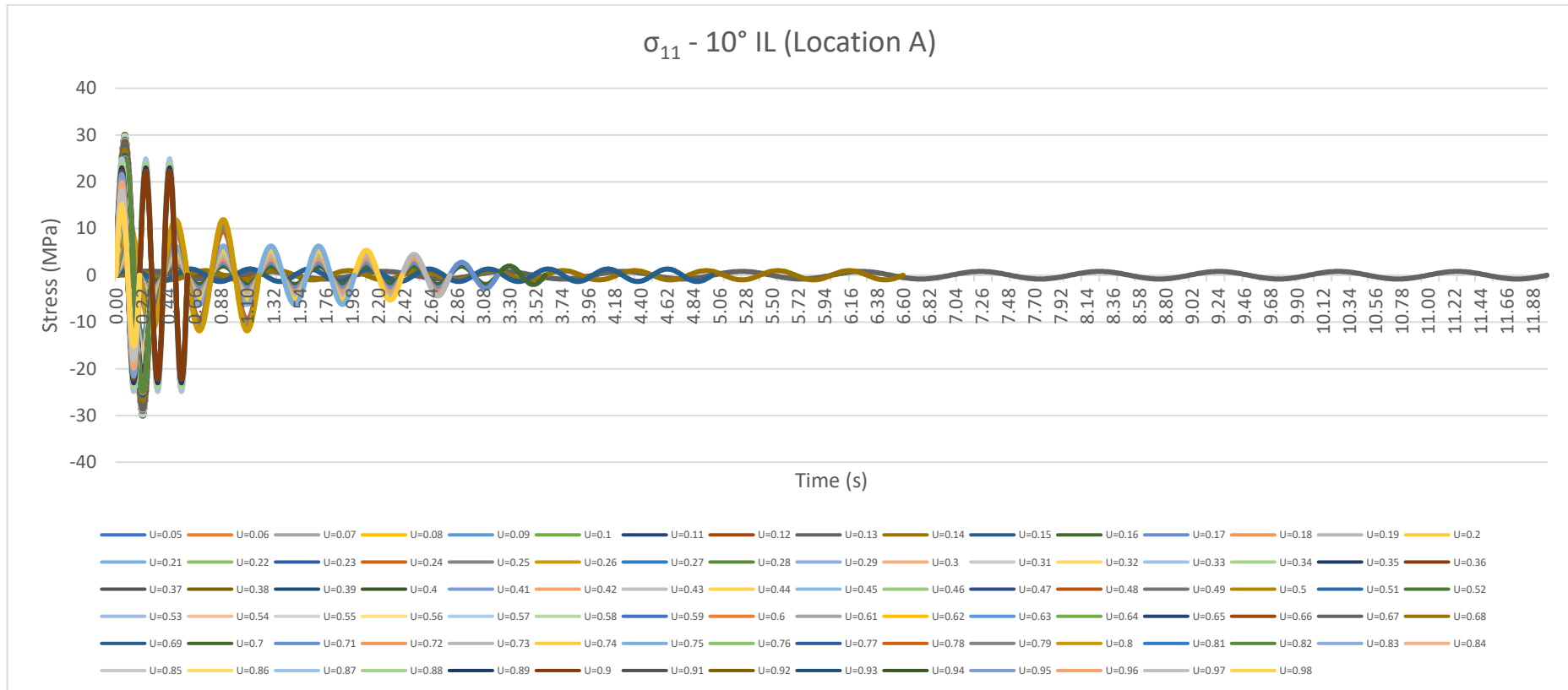


Figure 14-1: σ_{11} (Case-1(a) - 10° Flow IL) at Location A

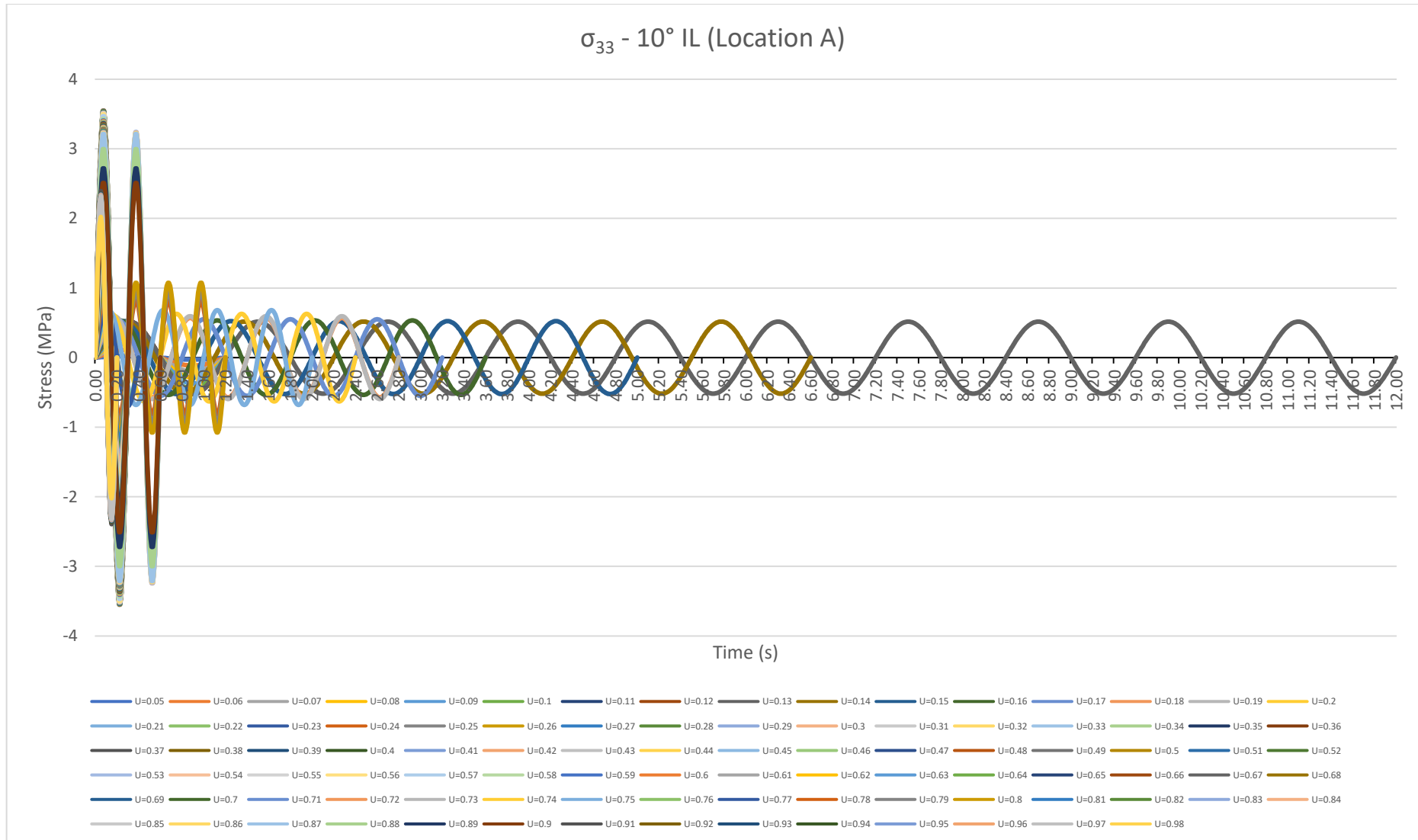


Figure 14-2: σ_{33} (Case-1(a) - 10° Flow IL) at Location A

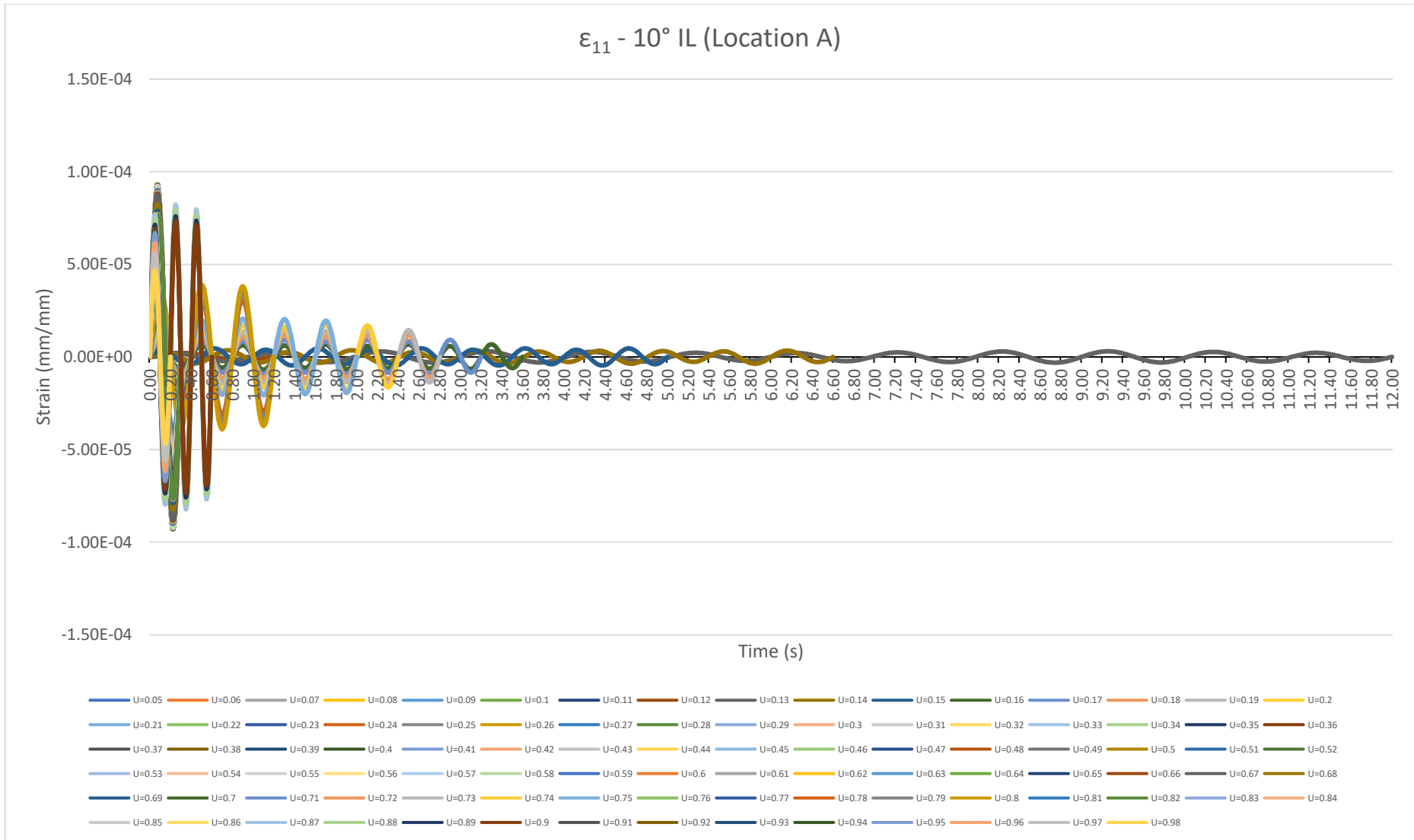


Figure 14-3: ϵ_{11} (Case-1(a) - 10° Flow IL) at Location A

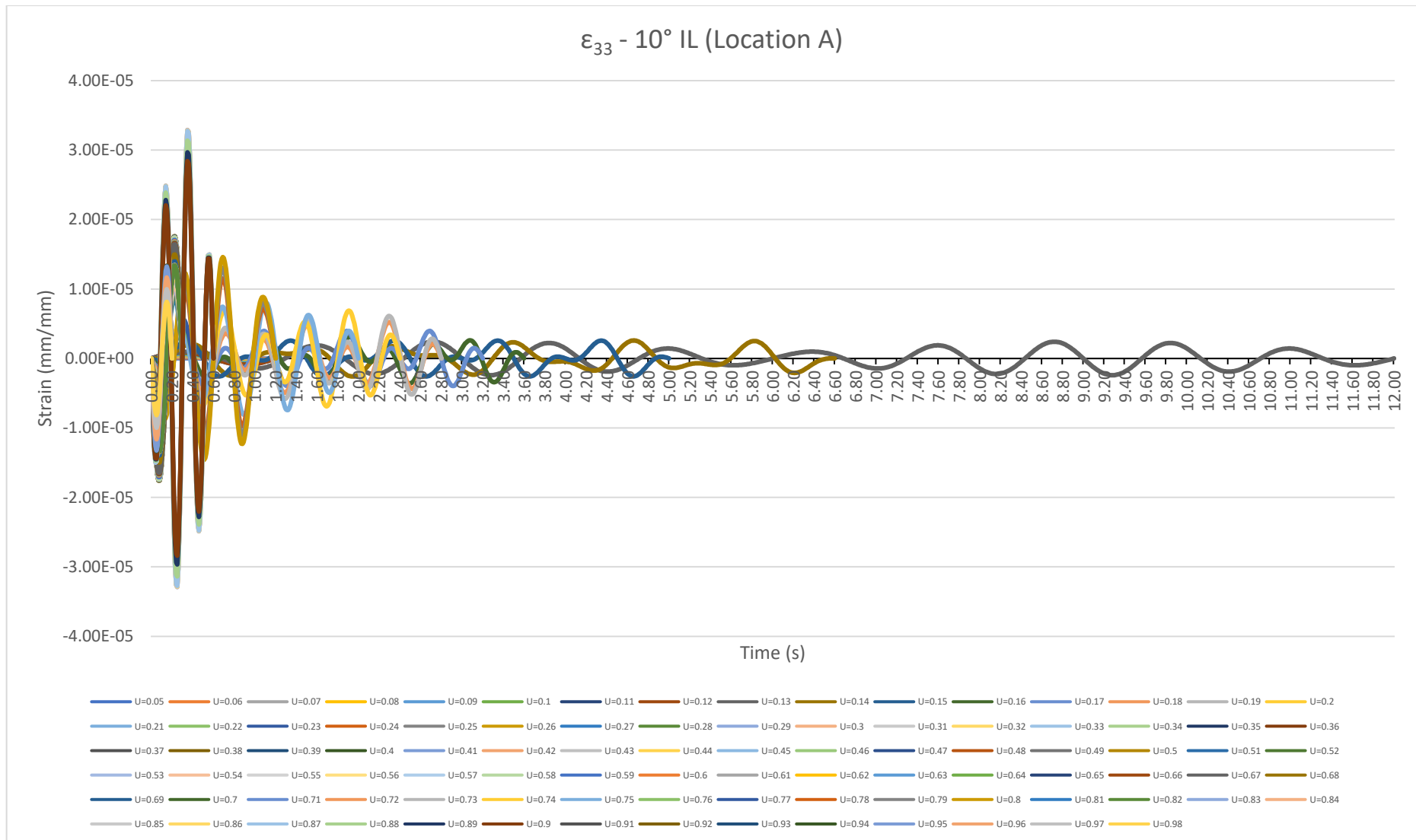


Figure 14-4: ϵ_{33} (Case-1(a) - 10° Flow IL) at Location A

2. Critical Plane

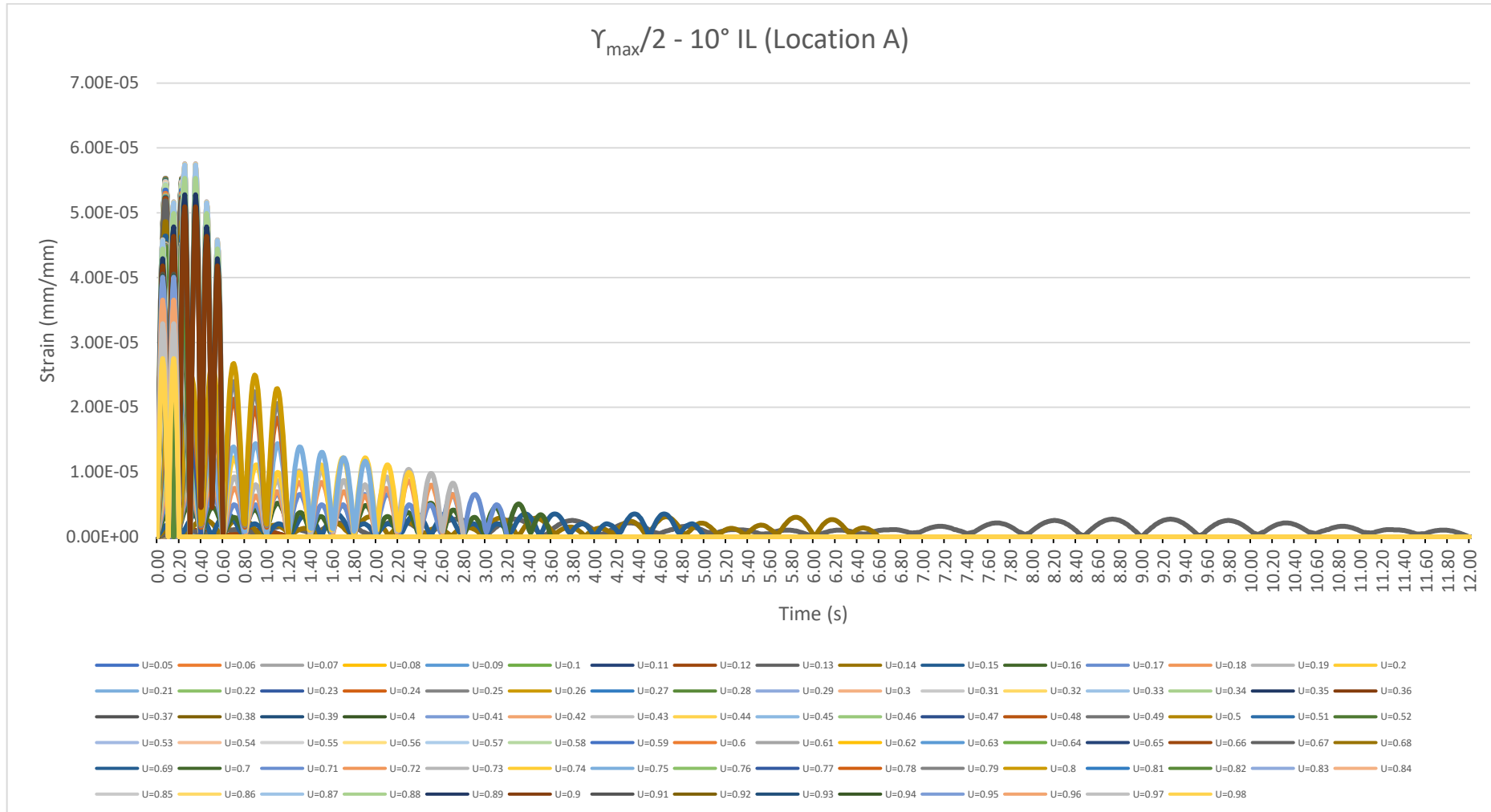


Figure 14-5: $\gamma_{\max}/2$ (Case-1(a) - 10° Flow IL) at Location A

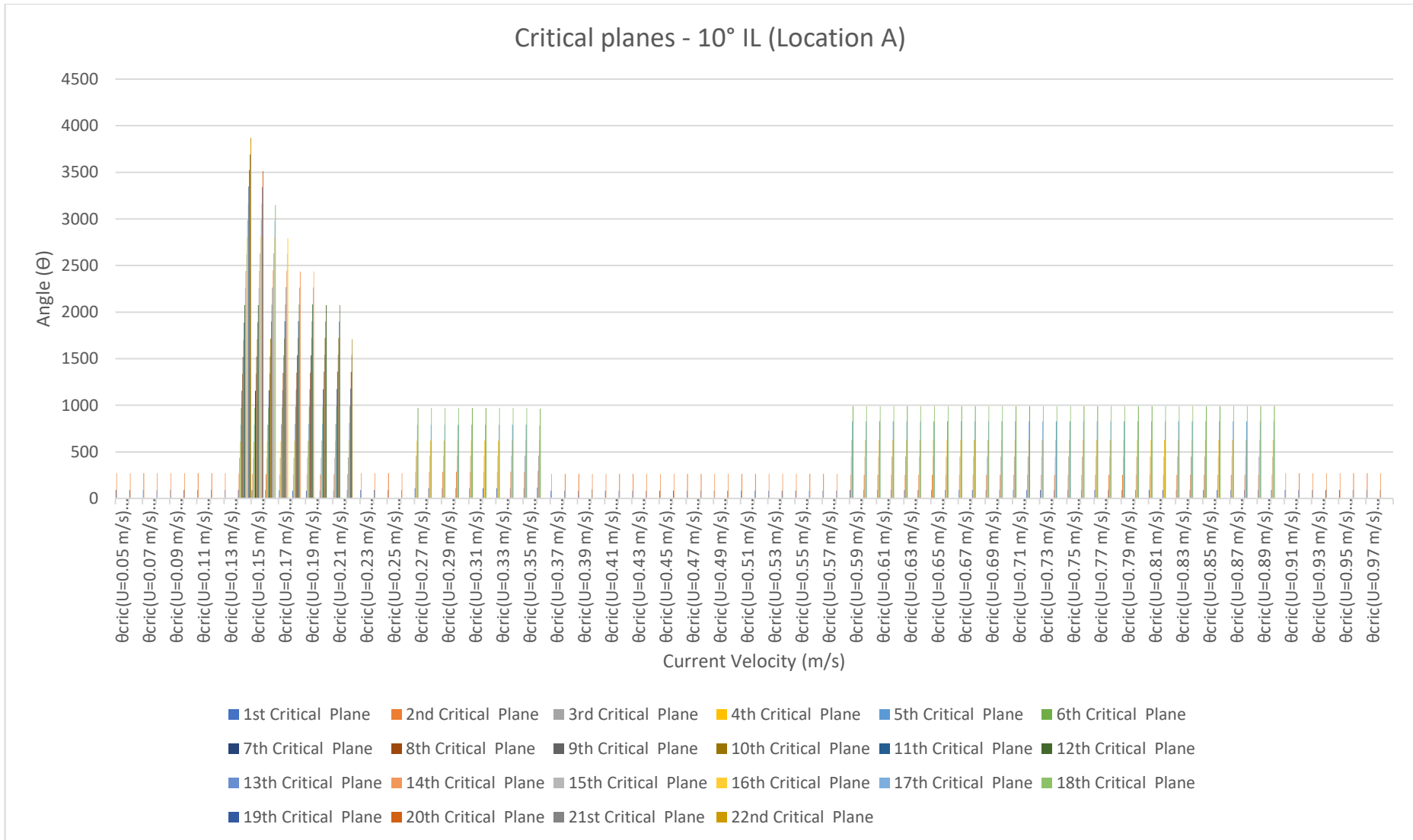


Figure 14-6: θ_{crit} (Case-1(a) - 10° Flow IL) at Location A

3. Normal and Shear Stress and Strain Range

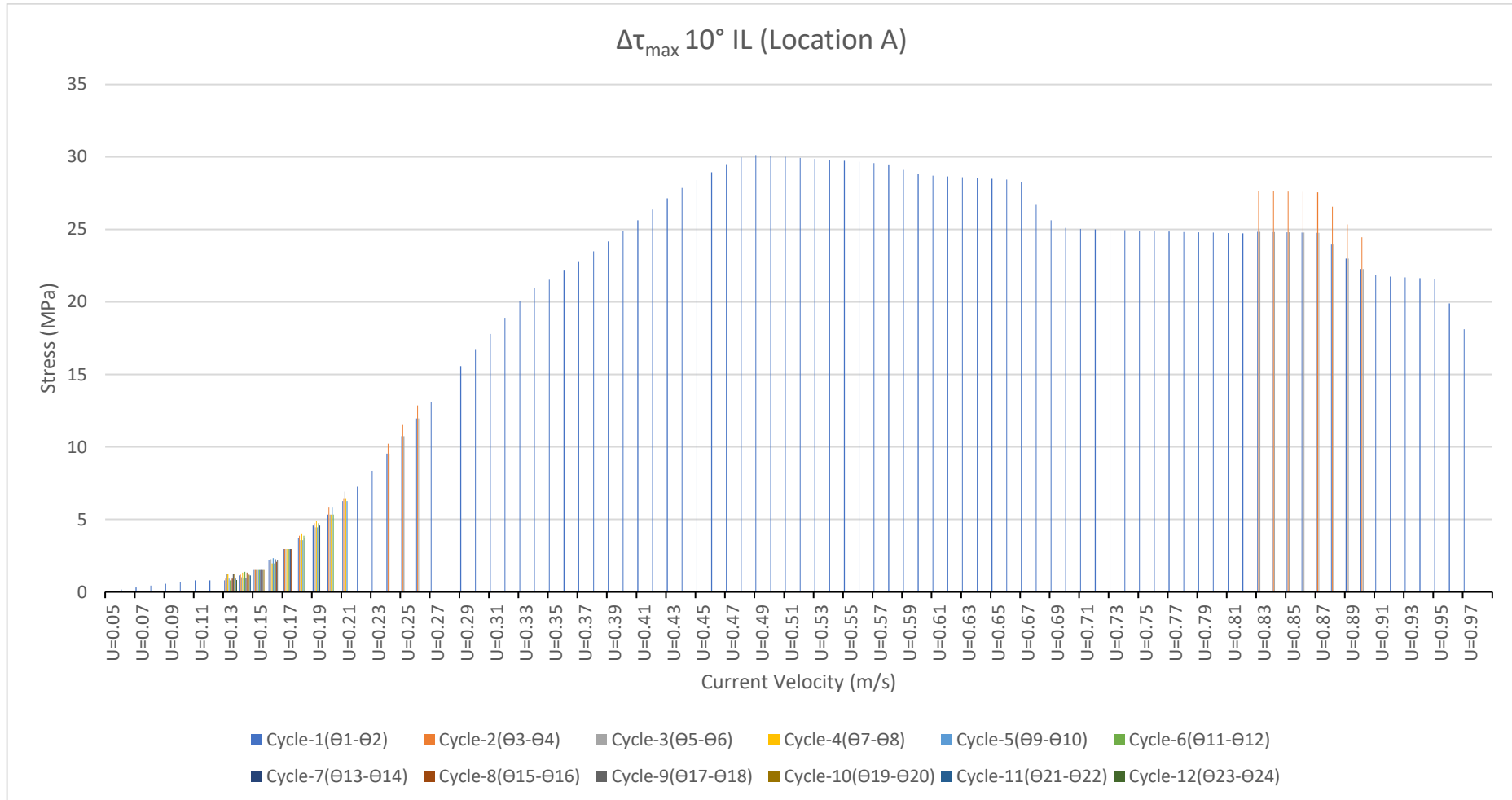


Figure 14-7: $\Delta\tau_{\max}$ (Case-1(a) - 10° Flow IL) at Location A

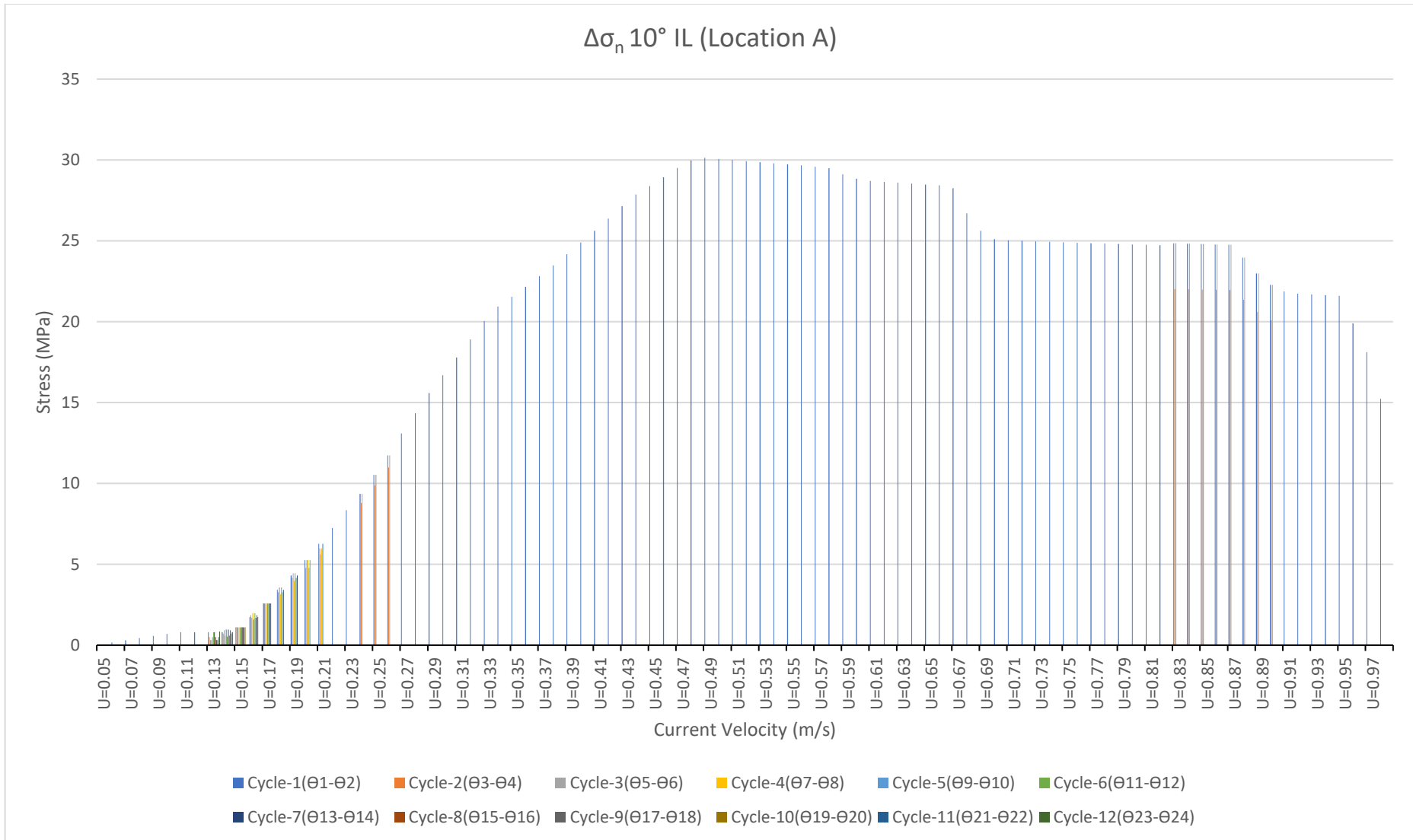


Figure 14-8: $\Delta\sigma_n$ (Case-1(a) - 10° Flow IL) at Location A

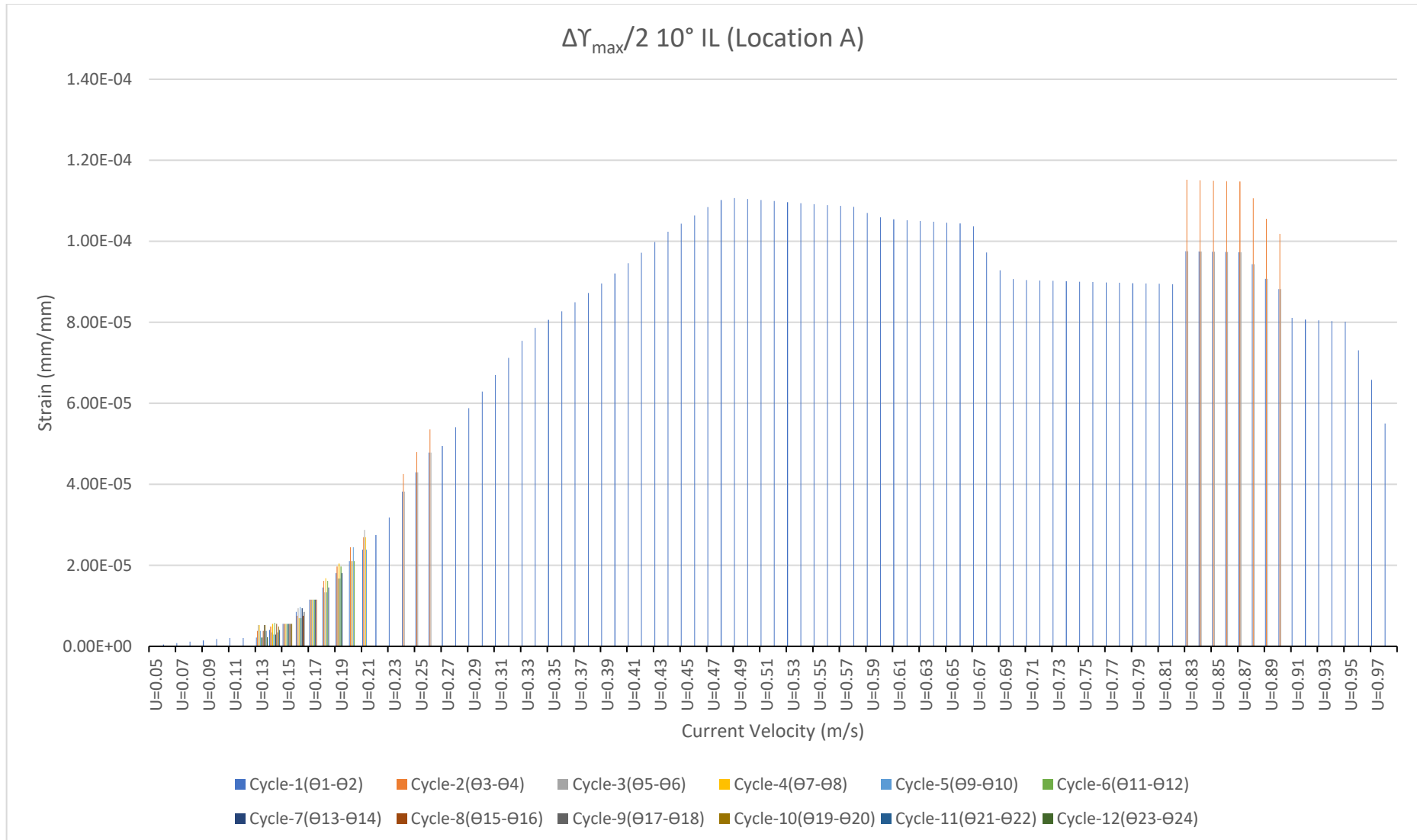


Figure 14-9: $\Delta\gamma_{\max}/2$ (Case-1(a) - 10° Flow IL) at Location A

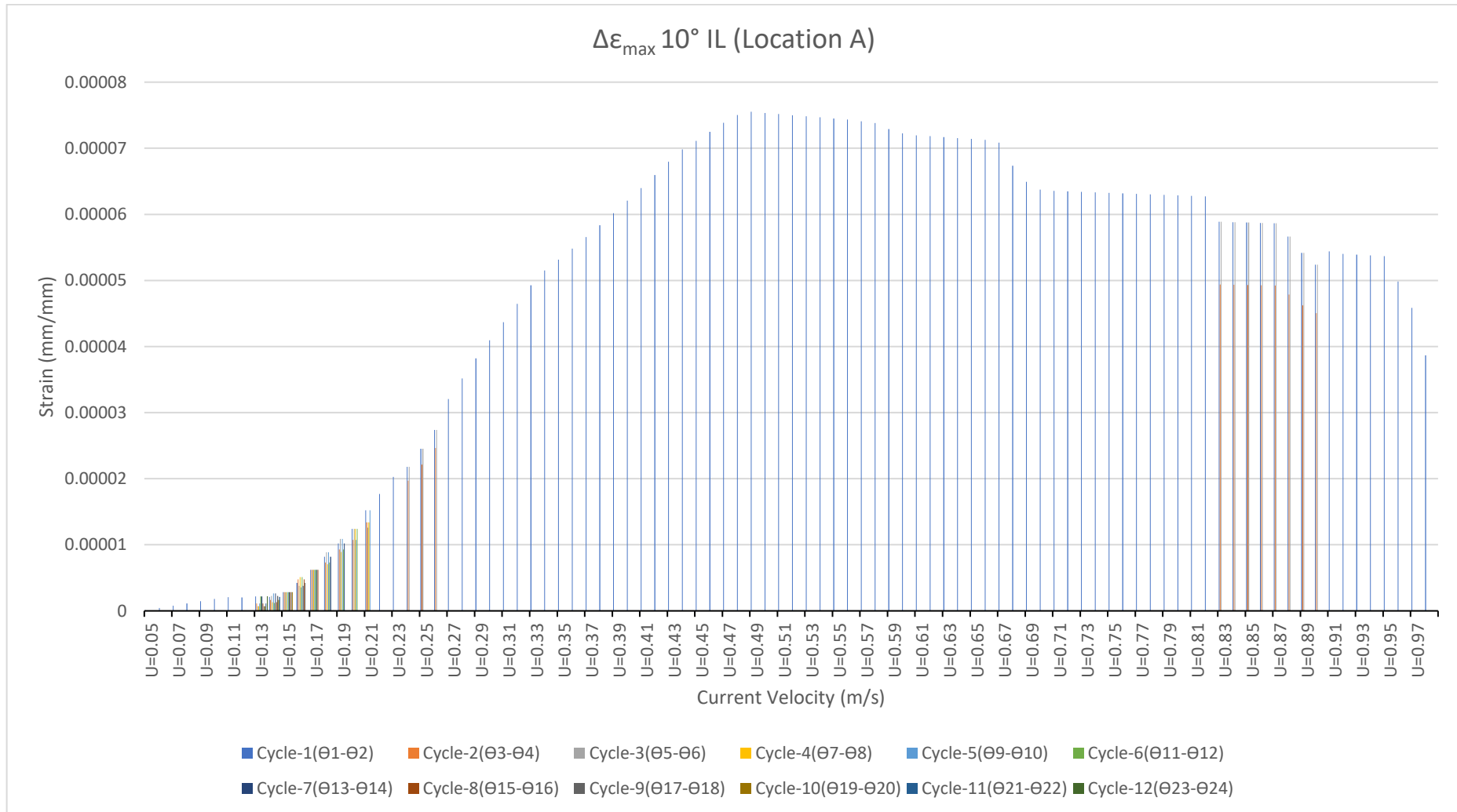


Figure 14-10: $\Delta\epsilon_n$ (Case-1(a) - 10° Flow IL) at Location A

4. Fatigue

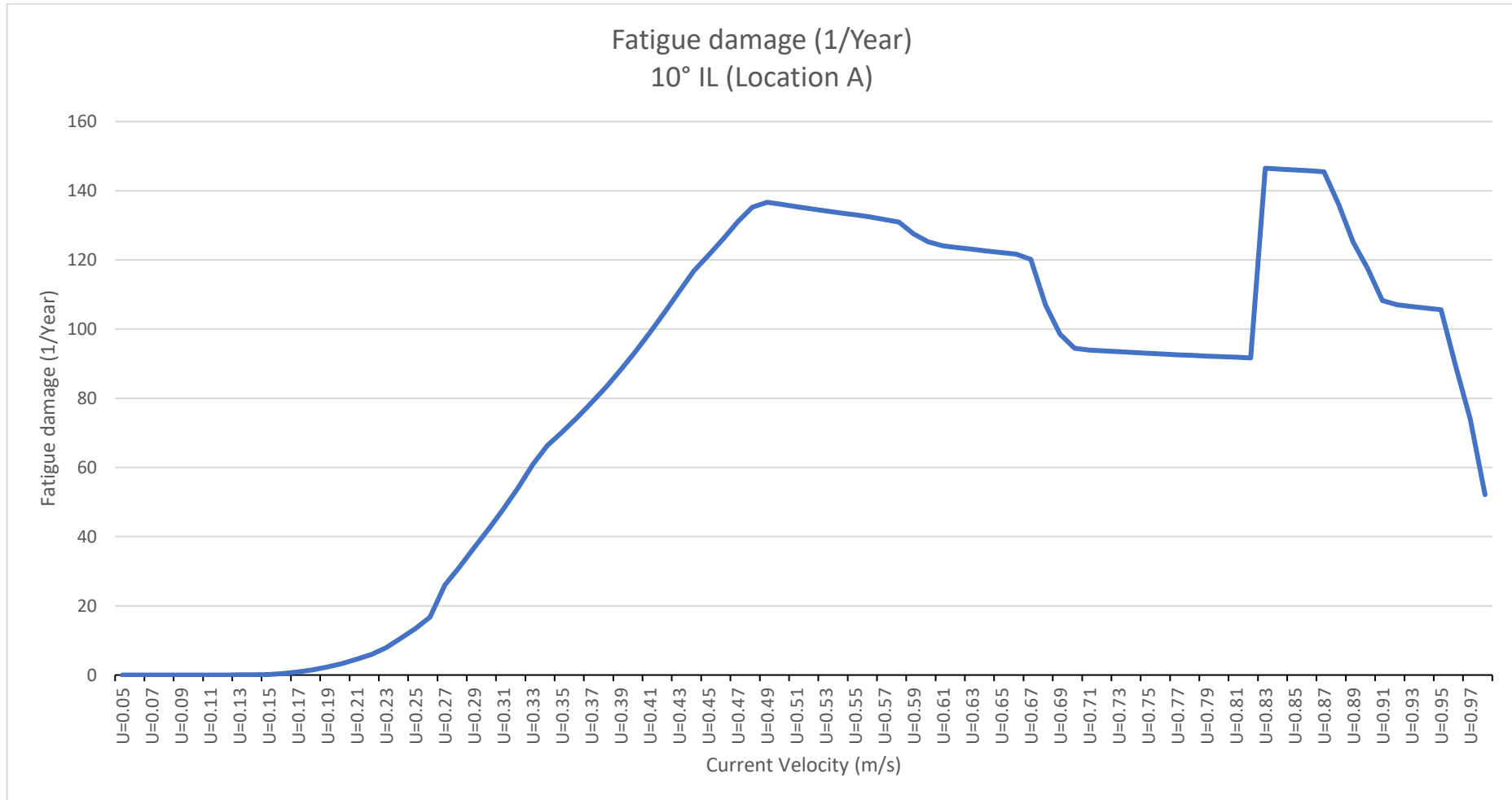


Figure 14-11: Fatigue damage per year for (Case-1(a) - 10° Flow IL) at Location A

Case-1 (a) – 10° IL Location B

1. Principal Stress and Strains

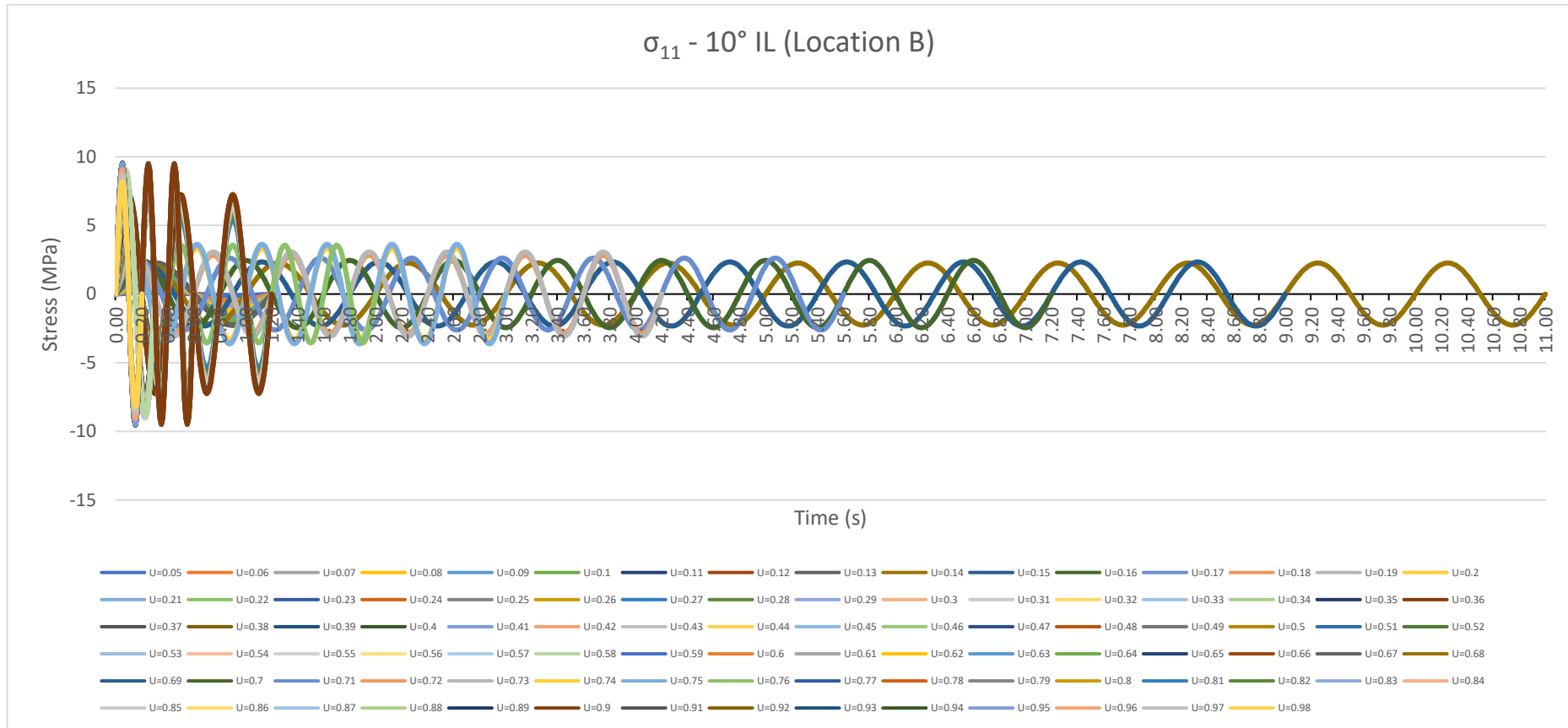


Figure 14-12: σ_{11} (Case-1(a) - 10° Flow IL) at Location B

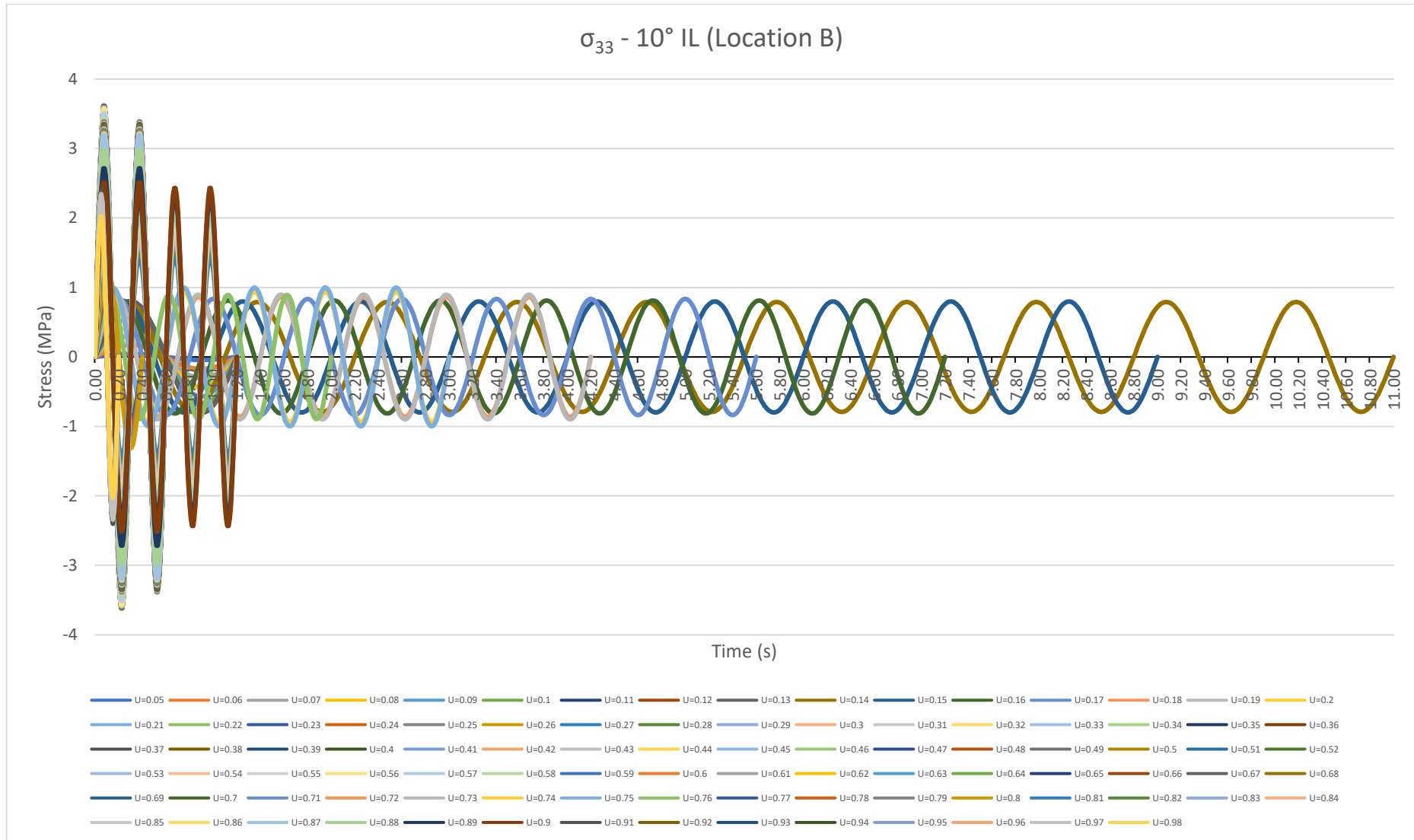


Figure 14-13: σ_{33} (Case-1(a) - 10° Flow IL) at Location B

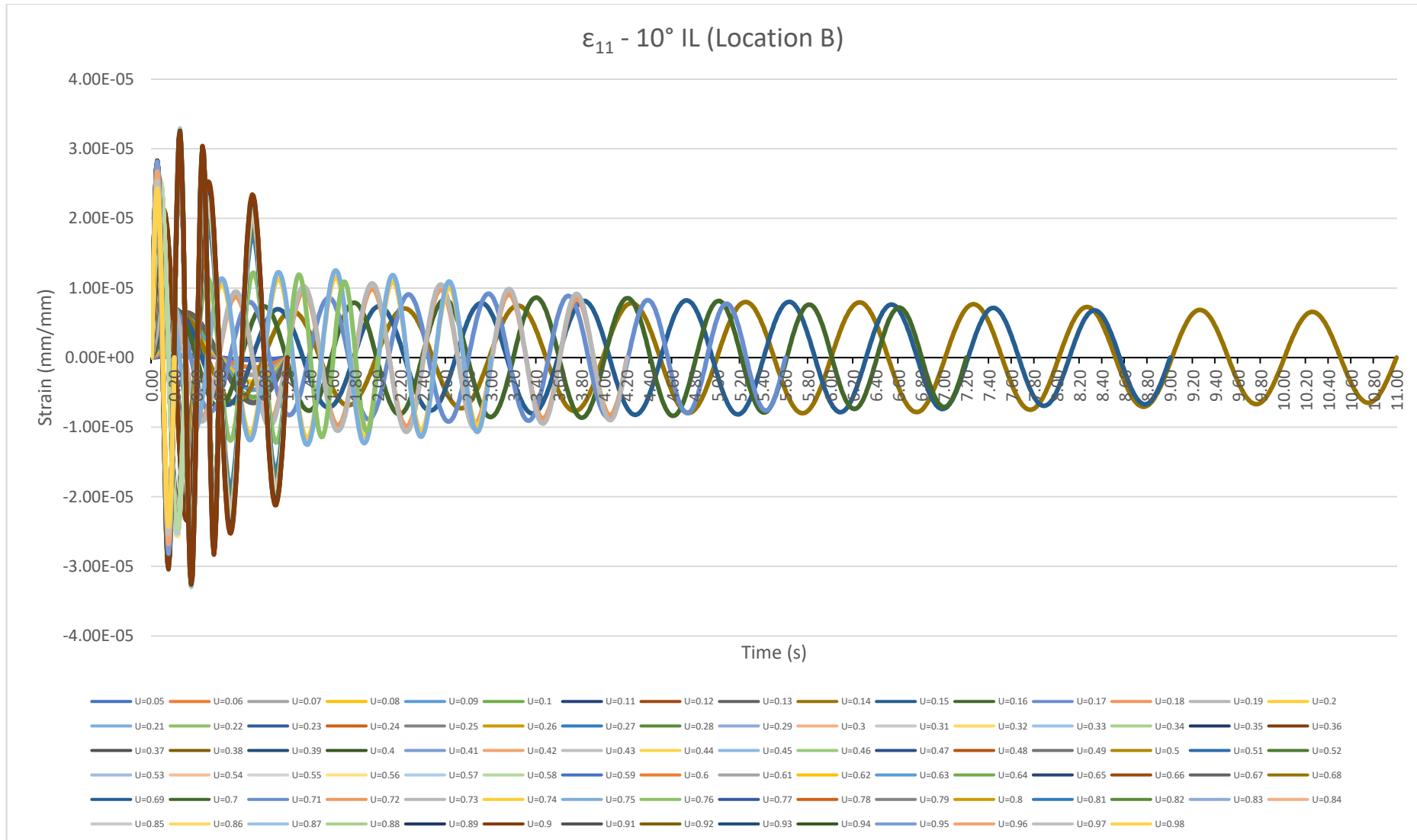


Figure 14-14: ϵ_{11} (Case-1(a) - 10° Flow IL) at Location B

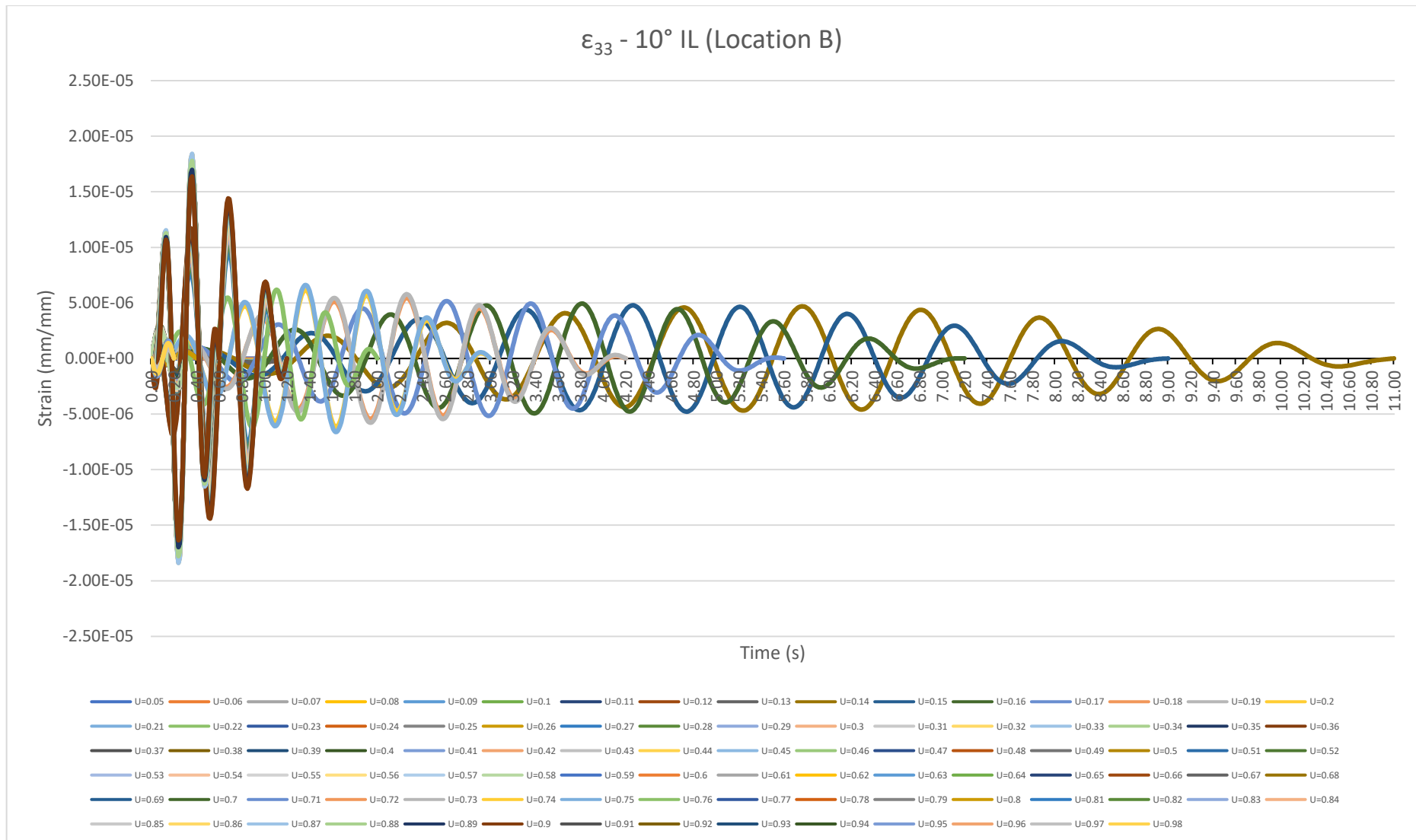


Figure 14-15: ϵ_{33} (Case-1(a) - 10° Flow IL) at Location B

2. Critical Plane

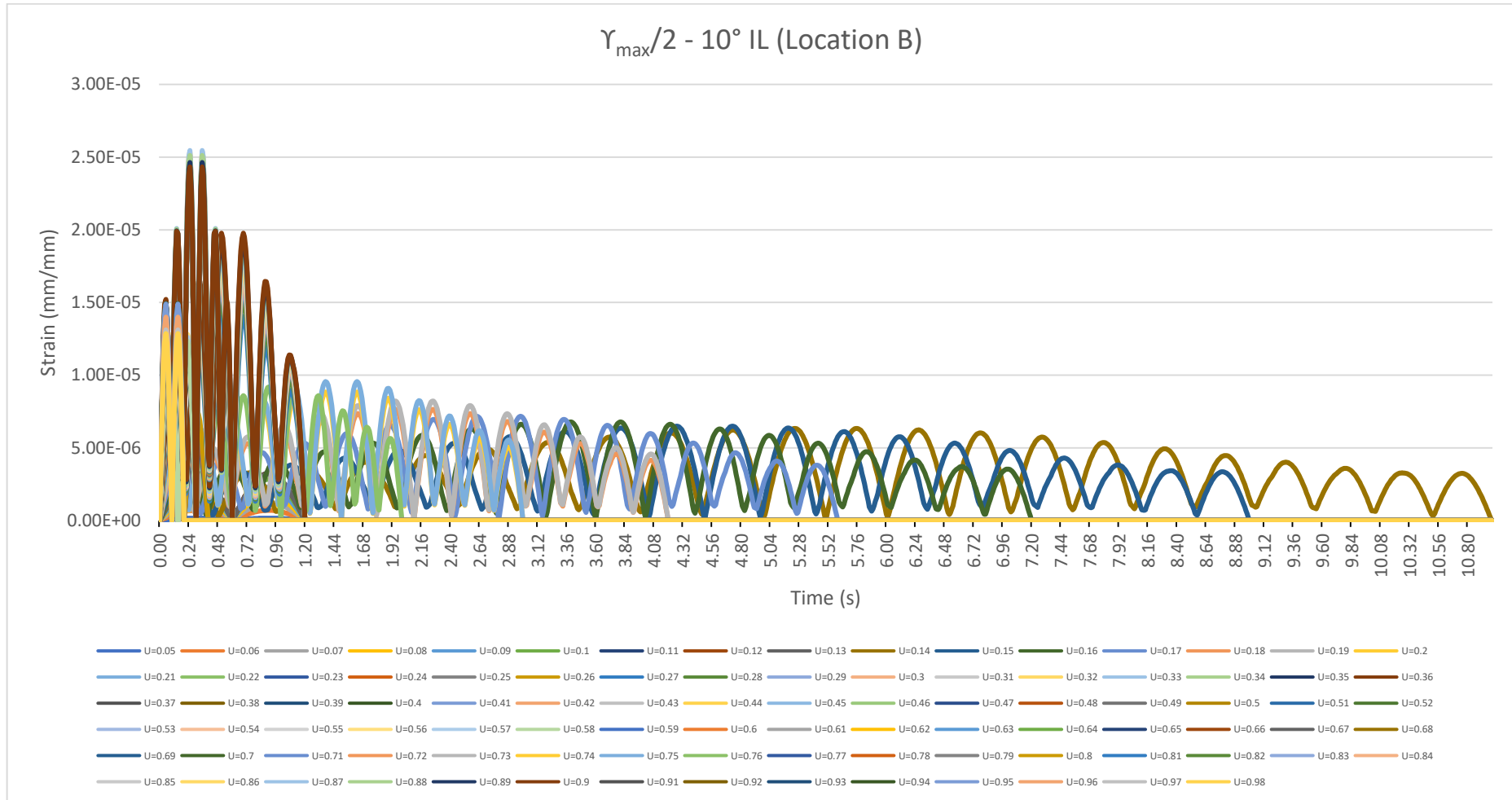


Figure 14-16: $\gamma_{\max}/2$ (Case-1(a) - 10° Flow IL) at Location B

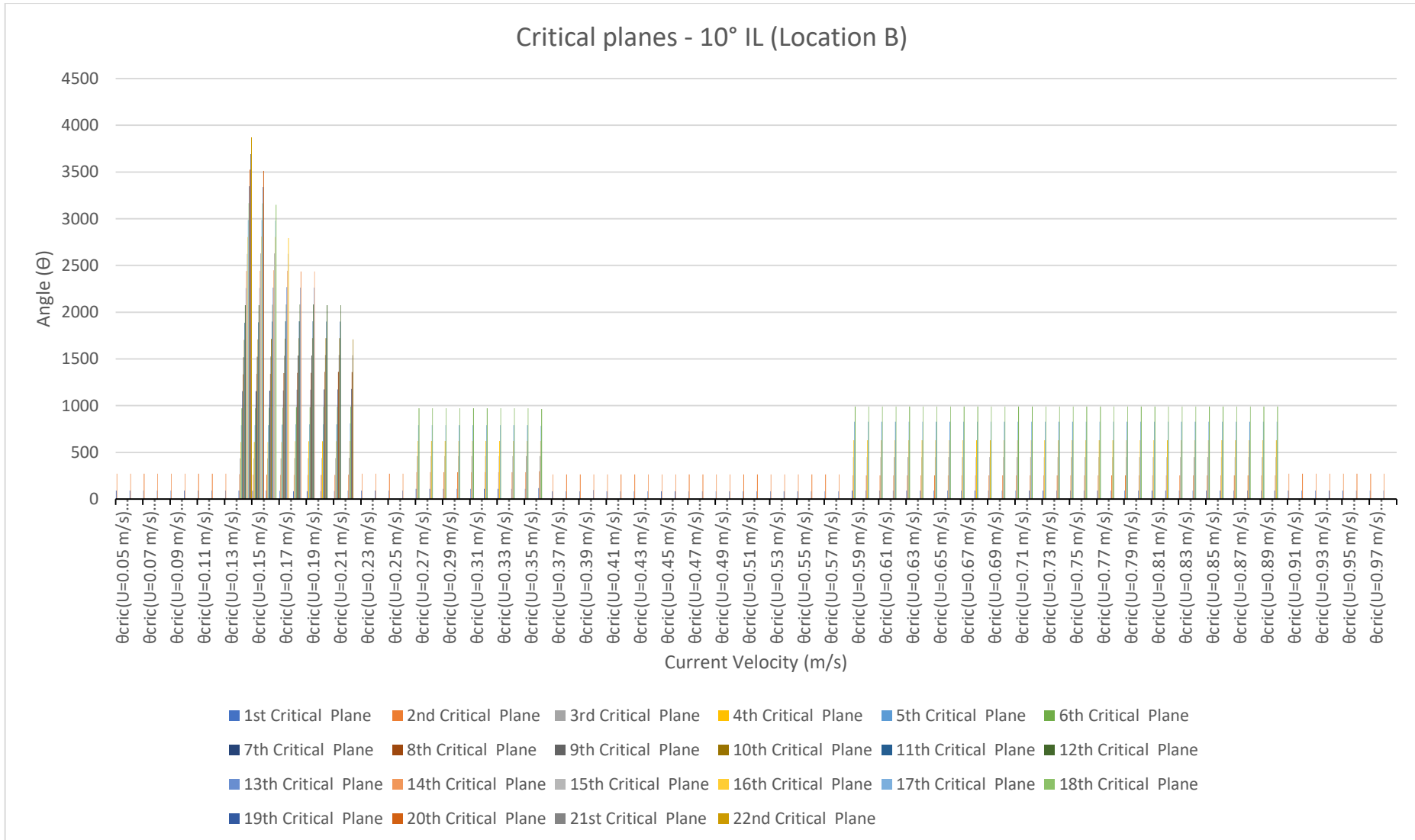


Figure 14-17: θ_{crit} (Case-1(a) - 10° Flow IL) at Location B

3. Normal and Shear Stress and Strain Range

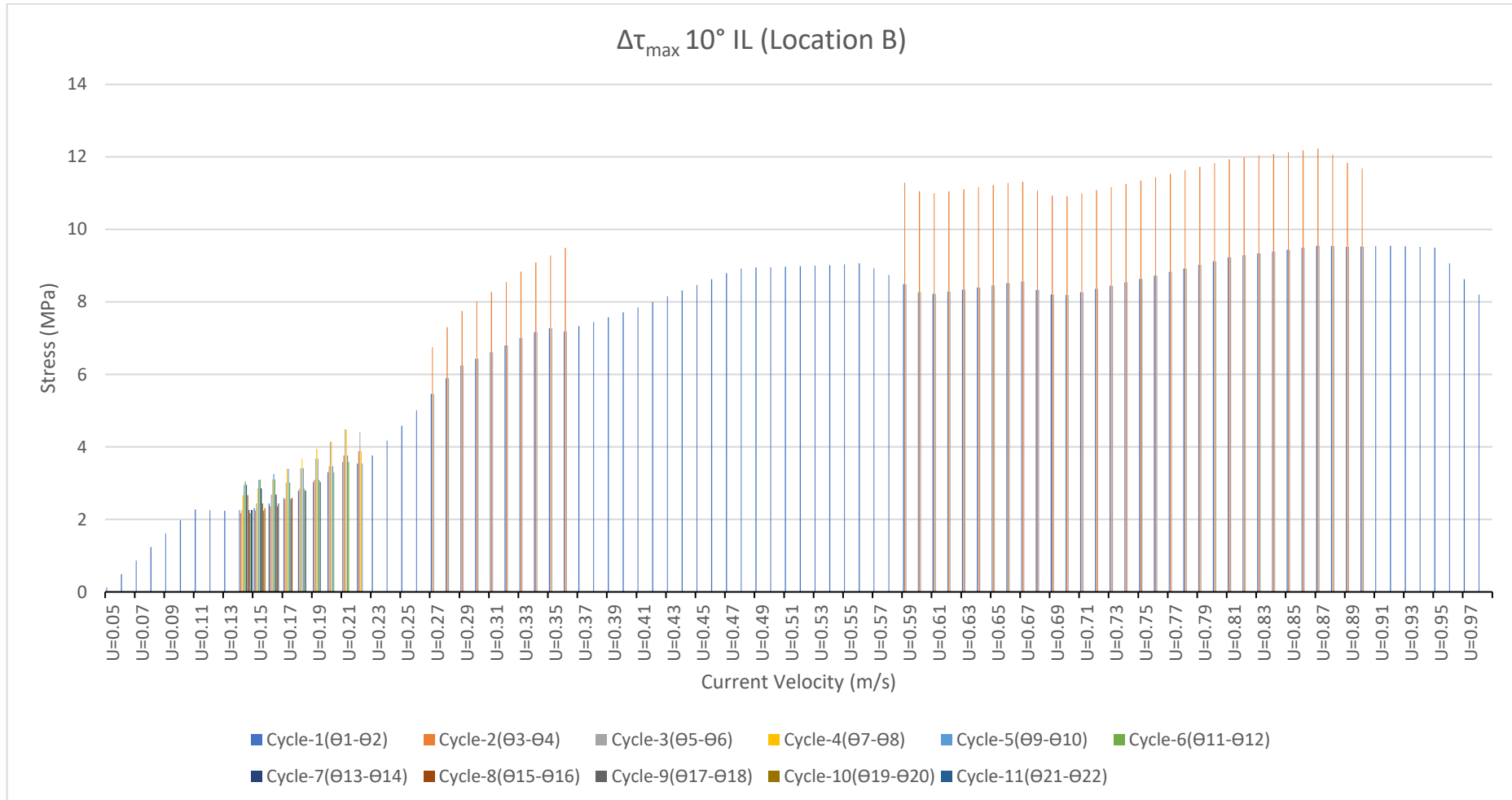


Figure 14-18: $\Delta\tau_{\max}$ (Case-1(a) - 10° Flow IL) at Location B

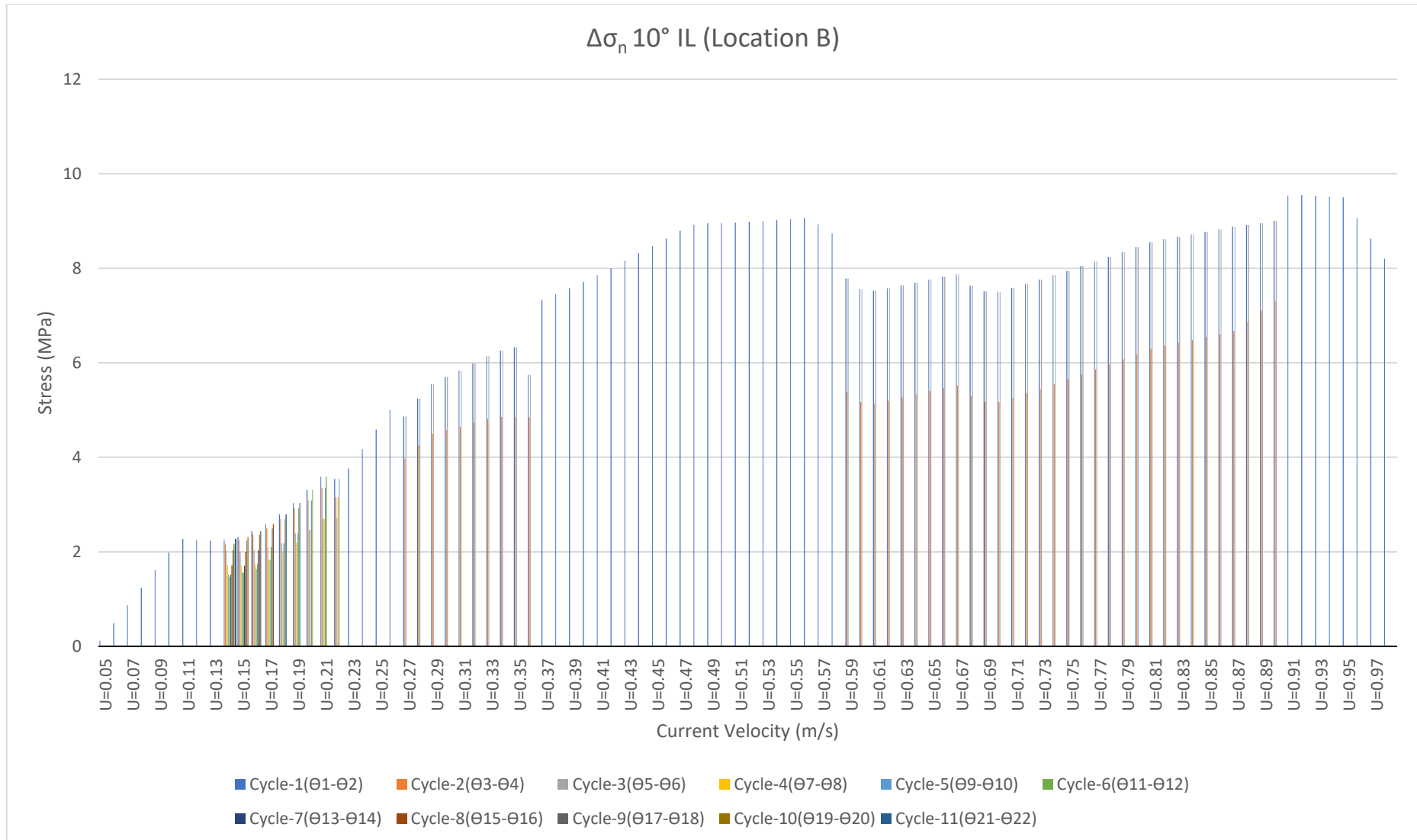


Figure 14-19: $\Delta\sigma_n$ (Case-1(a) - 10° Flow IL) at Location B

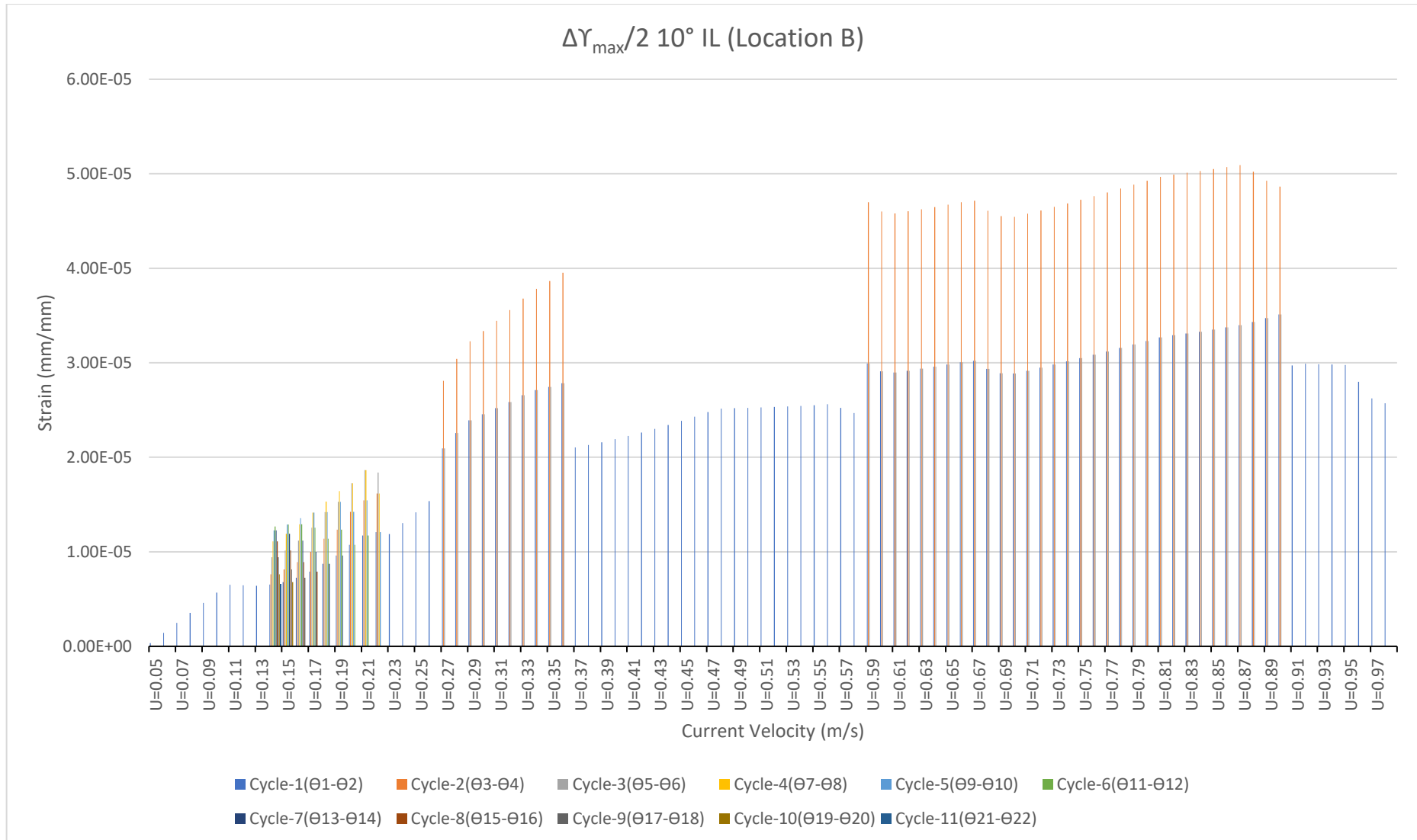


Figure 14-20: $\Delta\gamma_{\max}/2$ (Case-1(a) - 10° Flow IL) at Location B

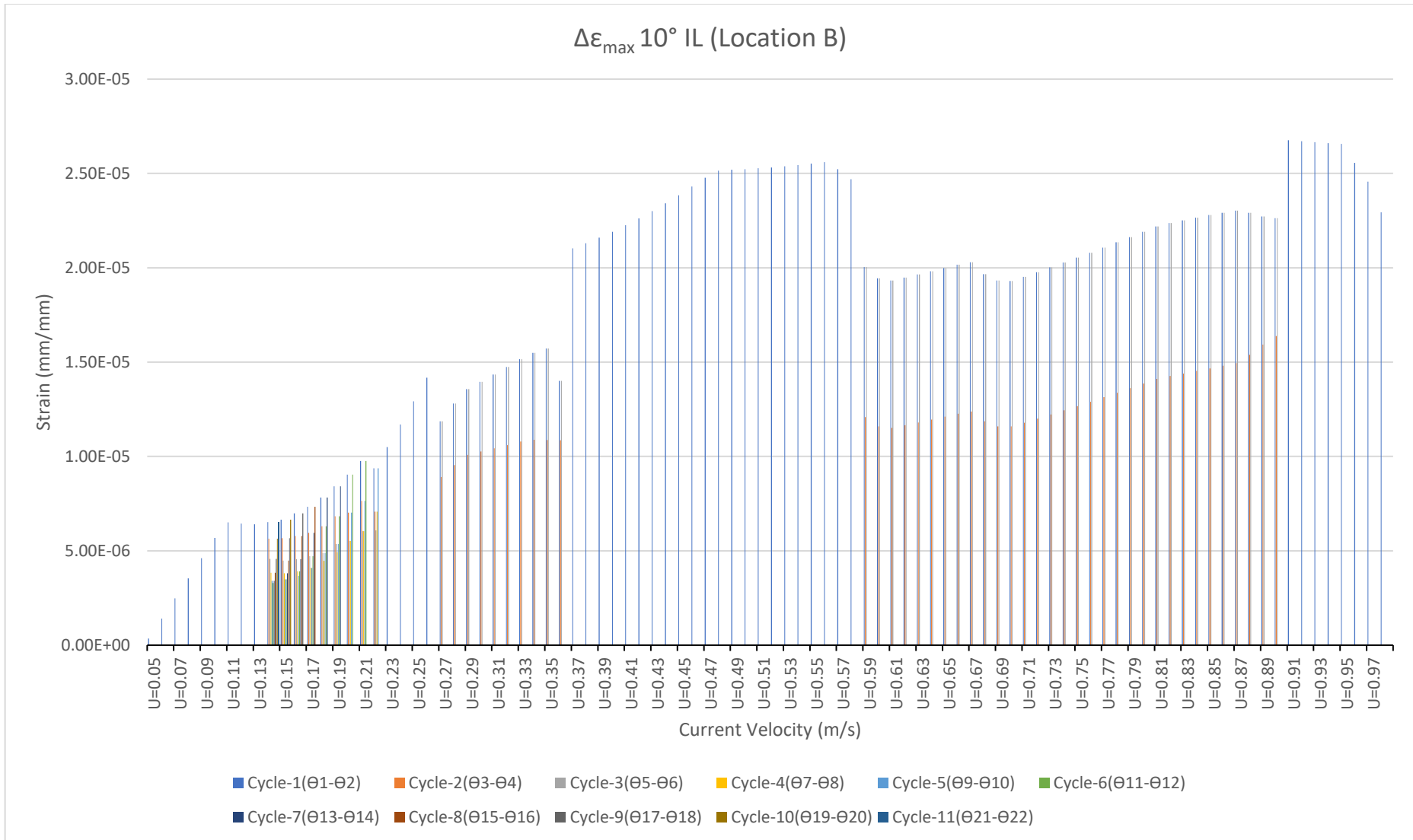


Figure 14-21: $\Delta\epsilon_n$ (Case-1(a) - 10° Flow IL) at Location B

4. Fatigue

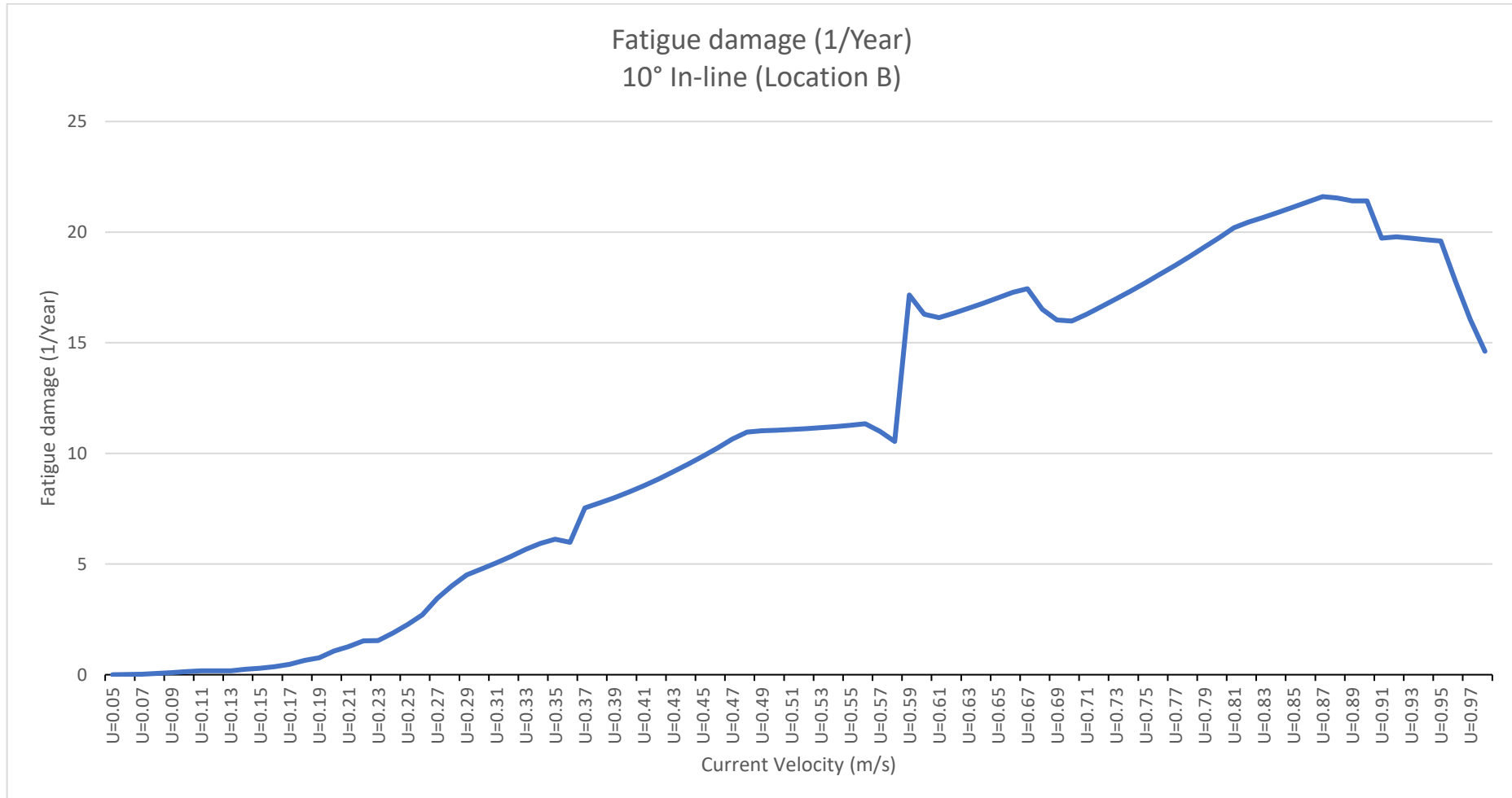


Figure 14-22: Fatigue damage per year for (Case-1(a) - 10° Flow IL) at Location B

Case-1 (b) – 10° CF Location A

1. Principal Stress and Strains

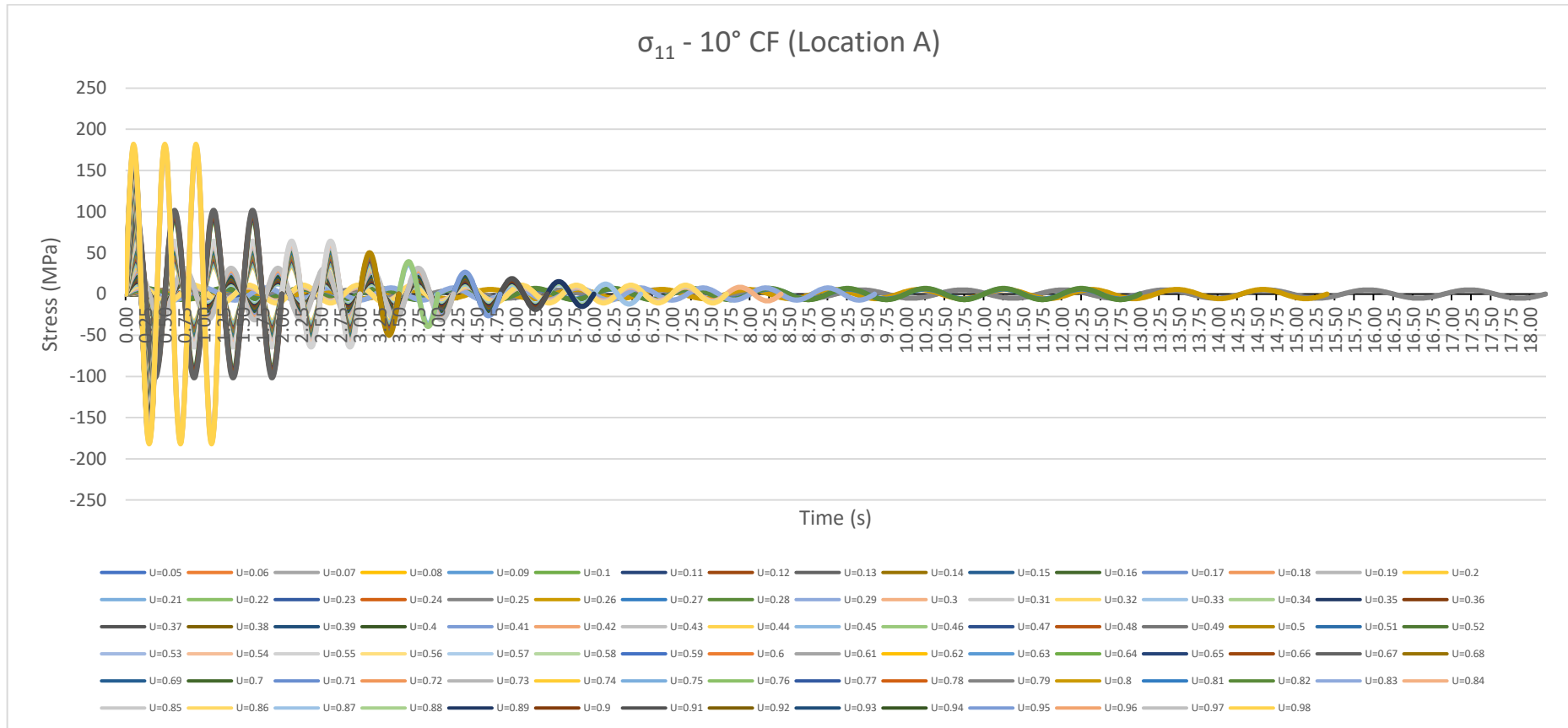


Figure 14-23: σ_{11} (Case-1(b) - 10° Flow CF) at Location A

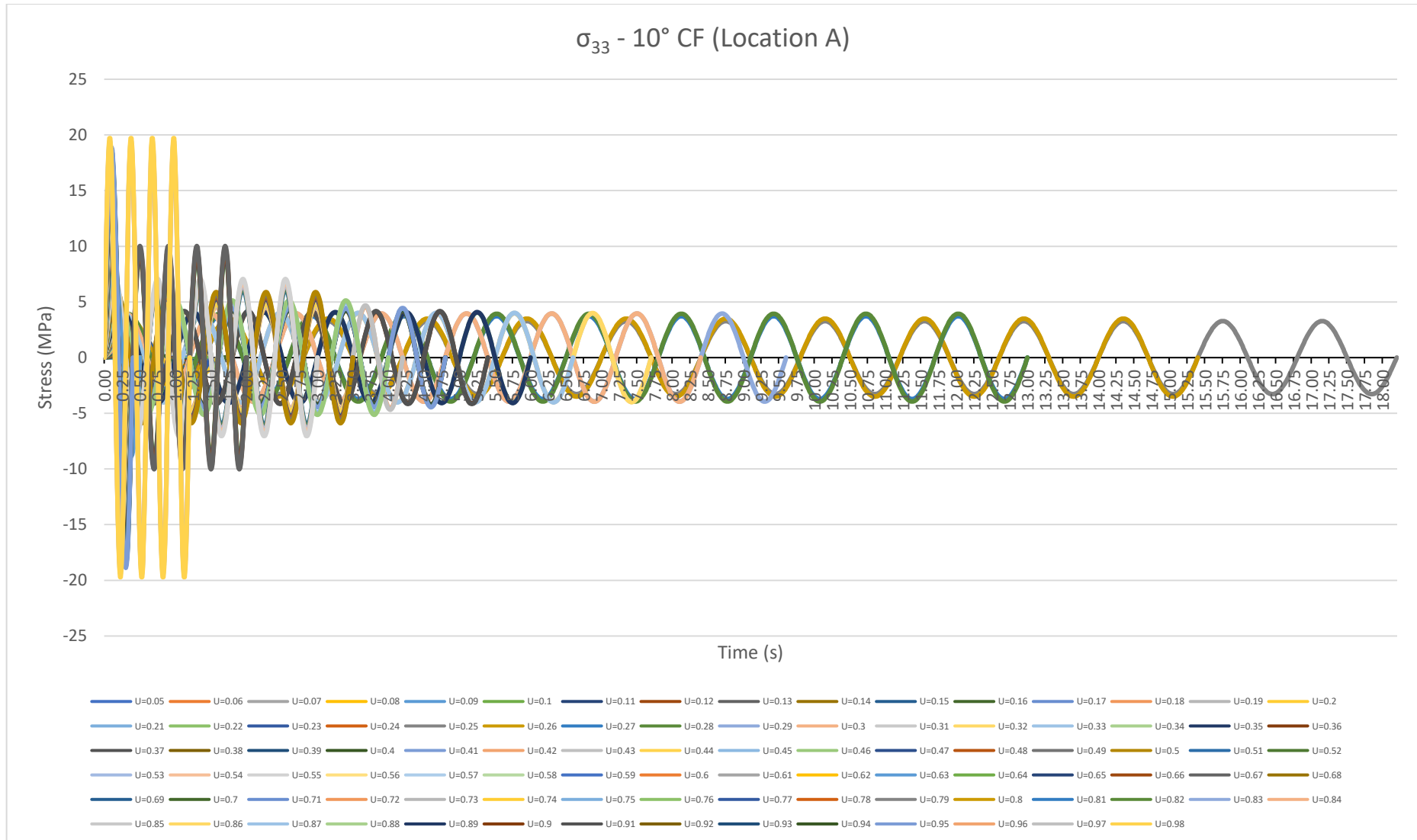


Figure 14-24: σ_{33} (Case-1(b) - 10° Flow CF) at Location A

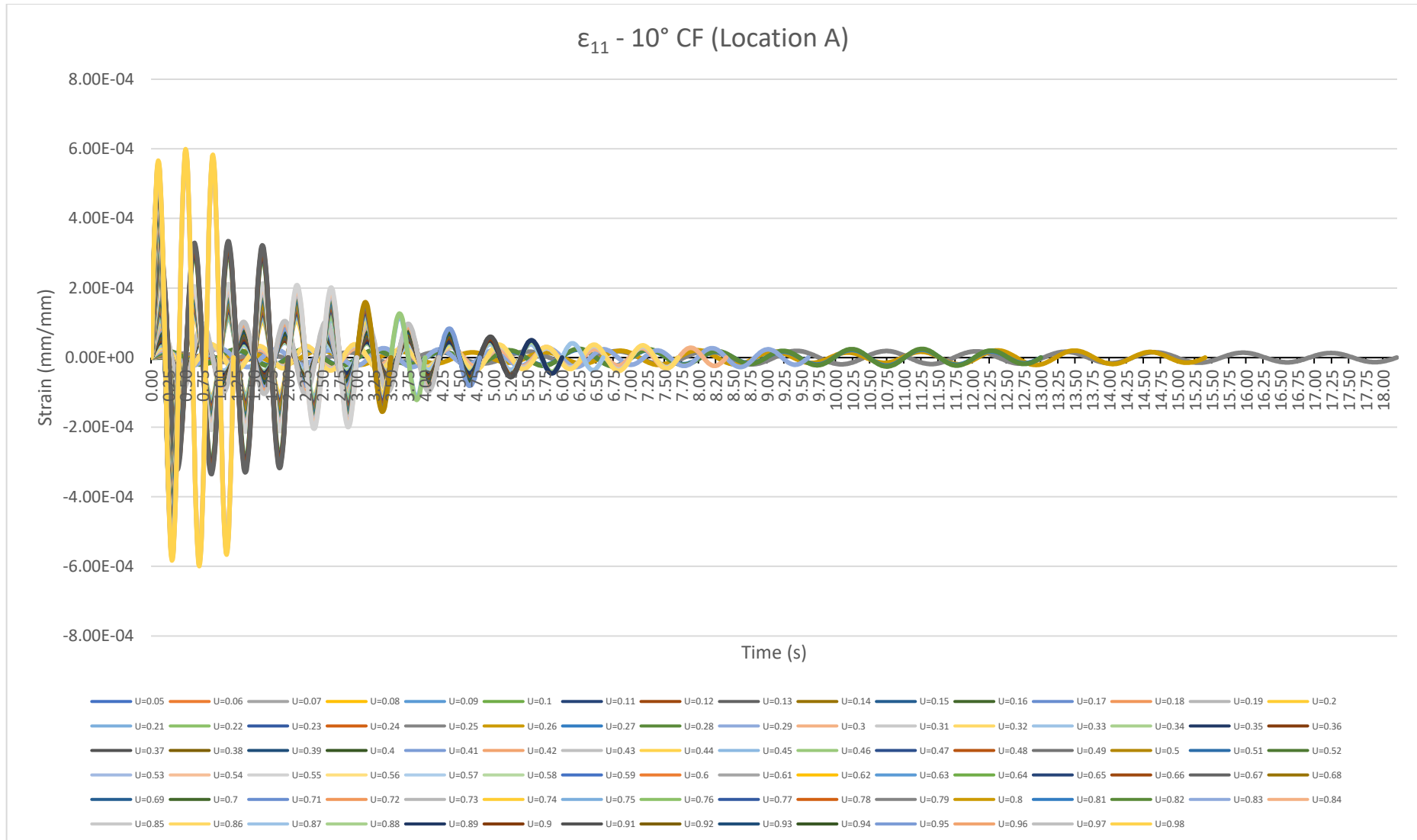


Figure 14-25: ϵ_{11} (Case-1(b) - 10° Flow CF) at Location A

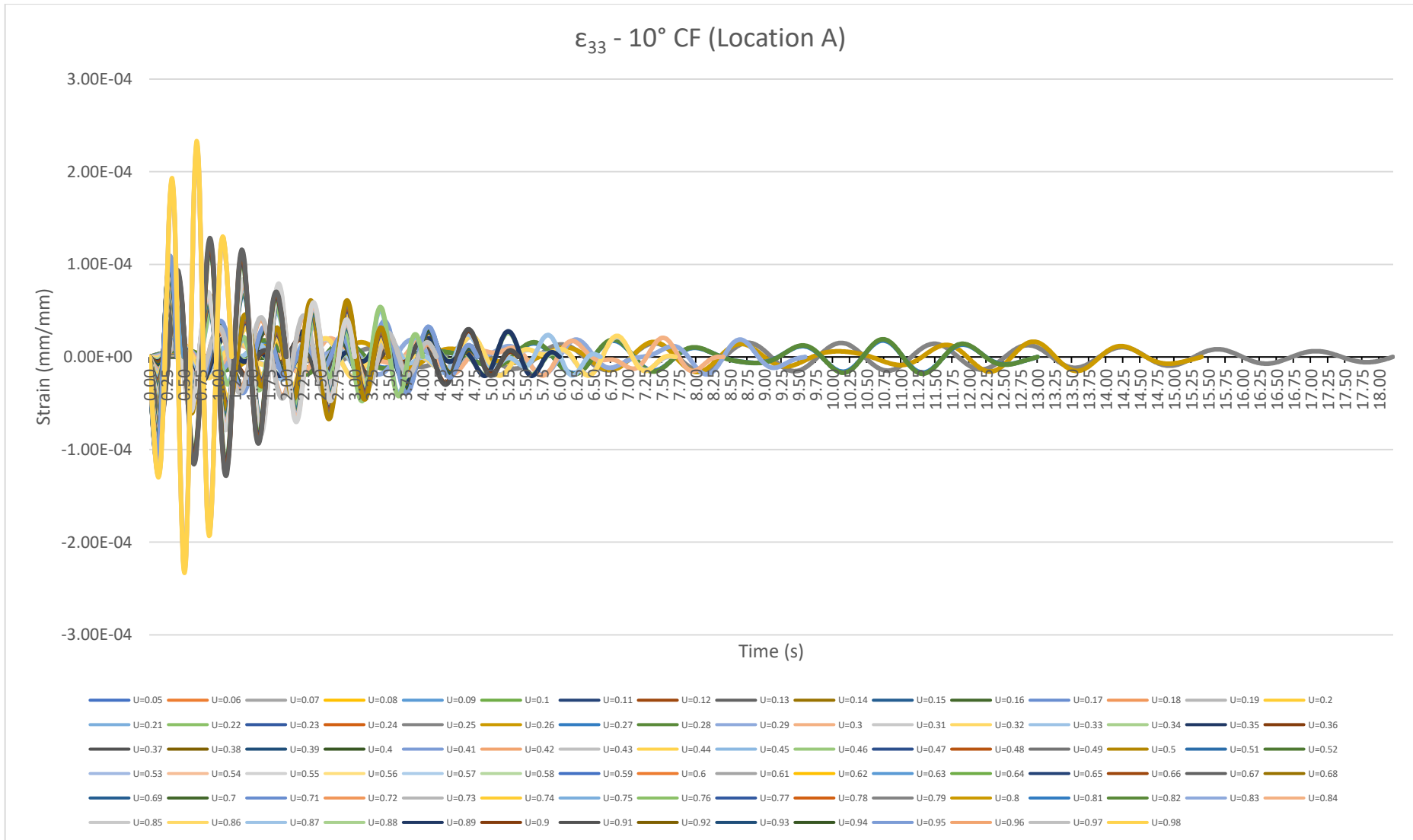


Figure 14-26: ϵ_{33} (Case-1(b) - 10° Flow CF) at Location A

2. Critical Plane

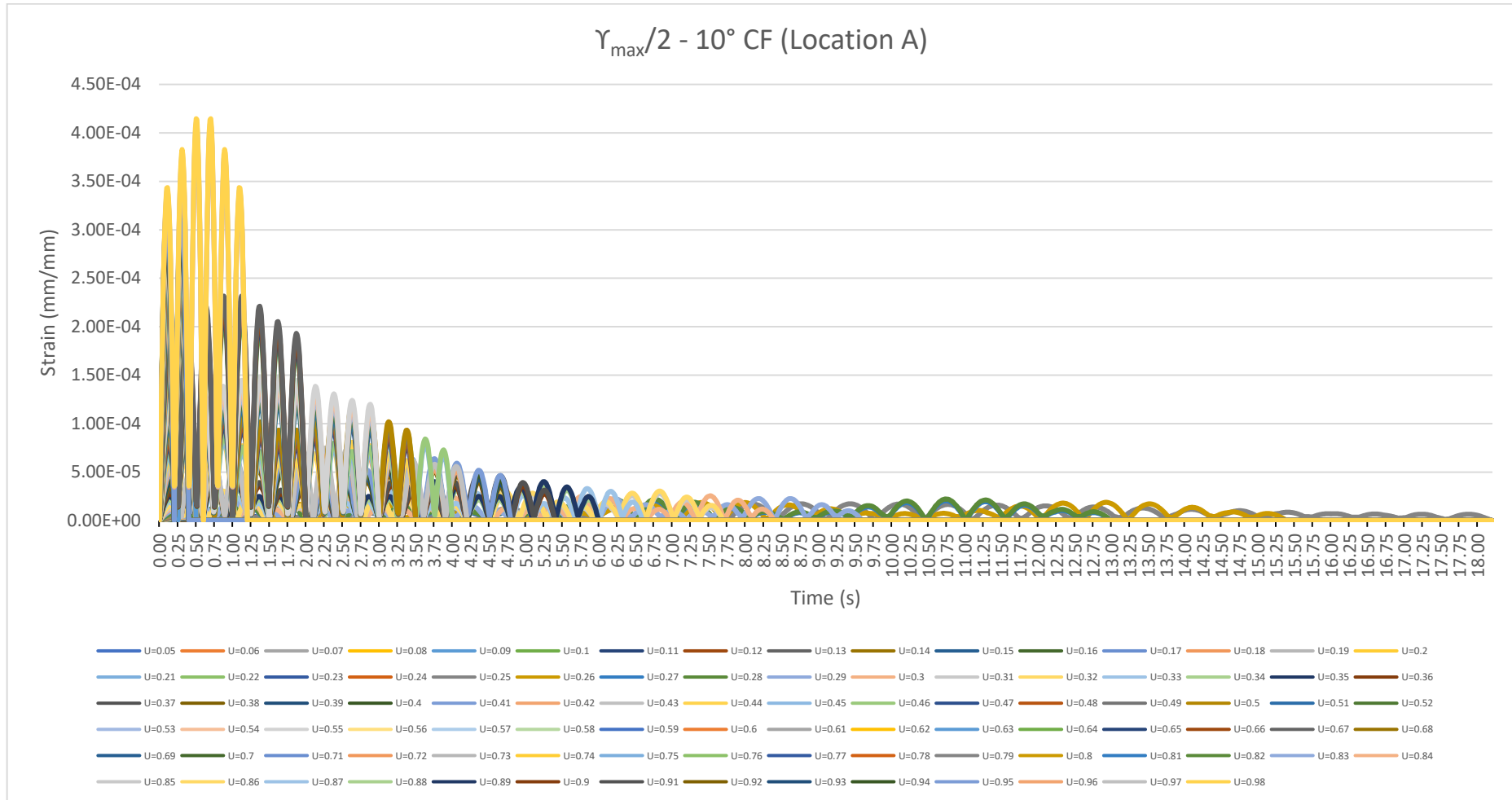


Figure 14-27: $\gamma_{\max}/2$ (Case-1(b) - 10° Flow CF) at Location A

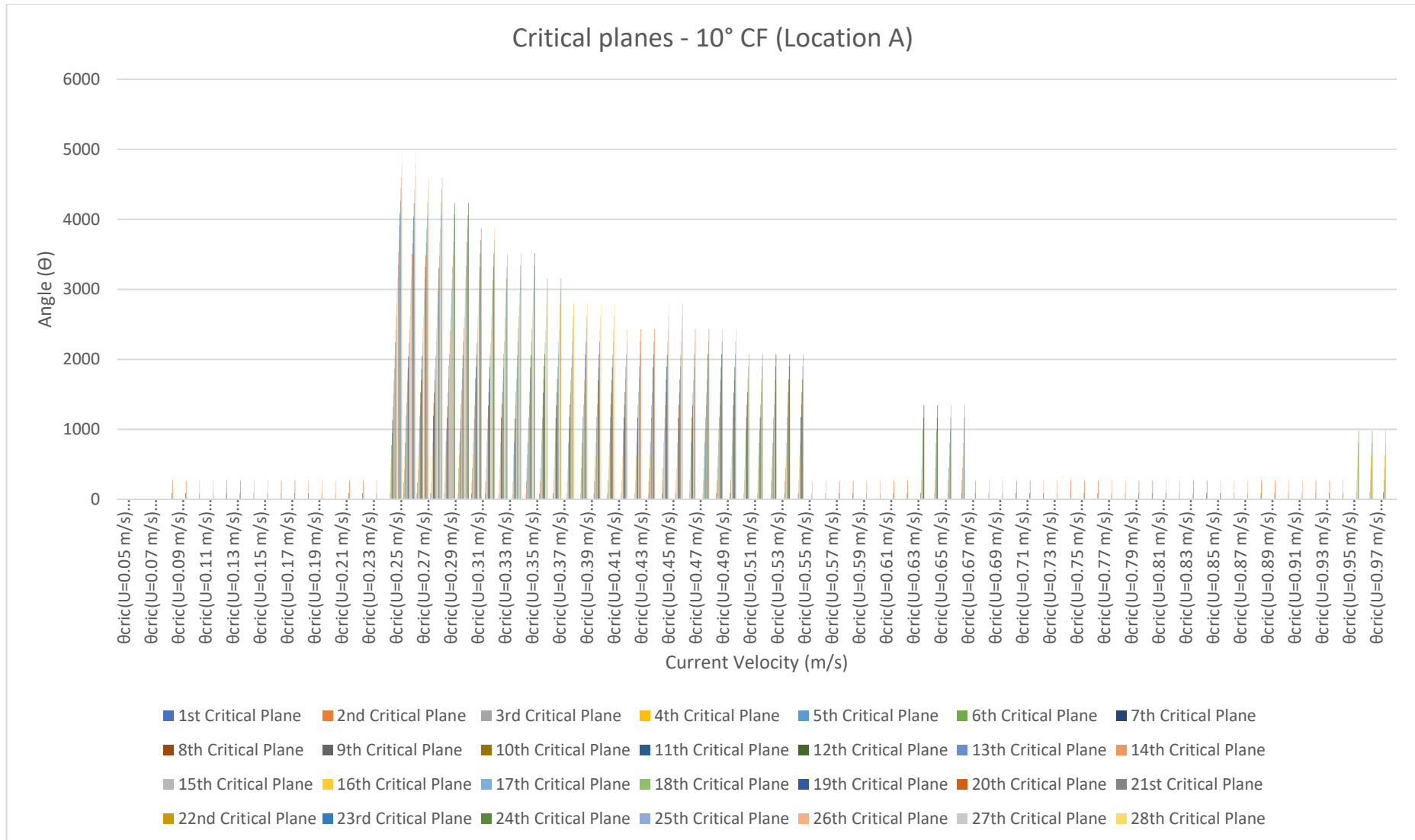


Figure 14-28: θ_{cric} (Case-1(b) - 10° Flow CF) at Location A

3. Normal and Shear Stress and Strain Range

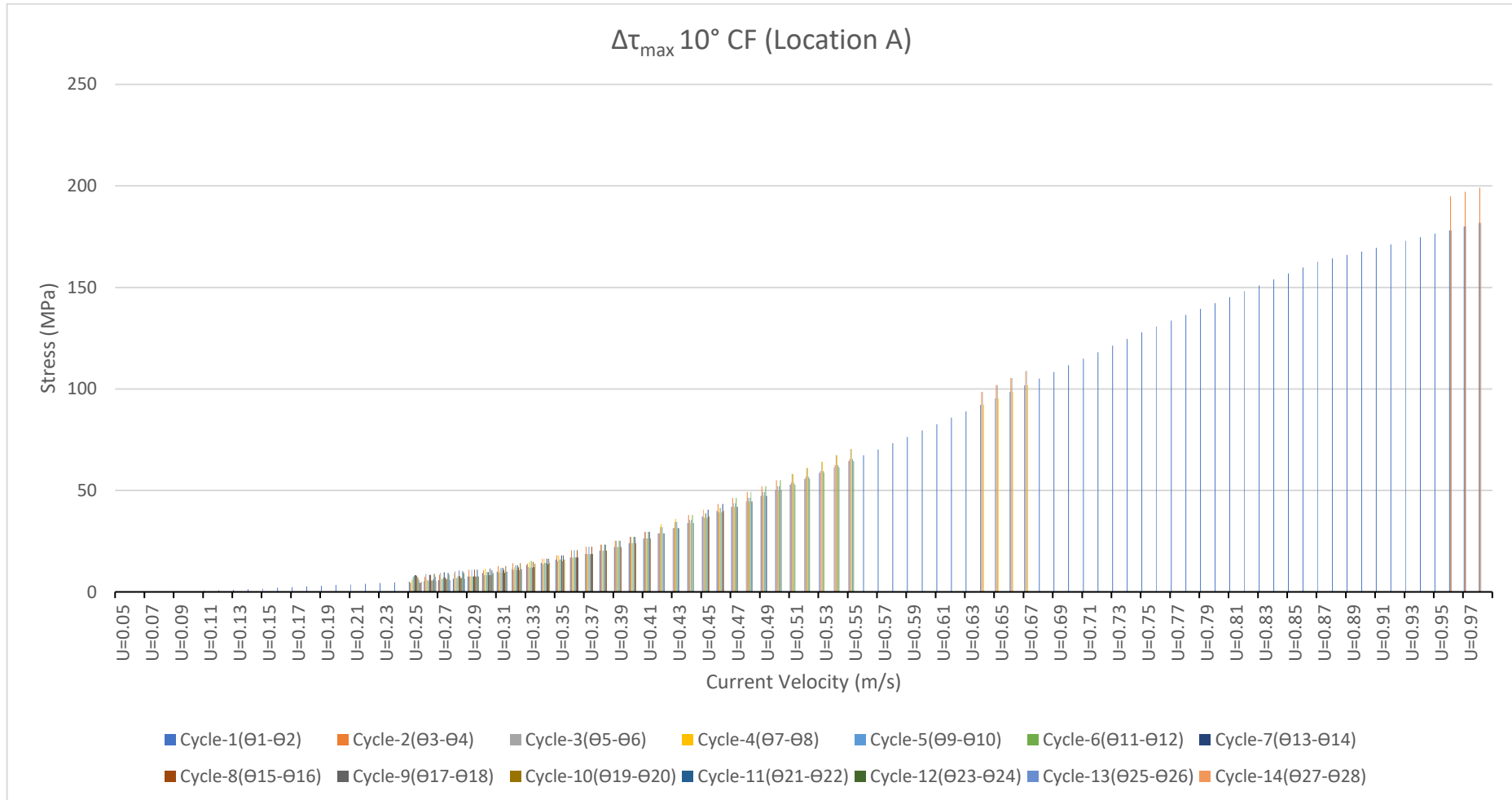


Figure 14-29: $\Delta\tau_{\max}$ (Case-1(b) - 10° Flow CF) at Location A

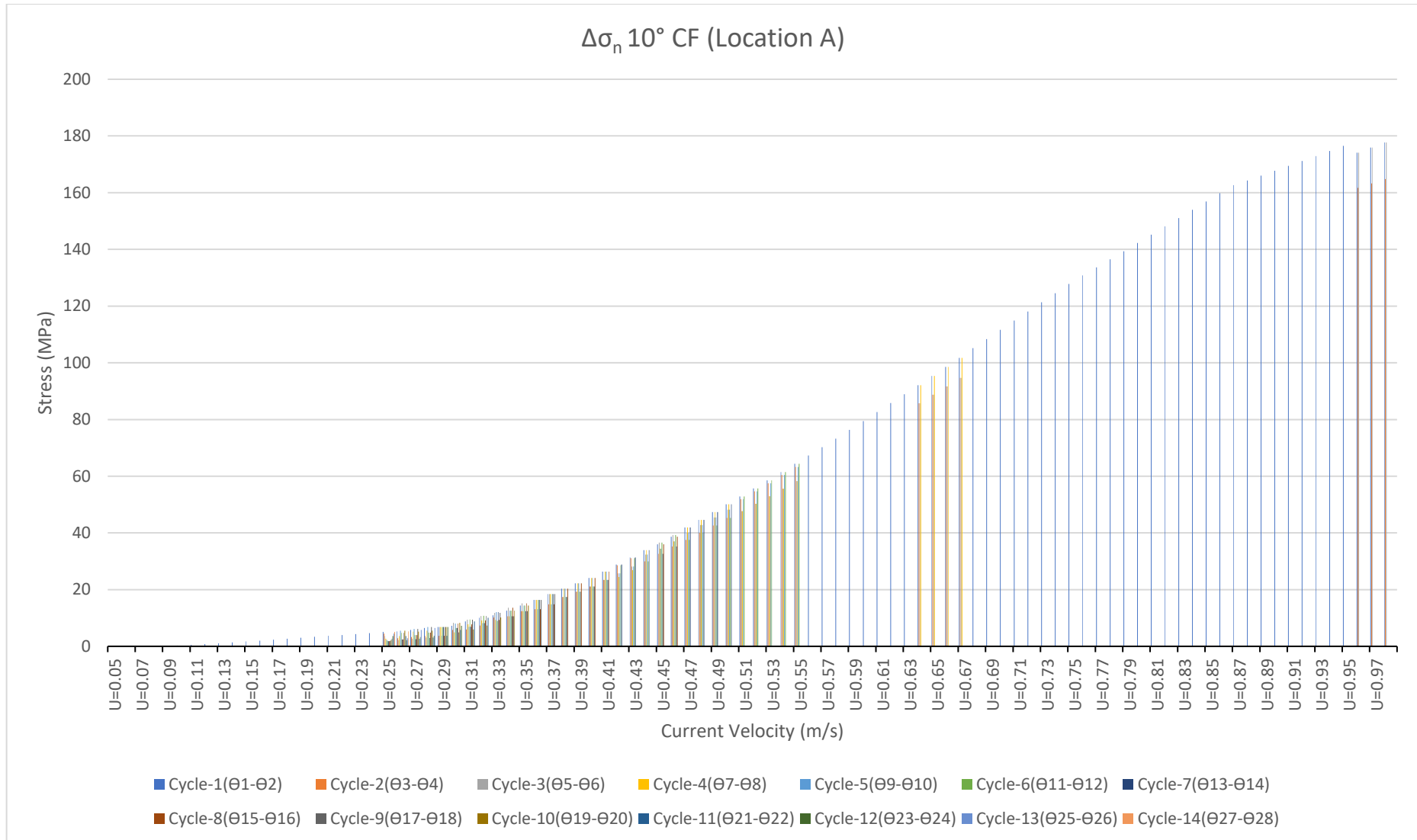


Figure 14-30: $\Delta\sigma_n$ (Case-1(b) - 10° Flow CF) at Location A

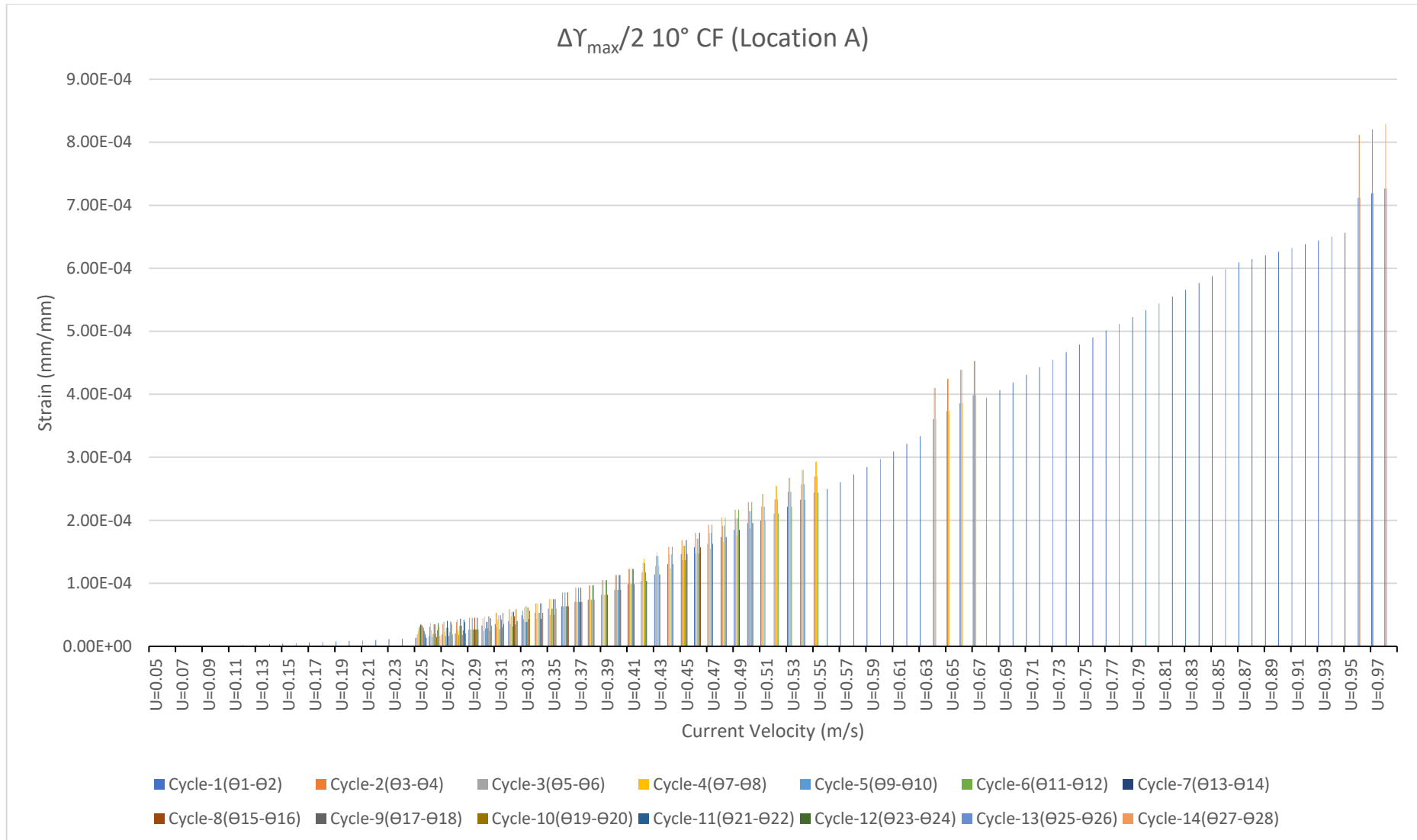


Figure 14-31: $\Delta\gamma_{\max}/2$ (Case-1(b) - 10° Flow CF) at Location A

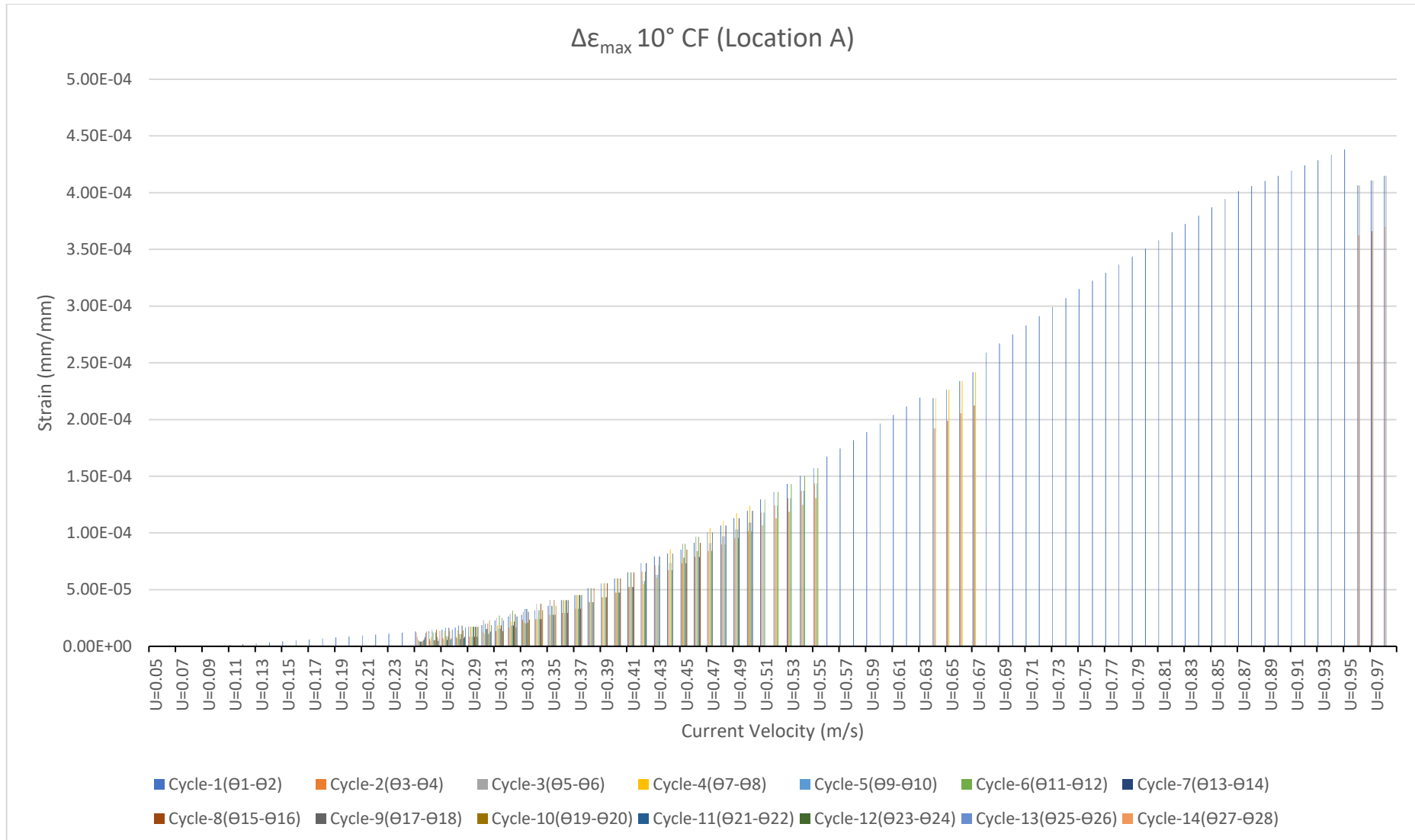


Figure 14-32: $\Delta\epsilon_n$ (Case-1(b) - 10° Flow CF) at Location A

4. Fatigue

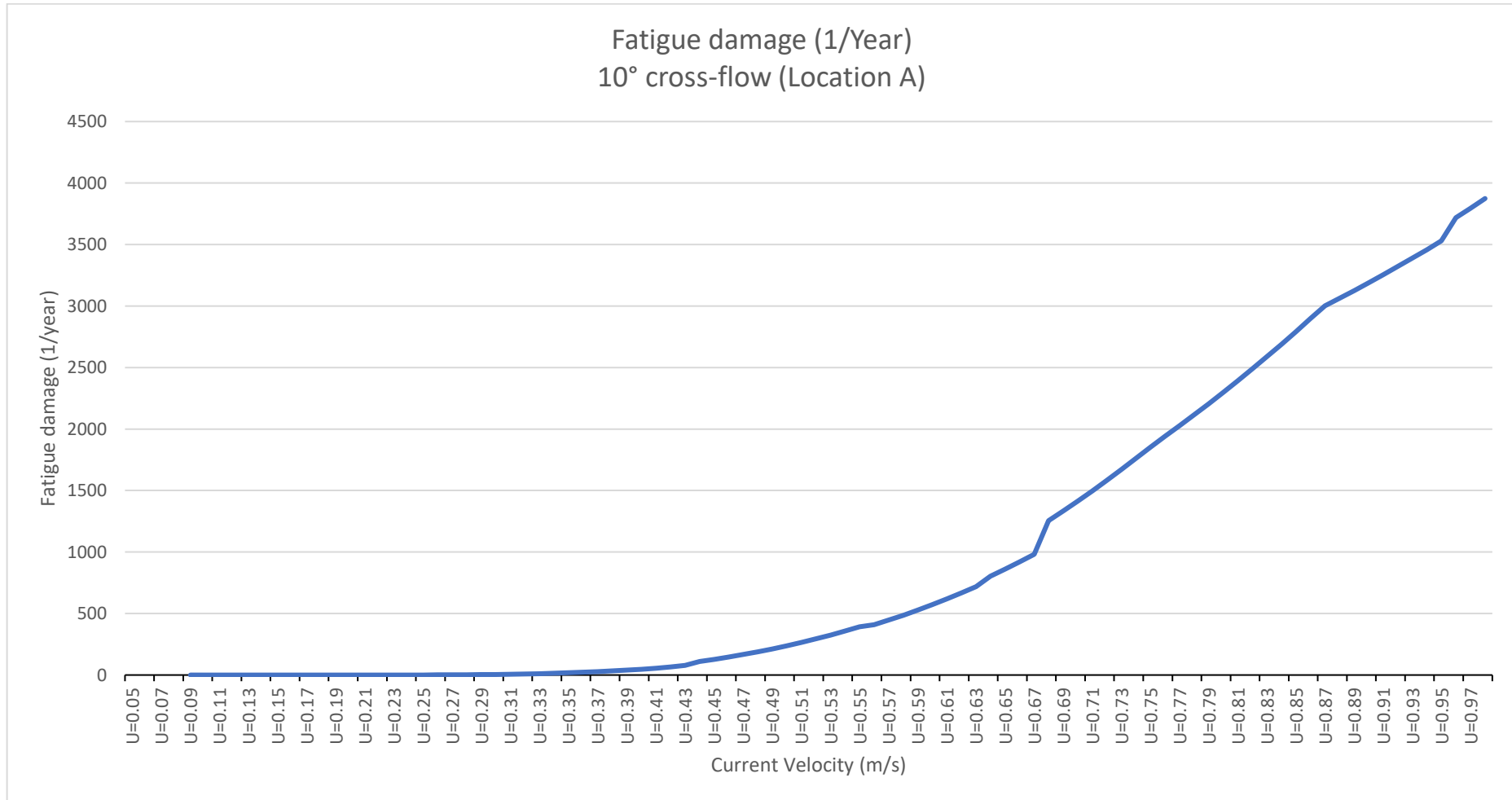


Figure 14-33: Fatigue damage per year for (Case-1(b) - 10° Flow CF) at Location A

Case-1 (b) – 10° CF Location B

1. Principal Stress and Strains

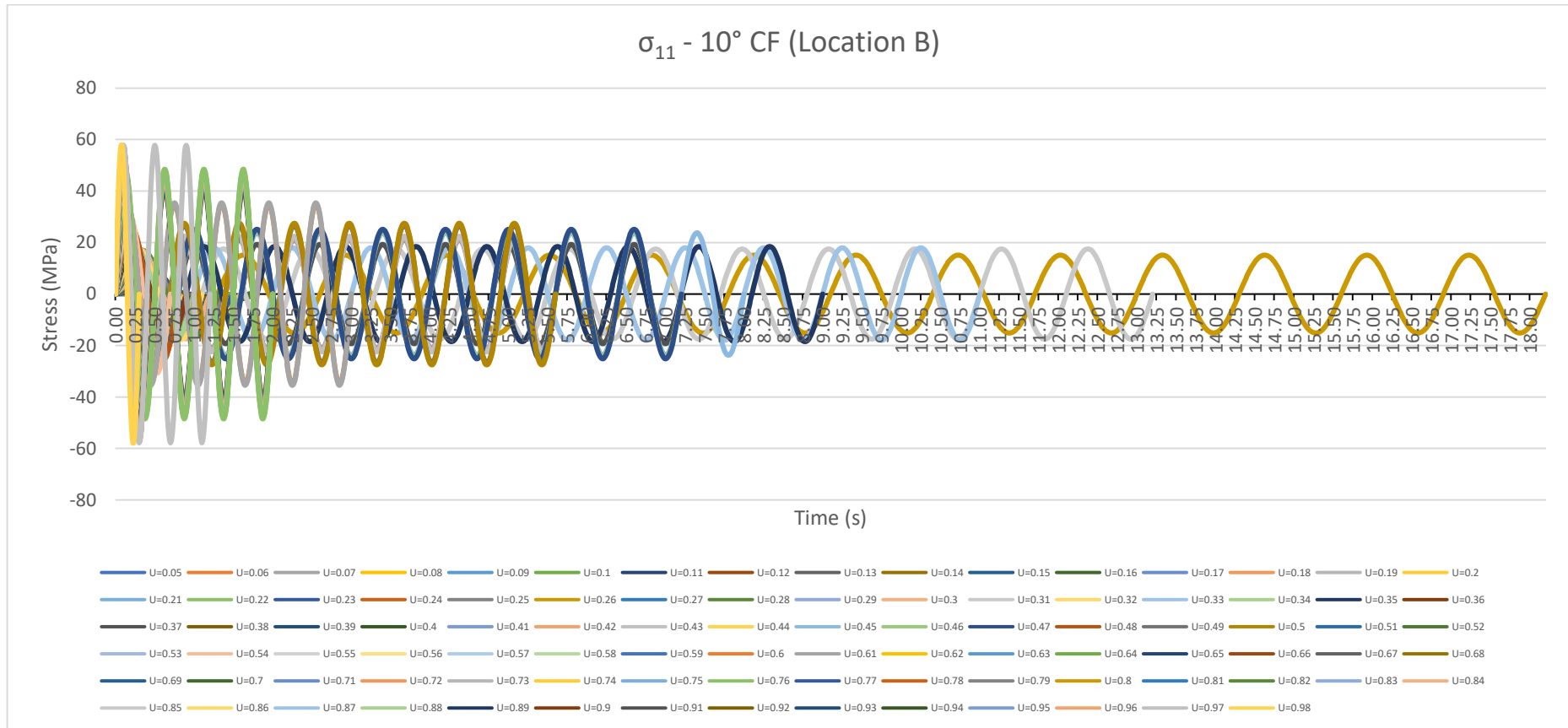


Figure 14-34: σ_{11} (Case-1(b) - 10° Flow CF) at Location B

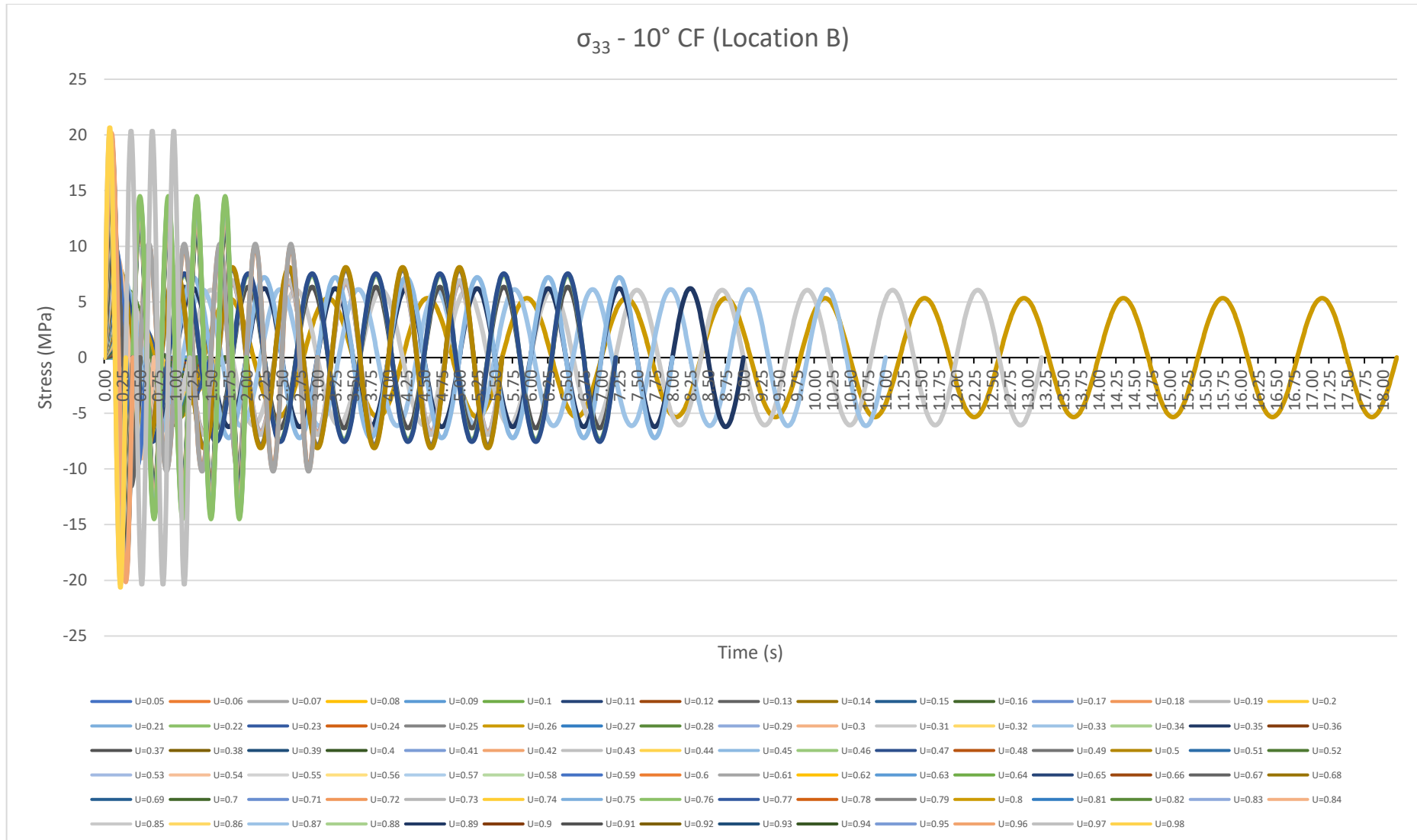


Figure 14-35: σ_{33} (Case-1(b) - 10° Flow CF) at Location B

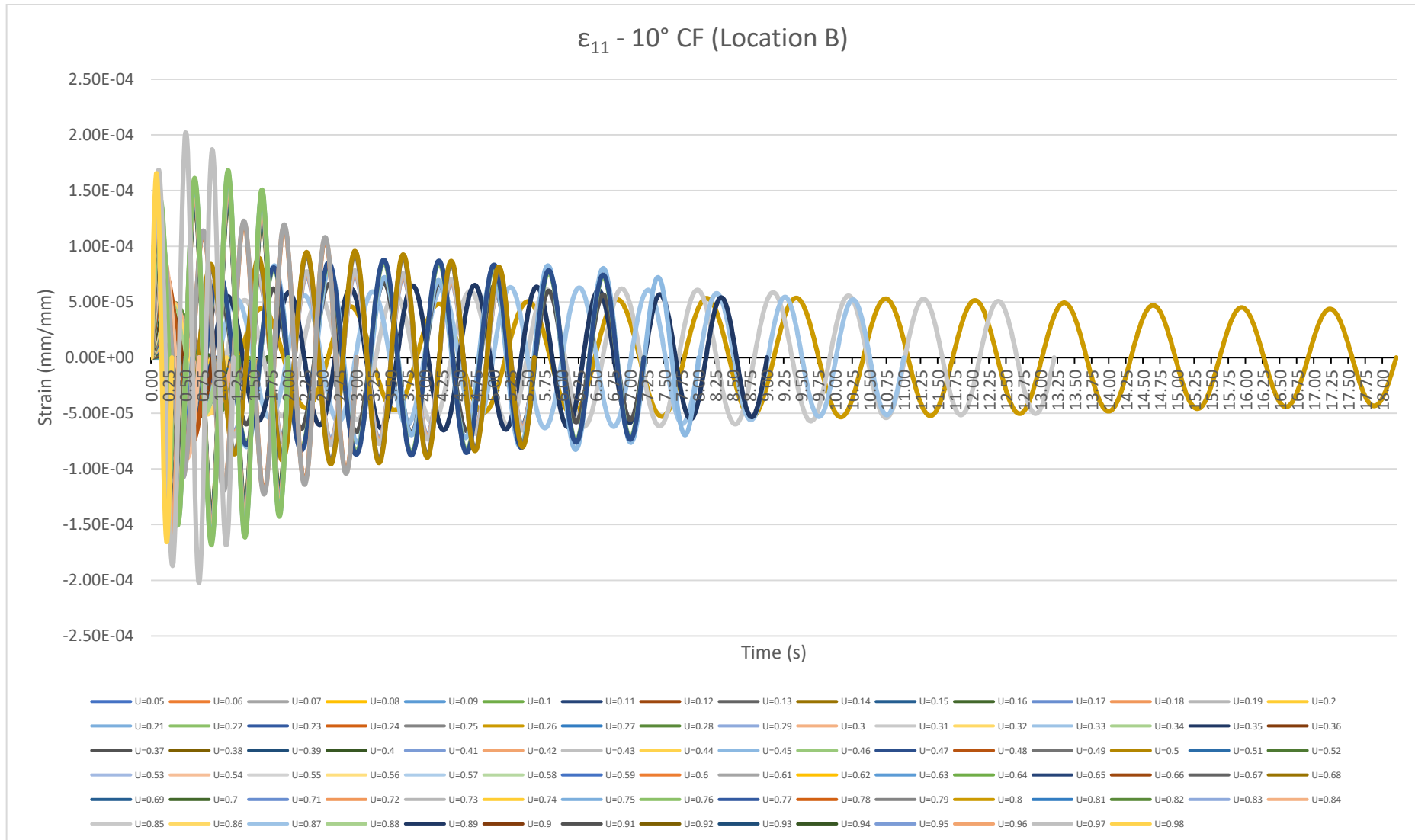


Figure 14-36: ϵ_{11} (Case-1(b) - 10° Flow CF) at Location B

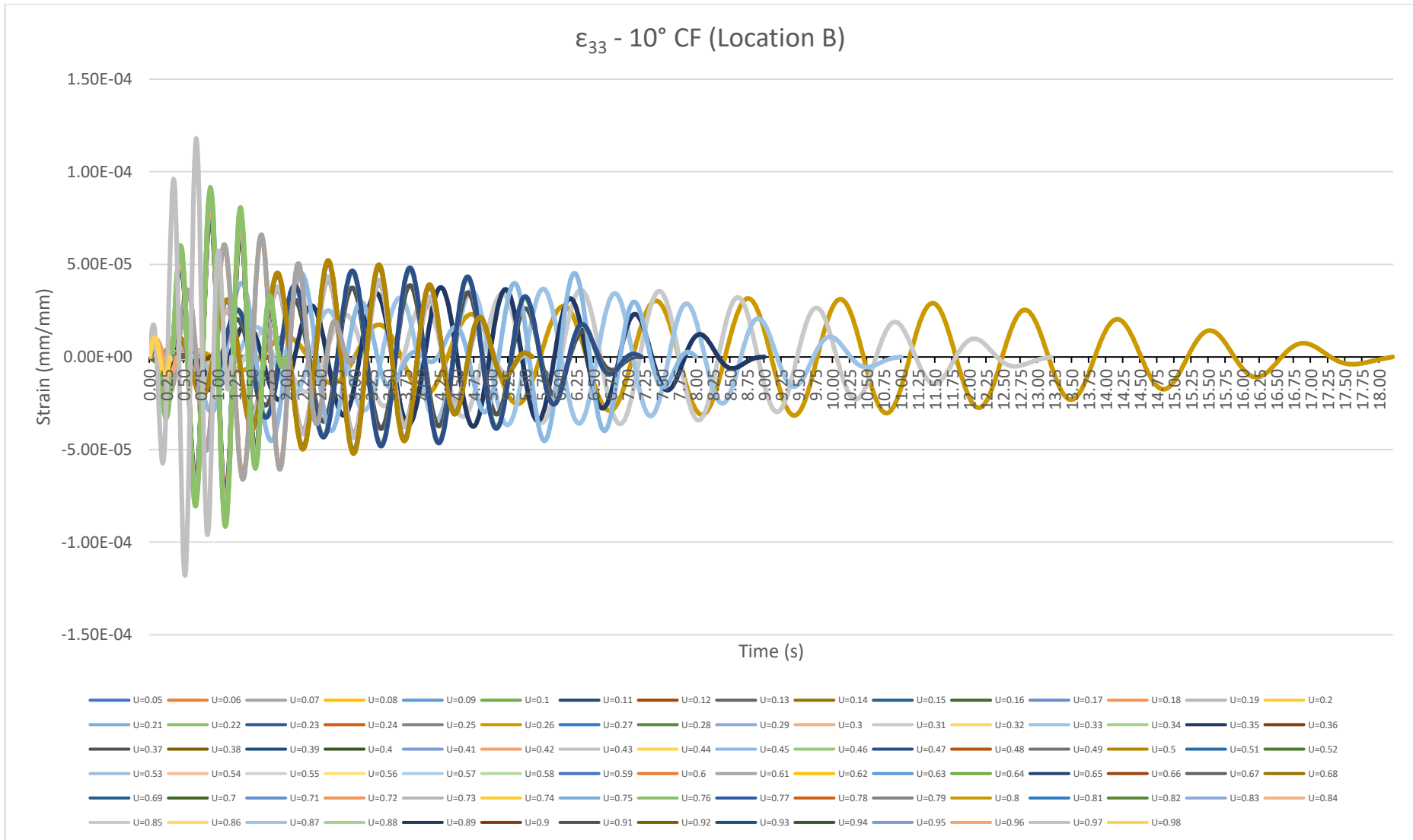


Figure 14-37: ϵ_{33} (Case-1(b) - 10° Flow CF) at Location B

2. Critical Plane

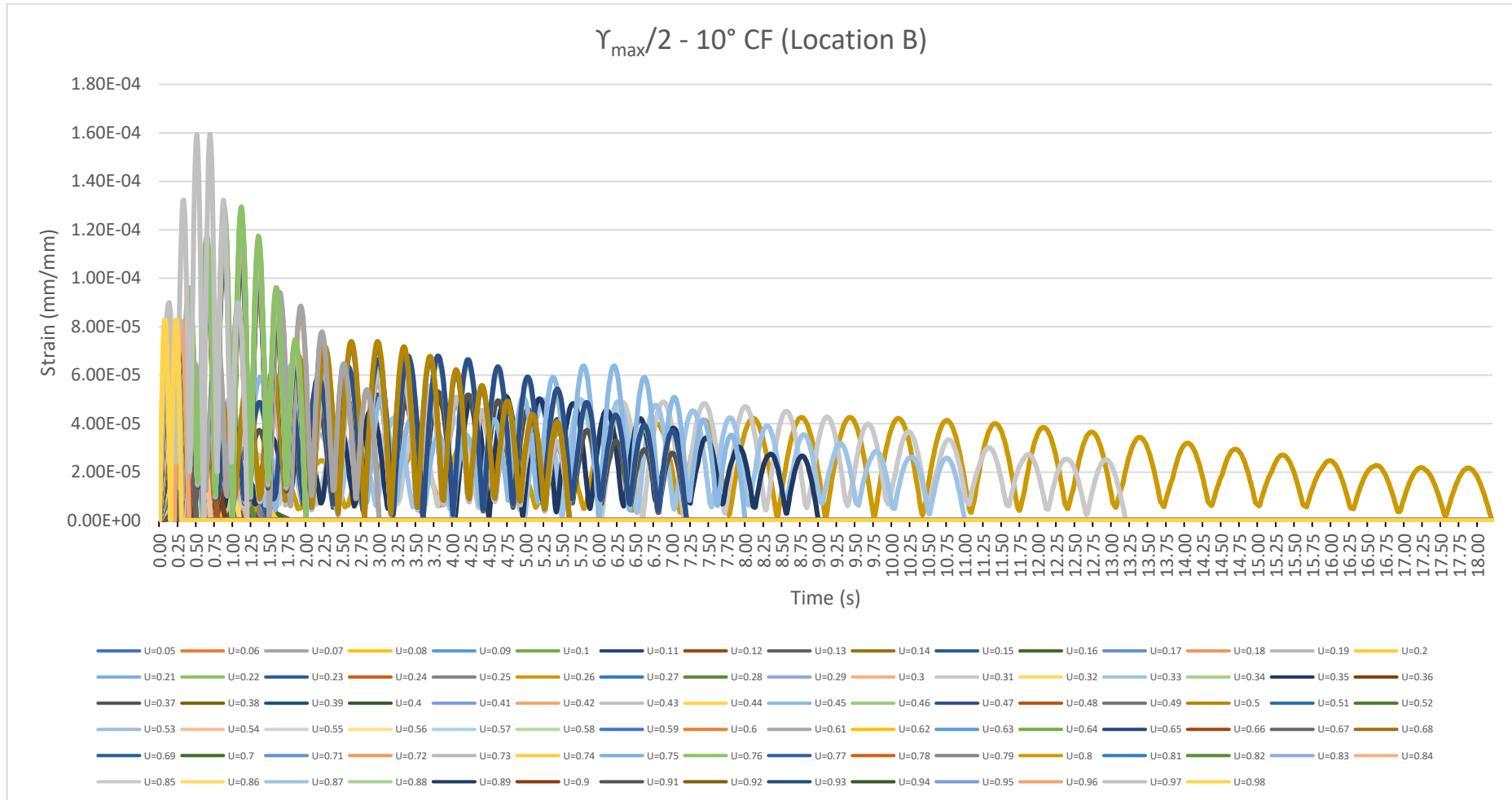


Figure 14-38: $\gamma_{\max}/2$ (Case-1(b) - 10° Flow CF) at Location B

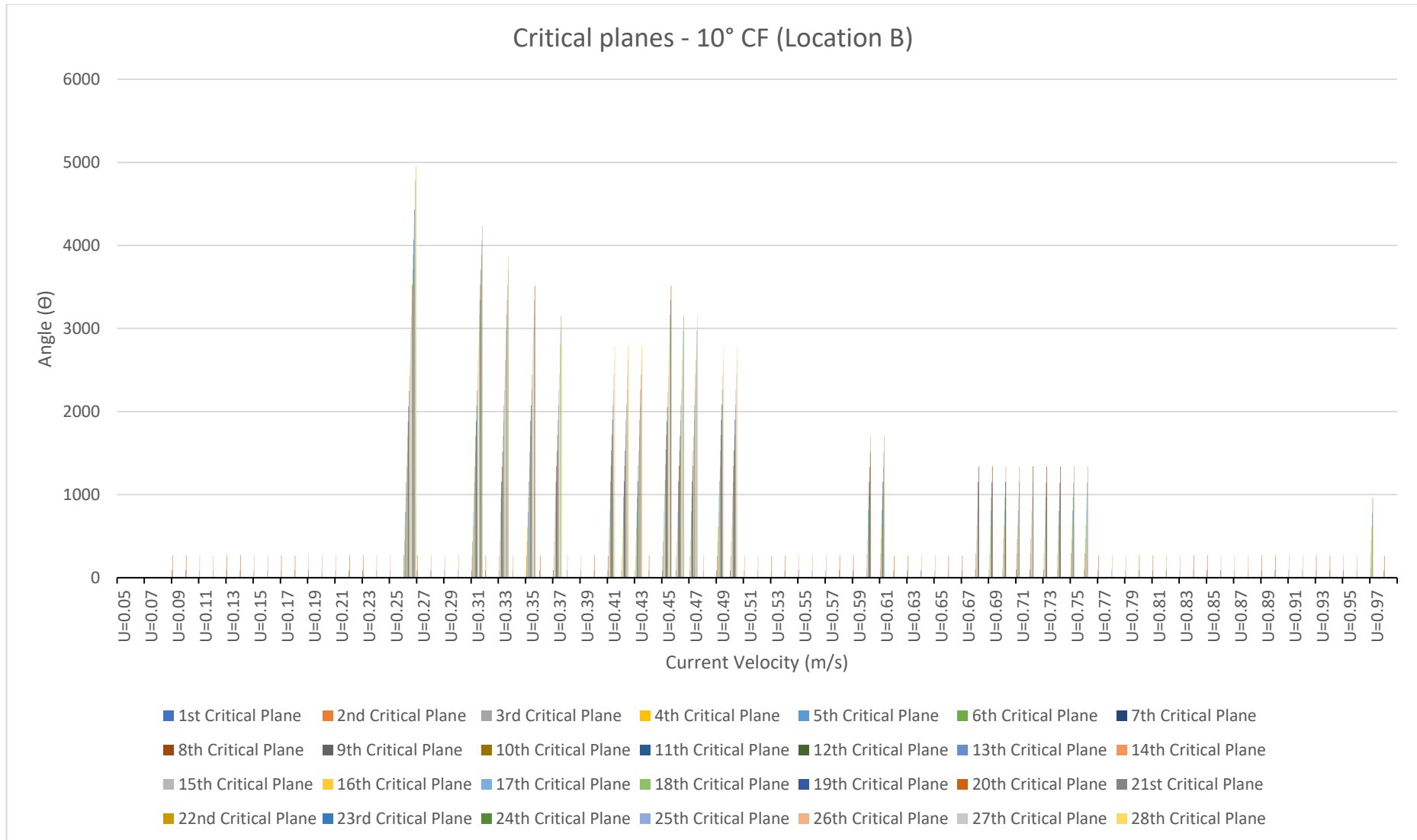


Figure 14-39: θ_{crit} (Case-1(b) - 10° Flow CF) at Location B

3. Normal and Shear Stress and Strain Range

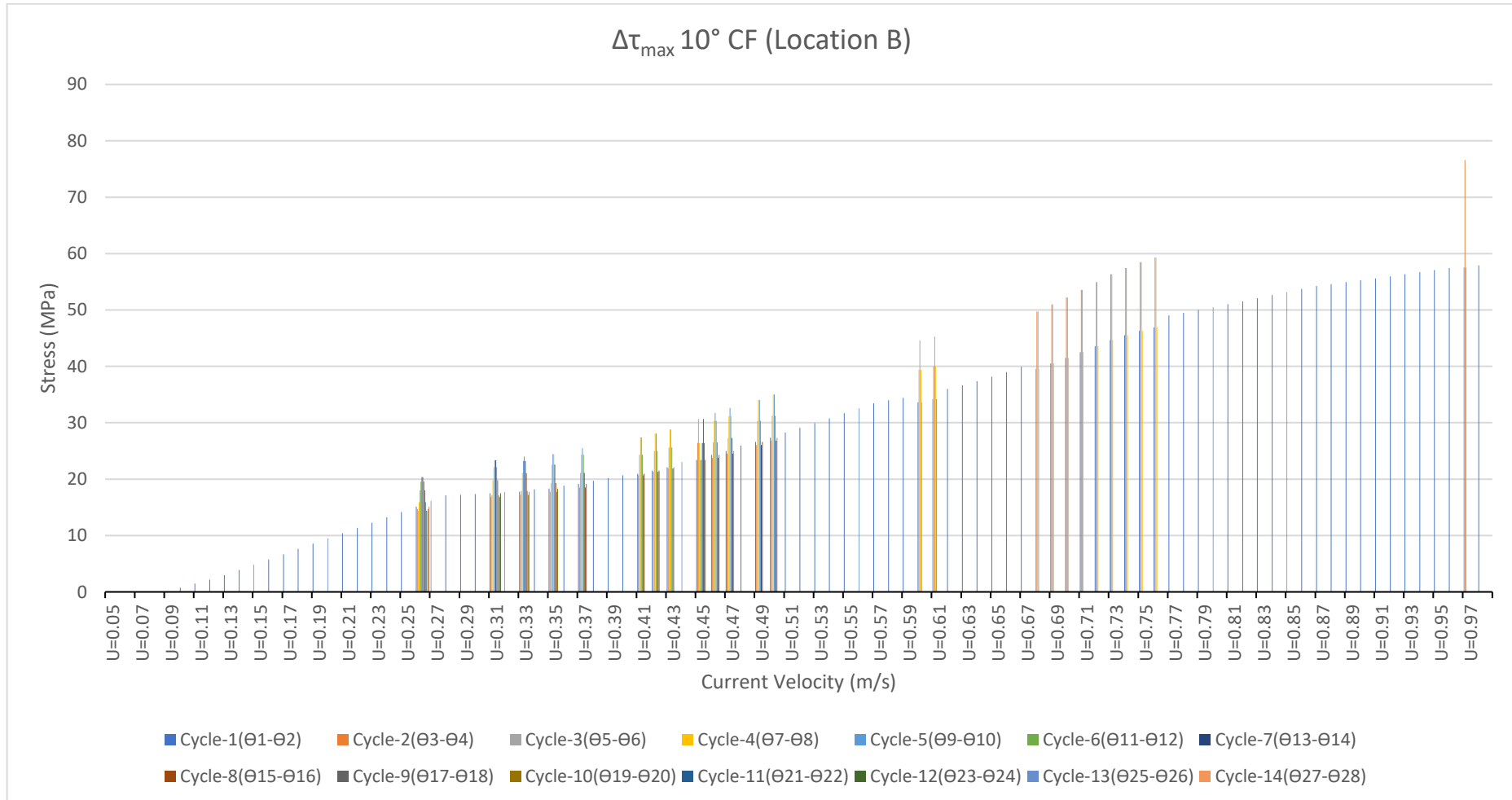


Figure 14-40: $\Delta\tau_{\max}$ (Case-1(b) - 10° Flow CF) at Location B

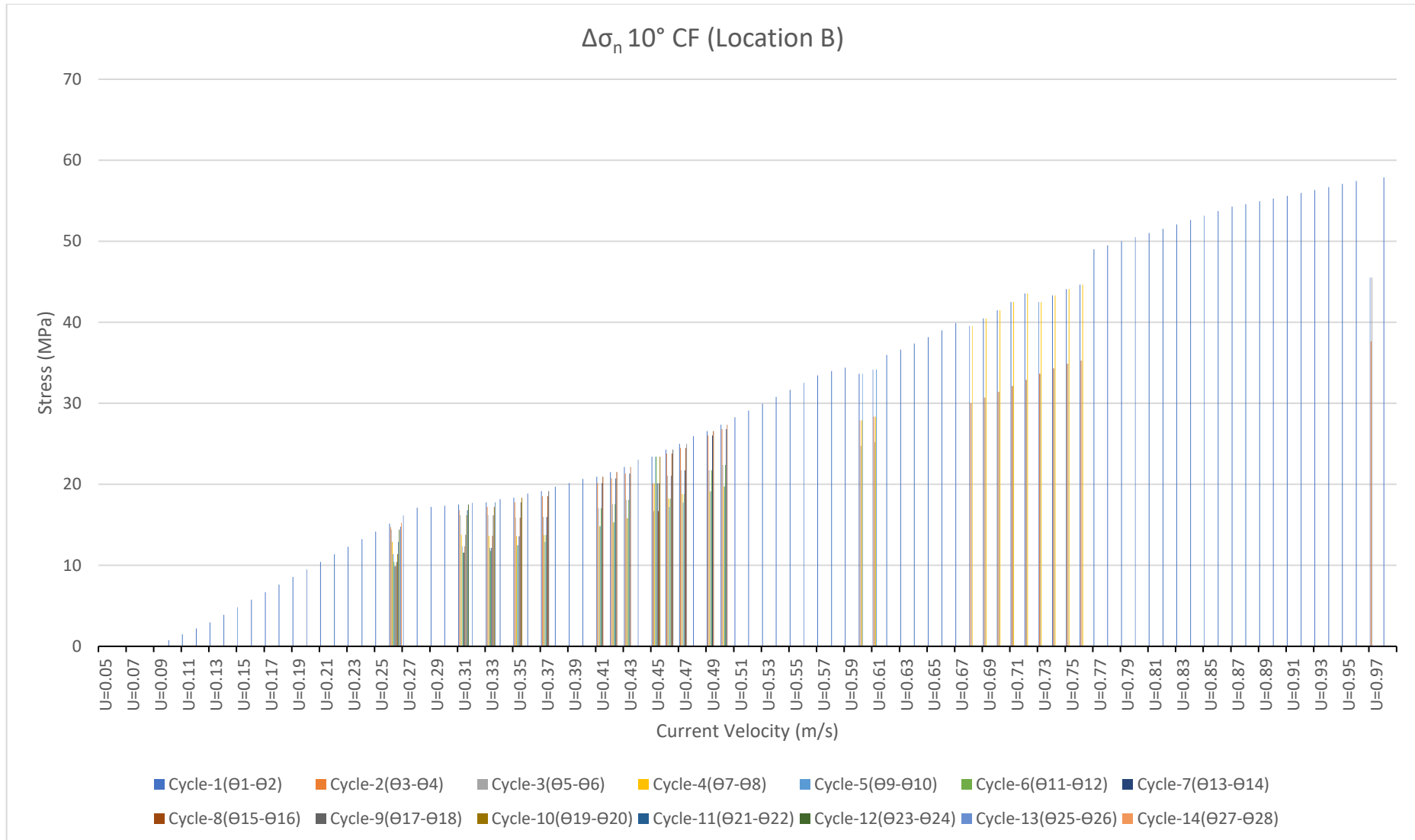


Figure 14-41: $\Delta\sigma_n$ (Case-1(b) - 10° Flow CF) at Location B

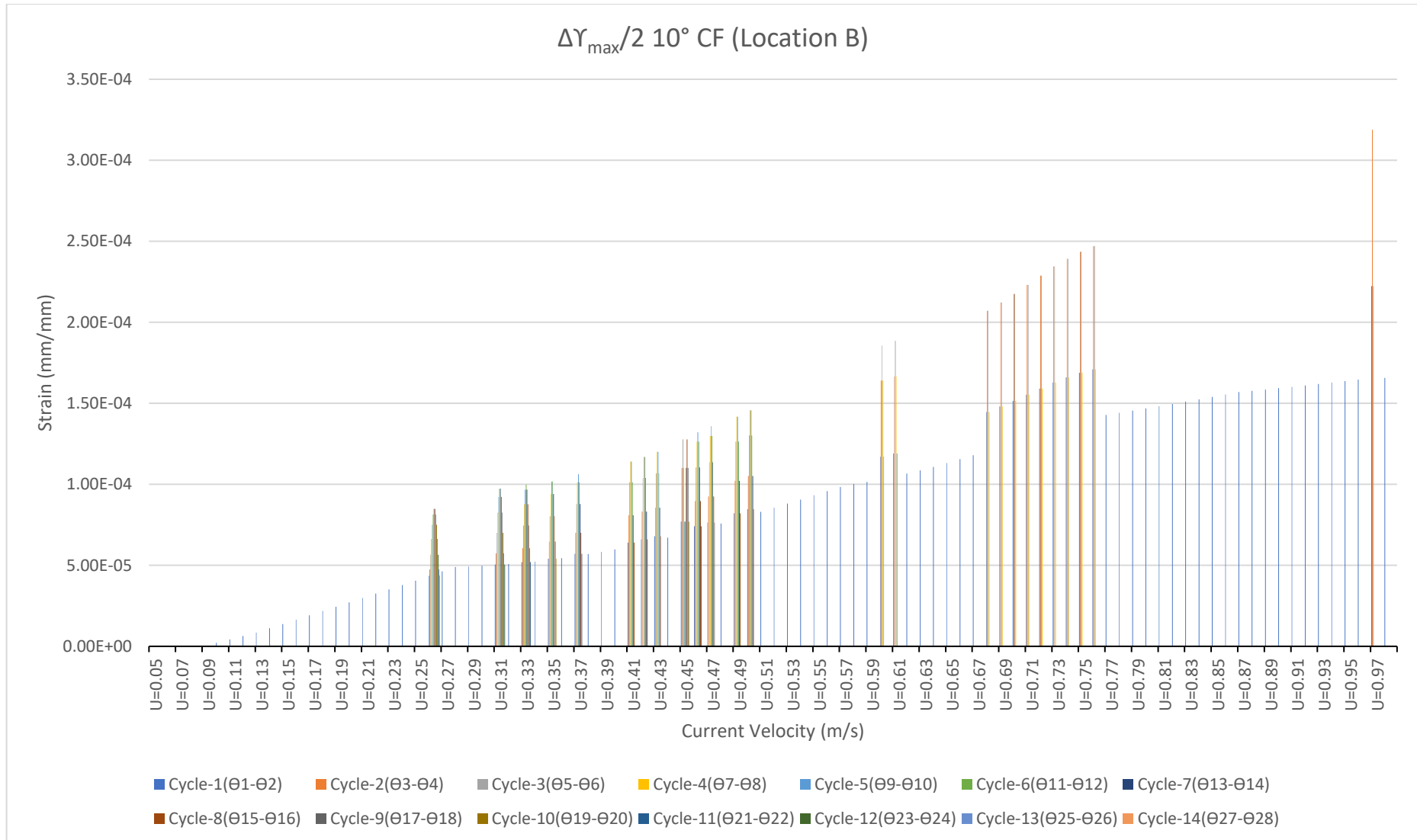


Figure 14-42: $\Delta\gamma_{\max}/2$ (Case-1(b) - 10° Flow CF) at Location B

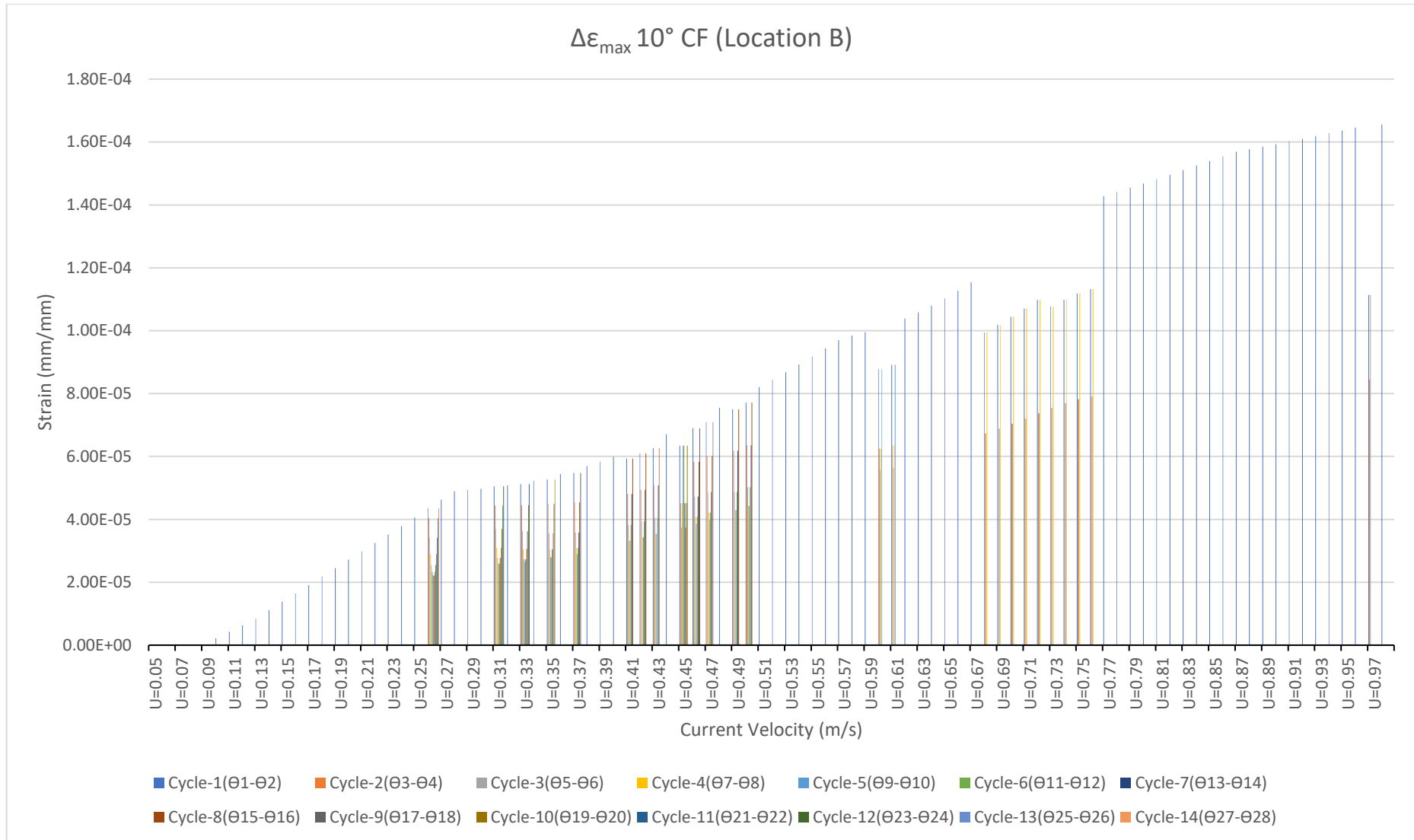


Figure 14-43: $\Delta \epsilon_n$ (Case-1(b) - 10° Flow CF) at Location B

4. Fatigue

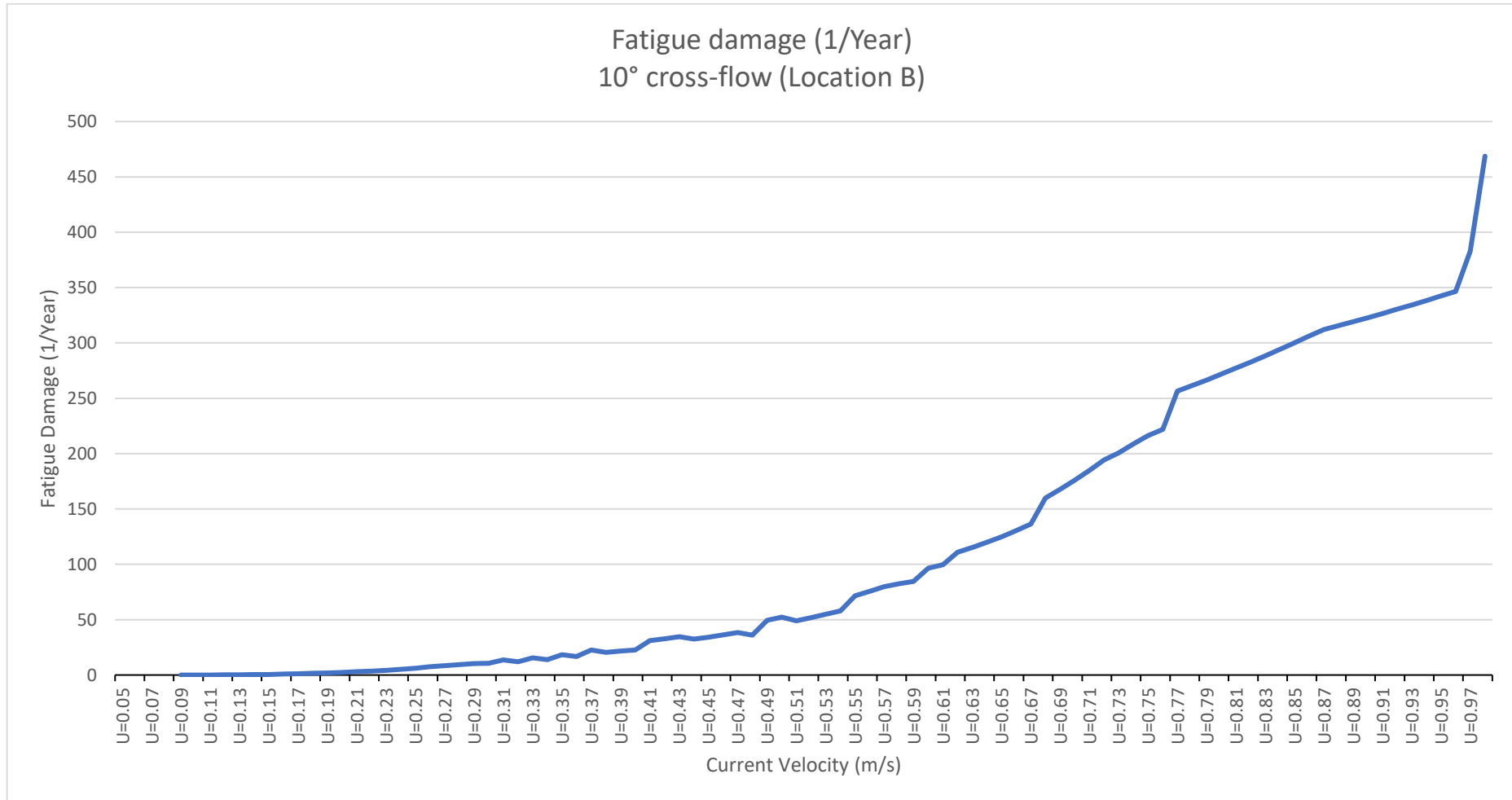


Figure 14-44: Fatigue damage per year for (Case-1(b) - 10° Flow CF) at Location B

Case-2 (a) – 90° IL Location A

1. Principal Stress and Strains

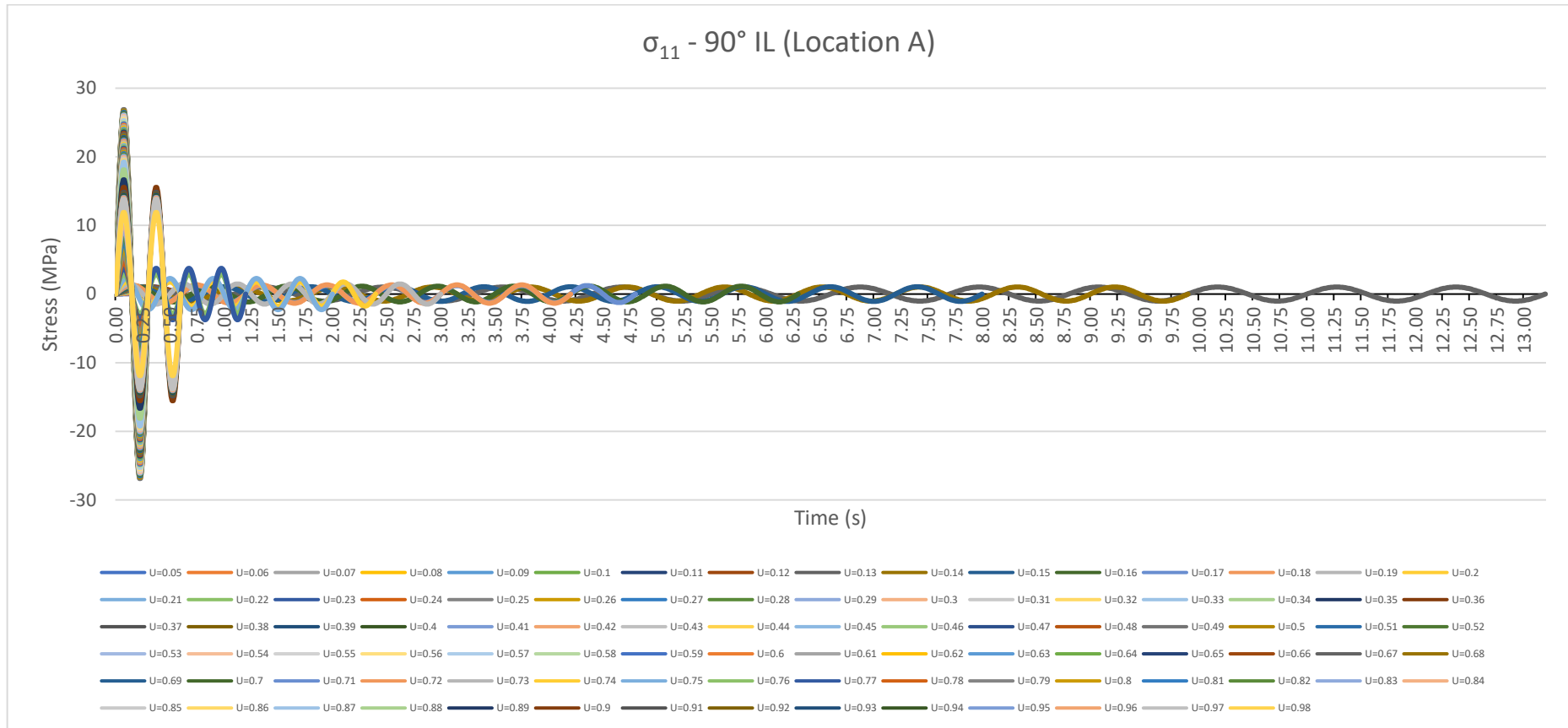


Figure 14-45: σ_{11} (Case-2(a) - 90° Flow IL) at Location A

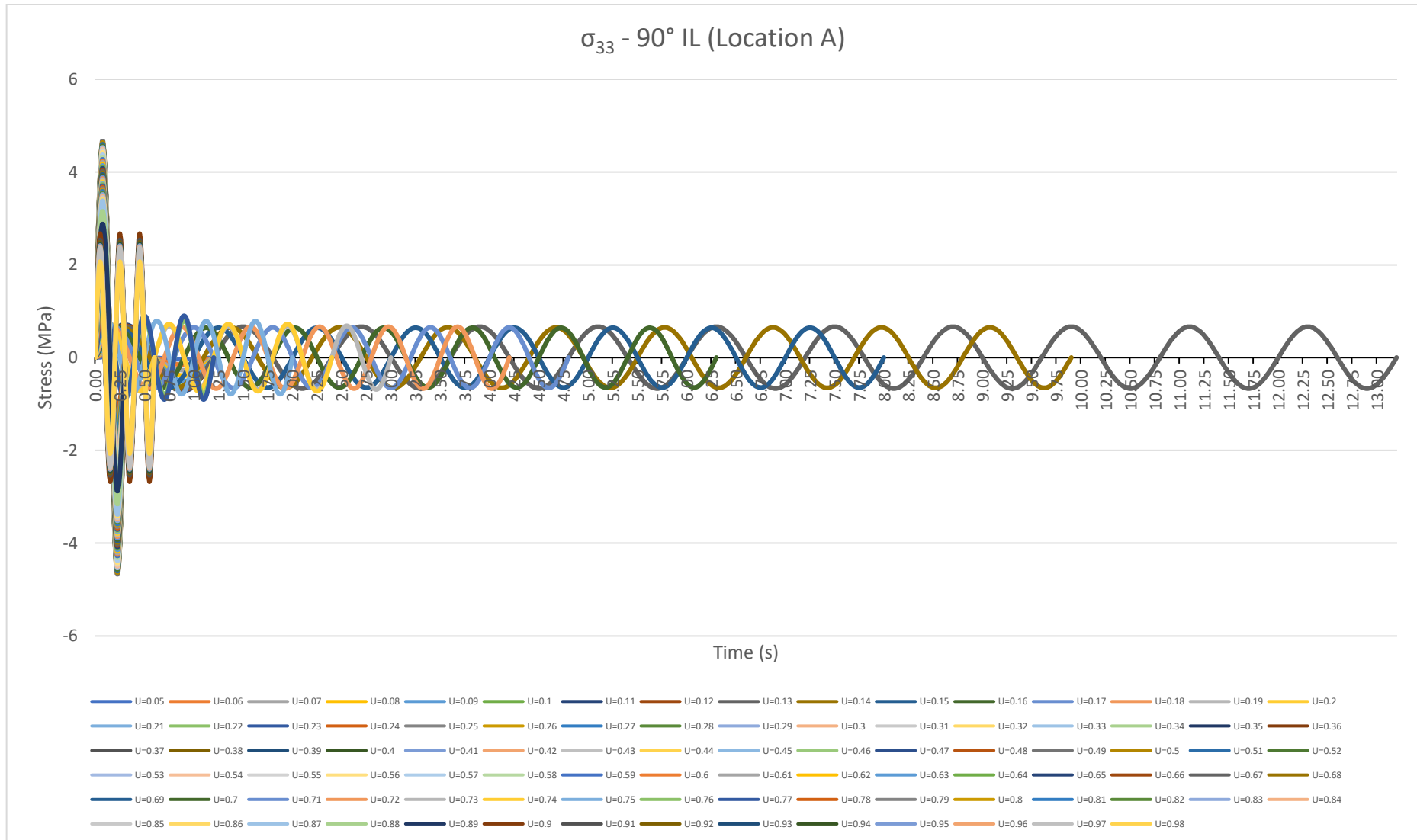


Figure 14-46: σ_{33} (Case-2(a) - 90° Flow IL) at Location A

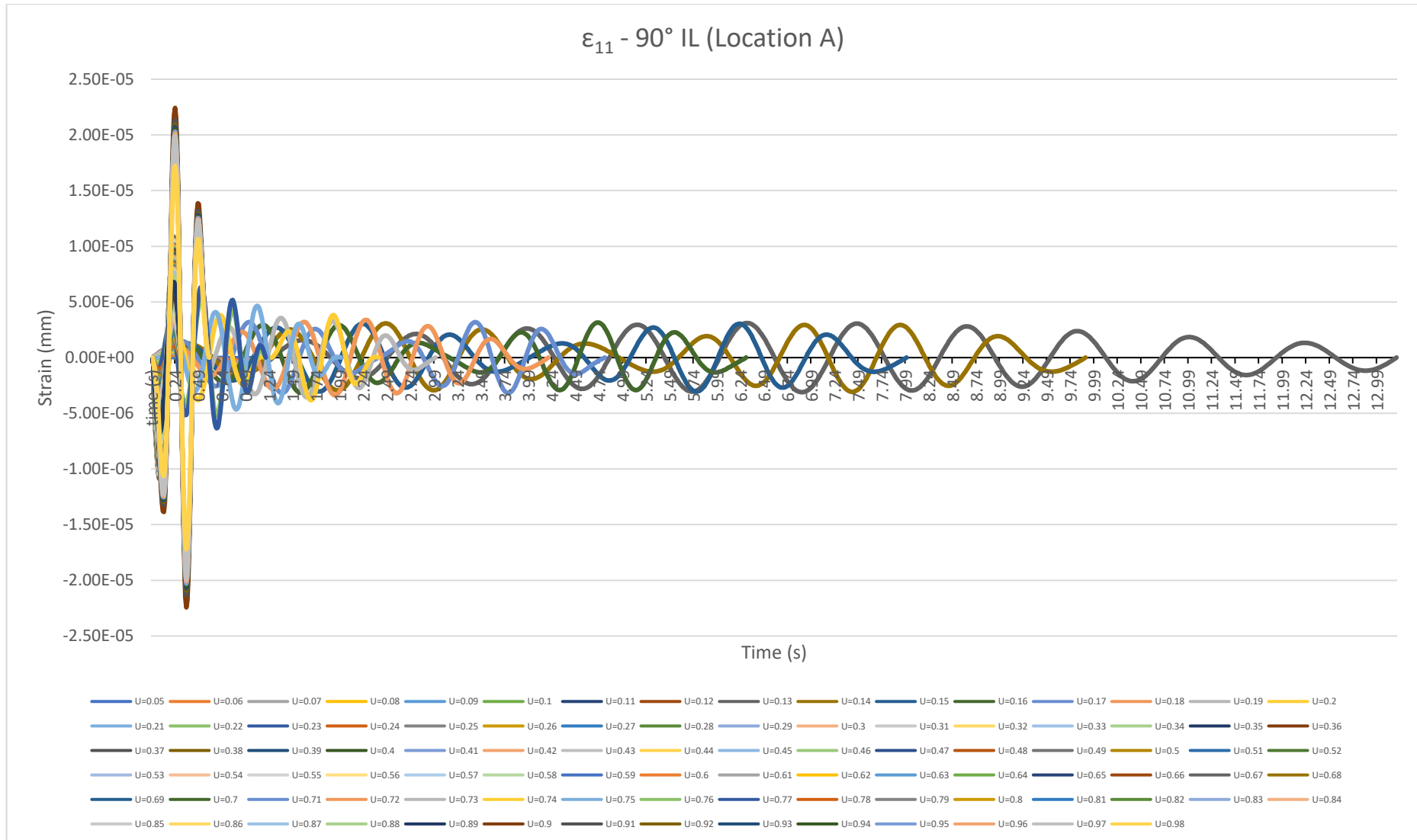


Figure 14-47: ϵ_{11} (Case-2(a) - 90° Flow IL) at Location A

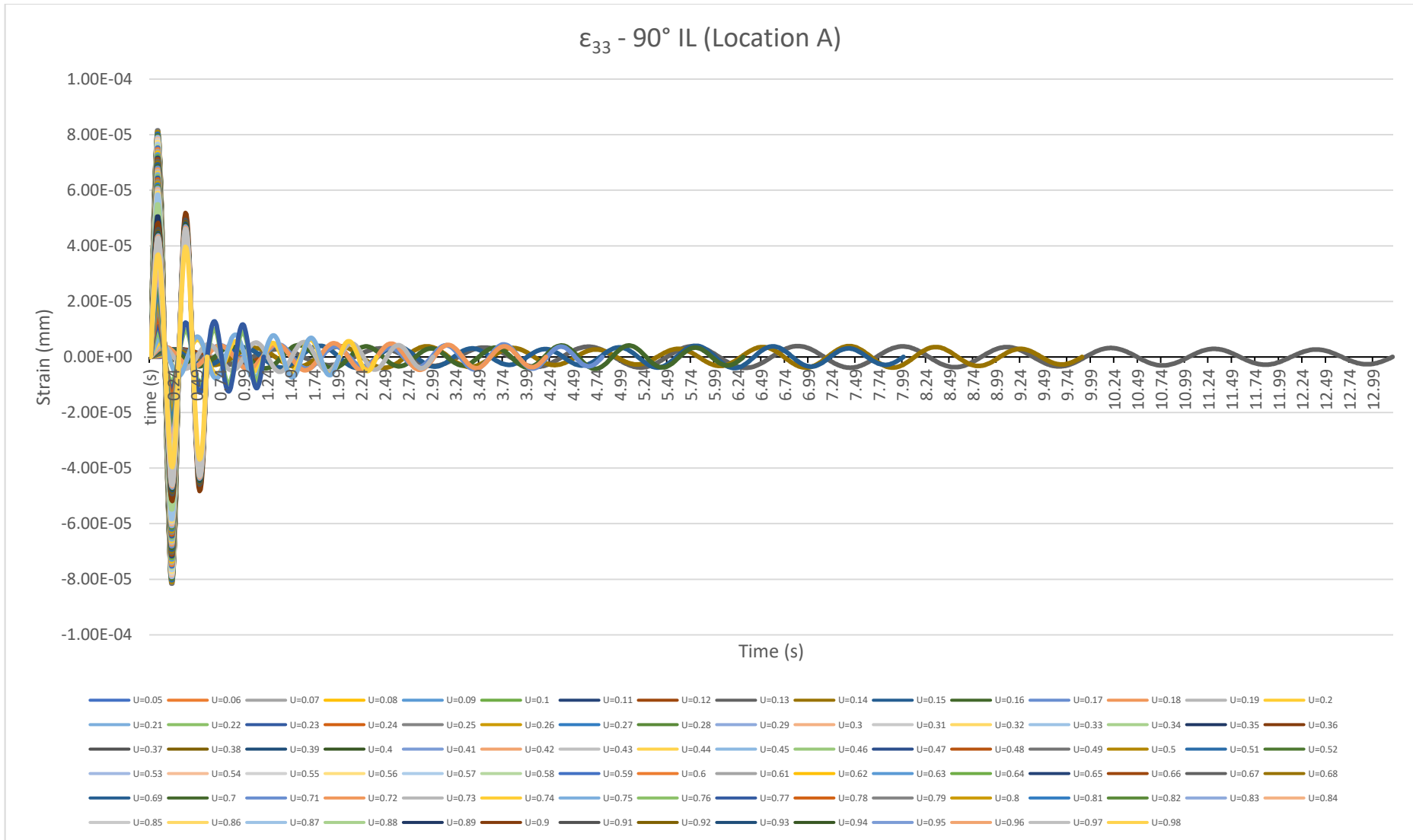


Figure 14-48: ϵ_{33} (Case-2(a) - 90° Flow IL) at Location A

2. Critical Plane

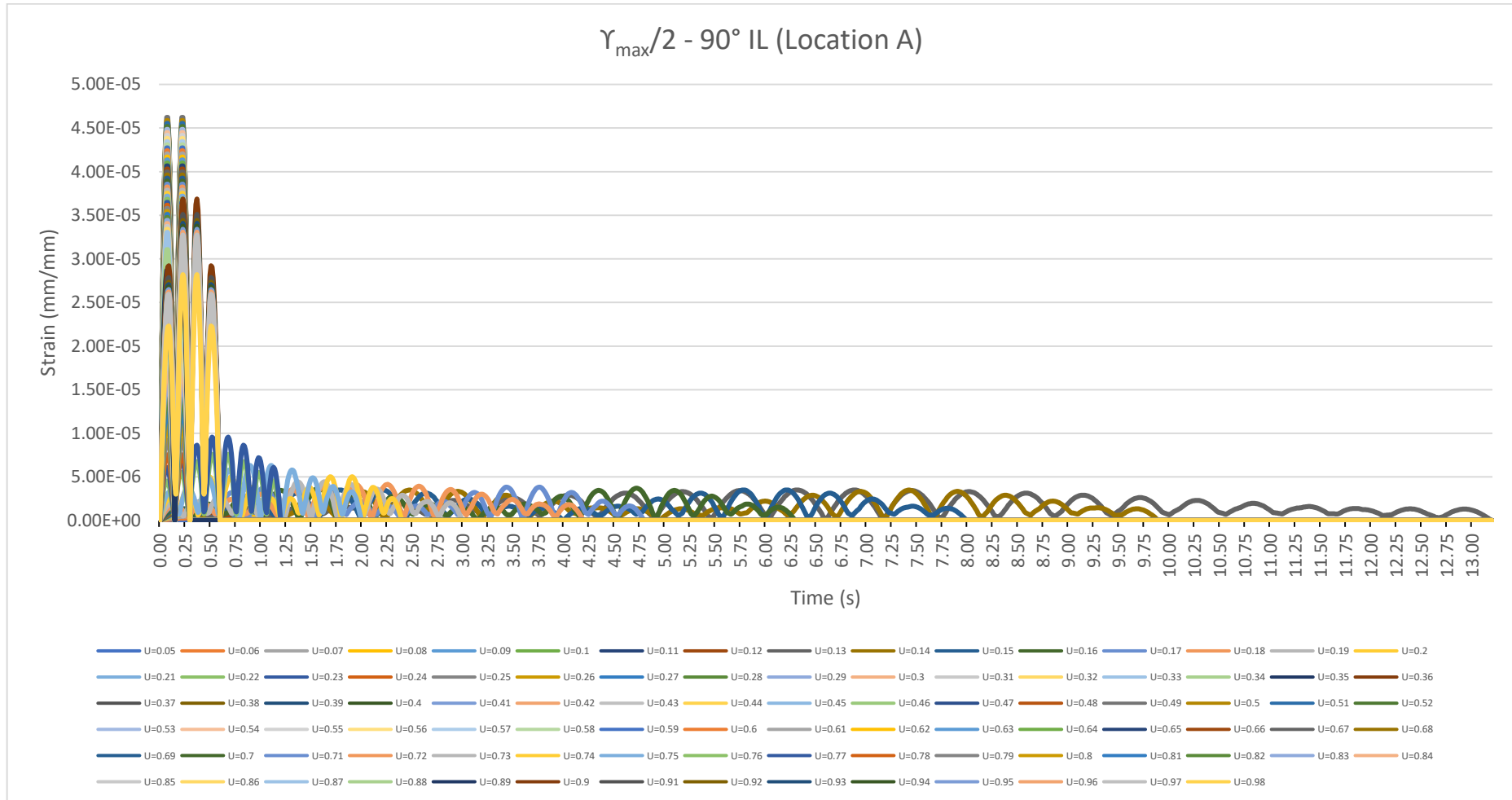


Figure 14-49: $\gamma_{\max}/2$ (Case-2(a) - 90° Flow IL) at Location A

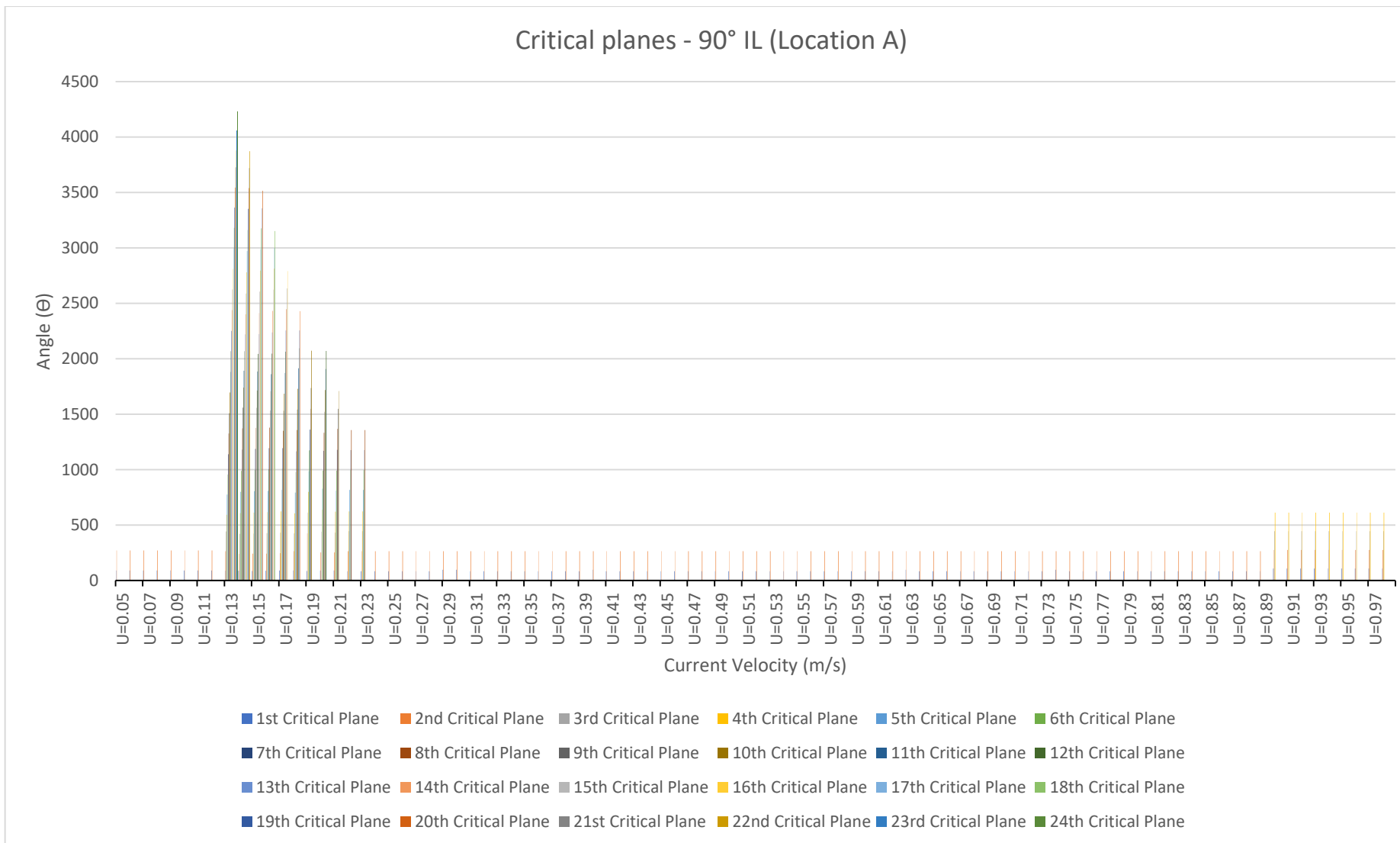


Figure 14-50: Θ_{crit} (Case-2(a) - 90° Flow IL) at Location A

3. Normal and Shear Stress and Strain Range

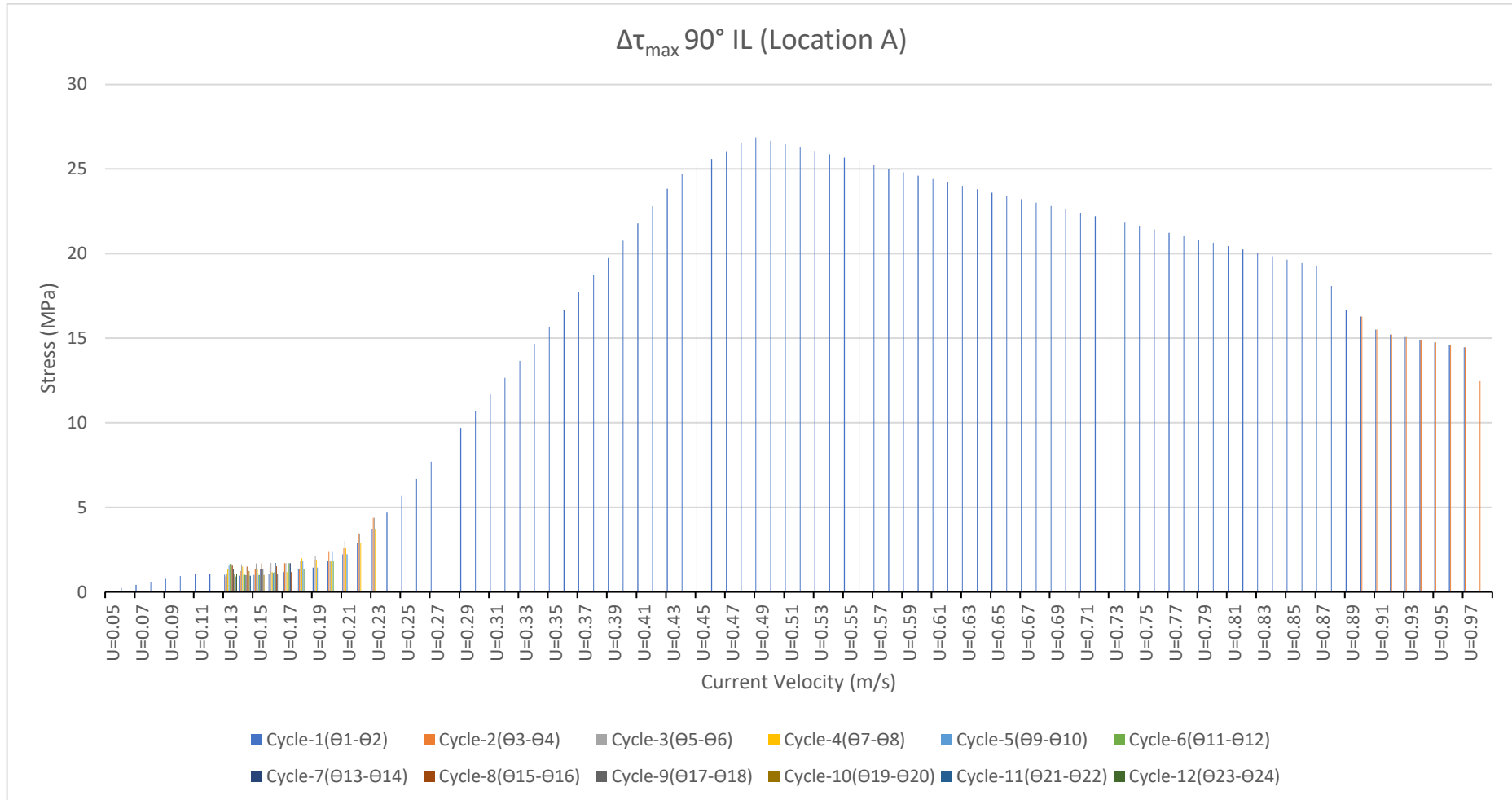


Figure 14-51: $\Delta\tau_{\max}$ (Case-2(a) - 90° Flow IL) at Location A

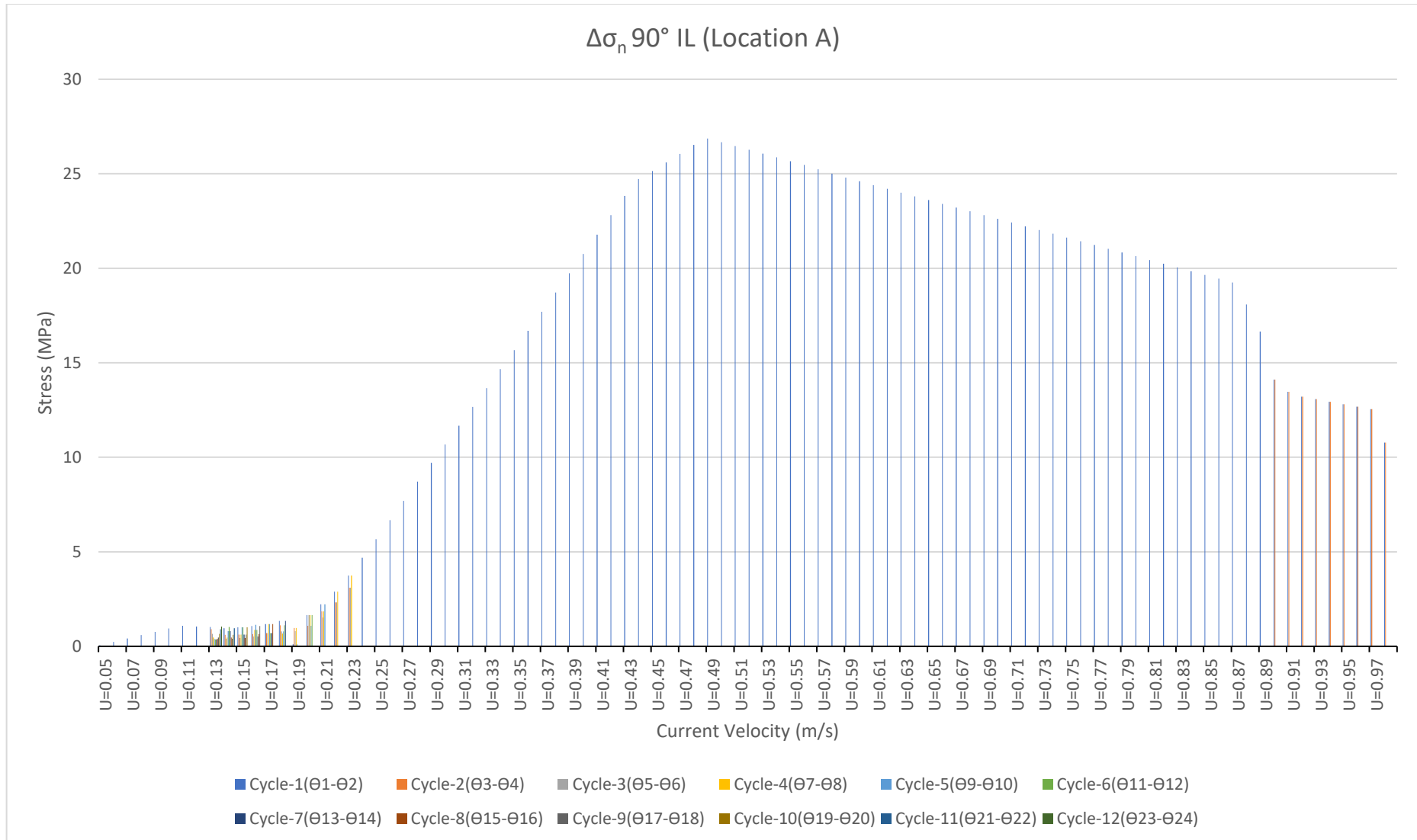


Figure 14-52: $\Delta\sigma_n$ (Case-2(a) - 90° Flow IL) at Location A

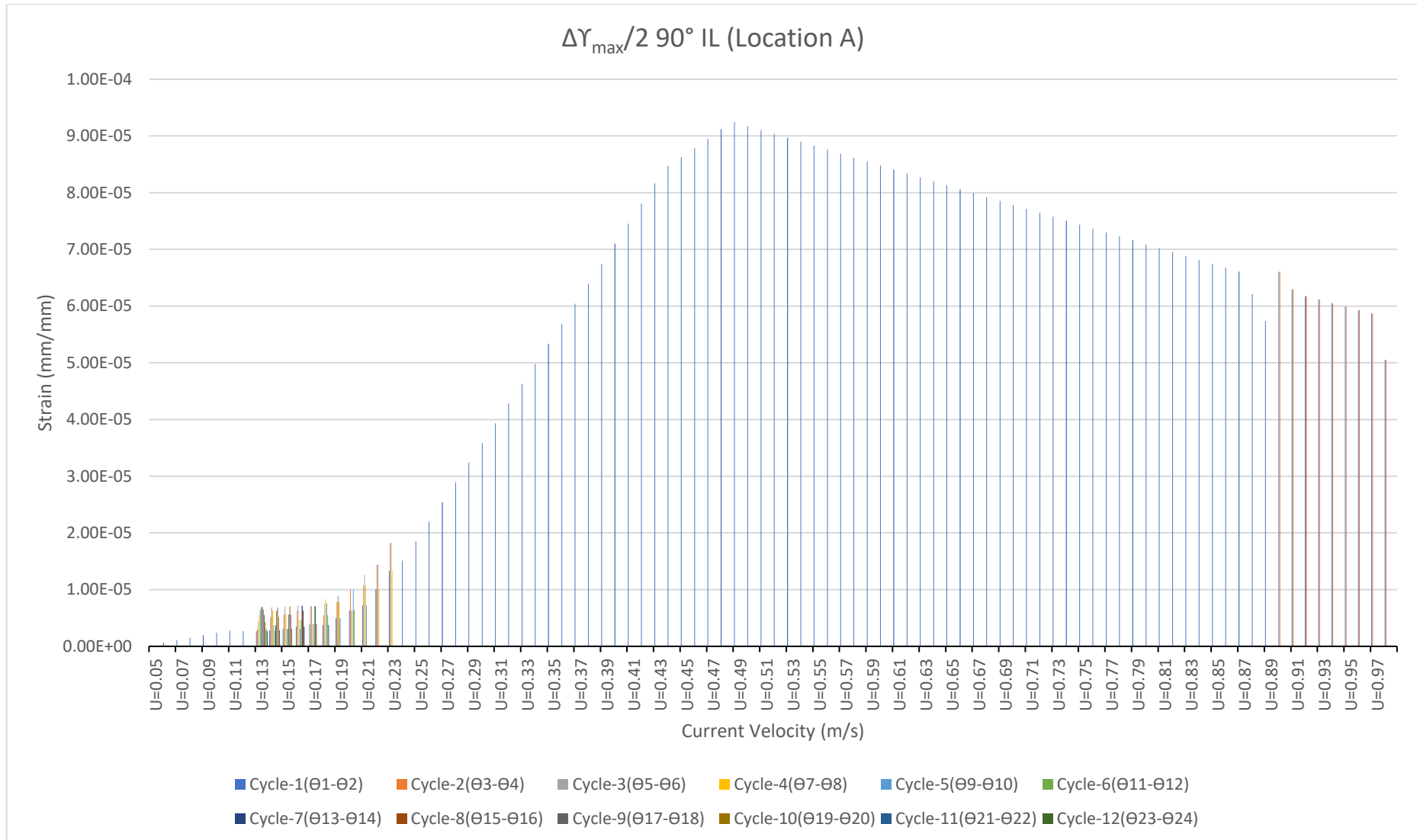


Figure 14-53: $\Delta\gamma_{\max}/2$ (Case-2(a) - 90° Flow IL) at Location A

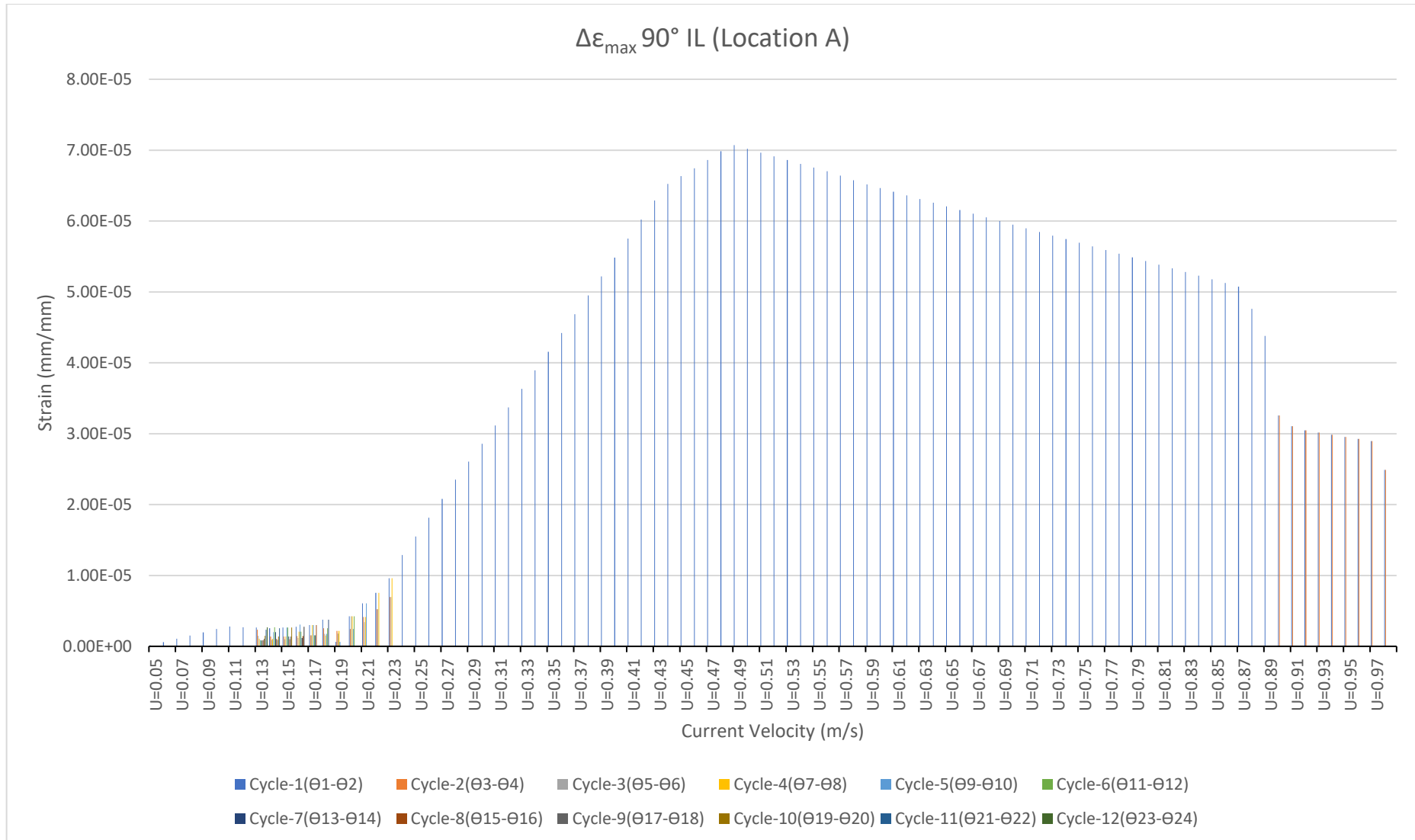


Figure 14-54: $\Delta\epsilon_n$ (Case-2(a) - 90° Flow IL) at Location A

4. Fatigue

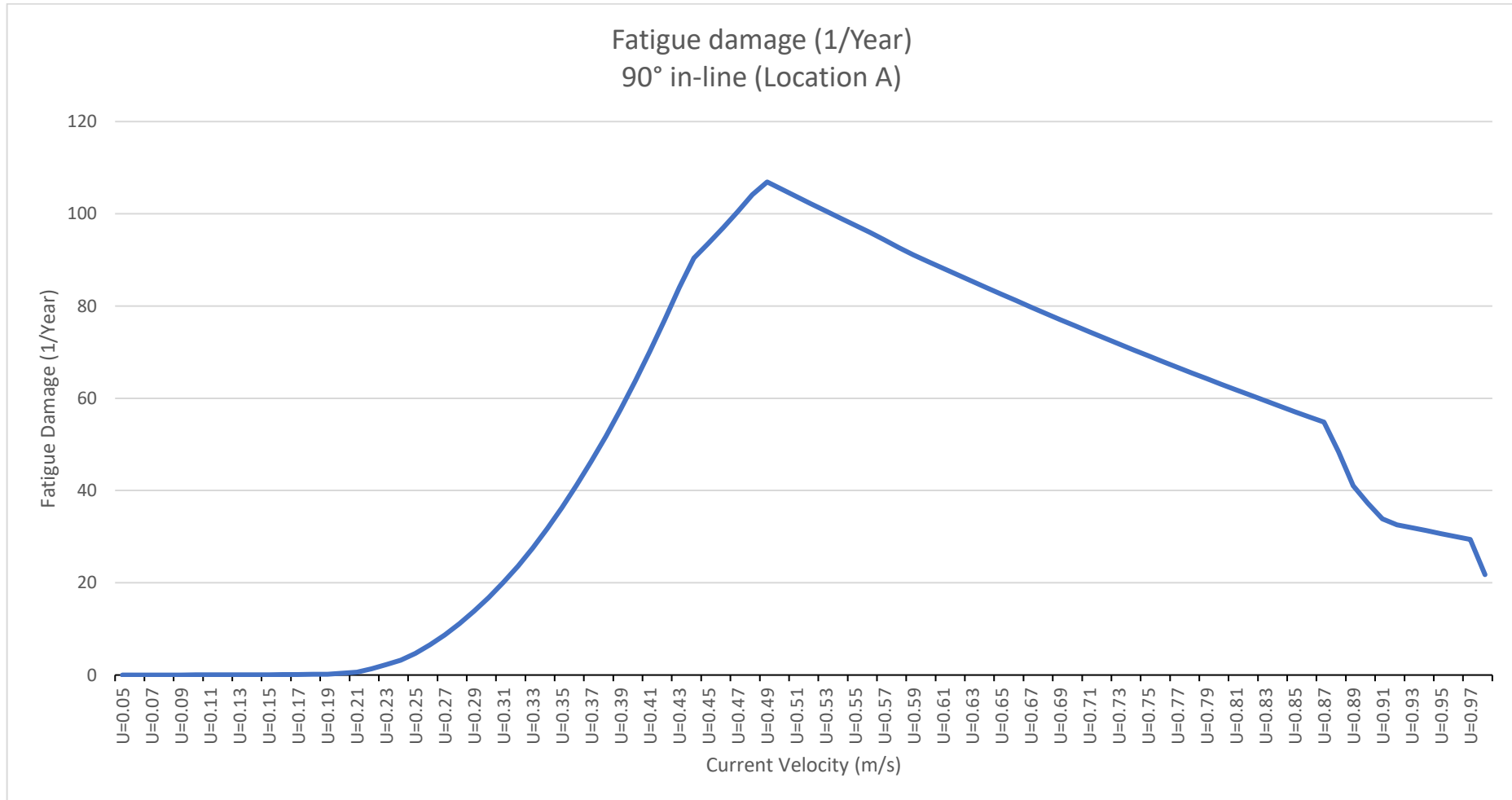


Figure 14-55: Fatigue damage per year for (Case-2(a) - 90° Flow IL) at Location A

Case-2 (a) – 90° IL Location B

1. Principal Stress and Strains

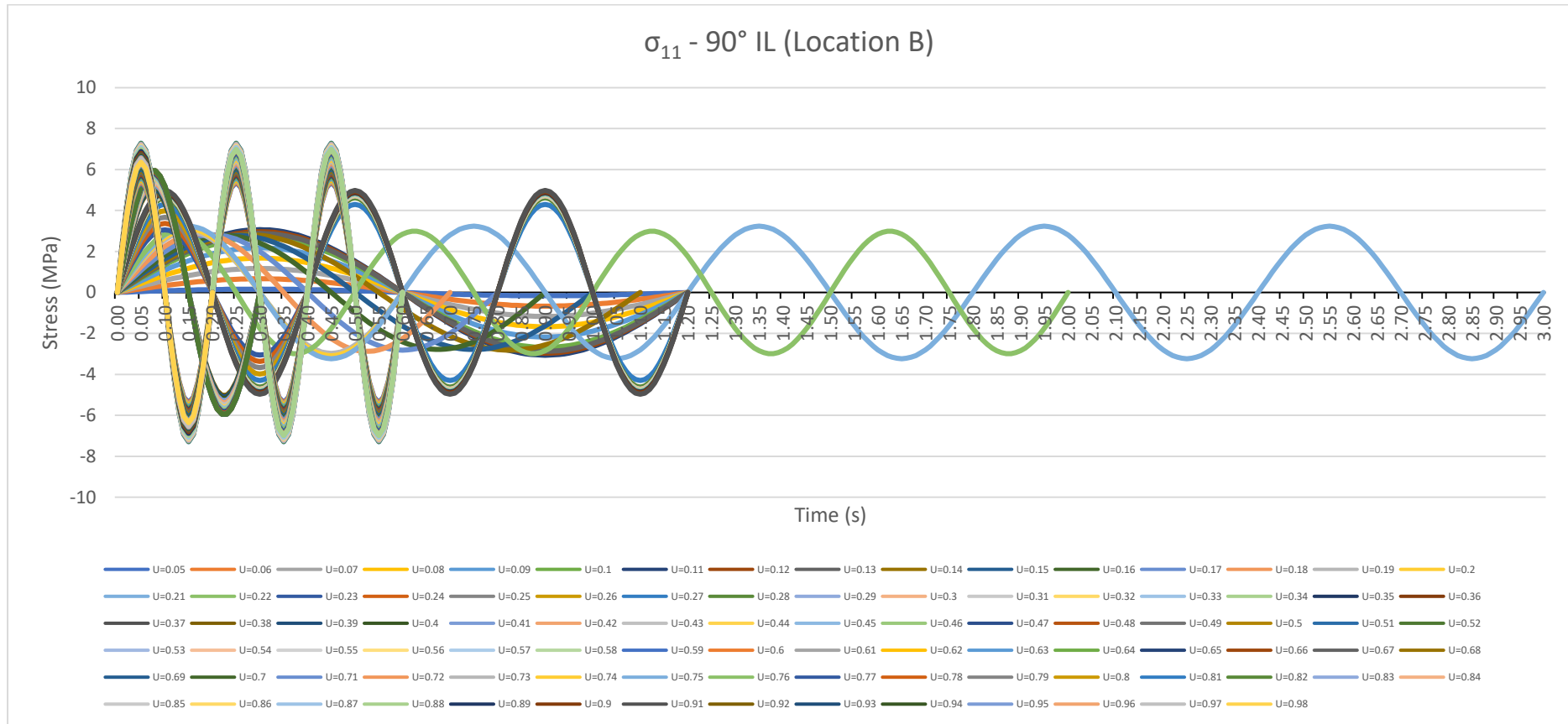


Figure 14-56: σ_{11} (Case-2(a) - 90° Flow IL) at Location B

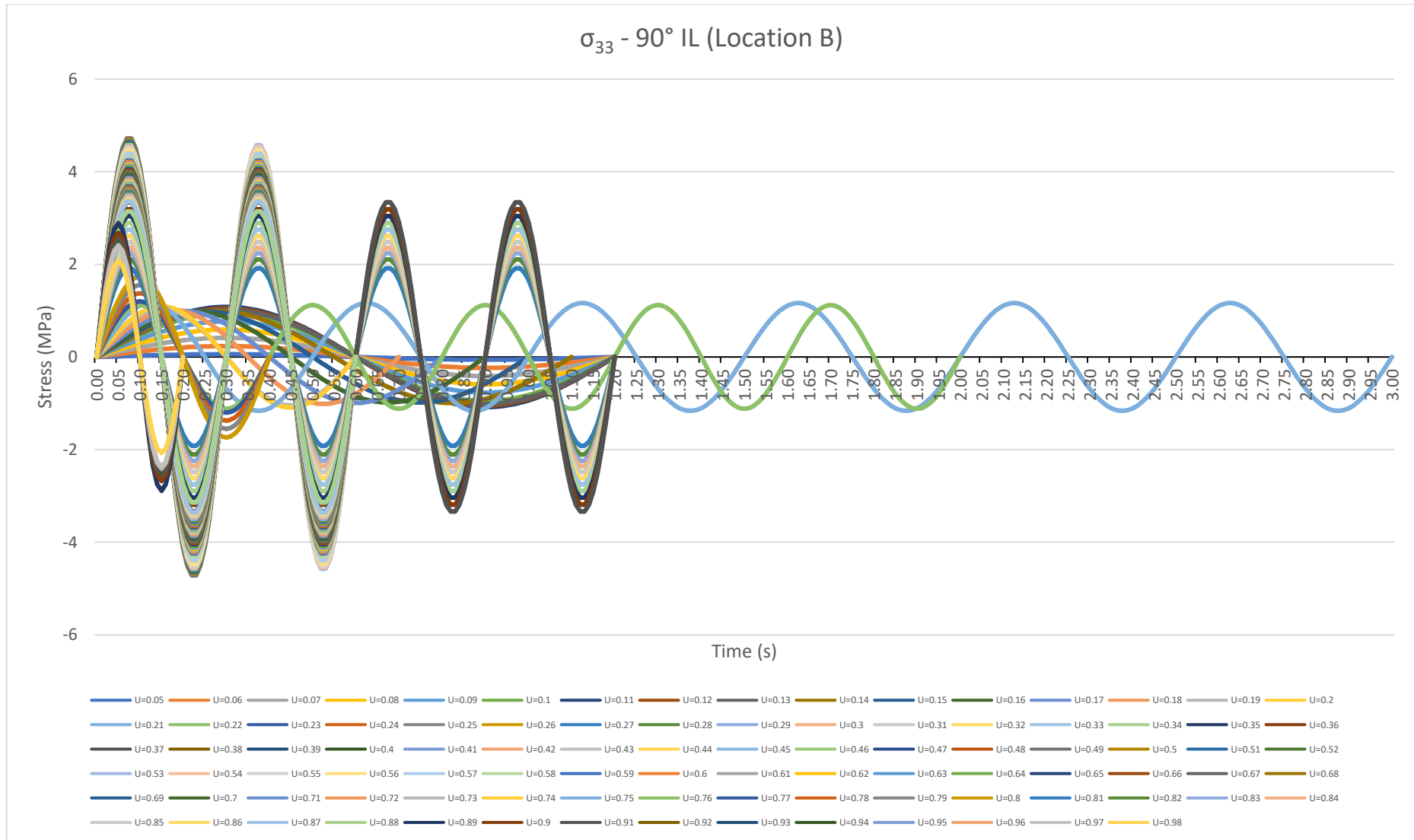


Figure 14-57: σ_{33} (Case-2(a) - 90° Flow IL) at Location B

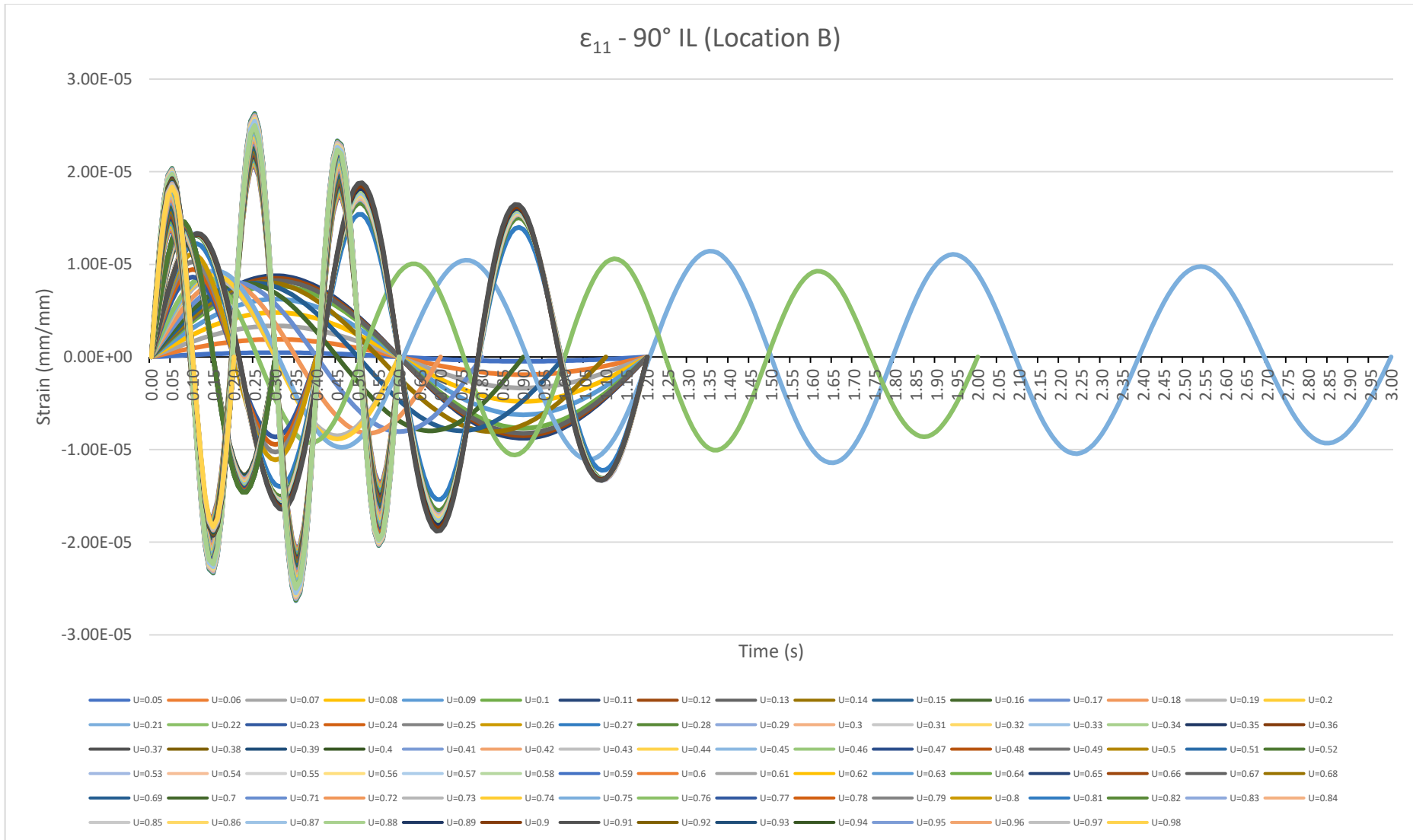


Figure 14-58: ϵ_{11} (Case-2(a) - 90° Flow IL) at Location B

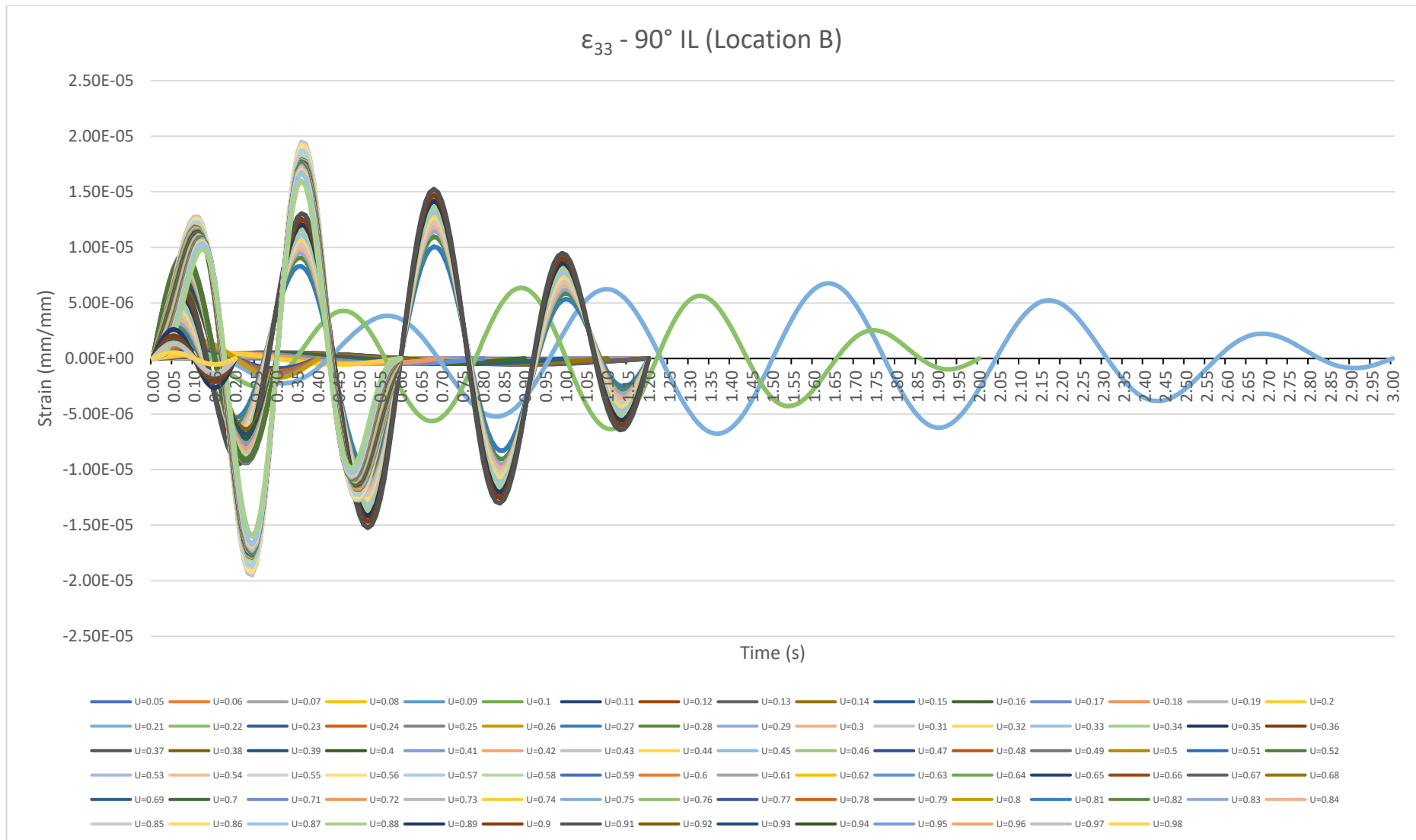


Figure 14-59: ϵ_{33} (Case-2(a) - 90° Flow IL) at Location B

2. Critical Plane

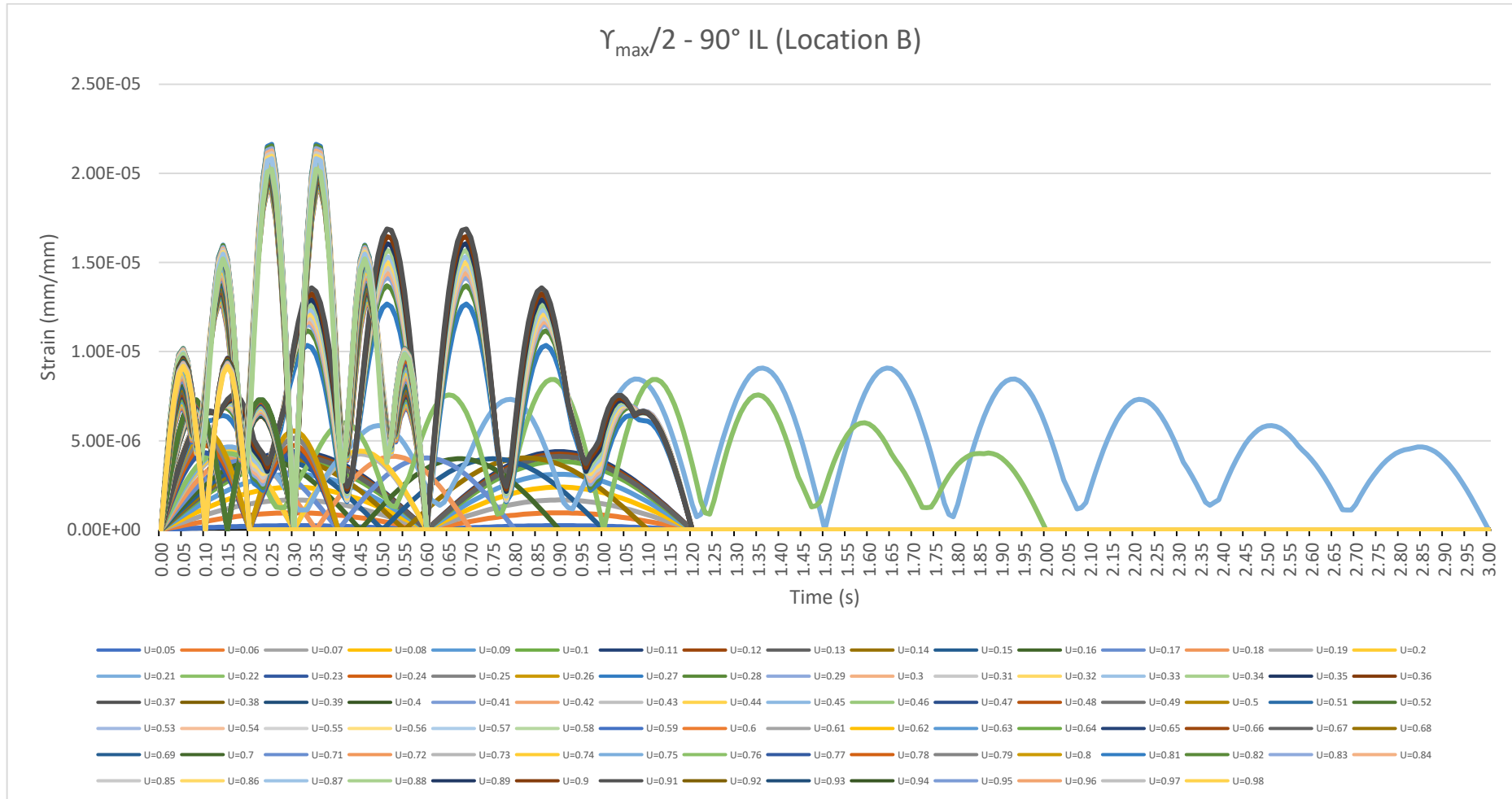


Figure 14-60: $\gamma_{\max}/2$ (Case-2(a) - 90° Flow IL) at Location B

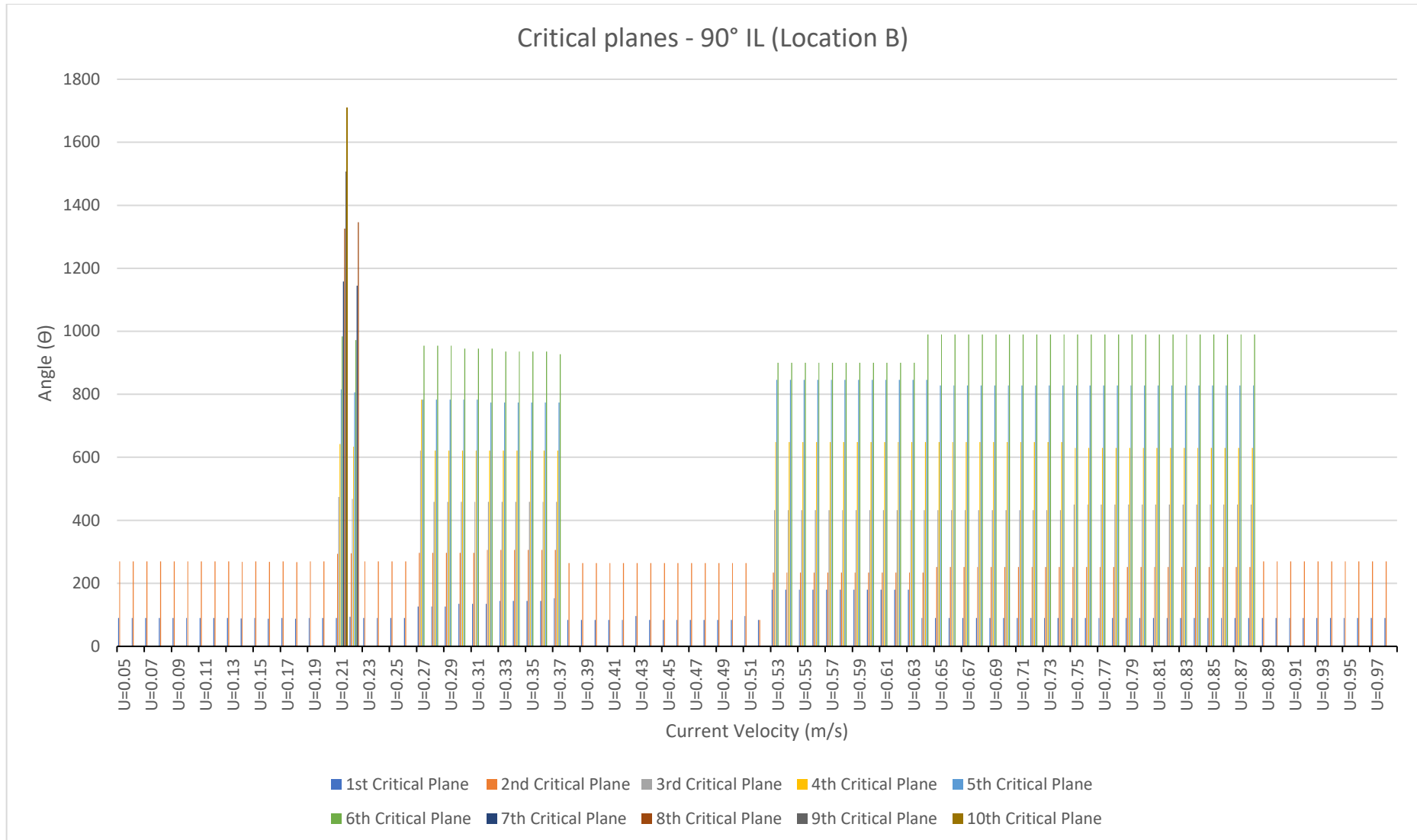


Figure 14-61: θ_{crit} (Case-2(a) - 90° Flow IL) at Location B

3. Normal and Shear Stress and Strain Range

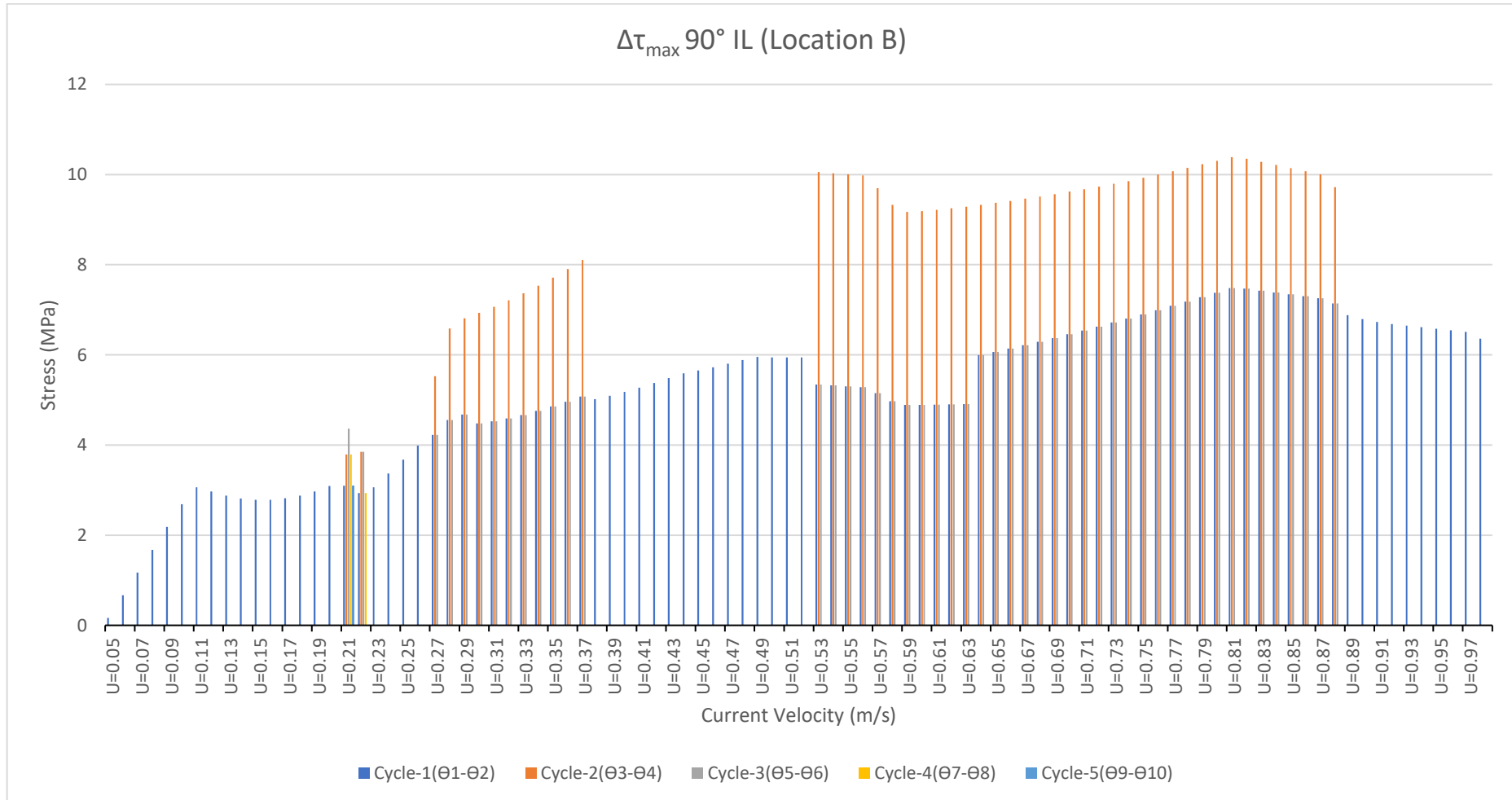


Figure 14-62: $\Delta\tau_{\max}$ (Case-2(a) - 90° Flow IL) at Location B

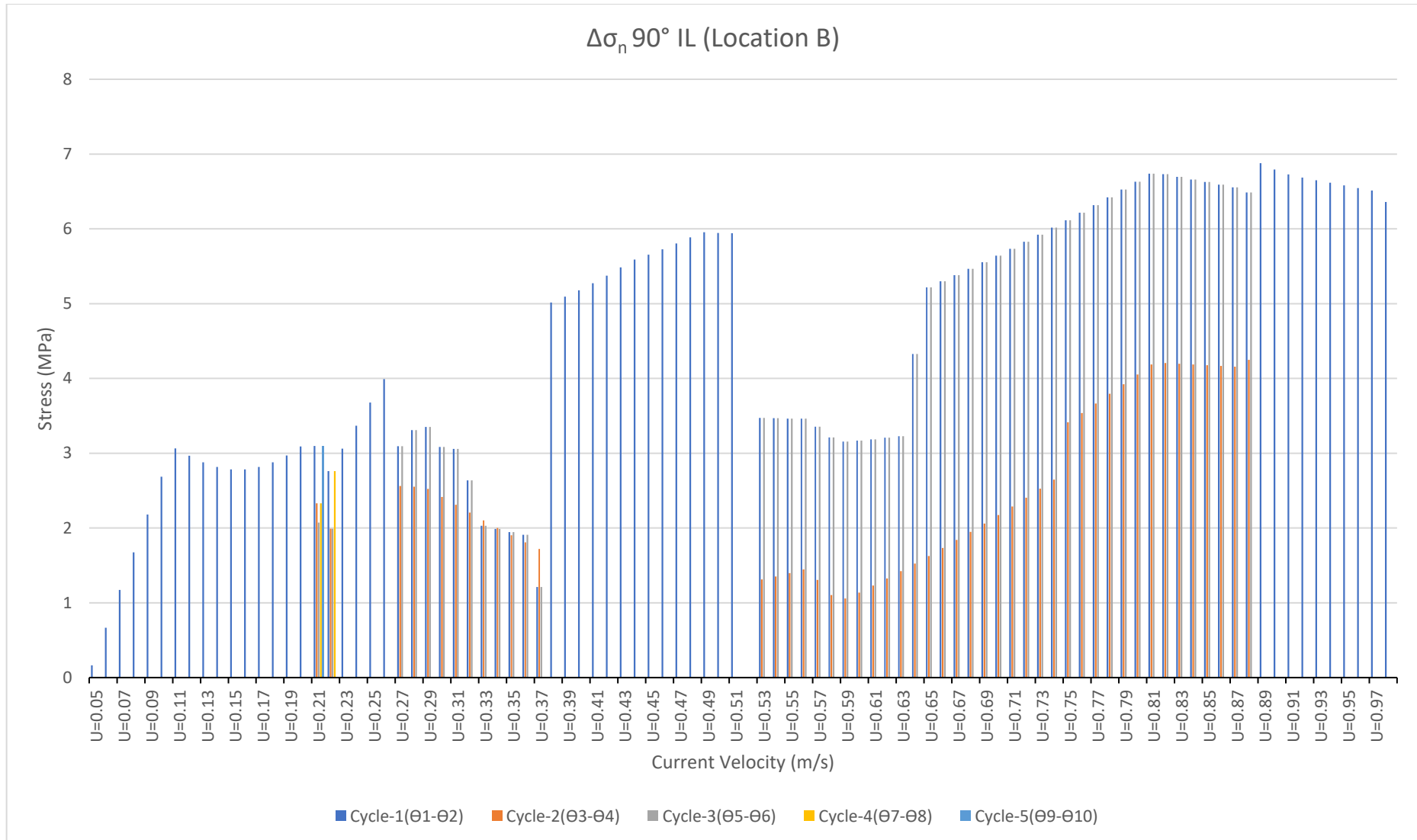


Figure 14-63: $\Delta\sigma_n$ (Case-2(a) - 90° Flow IL) at Location B

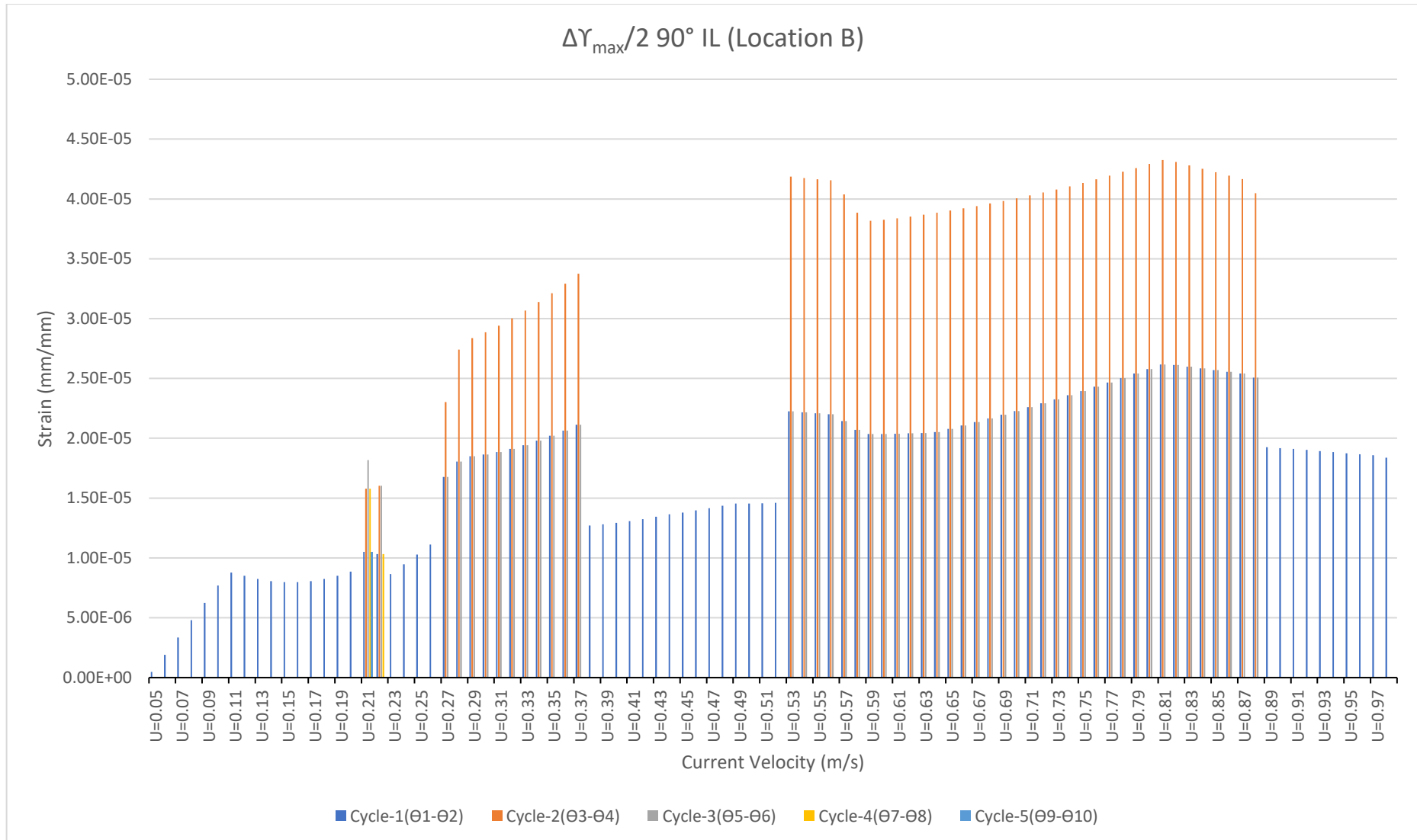


Figure 14-64: $\Delta\gamma_{\max}/2$ (Case-2(a) - 90° Flow IL) at Location B

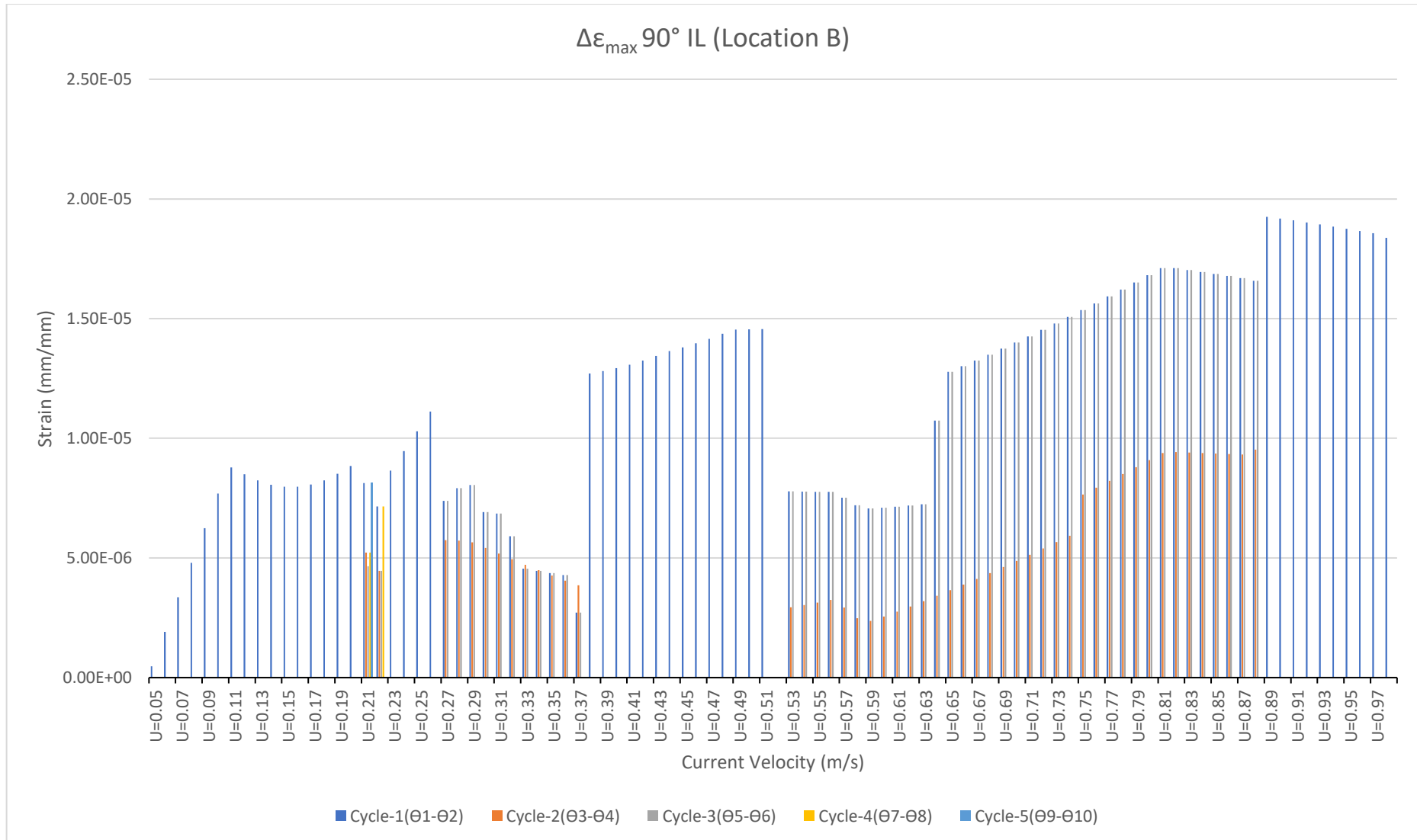


Figure 14-65: $\Delta\epsilon_n$ (Case-2(a) - 90° Flow IL) at Location B

4. Fatigue

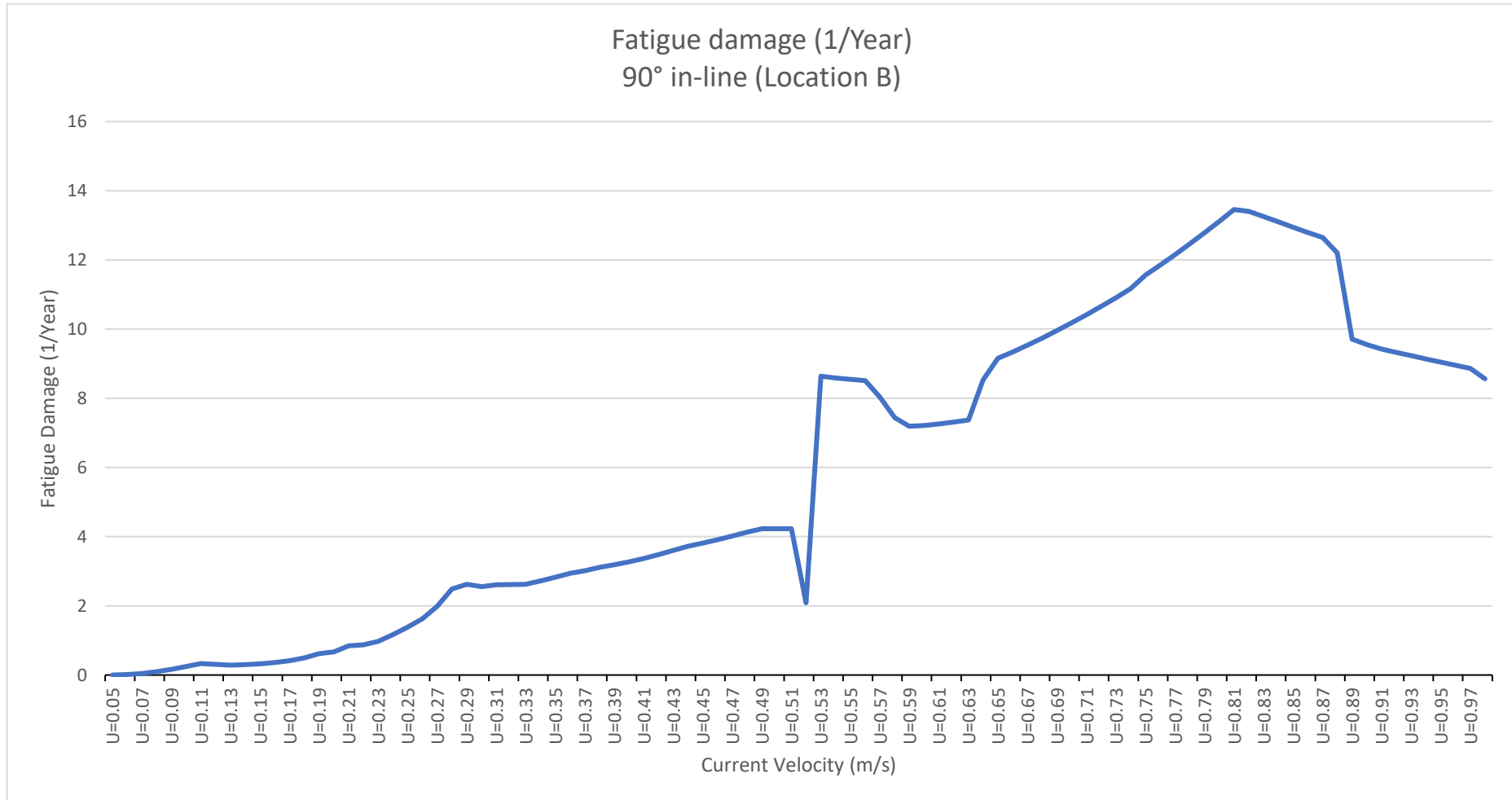


Figure 14-66: Fatigue damage per year for (Case-2(a) - 90° Flow IL) at Location B

Case-2 (b) – 90° CF Location A

1. Principal Stress and Strains

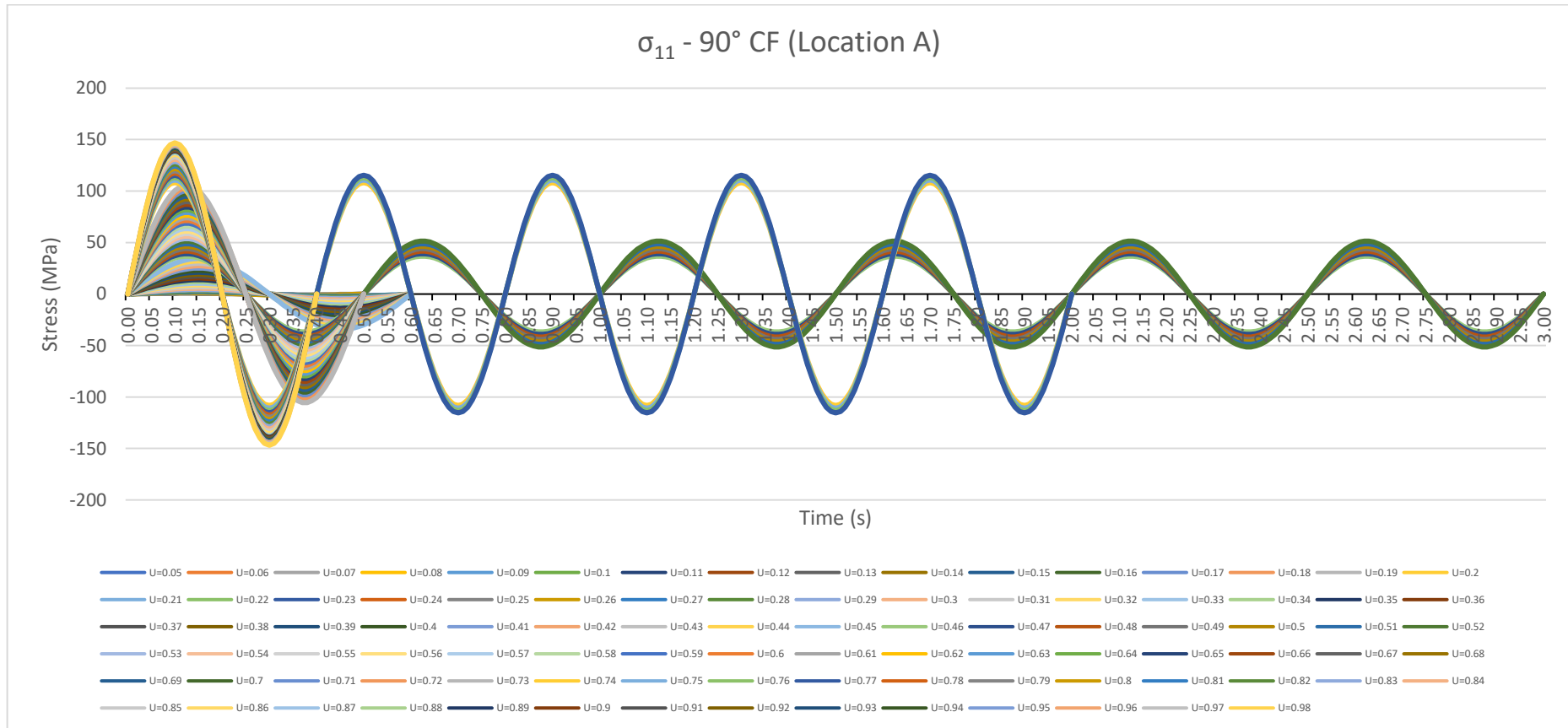


Figure 14-67: σ_{11} (Case-2(b) - 90° Flow CF) at Location A

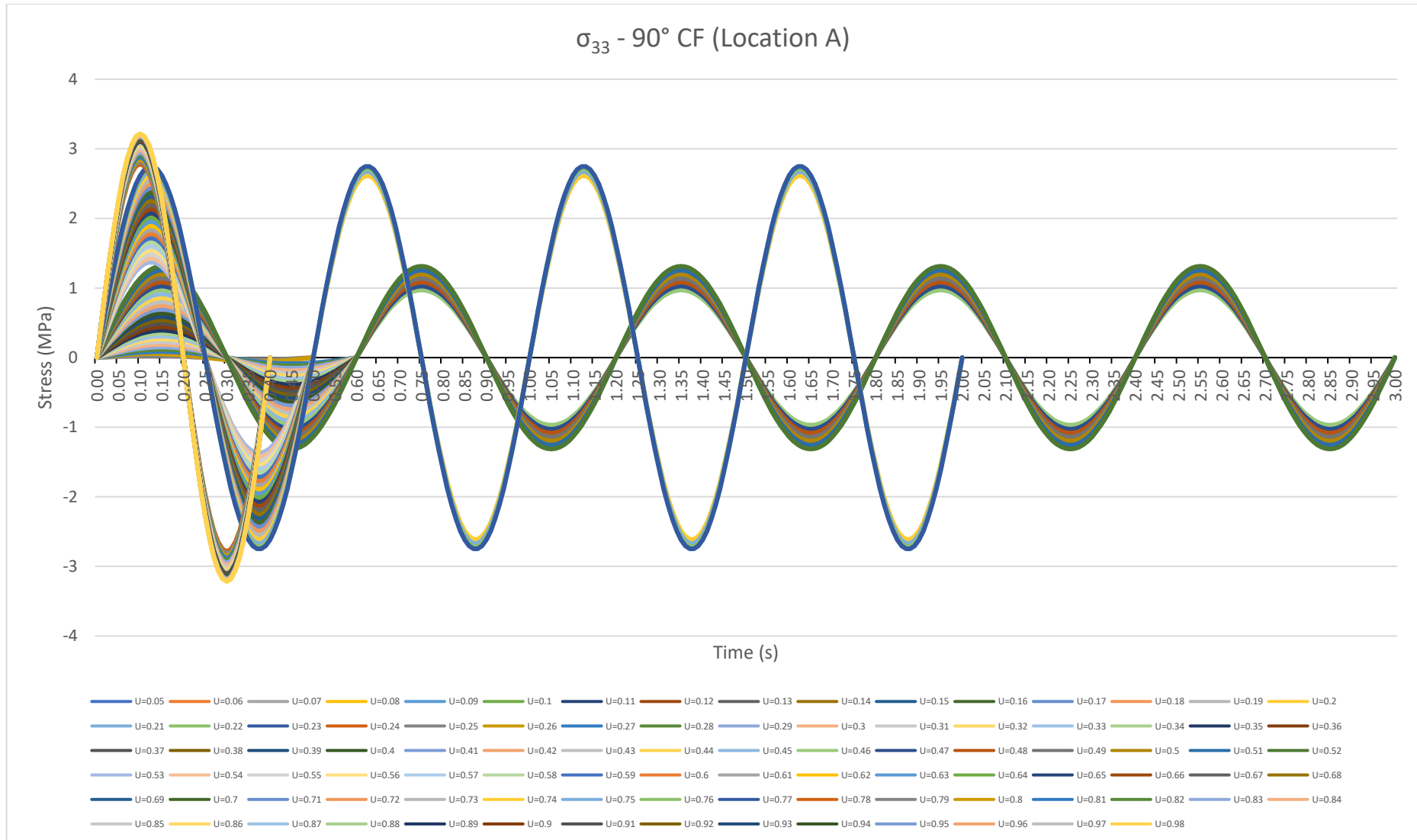


Figure 14-68: σ_{33} (Case-2(b) - 90° Flow CF) at Location A

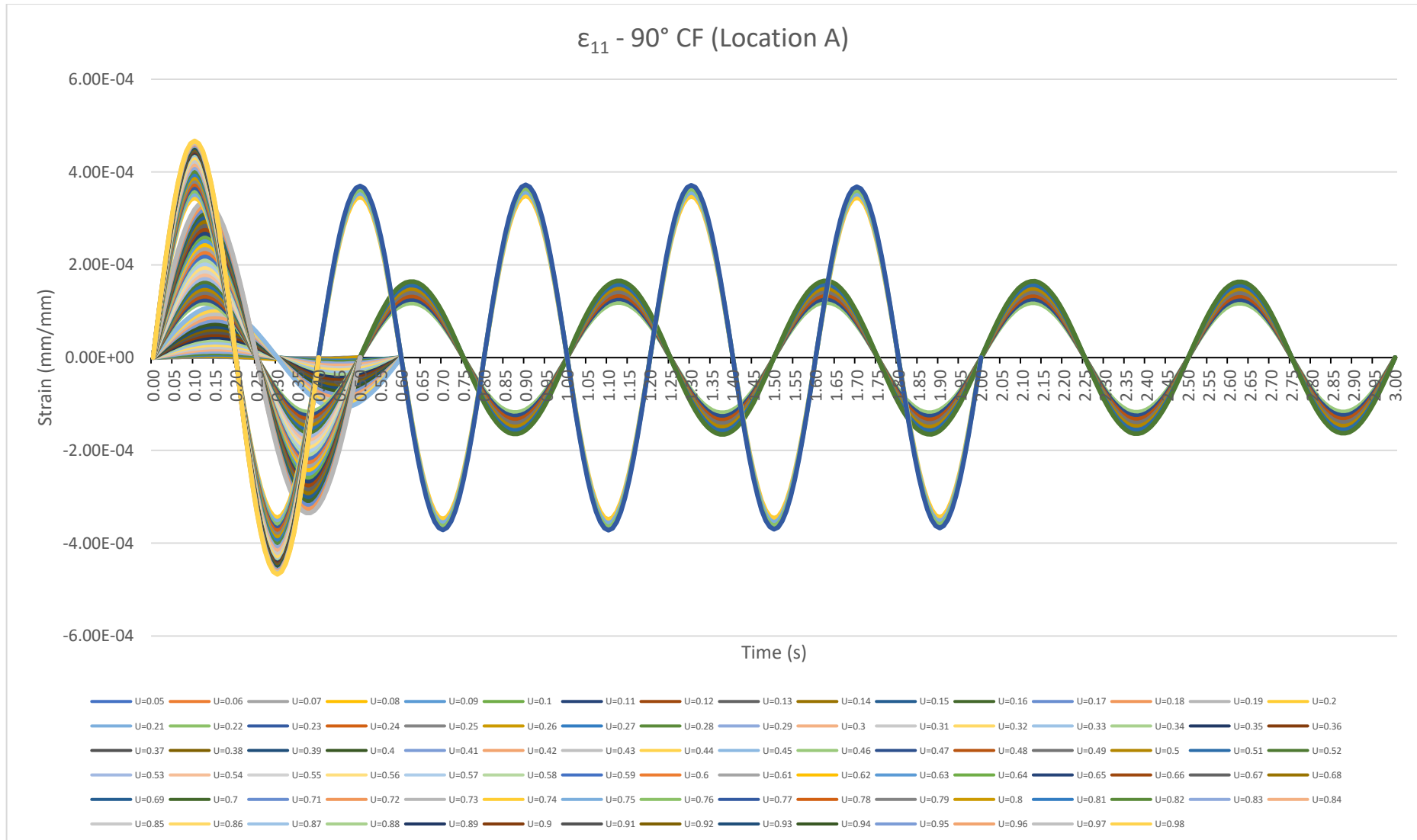


Figure 14-69: ϵ_{11} (Case-2(b) - 90° Flow CF) at Location A

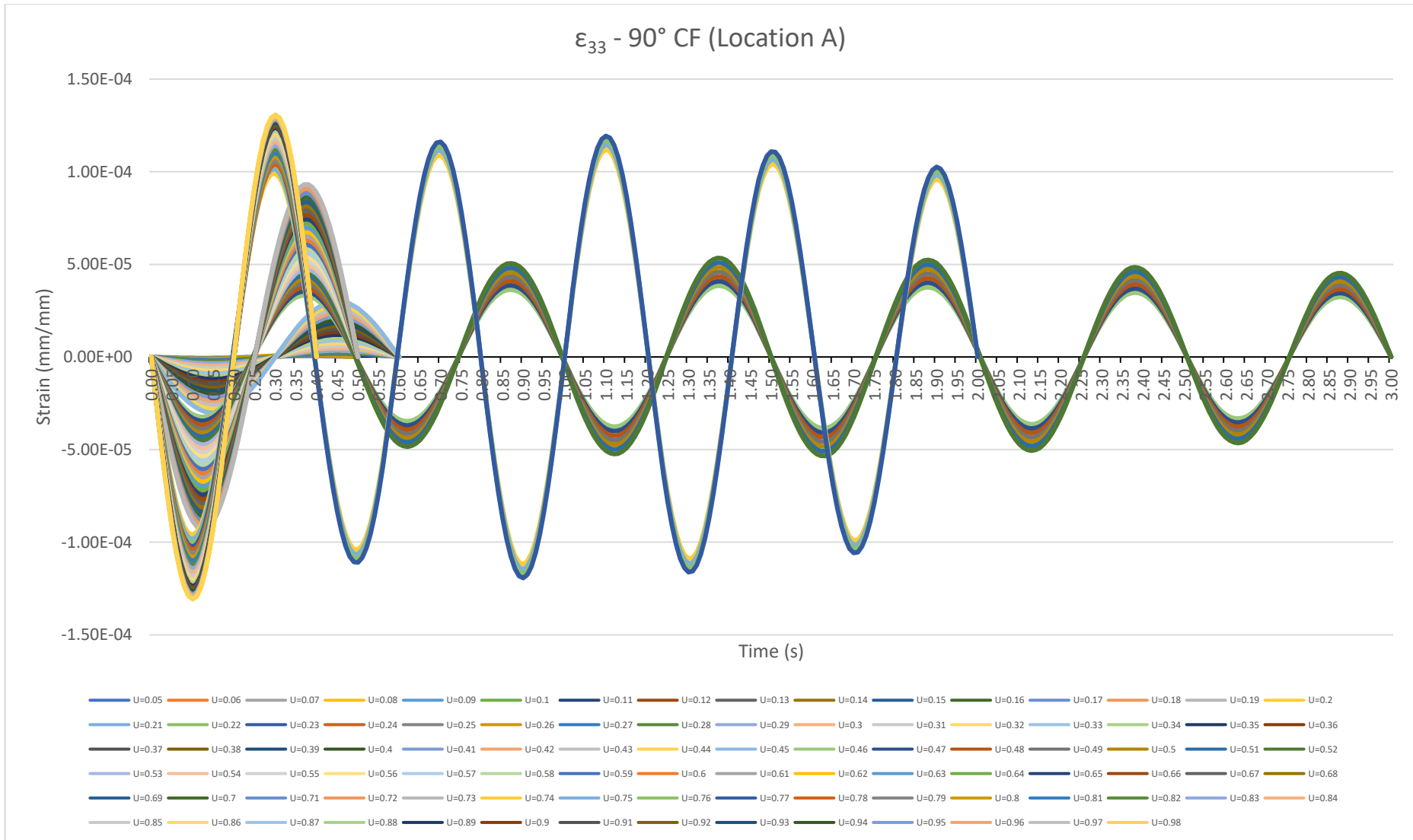


Figure 14-70: ϵ_{33} (Case-2(b) - 90° Flow CF) at Location A

2. Critical Plane

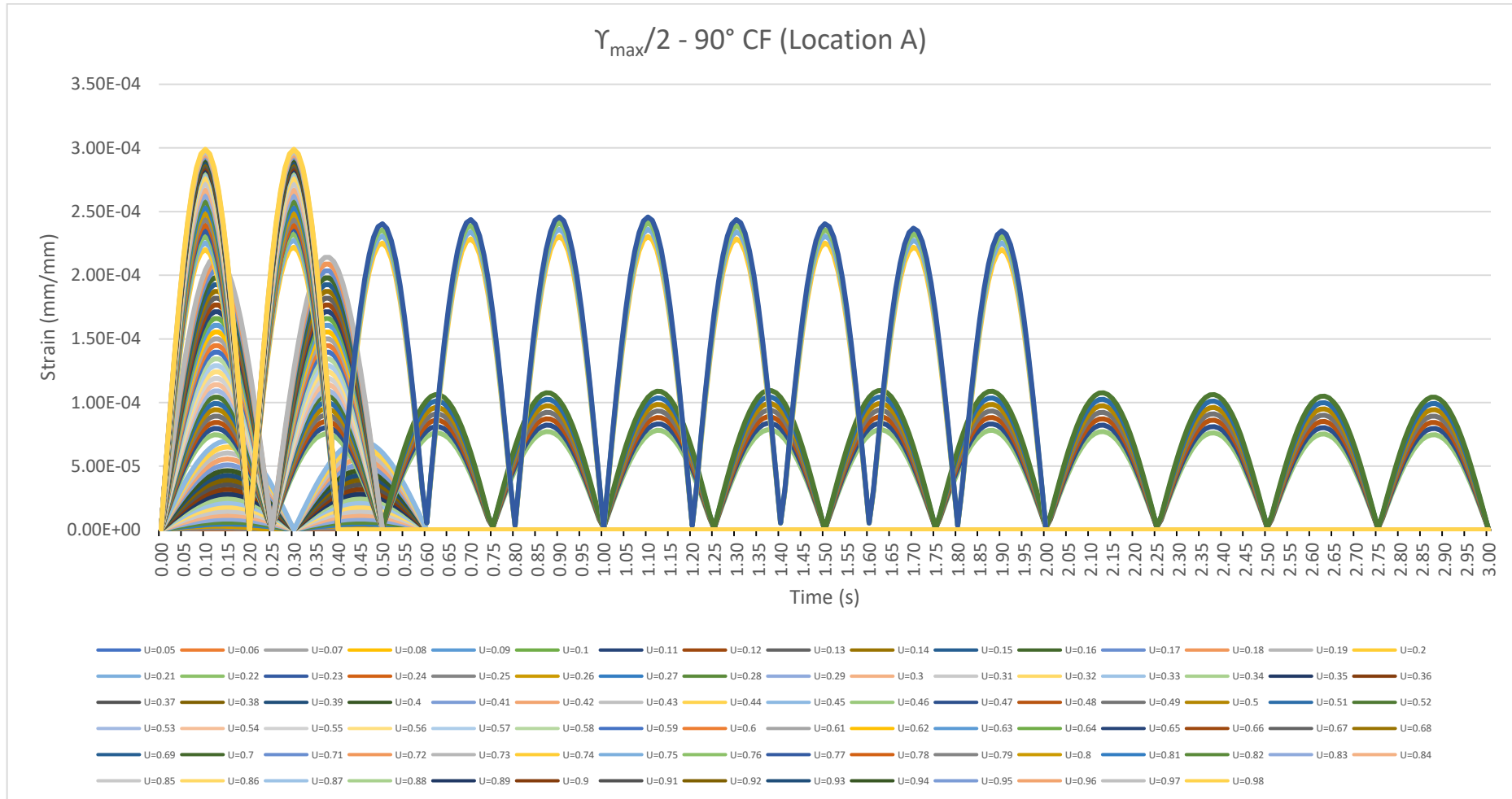


Figure 14-71: $\gamma_{\max}/2$ (Case-2(b) - 90° Flow CF) at Location A

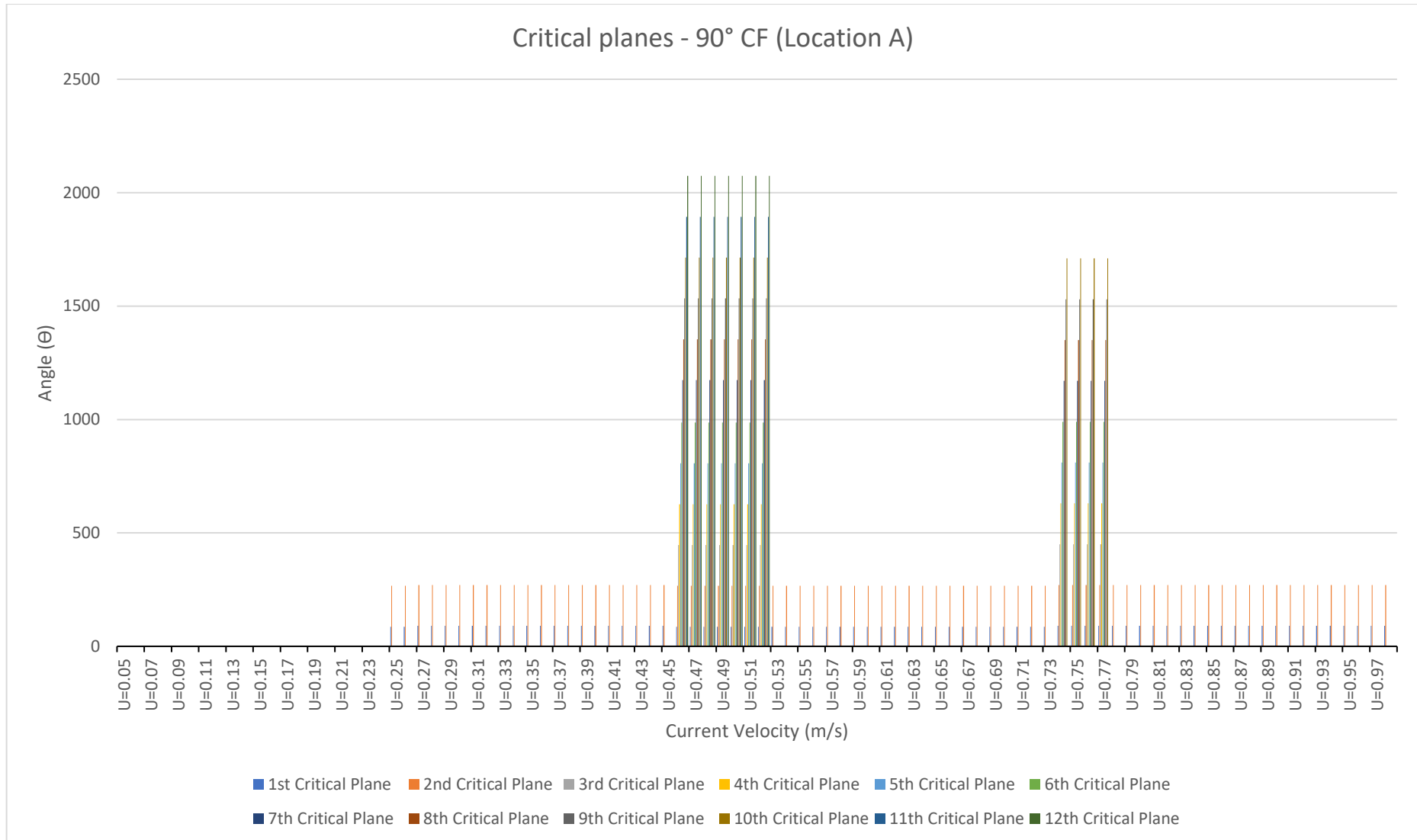


Figure 14-72: θ_{cric} (Case-2(b) - 90° Flow CF) at Location A

3. Normal and Shear Stress and Strain Range

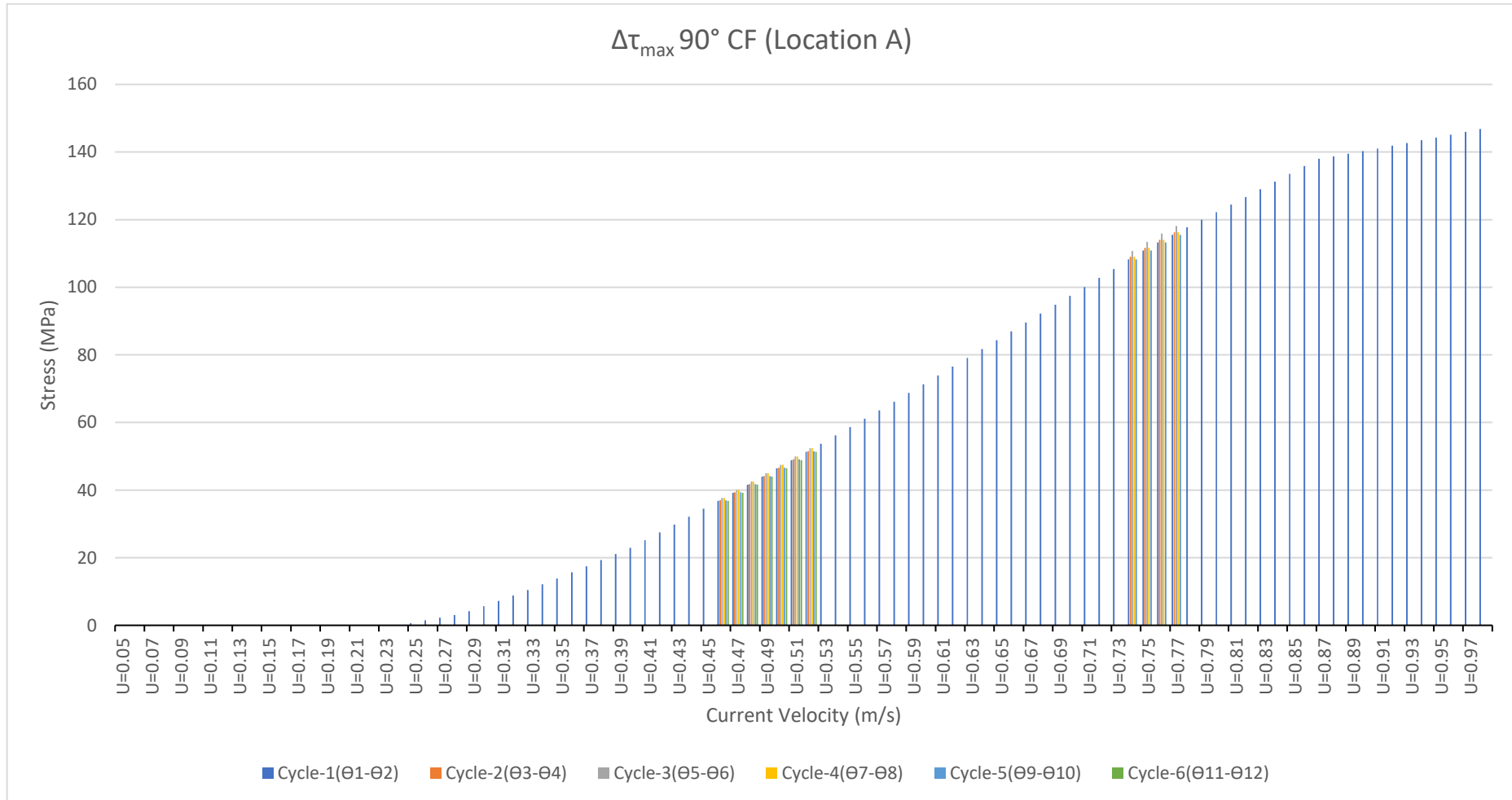


Figure 14-73: $\Delta\tau_{\max}$ (Case-2(b) - 90° Flow CF) at Location A

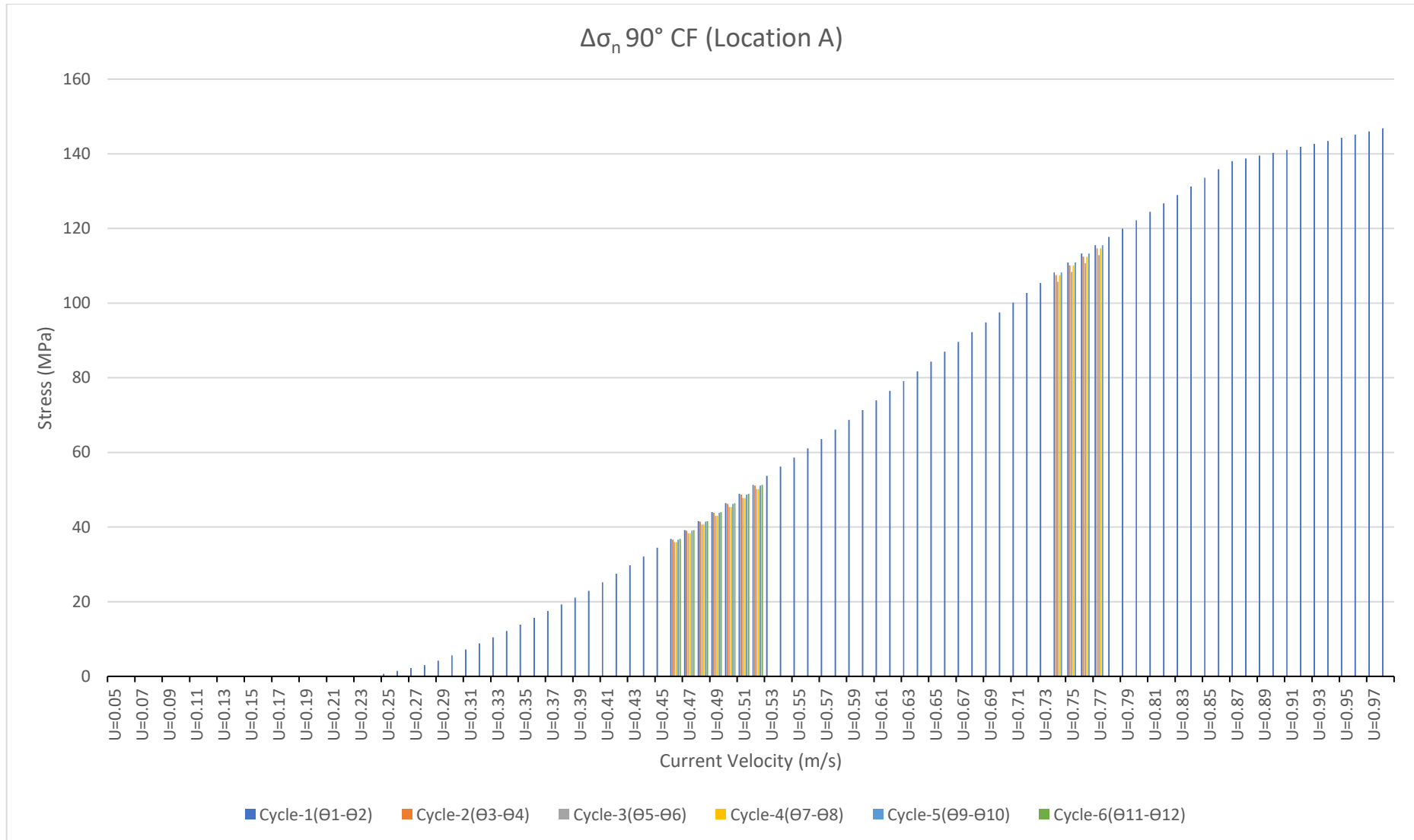


Figure 14-74: $\Delta\sigma_n$ (Case-2(b) - 90° Flow CF) at Location A

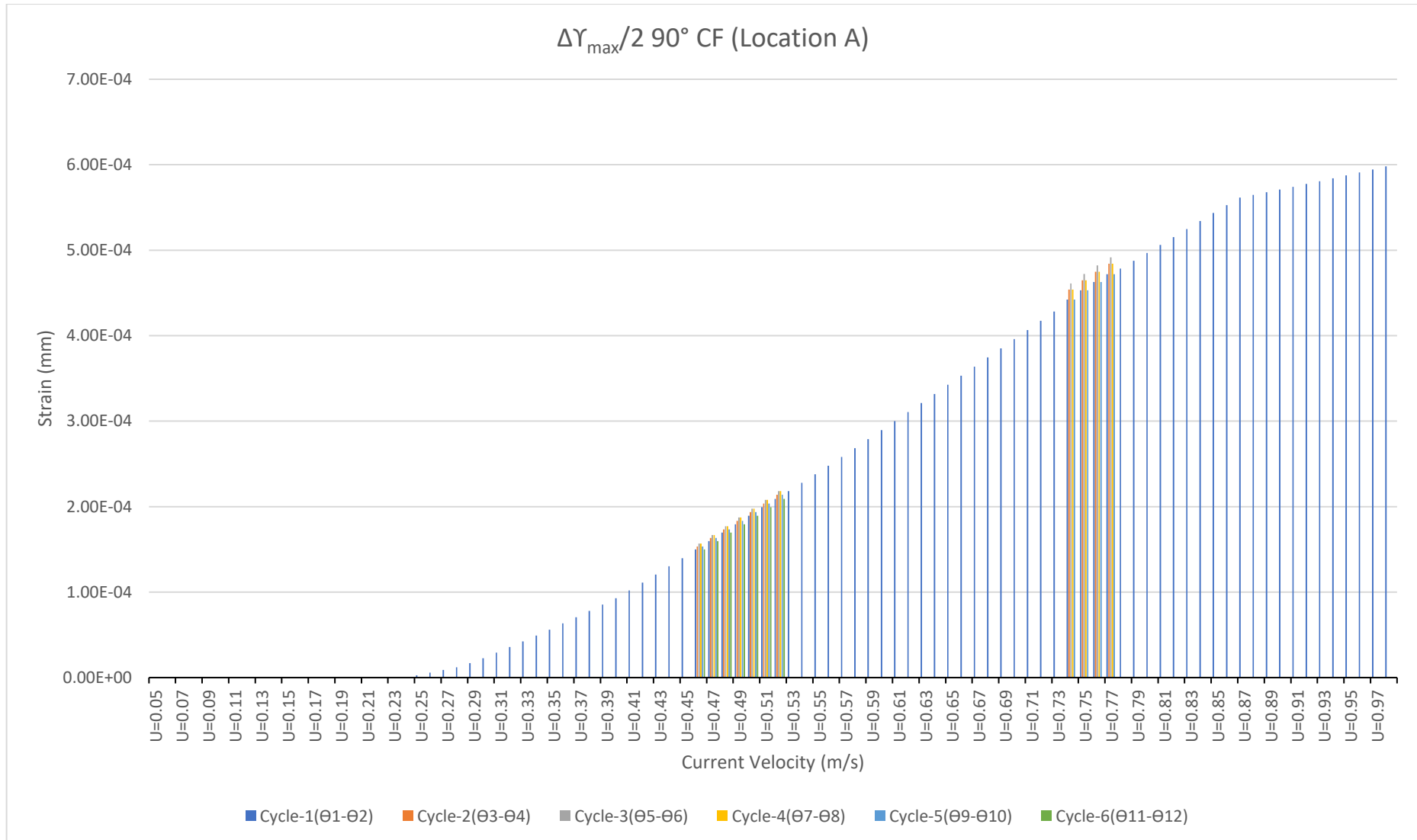


Figure 14-75: $\Delta\gamma_{\max}/2$ (Case-2(b) - 90° Flow CF) at Location A

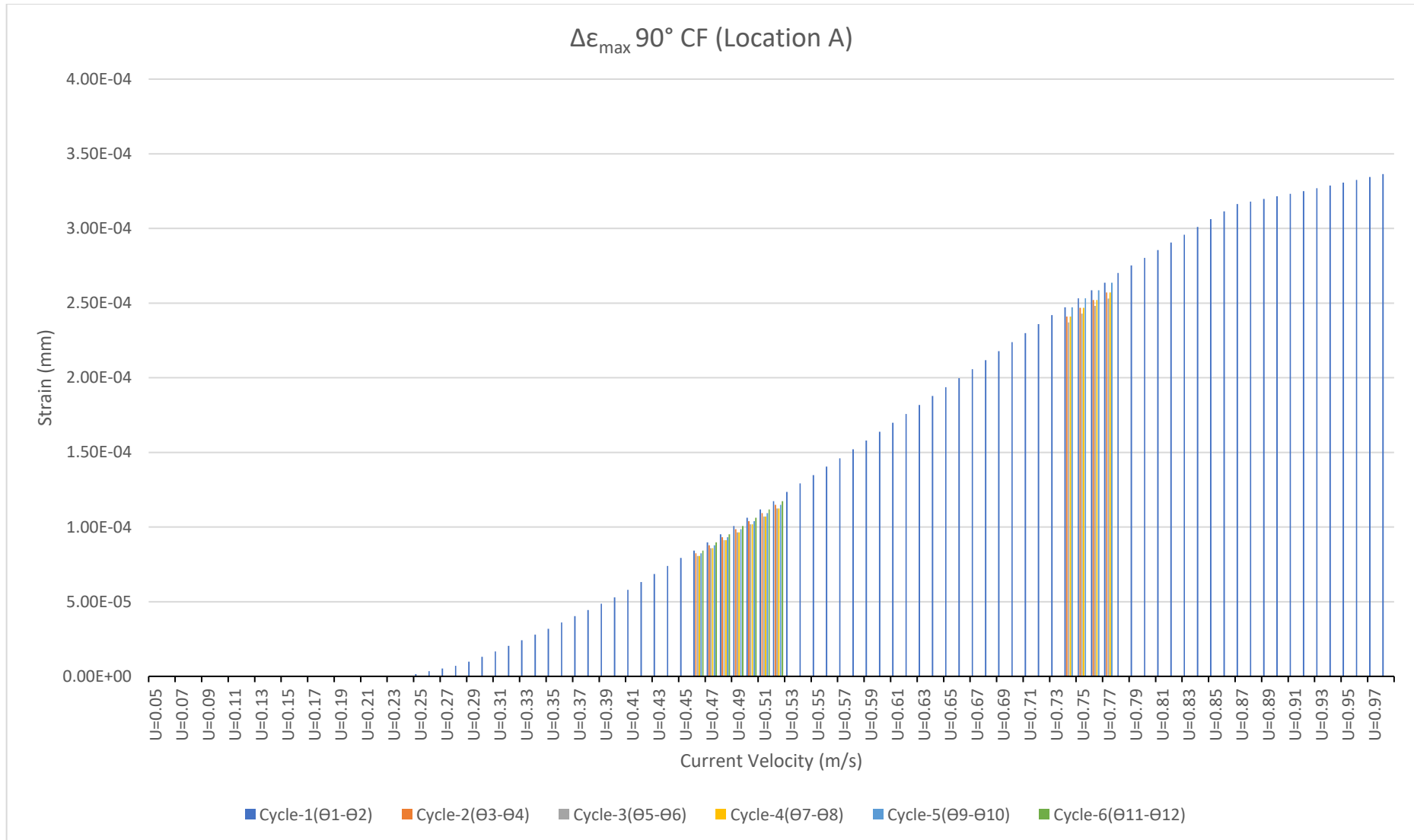


Figure 14-76: $\Delta\varepsilon_n$ (Case-2(b) - 90° Flow CF) at Location A

4. Fatigue

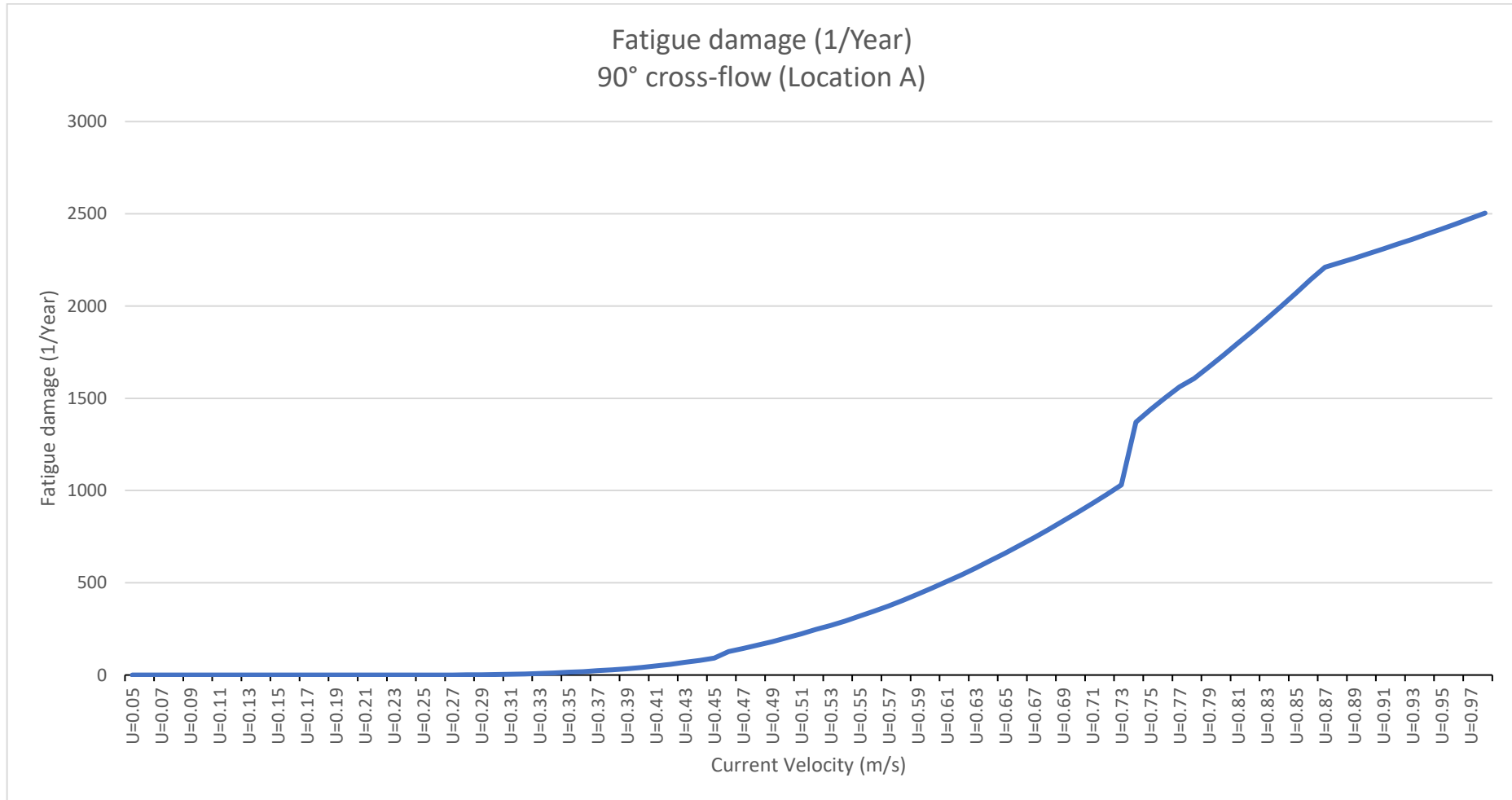


Figure 14-77: Fatigue damage per year for (Case-2(b) - 90° Flow CF) at Location A

Case-2 (b) – 90° CF Location B

1. Principal Stress and Strains

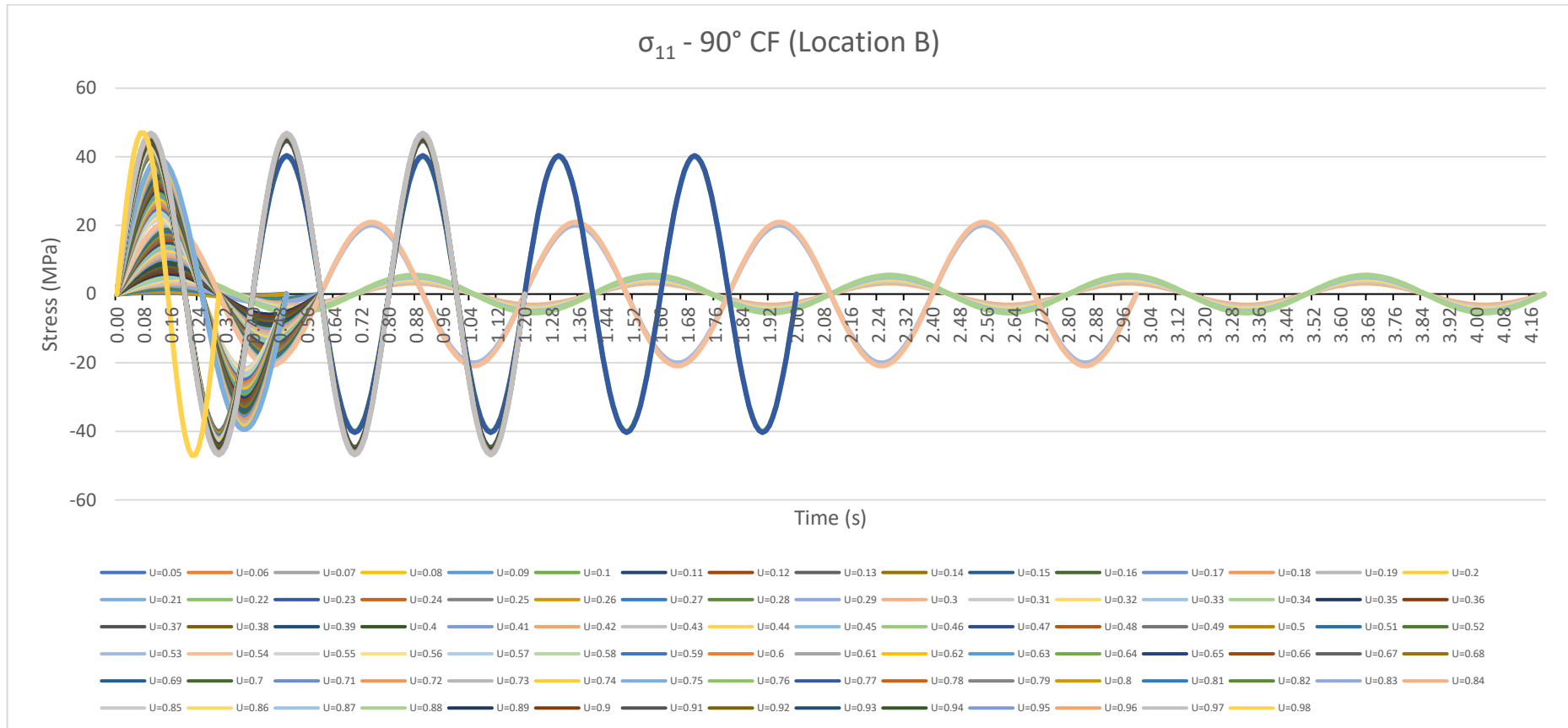


Figure 14-78: σ_{11} (Case-2(b) - 90° Flow CF) at Location B

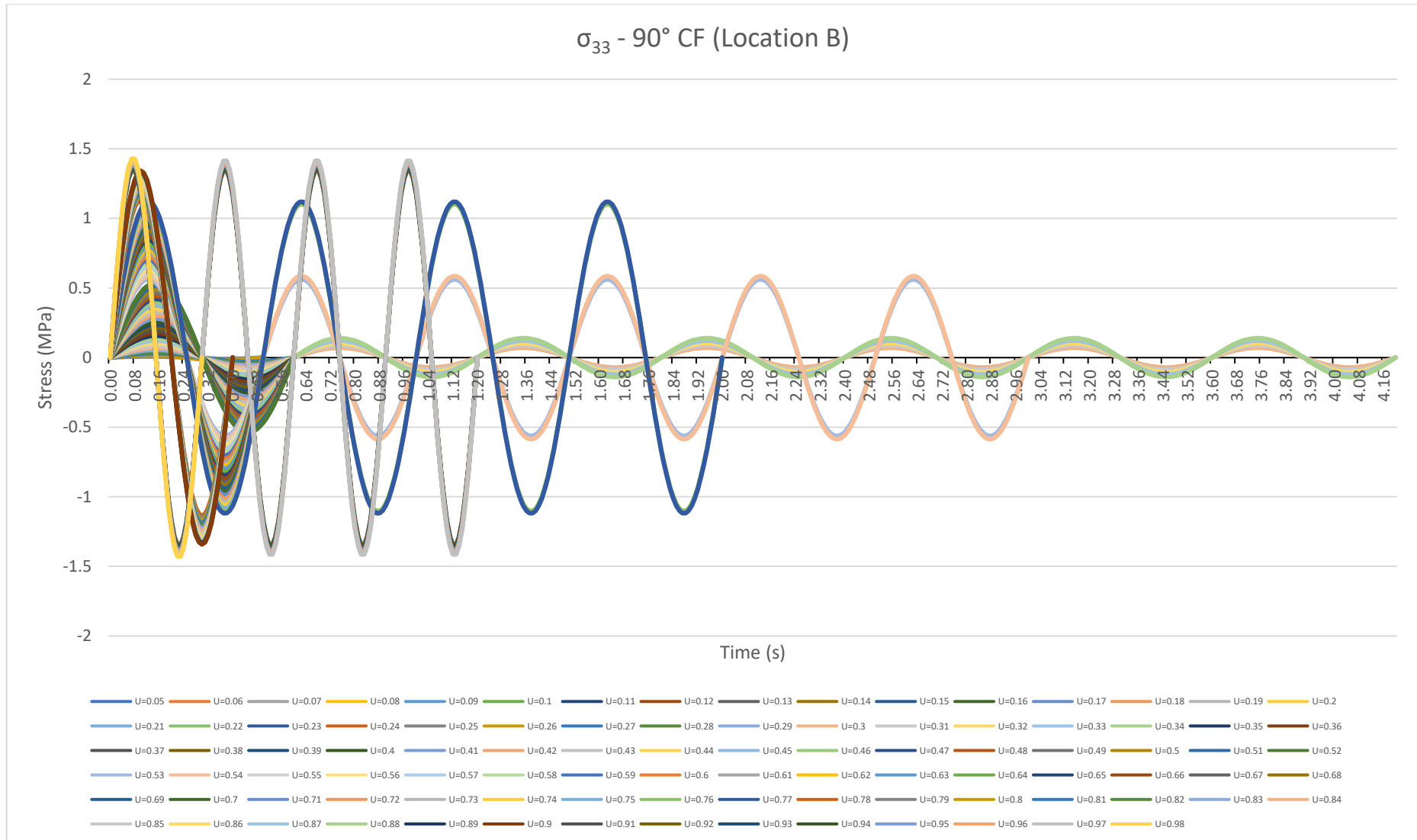


Figure 14-79: σ_{33} (Case-2(b) - 90° Flow CF) at Location B

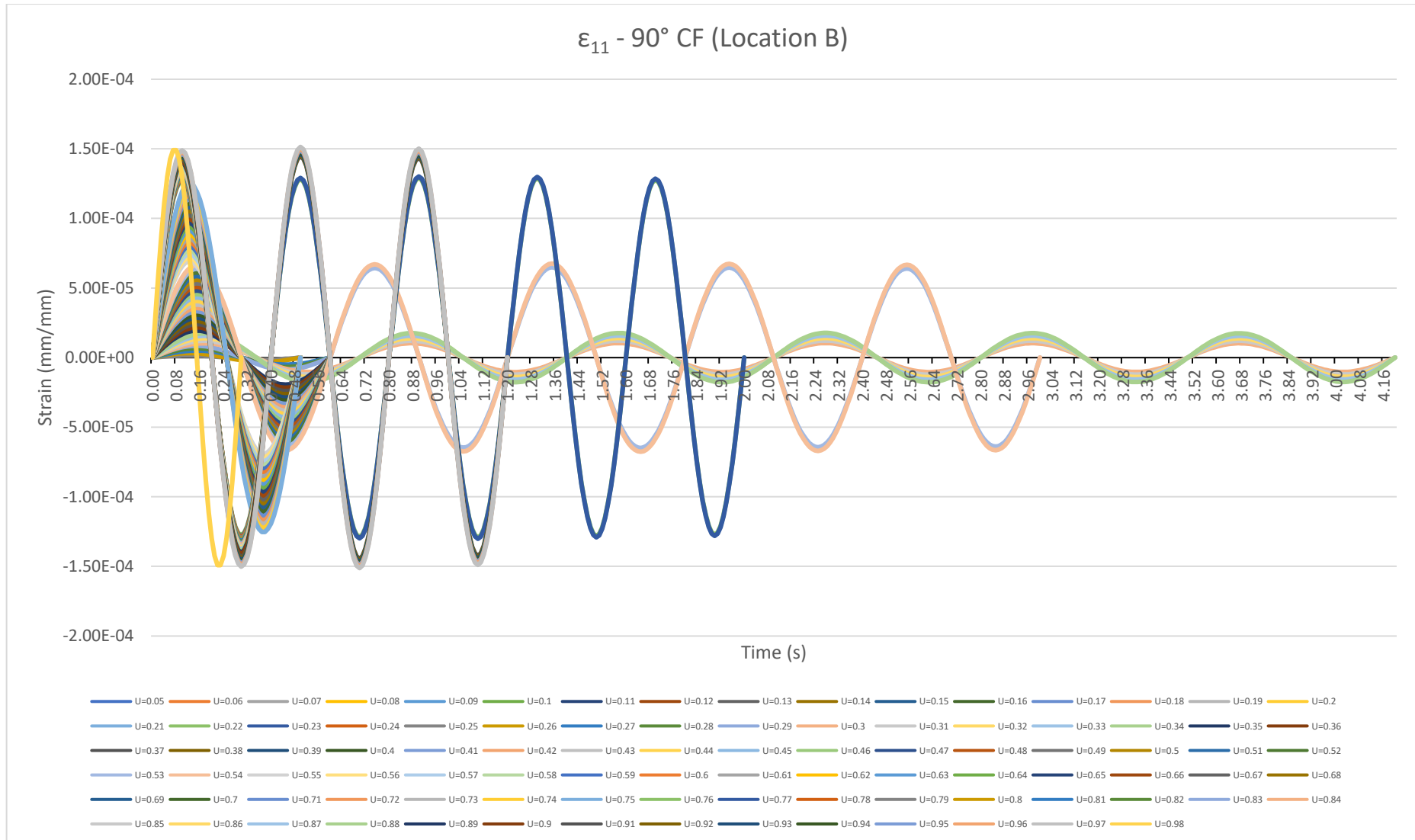


Figure 14-80: ϵ_{11} (Case-2(b) - 90° Flow CF) at Location B

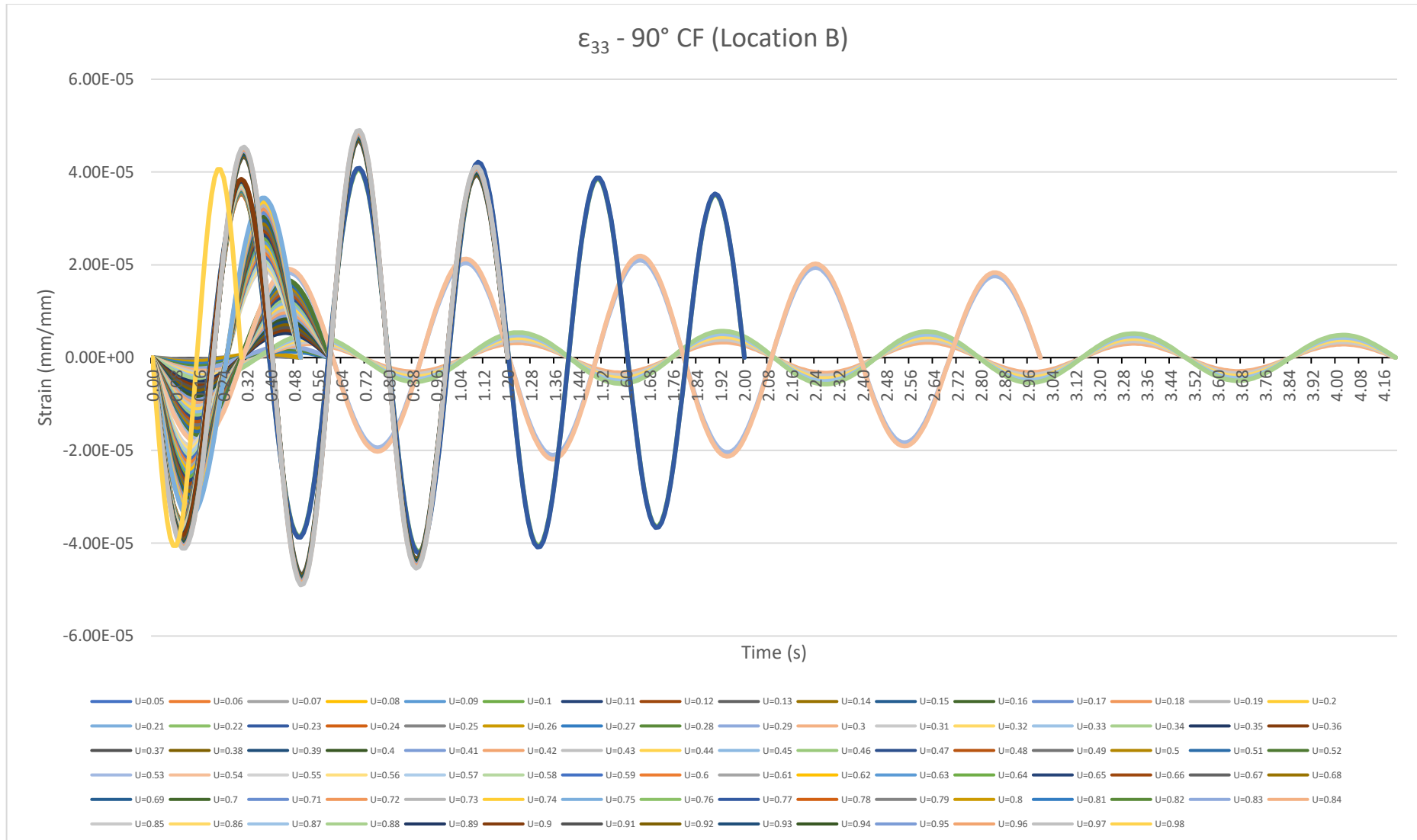


Figure 14-81: ϵ_{33} (Case-2(b) - 90° Flow CF) at Location B

2. Critical Plane

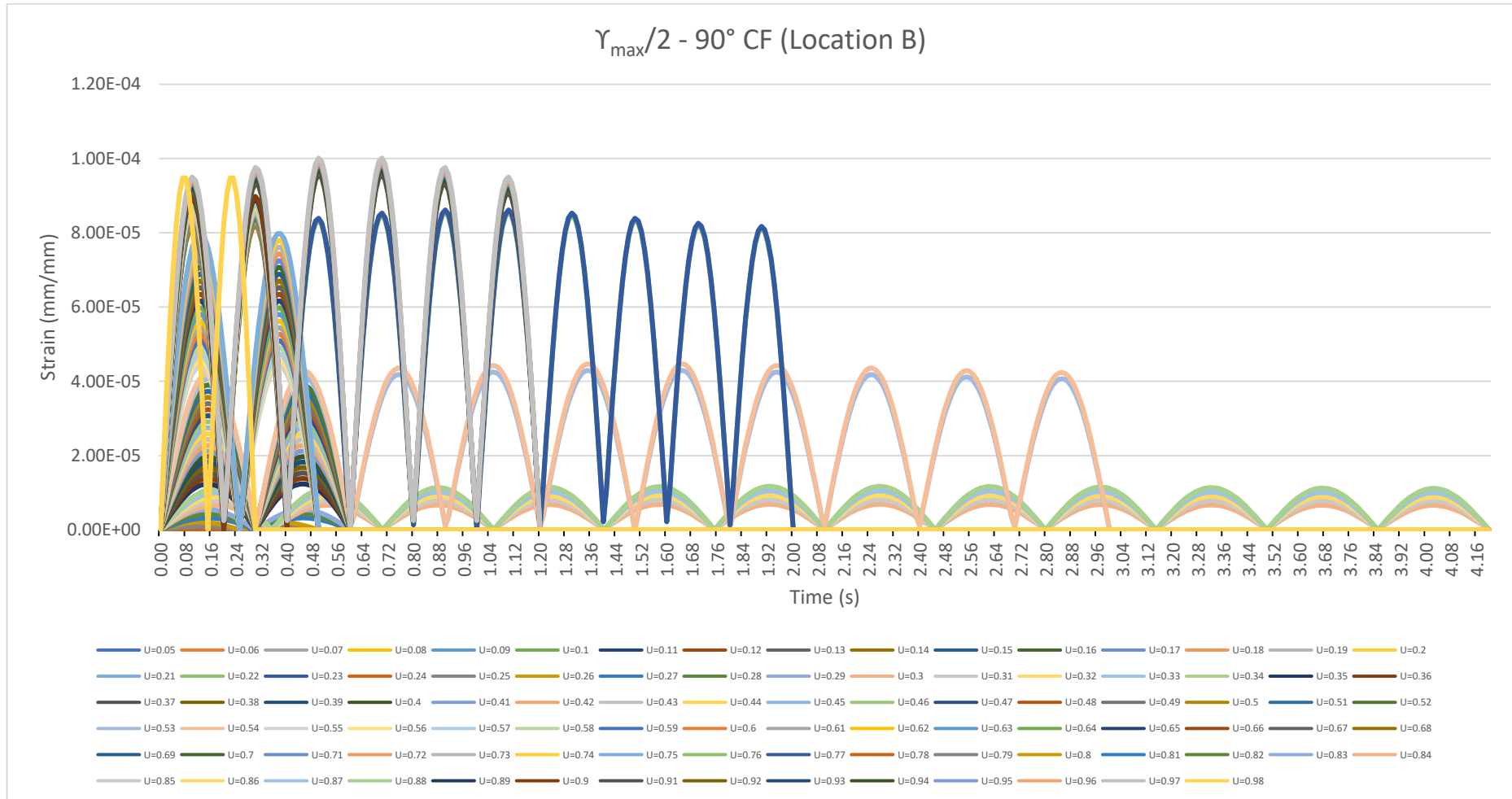


Figure 14-82: $\gamma_{\max}/2$ (Case-2(b) - 90° Flow CF) at Location B

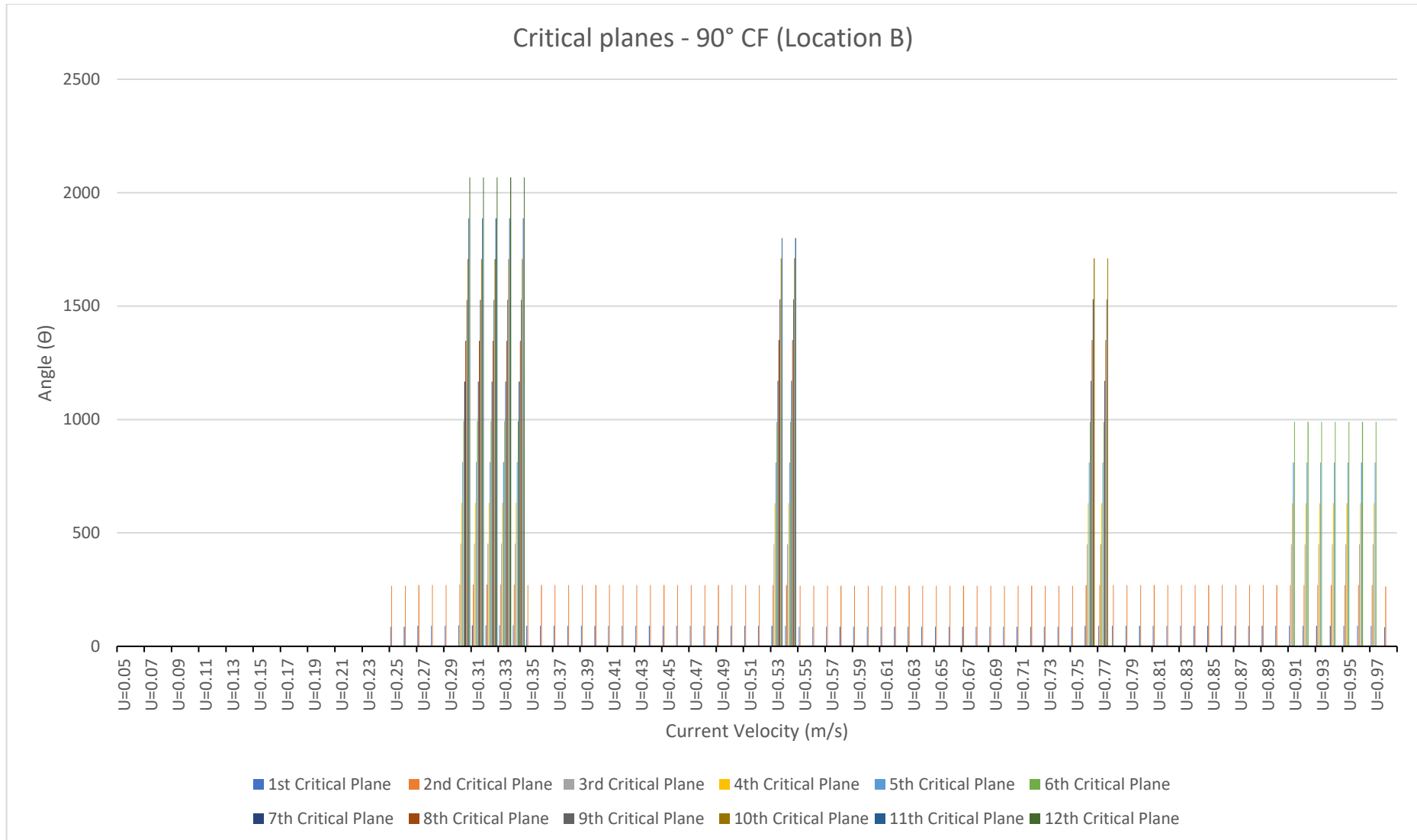


Figure 14-83: θ_{crit} (Case-2(b) - 90° Flow CF) at Location B

3. Normal and Shear Stress and Strain Range

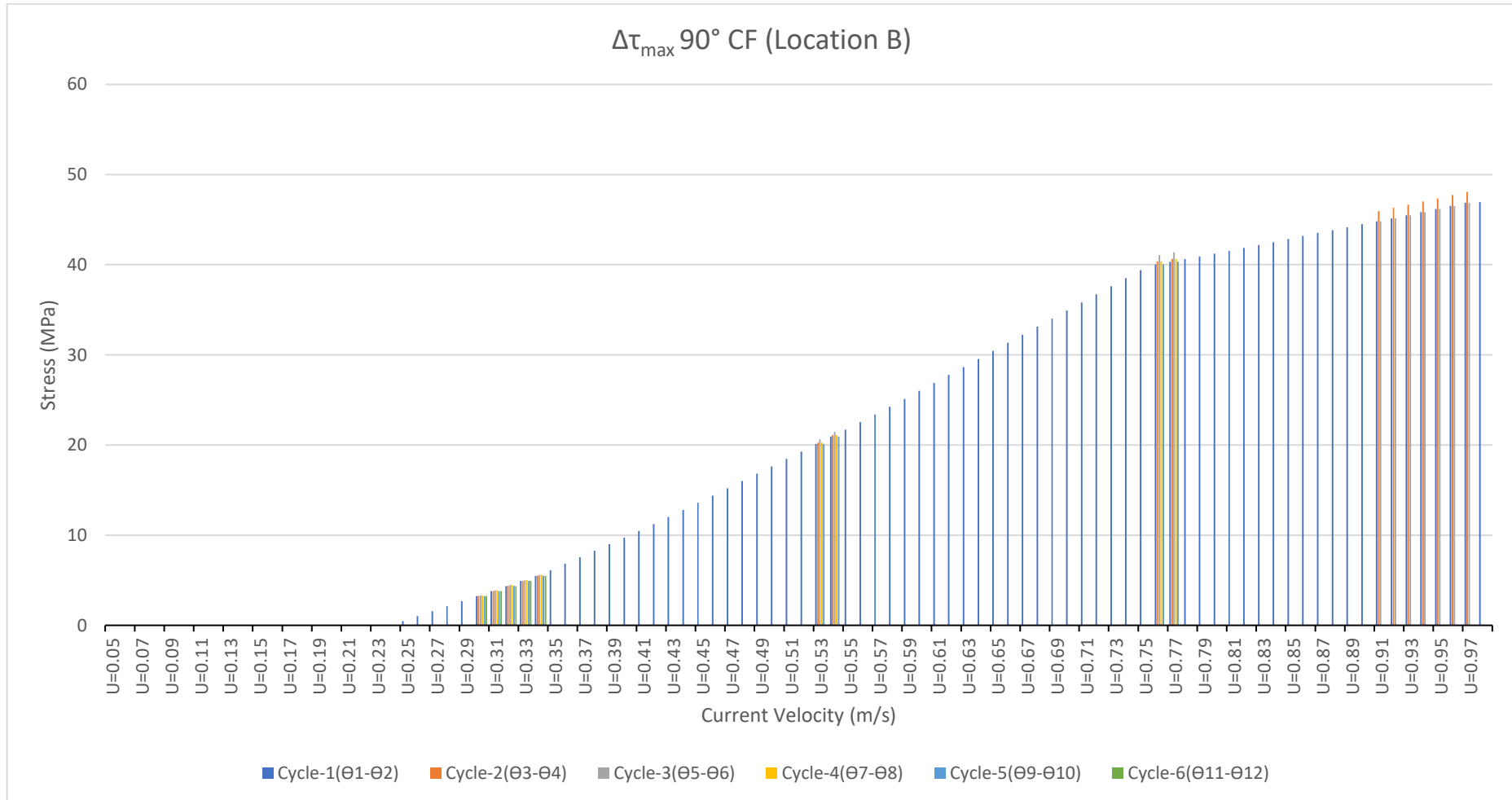


Figure 14-84: $\Delta\tau_{\max}$ (Case-2(b) - 90° Flow CF) at Location B

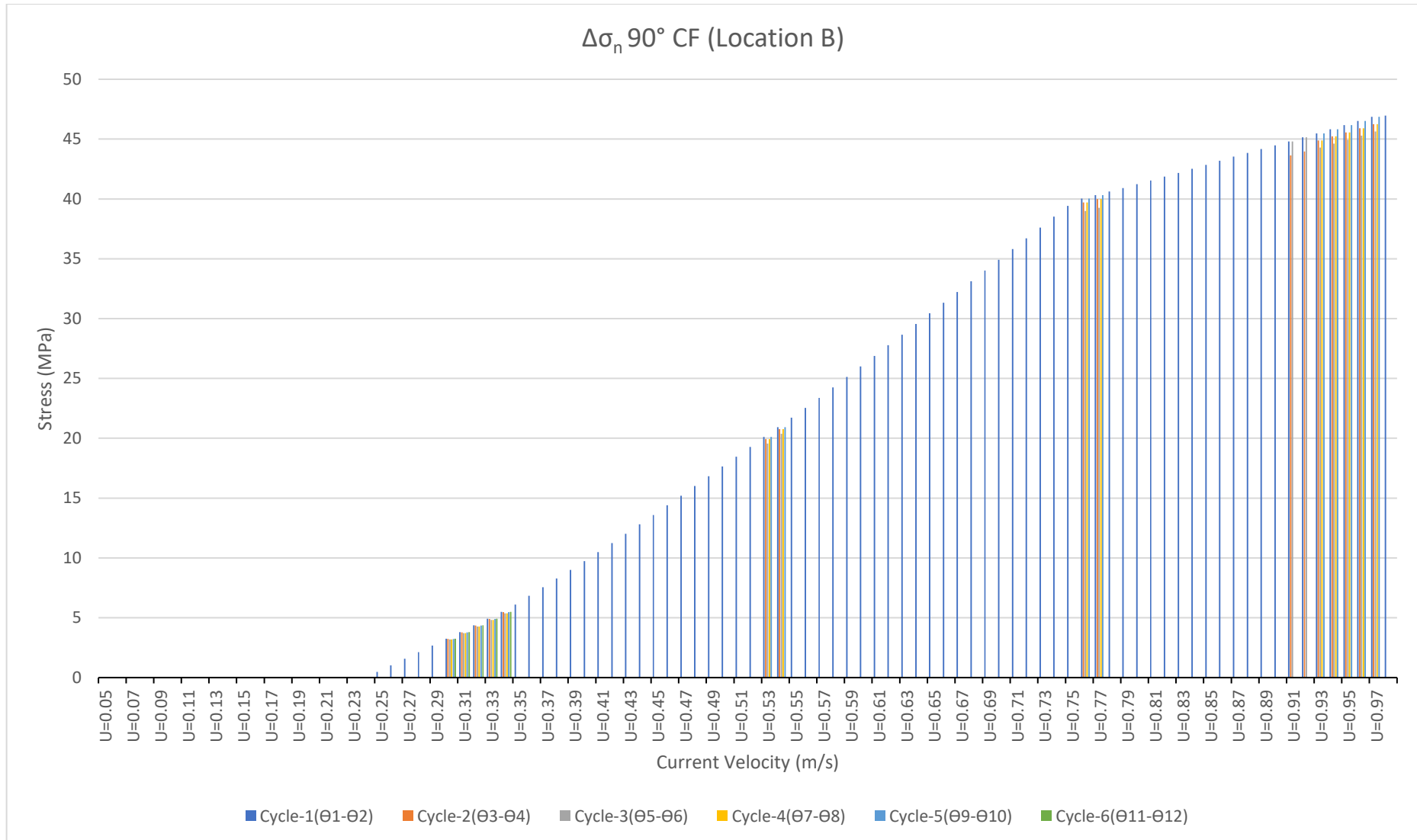


Figure 14-85: $\Delta\sigma_n$ (Case-2(b) - 90° Flow CF) at Location B

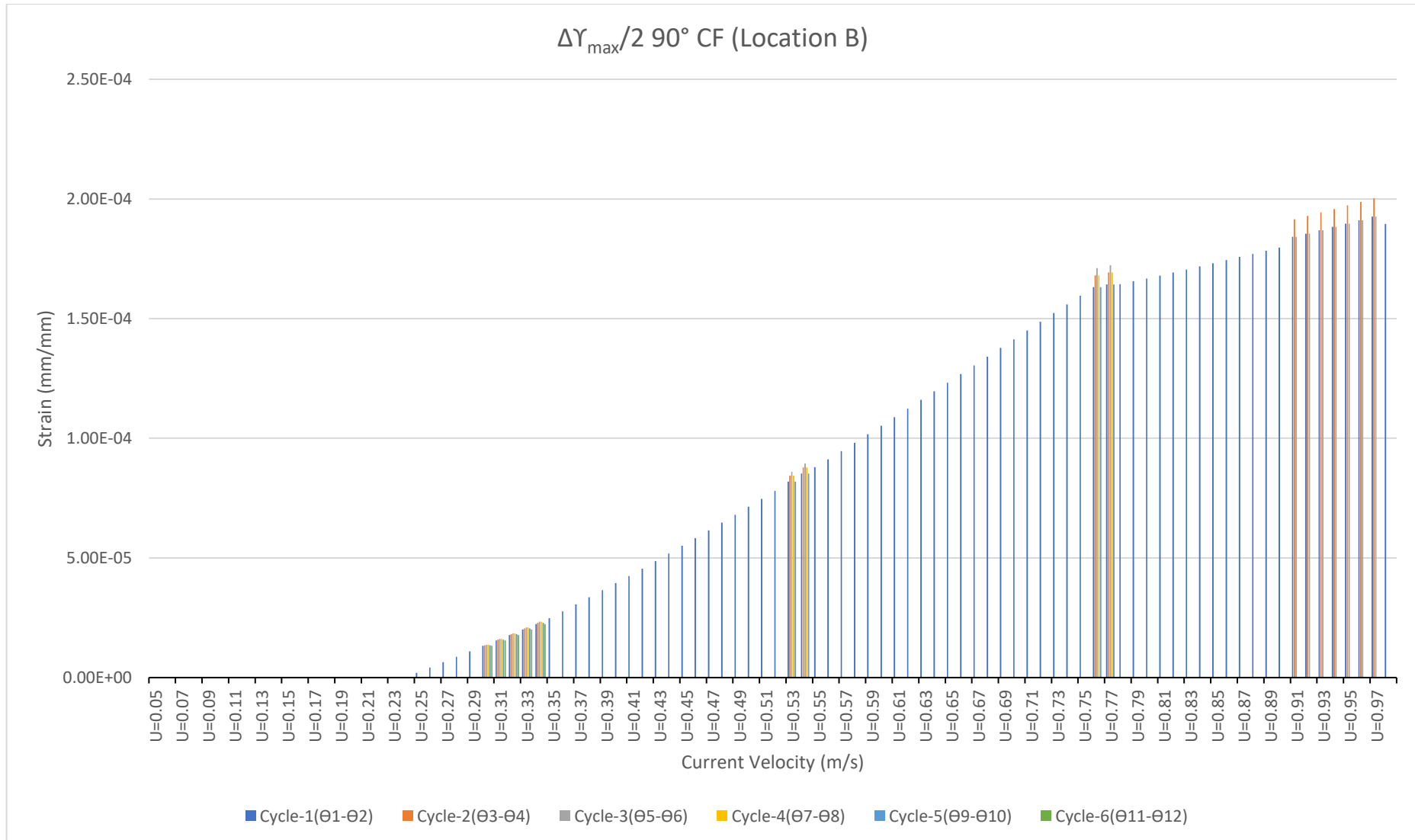


Figure 14-86: $\Delta\gamma_{\max}/2$ (Case-2(b) - 90° Flow CF) at Location B

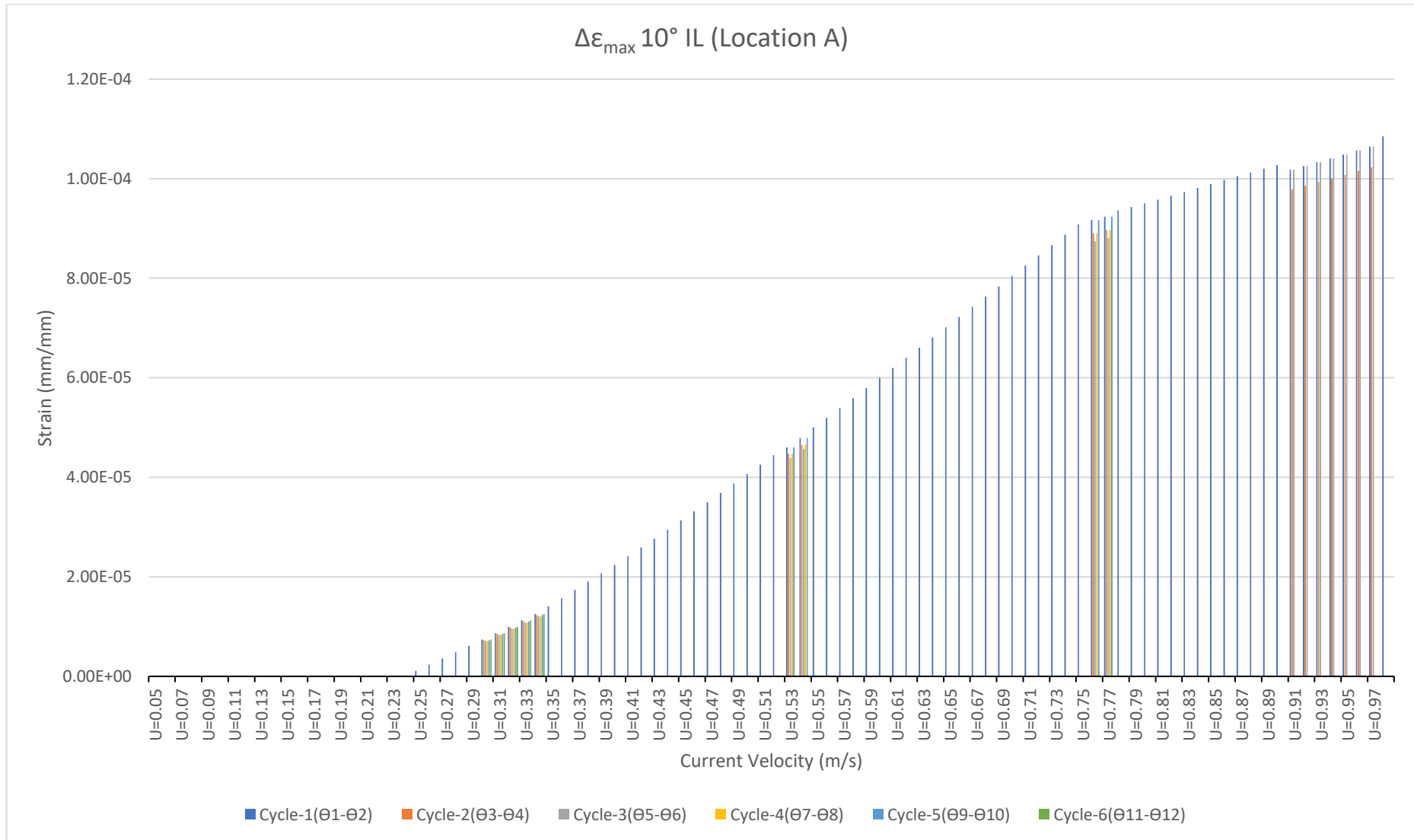


Figure 14-87: $\Delta\varepsilon_n$ (Case-2(b) - 90° Flow CF) at Location B

4. Fatigue

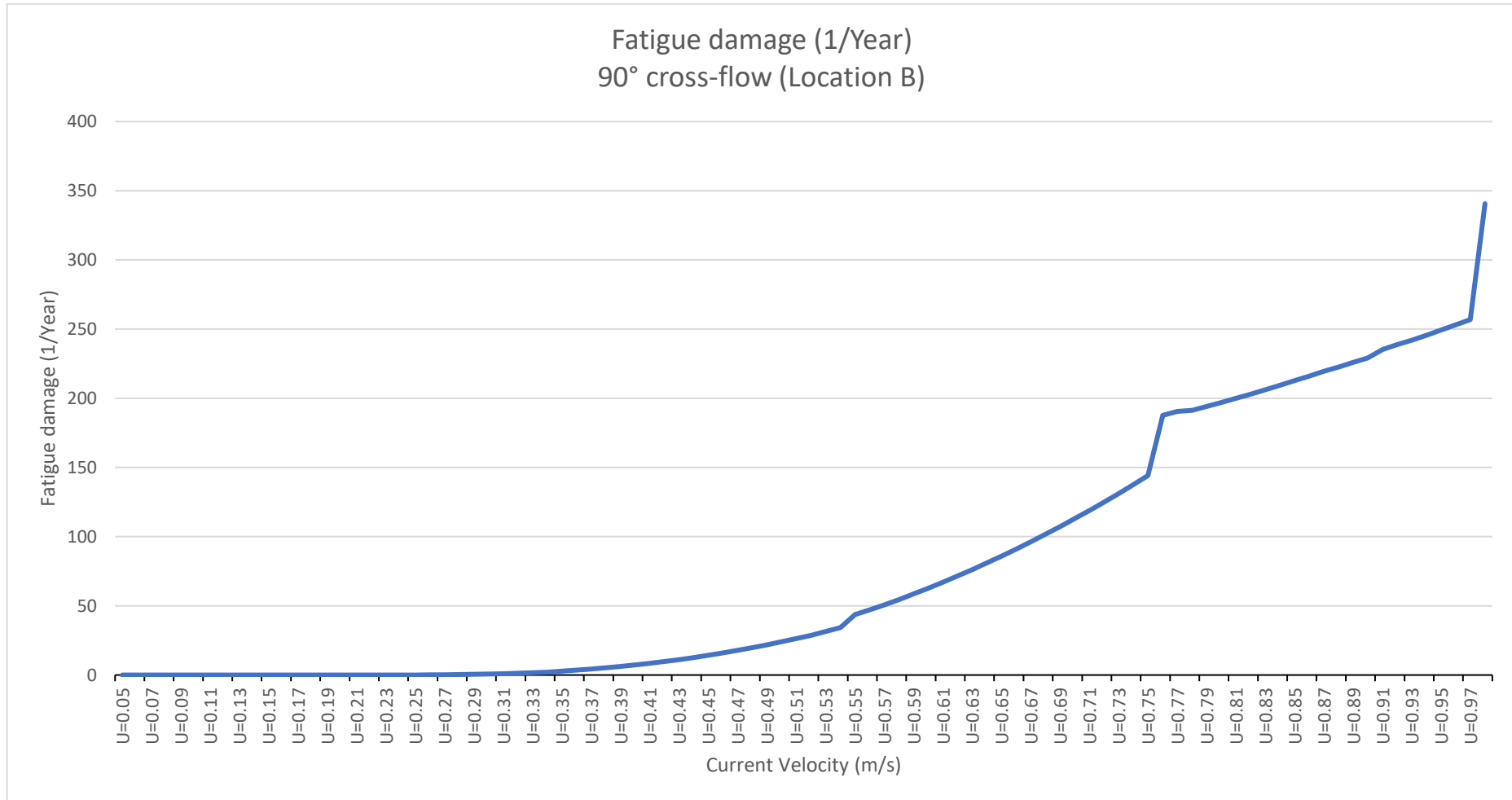


Figure 14-88: Fatigue damage per year for (Case-2(b) - 90° Flow CF) at Location B